



**HAL**  
open science

# Identification of Contact Forces and Thermomechanical Couplings in 2D Granular Systems Using Simulations and Full-field Measurement Techniques: VFM, LSA and IRT

Kunanon Jongchansitto

► **To cite this version:**

Kunanon Jongchansitto. Identification of Contact Forces and Thermomechanical Couplings in 2D Granular Systems Using Simulations and Full-field Measurement Techniques: VFM, LSA and IRT. Mechanical engineering [physics.class-ph]. Université Clermont Auvergne; Mahāwitthayālai Chāng Mai, 2023. English. NNT : 2023UCFA0129 . tel-04574583

**HAL Id: tel-04574583**

**<https://theses.hal.science/tel-04574583>**

Submitted on 14 May 2024

**HAL** is a multi-disciplinary open access archive for the deposit and dissemination of scientific research documents, whether they are published or not. The documents may come from teaching and research institutions in France or abroad, or from public or private research centers.

L'archive ouverte pluridisciplinaire **HAL**, est destinée au dépôt et à la diffusion de documents scientifiques de niveau recherche, publiés ou non, émanant des établissements d'enseignement et de recherche français ou étrangers, des laboratoires publics ou privés.



# Université Clermont – Auvergne

Ecole doctorale : Sciences Pour l'Ingénieur

Unité de recherche : Institut Pascal (UMR 6602, UCA/CNRS)

## Thèse de doctorat

Spécialité : Ingénierie mécanique

En co-tutelle avec : Chiang Mai University (CMU), Faculty of Engineering

---

*Identification of Contact Forces and Thermomechanical Couplings  
in 2D Granular Systems Using Simulations and Full-field  
Measurement Techniques: VFM, LSA and IRT*

---

**Kunanon JONGCHANSITTO**

Présentée et soutenue publiquement le 15 décembre 2023 devant le jury composé de

M. Supasit RODKWAN	Professor	Kasetsart University	Président, Rapporteur
M. Saeid NEZAMABADI	McF HDR	Université de Montpellier	Rapporteur
Mme Karine LAVERNHE-TAILLARD	McF HDR	ENS Paris-Saclay	Examinatrice
M. Wetchayan RANGSRI	Professor	Chiang Mai University	Examineur
M. Panupat CHAIWORN	Professor	Chiang Mai Rajabhat University	Examineur
M. Xavier BALANDRAUD	Professeur	Clermont Auvergne INP	Directeur de these
M. Michel GRÉDIAC	Professeur	Université Clermont Auvergne	Co-directeur de these
M. Itthichai PREECHAWUTTIPONG	Professor	Chiang Mai University	Co-directeur de these

Invités : M. Jean-Benoît LE CAM (Université Rennes 1), M. Benoit BLAYSAT (Université Clermont Auvergne), M. Thomas JAILIN (Université Clermont Auvergne), M. Chaiky RANGSIYAKULL (Chiang Mai University) et M. Pawarut JONGCHANSITTO (Chiang Mai University)



**Titre de la thèse** Identification des forces de contact et des couplages thermomécaniques dans des systèmes granulaires 2D à l'aide de simulations et de techniques de mesure de champs : MCV, ASL et TIR

**Doctorant** M. Kunanon JONGCHANSITTO

**Degré** Doctorat

**Directeurs de la thèse** Professeur Xavier BALANDRAUD

Professeur Michel GRÉDIAC

Assoc. Prof. Itthichai PREECHAWUTTIPONG

### **Résumé**

Les matériaux granulaires sont des ensembles de particules solides de formes, matériaux et tailles variés. Dans le passé, des expériences ont permis une première compréhension de leurs comportements complexes. Des simulations via la méthode des éléments discrets ont ensuite été largement utilisées. L'expérimentation n'a pas été aussi répandue à cause de difficultés de préparation et d'instrumentation. Au cours des dernières décennies, les techniques de mesure de champs sans contact par caméras se sont rependues dans la communauté de la mécanique expérimentale. Certaines ont été utilisées pour étudier des milieux granulaires bidimensionnels (2D) : vélocimétrie d'images de particules (VIP) pour mesurer des motifs de déformation ; corrélation d'images numériques (CIN) pour mesurer les déformations de particules ; photoélasticimétrie pour mesurer le cisaillement dans des particules biréfringentes ; analyse thermoélastique des contraintes (ATC) par thermographie infrarouge (TIR) pour mesurer la pression hydrostatique dans les particules. Certaines techniques ont permis d'identifier les forces interparticulaires via des traitements appropriés, dans les limites de chaque technique. Les milieux granulaires souples ont rarement été étudiés via ces techniques. Dans ce contexte, l'objectif de la thèse est de développer d'autres techniques de mesure de champs pour identifier : 1) les forces de contact par la méthode des champs virtuels (MCV) à partir des déformations obtenues par analyse spectrale localisée (ASL) ; 2) les couplages thermomécaniques dans des particules souples par TIR.

Des déformations fournies par modèle éléments finis ont d'abord été utilisées pour le premier objectif. Il a été démontré que si la réponse mécanique du matériau constitutif



est connue, les forces peuvent être identifiées puisqu'elles sont proportionnelles à une intégrale des déformations mesurées, pondérées par leurs pendants virtuels. Différentes stratégies ont été testées pour proposer des champs de déplacements virtuels cinématiquement admissibles. La robustesse de l'identification a été étudiée par rapport à diverses sources d'erreur. Des mesures par ASL, offrant un compromis pertinent entre résolution de déformation et résolution spatiale, ont ensuite été effectuées sur un système à trois particules et sur des systèmes plus grands constitués de particules cylindriques en PA66. Outre les équations de la MCV, l'équilibre des particules et la troisième loi de mouvement de Newton ont été pris en compte pour proposer une stratégie adaptée au traitement de données expérimentales. L'analyse statistique de systèmes bidisperses et tridisperses a permis de caractériser les lois exponentielles et lois de puissance dans les réseaux de forces forts et faibles respectivement, que l'on trouve habituellement dans les systèmes polydisperses secs.

Pour le second objectif, des milieux granulaires constitués de cylindres en polyuréthane thermoplastique (TPU) de section ellipsoïdale ont été soumis à une compression cyclique confinée. Le TPU a été choisi pour son élasticité entropique, lui conférant une signature thermique supérieure à celle des matériaux utilisés pour la ATC. Ce matériau confère également un caractère souple aux systèmes granulaires produits. Sur la base de considérations d'adiabaticité et de cycles thermodynamiques, un fort couplage thermoélastique (CTE) a été révélé dans toutes les zones de contact entre particules en raison des concentrations de contrainte. Une forte dissipation mécanique liée à l'endommagement, la viscosité et le frottement a été constatée à des contacts spécifiques et au sein de certaines particules. Les données CTE ont été traitées pour un système granulaire comprenant environ 600 contacts, fournissant ainsi des informations statistiques. Il est montré que la TIR fournit des informations précieuses qui ouvrent des perspectives pour la construction de modèles thermodynamiques pertinents adaptés aux matériaux granulaires souples.

**Mots-clés:** Matériaux granulaires, Techniques de mesure de champs, Méthode des Champs Virtuels, Analyse Spectrale Localisée, Thermomécanique, Force de contact

<b>Dissertation Title</b>	Identification of Contact Forces and Thermomechanical Couplings in 2D Granular Systems using Simulations and Full-field Measurement Techniques: VFM, LSA and IRT
<b>Author</b>	Mr. Kunanon Jongchansitto
<b>Degree</b>	Doctor of Philosophy in Mechanical Engineering
<b>Advisory Committee</b>	Professeur Xavier Balandraud Professeur Michel Grédiac Assoc. Prof. Itthichai Preechawuttipong

### **Abstract**

Granular materials are collections of solid particles of various shapes, materials and sizes, making their behavior complex. In the past, effective understanding was mainly derived from experiments, which were limited by the equipment available at the time. Numerical approaches based on the Discrete Element Method were then developed. These are powerful, reliable and widely used as efficient tools for studying granular media. In comparison, experimentation was not as widespread due to difficulties of preparation and instrumentation. In recent decades, non-contact full-field measurement techniques based on cameras have become increasingly familiar and attractive in the experimental mechanics community. This is due to rapid advances in equipment. Some of these were used to study two-dimensional (2D) granular media under mechanical loading: particle image velocimetry (PIV) to measure strain patterns; digital image correlation (DIC) to measure strains within deformable particles; photoelasticimetry to measure shear stresses in particles made of birefringent material; and thermoelastic stress analysis (TSA) based on infrared thermography (IRT) to measure hydrostatic stresses in particles. Some of these techniques enabled identifying the interparticle forces using appropriate image processing. However, there are certain limitations due to the specifications of each technique. Besides, soft granular materials have rarely been studied with these techniques. In this context, the aim of the thesis is to develop other full-field techniques for two purposes: 1) to identify contact forces using the virtual fields method (VFM) from knowledge of the strain distribution obtained by localized spectrum analysis (LSA); 2) to identify thermomechanical couplings in soft particles using IRT.

Synthetic strain data provided by a finite element model were first used for the first objective. It was shown that if the mechanical response of the constitutive material is known, the contact forces applied to a particle can be identified since they are proportional to an integral of the measured strains weighted by their virtual counterparts. Various strategies were tested to propose kinematically admissible fields for the virtual displacements. Identification robustness was studied with respect to various sources of error. Measurements by LSA, providing a relevant compromise between strain resolution and spatial resolution, were then performed on a three-particle system and bigger systems made of PA66 cylindrical particles. In addition to the VFM equations, particle equilibrium and Newton's third law of motion were considered to propose a relevant strategy for processing the experimental data. The statistical analysis for bidisperse and tridisperse systems allowed to characterize the exponential and power laws for the strong and weak force networks, respectively, that are usually found in polydisperse dry systems.

For the second objective, granular media made of thermoplastic polyurethane (TPU) cylinders with ellipsoidal cross-section were subjected to cyclic confined compression while being observed by an IRT camera. TPU was chosen because it features entropic elasticity, which gives a higher thermal signature than the materials used for TSA. This material also lends a soft character to the granular systems produced. Based on considerations of adiabaticity and thermodynamic cycle completion, strong thermoelastic coupling (TEC) was revealed in the contact areas between all particles due to stress concentrations. Strong mechanical dissipation (MD) was found at specific contacts and within some particles due to damage, viscosity and friction. TEC data was processed for a granular system comprised of about 600 interparticle contacts, providing statistical information. It is demonstrated that IRT provides valuable information to open prospects for building thermodynamically relevant models suitable for soft granular materials.

**Keywords:** Granular materials, Full-field measurement techniques, Virtual Fields Method, Localized Spectrum Analysis, Thermomechanics, Contact force

# CONTENTS

	Page
Résumé	a
Abstract	c
List of Tables	g
List of Figures	h
Résumé étendu	n
General Introduction	1
Chapter 1 Theoretical Background	7
1.1 Introduction	7
1.2 Mechanics of granular material	8
1.3 Thermomechanics of continuous material	32
1.4 Full-field measurement techniques and post-processing for thermomechanical analysis	37
1.5 Full-field measurement techniques applied to granular materials	47
1.6 Conclusion	53
Chapter 2 Identification of contact forces from synthetic strain data	55
2.1 Introduction	55
2.2 Additional assumptions for contact force identification	56
2.3 Defining virtual fields	60
2.4 Influence of the noise magnitude	71
2.5 Sensitivity of the identification technique to other sources of error	73
2.6 Accounting for friction at the contacts	77
2.7 Estimating contact forces with fewer pixels	80
2.8 Conclusion	82
Chapter 3 Application of VFM to experimental strain data obtained by LSA	84
3.1 Introduction	84
3.2 Application to a three-particle system	84
3.3 Application to bigger granular systems	97
3.4 Comparison between experiments and numerical simulations	119

3.5 Conclusion	127
Chapter 4 Towards a thermo-mechanical analysis	128
4.1 Introduction	128
4.2 Material and Methods	130
4.3 Preliminary observations	136
4.4 Data processing	138
4.5 Application to small granular system	142
4.6 Thermomechanical behavior of a larger granular system	154
4.7 Conclusion	162
Chapter 5 Conclusion and Perspectives	164
References	168
Appendix A	180
Appendix B	187

## LIST OF TABLES

	Page
Table 2.1	71
Table 2.2	80
Table 3.1	96
Table 3.2	98
Table 4.1	134
Table 4.2	148
Table A.1	182

## LIST OF FIGURES

		Page
Figure 1.1	Examples of granular materials.	9
Figure 1.2	Gas, liquid, and solid region of a bead pile [1].	9
Figure 1.3	Schematic sketch of an Apollonius packing [2].	14
Figure 1.4	Example of normal force network obtained by simulation [3].	16
Figure 1.5	Contact force measurement in the literature: a) photoelastic image of a 2D system under isotropic compression [4], b) setup for the carbon paper method [5], c) setup and result using geomembranes [6], d) setup and result of the contact paper method [7].	17
Figure 1.6	Probability density function (PDF) of the normal contact forces normalized by the mean normal contact force [8], for two values of the coefficient of friction between particles (white, 0.1 and black, 0.4).	18
Figure 1.7	Probability density function of the normal forces normalized by the mean normal contact force, for frictionless contacts, for different volume fractions [9]: a) pentagon packings, b) disk packings.	20
Figure 1.8	Probability density function of the normal contact forces normalized by the mean of normal contact force for different particle size spans [10].	21
Figure 1.9	Angular distribution of contact directions for three granular packings [2]: a) under gravity, b) under isotropic compression, c) under vertical loading.	22
Figure 1.10	Angular distribution of contact forces in the strong and weak networks for a packing under vertical loading [11].	23
Figure 1.11	Flowchart of molecular dynamics algorithm.	28
Figure 1.12	Schematic of two particles, $i$ and $j$ , in contact.	28
Figure 1.13	Three cases of thermomechanical evolution [12].	36
Figure 1.14	Spectrum of electromagnetic waves [13].	38
Figure 1.15	Plane stress problem [14].	45
Figure 1.16	Use of photoelasticimetry to identify interparticle force networks: a) schematic of the experimental loading system; b) typical images for an isotropically compressed state (top) and a sheared state (bottom); c) example of photoelastic pattern in a single disk [4].	48
Figure 1.17	Examples of experiments using PIV: a) granular flow in silo [15], b) landslide and a giant tsunami [16], and c) granular flow under gravity [17].	50
Figure 1.18	Experiment and contact force network: a) Tolomeo's study [18]; b) Fanxiu's study [19].	51

Figure 1.19	Application of infrared thermography to the analysis of the mechanics of granular materials: a) temperature patterns associated to mechanical dissipation in a dry siliceous sand under shearing [20]; b) temperature changes associated to thermoelastic coupling, converted in hydrostatic stress, in two-dimensional granular systems under cyclic confined compression [21]; c) evidence of differences in thermal response between particles made in energetic material and entropic material [22].	53
Figure 2.1	Cylindrical particle subjected to several contacts. The objective is to apply VFM to identify the two components of the in-plane interparticle force $\mathbf{F}$ at point P.	58
Figure 2.2	Illustration in the case of two opposite frictional contacts: a) force $\mathbf{F}$ at point P to be identified by VFM; b-c) shape of the particle subjected to two virtual displacement fields $\mathbf{u}^{*(1)}$ and $\mathbf{u}^{*(2)}$ enabling the identification of the two components of $\mathbf{F}$ .	60
Figure 2.3	Finite element models to obtain real strain fields: a) Configuration C1; b) Configuration C2; c) Configuration C3.	62
Figure 2.4	Different procedures for the identification of the force component $F_2$ at Point A for Configuration C1 in Figure 2.3-a: a) field of the virtual displacement component $u_2^*$ ; b) corresponding virtual strain fields $\varepsilon_2^*$ . First column: closed-form expressions (Procedure #1). Second column: randomly defined from a coarse mesh (Procedure #2). Third column: triangulation-based linear interpolation (Procedure #3). Fourth column: triangulation-based natural neighbor interpolation (Procedure #4).	67
Figure 2.5	Four-contact system: comparison between the four procedures for the identification of the force component $F_2$ at Point A with respect to the reference value ( $-10$ kN).	69
Figure 2.6	Six-contact system (Configuration C2): comparison between the four procedures for the identification of the force component $F_2$ at Point A with respect to the reference value ( $-10$ kN).	70
Figure 2.7	Real strain fields $\varepsilon_2$ obtained by the FE model for Configuration C1. Gaussian noise with different standard deviations (SDs) is added. Pixel size is equal to $25 \mu\text{m}$ , as in the experiment with the three-particle system in the Chapter 3.	72
Figure 2.8	Influence of the noise level on the mean and standard deviation (SD) of the relative error on force $F_2$ identified at Point A.	73
Figure 2.9	Effect of a shift between virtual and real strain fields: a) schematic representation for the top particle for Configuration C3; b) mean force components identified at points A, B and C.	75
Figure 2.10	Effect of data missing along the boundary of a particle: a) schematic representation for the top particle in Configuration C3; b) mean and standard deviation of the relative error compared to the data provided by the FE model.	78



Figure 2.11	Comparison of the contact forces identified with VFM and their reference counterparts obtained by the FE model: mean and standard deviation (SD) of the relative error at each contact for Configuration C3.	79
Figure 2.12	Comparison of the contact forces identified with VFM, and their reference counterparts obtained by the FE model (with a number of pixels reduced by 4 in both directions): mean and standard deviation (SD) of the relative error at each contact for Configuration C3.	82
Figure 2.13	Comparison of the contact forces identified with VFM, and their reference counterparts obtained by the FE model (with and without a number of pixels reduced by 4 in both directions): mean deviation (SD) of the relative error at each contact for Configuration C3.	82
Figure 3.1	Experiment on a three-particle system: a) cylindrical particles; b) experimental set-up.	87
Figure 3.2	Experimental strain maps used as inputs for the contact force identification procedure.	88
Figure 3.3	Flowchart of the five strategies to identify the contact force components in the case of experimental strain data.	92
Figure 3.4	Comparison of the different strategies for contact force identification from experimental data: a) deviation from the local force equilibrium; b) deviation from the local moment equilibrium; c) deviation from Newton's third law of motion.	95
Figure 3.5	Contact force at each contact identified using the five strategies.	96
Figure 3.6	Photo of the three experimental configurations tested: a) monodisperse; b) bidisperse; c) tridisperse.	98
Figure 3.7	Experimental setup for the big granular systems: a) checkerboard on a particle, exhibiting an angle of about 10 degrees with respect to the horizontal direction; b) experimental equipment.	101
Figure 3.8	In-plane strain components for the monodisperse case.	102
Figure 3.9	In-plane strain components for the bidisperse case.	103
Figure 3.10	In-plane strain components for the tridisperse case.	104
Figure 3.11	Results for the monodisperse configuration: a) contact force network; b) angular force distribution; c) normal force network.	106
Figure 3.12	Results for the bidisperse configuration: a) contact force network; b) angular force distribution; c) normal force network.	108
Figure 3.13	Results for the tridisperse configuration: a) contact force network; b) angular force distribution; c) normal force network.	109
Figure 3.14	Normal force network and angular force distribution distinguishing between strong forces and weak forces: a) monodisperse configuration; b) bidisperse configuration; c) tridisperse configuration.	112

Figure 3.15	Probability density function (PDF) of the normalized normal forces: a) in the force network b) in the weak network; c) in the strong network; d) in the weak network in semi-natural logarithmic scale; e) in the strong network in semi-natural logarithmic scale.	114
Figure 3.16	Tangential force network: a) monodisperse configuration; b) bidisperse configuration; c) tridisperse configuration.	116
Figure 3.17	Histogram of ratio between tangential and normal forces: a) monodisperse configuration; b) bidisperse configuration; c) tridisperse configuration.	117
Figure 3.18	Example of fringes appearing in the strain fields in the case of an incorrect angular orientation of the checkerboard.	118
Figure 3.19	Comparison between the normal force networks obtained by experiment and by simulation, with the particles in the same locations: a) monodisperse configuration; b) bidisperse configuration; c) tridisperse configuration.	121
Figure 3.20	Comparison between the angular force distributions obtained by experiment and by simulation, with the particles in the same locations: a) monodisperse configuration; b) bidisperse configuration; c) tridisperse configuration.	123
Figure 3.21	Comparison between the probability density functions (PDFs) of normalized normal forces obtained by experiment and by simulation, with the particles in the same locations: a) in the force network; b) in the weak network; c) in the strong network; d) in the weak network in semi-natural logarithmic scale; e) in the strong network in semi-natural logarithmic scale.	124
Figure 3.22	Same as Figure 3.21 but adding results with random locations of the particles for the simulations: a) monodisperse configuration; b) bidisperse configuration; c) tridisperse configuration. For each configuration, three simulations were performed for the random location case. Left column: in the weak network. Right: in the strong network.	126
Figure 4.1	Material elaboration and elliptical particles.	131
Figure 4.2	Experimental setup: a), b) a small granular system and c), d) a large granular system.	132
Figure 4.3	a) Schematic representation of the mechanical loading and b-e) temperature changes during test T6 (monodisperse configuration, force rate $\pm 5$ kN/s, maximum 3 kN). The spatial resolution of the thermal maps is equal to 131.6 $\mu\text{m}$ .	135
Figure 4.4	Schematic temperature variations reflecting thermoelastic coupling (TEC) and mechanical dissipation (MD) contributions assuming adiabatic conditions.	140

Figure 4.5	Influence of the loading rate (monodisperse configuration, maximum 3 kN, tests T1 to T6). $\theta_{\text{half}}(\#1)$ and $\theta_{\text{MD}}(\#20)$ are the temperature changes in the middle of the 1 <sup>st</sup> cycle and at the end of the 20 <sup>th</sup> cycle, respectively. The spatial resolution of the maps is equal to 131.6 $\mu\text{m}$ .	144
Figure 4.6	Comparison between monodisperse configuration (test T6) and bidisperse configuration (test T8) with same loading conditions (force rate $\pm 5$ kN/s, maximum 3 kN). The spatial resolution of the thermal maps is equal to 131.6 $\mu\text{m}$ .	146
Figure 4.7	Comparison between monodisperse and bidisperse configurations with the same loading conditions (force rate $\pm 2.5$ kN/s, maximum 3 kN) but using smaller spatial resolution compared to tests T5 and T7, respectively. See Table 4.2 and Figure 4.6 for comparison with measurements at 131.6 $\mu\text{m}$ spatial resolution.	149
Figure 4.8	Comparison of results depending on the spatial resolution in zone Z1 for two similar tests (monodisperse configuration, force rate $\pm 2.5$ kN/s, maximum 3 kN, minimum 0.3 kN).	150
Figure 4.9	Temperature changes at various points in the two small granular systems (see locations in Figure 4.7) as a function of a pixel size projected on the measurement surface, and for the same loading conditions (force rate $\pm 2.5$ kN/s, maximum 3 kN, minimum 0.3 kN).	151
Figure 4.10	Heat produced by mechanical dissipation (MD) during each mechanical cycle during test T6 (monodisperse configuration, force rate $\pm 5$ kN/s, maximum 3 kN): a) variations along the cycles at four points in the granular system; b) over the first cycle; c) average over the fifth to twentieth cycles. The spatial resolution of the maps is equal to 131.6 $\mu\text{m}$ .	153
Figure 4.11	Heat produced by thermoelastic coupling (TEC) over the loading phase during test T6 (monodisperse configuration, force rate $\pm 5$ kN/s, maximum 3 kN): a) in the first cycle; b) in the twentieth cycle. The spatial resolution of the maps is equal to 131.6 $\mu\text{m}$ .	154
Figure 4.12	Thermoelastic coupling in the tridisperse granular material during the first half cycle. Left column: heat density over half a cycle; right column: corresponding mean heat rate density.	156
Figure 4.13	Mechanical dissipation in the tridisperse granular material: heat density over the first cycle.	157
Figure 4.14	Movement of the particles: a) example for test T11; b) illustration of interparticle movement indicators; c) identification of normal (small white lines) and tangential (small red lines) directions at each contact.	159
Figure 4.15	Comparison between interparticle movement indicators and contact calorific indicators for test T11.	161
Figure 4.16	Calorific signature associated with thermoelastic coupling at the interparticle contacts in the tridisperse system: a) example of histogram and corresponding probability density function (PDF) using a generalized extreme value distribution; b) comparison of the PDFs for the three loading levels.	162

Figure A.1	Fields of normalized temperature changes generated by simulations: a) Sample #1; b) Sample #2; c) Sample #3.	184
Figure A.2	Probability density function of normalized temperature change obtained from both simulations in semi-natural logarithmic scale for: a) Sample #1; b) Sample #2; c) Sample #3. Note that simulations “A”, “B”, “C”, “D”, and “E” were performed under the same experimental configuration, excluding the particle locations, while the simulation “SP” was conducted under all the same as in the experiments (the simulation in the previous section).	186
Figure B.1	Schematic view of the cross-sections of two cylinders in contact at point I.	189



## Résumé étendu

Les matériaux granulaires sont un type de matière que l'on trouve partout et que l'on utilise dans la vie quotidienne (par exemple : le sucre, le sel et le poivre) et dans de nombreux domaines industriels (par exemple : le sable, les cailloux et les briques sont nécessaires à la construction ; les poudres sont utilisées dans certains processus de fabrication industrielle). Un matériau granulaire se définit comme un ensemble de particules solides. Ces dernières peuvent être constituées de grains de forme, de matériau et de taille variés. Ils peuvent aller du sable à la roche, voire à des agrégats interplanétaires (anneaux de planètes, astéroïdes). Le comportement des matériaux granulaires est complexe et difficile à prévoir à l'échelle des particules. Les matériaux discrets peuvent se comporter macroscopiquement comme des solides ou des liquides, en fonction de nombreux paramètres. C'est l'une des raisons pour lesquelles ils sont complexes à modéliser de manière générale.



*Exemples de matériaux granulaires.*

Il y a plusieurs décennies, des chercheurs et des scientifiques se sont intéressés aux matériaux discrets alors que la théorie de la mécanique des milieux continus semblait plutôt bien développée. En 1944, Casagrande et Carillo ont été des pionniers en étudiant le comportement des matériaux granulaires par le biais d'expériences et de simulations numériques. Ils ont distingué deux types de résistance, à savoir l'anisotropie induite et

l'anisotropie inhérente. Quelques décennies plus tard, Dantu a mis en évidence une hétérogénéité significative dans la distribution des forces de contact dans des matériaux granulaires bidimensionnels (2D) en utilisant la photoélasticité. Biarez a développé le concept de *fabric anisotropy* en relation avec la distribution des orientations de contact en étudiant des empilements de disques. La relation contrainte-dilatation proposée par Rowe est aujourd'hui largement utilisée en mécanique des sols. En 1966, Weber a proposé une formule reliant les forces de contact locales à un tenseur de contrainte spécifique de type Cauchy, à savoir un tenseur de contrainte moyen sur un groupe de particules. Ces résultats significatifs et la compréhension des milieux granulaires au cours de ces décennies ont été principalement obtenus à partir d'expériences menées sur des matériaux analogues ainsi que sur des matériaux réels. Des études théoriques basées sur des mélanges de particules idéalisées ont également été développées. Cependant, ces types de matériaux étaient plutôt difficiles à analyser expérimentalement à l'échelle locale en raison des techniques et des instrumentations disponibles à l'époque. En 1971, Cundall a mis au point une approche numérique appelée méthode des éléments distincts (*Distinct Element Method*, ou DEM) qui s'appuie sur la mécanique des roches. Cette méthode considère la matière comme un système à contacts multiples, contrairement à la méthode classique des éléments finis. Chaque grain d'un matériau granulaire est considéré comme un corps rigide individuel régi par les lois du mouvement de Newton et interagissant avec ses voisins par le biais de lois de contact frictionnel. Il existe deux approches de la DEM : la méthode dite *smooth DEM* connue sous le nom de dynamique moléculaire (*Molecular Dynamics*, ou MD) et la méthode dite *non-smooth DEM* connue sous le nom de dynamique non régulière des contacts (*Non-Smooth Contact Dynamics* – NSCD ou *Contact Dynamics* – CD). La première approche est basée sur un algorithme explicite qui prend en compte l'interaction entre les contacts en fonction des déplacements relatifs et des vitesses des particules. La seconde approche est basée sur l'analyse convexe, proposant un cadre cohérent pour les lois « *non-smooth* » impliquées dans le contact, comme le frottement sec. Les simulations numériques constituent un outil de recherche puissant, fiable et largement utilisé dans le domaine des matériaux granulaires. En parallèle, l'expérimentation n'est pas si répandue en raison des difficultés de préparation et d'instrumentation, ainsi que du nombre souvent limité de particules utilisables dans les

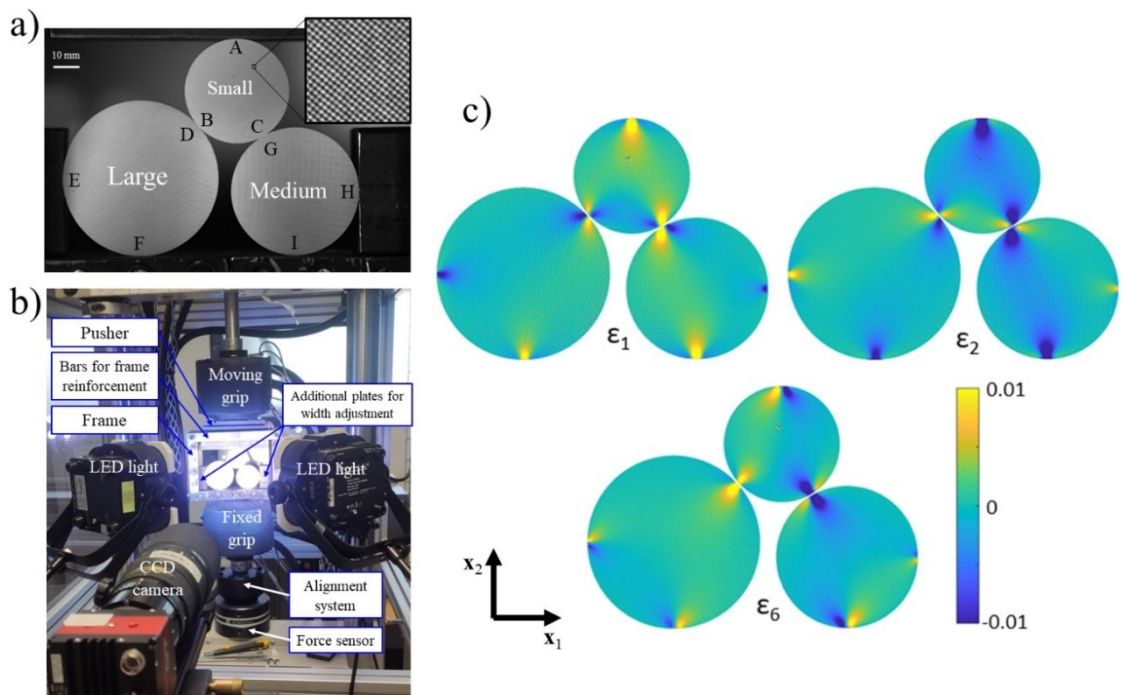
tests. De nos jours, les techniques de mesure de champs, qui sont sans contact et non destructives, sont de plus en plus populaires parmi les ingénieurs et les scientifiques en mécanique expérimentale grâce aux progrès des équipements, c'est-à-dire des caméras, des capteurs, des ordinateurs et des systèmes de traitement d'images. Certaines de ces techniques ont été utilisées pour étudier des milieux granulaires 2D : la méthode dite Vélométrie d'Image de Particules (VIP) pour mesurer des motifs globaux de déformation ; la Corrélation d'Images Numériques (VIN) pour mesurer les déformations des particules elles-mêmes ; la photoélasticimétrie pour mesurer les contraintes de cisaillement dans des particules faites en matériau biréfringent ; et la Analyse Thermoélastique des Contraintes (ATC) basée sur la thermographie infrarouge (TIR) permettant de mesurer les contraintes hydrostatiques dans les particules. Ces techniques permettent d'accéder à des grandeurs physiques distribuées spatialement, telles que des températures, des déplacements et des déformations, en fonction du type de capteur et du post-traitement des données. Elles sont puissantes et avantageuses par rapport aux méthodes traditionnelles qui reposent sur des mesures locales effectuées à l'aide d'équipements courants tels que des thermocouples, des capteurs de déplacement ou des jauges de déformation. Elles peuvent fournir des champs de caractérisation locale permettant de mieux comprendre la réponse globale du matériau. On peut noter que les techniques de mesure de champs ne sont pas nouvelles en mécanique des matériaux granulaires. En effet, Dantu a utilisé la photoélasticimétrie pour étudier ces matériaux en 1950. Depuis, la littérature sur les matériaux granulaires étudiés par des techniques de mesure de champs s'est multipliée.

Dans ce contexte, l'objectif de cette thèse est de développer d'autres techniques de mesure de champs dans deux buts : 1) identifier les forces de contact en utilisant la méthode des champs virtuels (MCV) à partir de la connaissance de la distribution des déformations par analyse spectrale localisée (ASL) ; 2) identifier les couplages thermomécaniques dans des particules souples en faisant de la calorimétrie de déformation (*Deformation Calorimetry*, ou DC) à partir de champs de température obtenus par TIR.



L'identification des forces de contact interparticulaires est un problème difficile dans la communauté des matériaux granulaires. Cette thèse a traité ce problème dans un cas 2D (en utilisant des cylindres empilés) en employant la MCV et la ASL, qui sont respectivement une technique de mesure de champs de déformation et une stratégie d'identification. Des données de déformation synthétiques fournies par un modèle éléments finis (avec du bruit ajouté) ont d'abord été utilisées comme données d'entrée pour adapter et développer la MCV afin d'identifier les forces de contact dans des systèmes granulaires 2D simples. Plusieurs cas ont été simulés : une particule soumise à 4 contacts puis à 6 contacts ; trois particules soumises à une compression confinée. La MCV, qui repose sur la forme faible de l'équation d'équilibre, est généralement utilisée pour identifier des paramètres « matériau » lorsque l'on connaît le chargement mécanique. Inversement, elle a rarement été utilisée pour mesurer les forces appliquées lorsque l'on connaît l'équation constitutive du comportement mécanique du matériau et les valeurs des paramètres associés. Les forces de contact appliquées à une particule peuvent être identifiées via la MCV car elles sont proportionnelles à la moyenne pondérée des composantes de la déformation, les poids étant les composantes des déformations virtuelles. En résumé, chaque particule peut être considérée comme un capteur de force multidirectionnel, qui fournit directement les forces de contact qui lui sont appliquées en traitant convenablement la distribution des déformations avec le principe du travail virtuel. Différentes stratégies ont été testées pour proposer des champs de déplacement virtuels cinématiquement admissibles (*kinematically admissible*, ou KA). Il a été démontré qu'un choix pertinent de champs de déplacement virtuel KA consiste à utiliser une interpolation naturelle basée sur une triangulation entre les points de contact. Diverses simulations ont illustré l'impact du choix des champs virtuels et la robustesse de la technique d'identification, à savoir l'influence de l'amplitude du bruit, un décalage potentiel entre les champs de déformation virtuels et réels, et des données manquantes le long des bords des particules. Différents systèmes multi-contacts ont été étudiés pour cette étude, ce qui a ouvert des perspectives d'application expérimentale. Une première expérience a été réalisée sur un système composé de trois particules soumises à une compression confinée en s'appuyant sur des mesures de déformation obtenues par ASL. Des cylindres en PA66 de 40 mm, 50 mm et 60 mm de diamètre et de 30 mm de longueur

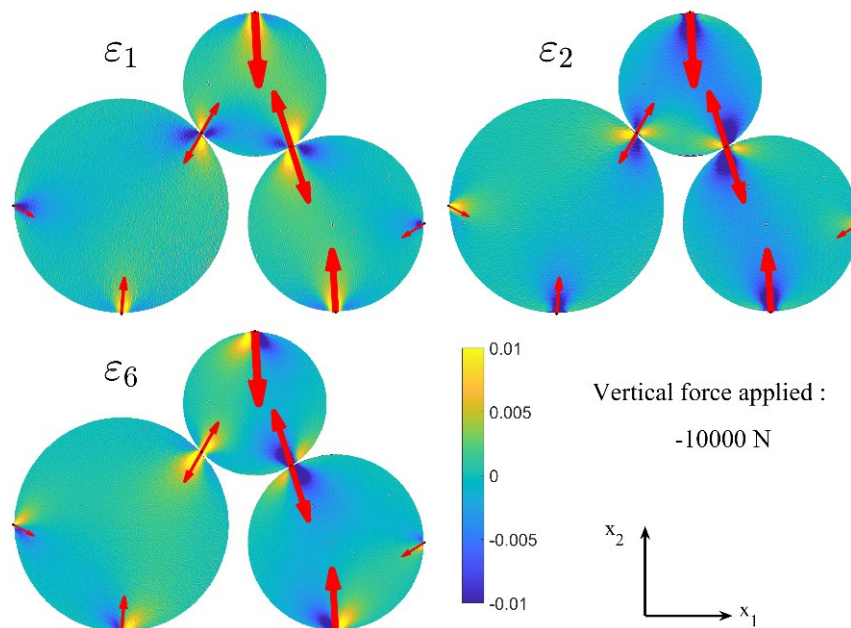
ont été utilisés pour constituer les particules. La ASL est une technique de mesure de champs permettant d'obtenir des champs de déformation en s'appuyant sur les images d'un motif périodique placé à la surface du matériau avant et après chargement mécanique, offrant un compromis intéressant entre résolution de mesure et résolution spatiale. Un motif en damier avec des carrés de  $75\ \mu\text{m}$  de côté a été créé à la surface des cylindres à l'aide d'une graveuse laser. Les cylindres ont ensuite été placés dans un cadre rectangulaire en acier de 150 mm de largeur et soumis à une compression confinée à l'aide d'une machine d'essais uniaxiale. Une force de compression verticale de 10 kN a été appliquée à très faible vitesse de chargement afin de limiter la part visqueuse de la déformation et de supposer une loi de comportement élastique linéaire isotrope pour l'utilisation de la MCV. Il a été estimé que le bruit sur les cartes de déformation présentait un écart-type de l'ordre de  $2 \times 10^{-4}$ , pour une résolution spatiale de 1.05 mm.



*Expérience sur un système à trois particules : a) particules cylindriques en PA66 soumises à une compression confinée ; b) photo du dispositif expérimental ; c) cartes de déformation mesurées par ASL pour une force de compression verticale de 10 kN.*

L'expérience a montré que les forces de contact obtenues par la MCV seule ne vérifiaient pas parfaitement l'équilibre des forces, l'équilibre des moments et la troisième loi du mouvement de Newton (principe d'action-réaction au niveau des contacts

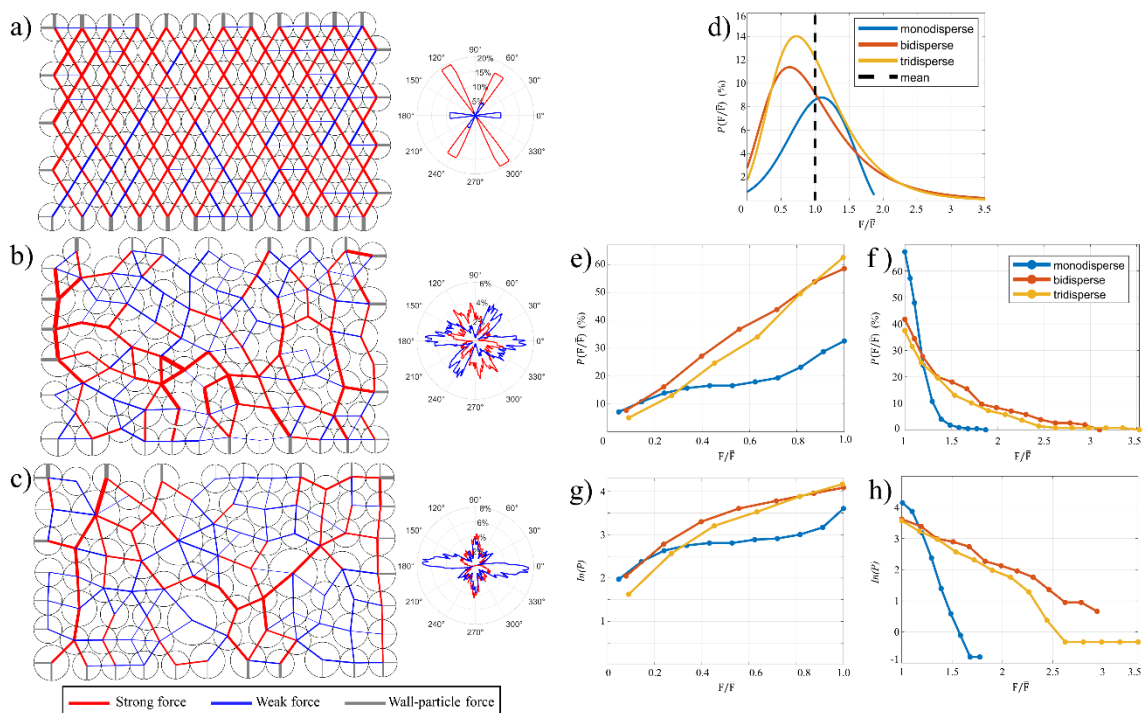
interparticulaires). Cela peut être dû à des mouvements hors-plan ou à une erreur dans les paramètres élastiques du matériau des particules. D'autres approches d'identification des forces ont donc été proposées en ajoutant des équations issues de l'équilibre local de chaque particule et de la troisième loi du mouvement de Newton. Étant donné que le nombre d'équations disponibles devient alors supérieur au nombre d'inconnues (les composantes des forces de contact), plusieurs stratégies ont été comparées afin de déterminer la meilleure façon de traiter ces équations pour l'identification des forces de contact. La meilleure stratégie a été obtenue en utilisant les équations de la MCV avec des multiplicateurs de Lagrange permettant respecter strictement l'équilibre des forces et des moments pour chaque particule ainsi que la troisième loi du mouvement de Newton à chaque contact interparticulaire.



*Forces de contact identifiées par MCV superposées aux champs de déformation mesurés, pour une force de compression verticale de 10 kN.*

Cette stratégie a ensuite été employée sur trois systèmes granulaires correspondant à des configurations monodisperse, bidisperse et tridisperse, à partir de cylindres en PA66 de diamètre 12 mm, 15 mm et 20 mm, tous de longueur 20 mm. La configuration monodisperse était composée uniquement de petites particules, au nombre de 108. La configuration bidisperse était composée de particules petites et moyennes : 56 et 29 respectivement. La configuration tridisperse est composée des trois types de particules :

54 petites, 22 moyennes et 4 grosses. Pour chaque configuration, les cylindres ont été empilés aléatoirement dans le même cadre rectangulaire que précédemment, lui-même placé dans la machine d'essais afin d'appliquer la compression confinée. Les difficultés de préparation et de mise en œuvre et les solutions trouvées pour y remédier sont décrites dans la thèse. Les forces de contact identifiées ont ensuite été analysées en termes de réseaux de forces, de distributions de forces angulaires et de fonctions de distribution de probabilité (*Probability Density Function*, ou PDF) des forces normales. Les réseaux de forces ont été séparés en deux ensembles pour l'analyse : les réseaux dits forts et faibles, selon que la force normale est supérieure ou inférieure à la force normale moyenne. Les forces « fortes » ont été trouvées orientées en diagonale pour la configuration monodisperse, tandis qu'elles étaient orientées à la fois en diagonale et verticalement pour les configurations bidisperse et tridisperse. En termes de PDF des forces normales, il est clairement apparu que les forces « fortes » et « faibles » sont caractérisées par une décroissance exponentielle et une loi de puissance respectivement, comme prévu pour des configurations polydisperses selon la littérature.

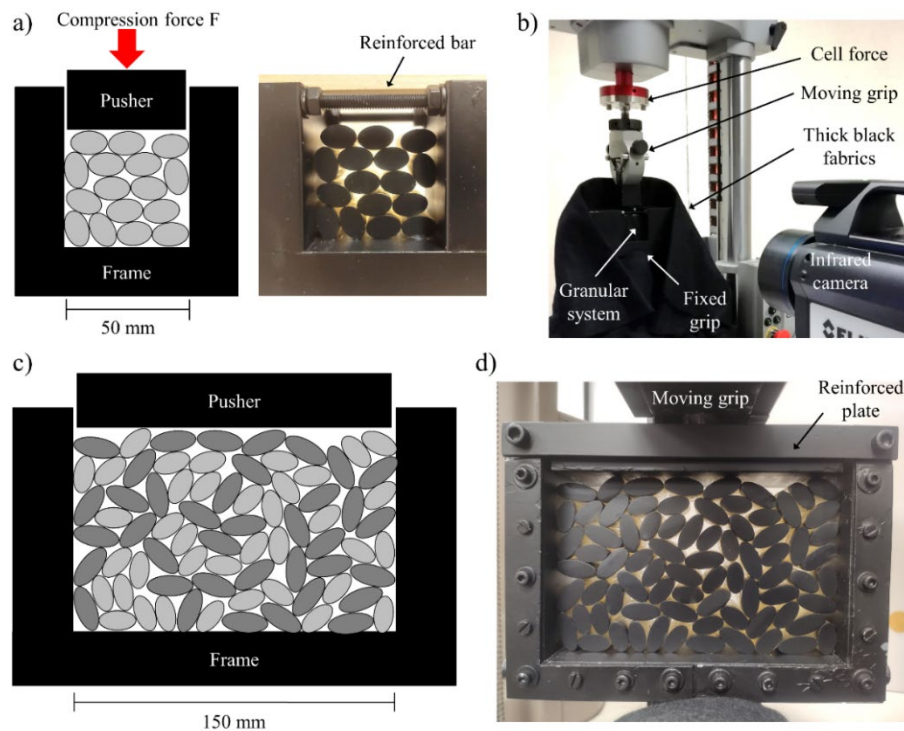


Résultats expérimentaux utilisant la ASL et la MCV : a)-c) réseaux de forces normales et distributions de forces angulaires ; d)-h) fonctions de distribution de probabilité (PDF) des forces normales normalisées.

Il a été démontré que les résultats statistiques étaient cohérents avec ceux des études numériques et expérimentales réalisées dans le passé. On peut noter que l'identification des forces de contact proposée ici est théoriquement applicable à tout type de système granulaire 2D si l'équation constitutive du matériau de base est connue. Notons également que la procédure permet d'identifier complètement les deux composantes de toutes les forces de contact dans un système granulaire 2D : les forces normales et les forces tangentielles sont simultanément identifiées à partir des champs de déformation mesurés. Des simulations de type MD ont ensuite été réalisées pour valider les résultats expérimentaux. Il a été conclu que la procédure expérimentale basée sur la MCV et la ASL est opérationnelle pour l'analyse statistique de systèmes granulaires 2D réels. L'approche expérimentale peut donc être utilisée pour d'autres travaux, en particulier pour réaliser des tests avec beaucoup plus de contacts, des formes de particules plus complexes ou des particules souples.

L'identification des couplages thermomécaniques dans des matériaux granulaires souples 2D a ensuite été réalisée par TIR et DC. Il convient de noter que l'analyse du comportement mécanique des solides continus a déjà bénéficié d'une telle approche dans le passé. En effet, la mise en évidence expérimentale de couplages locaux entre les réponses mécaniques et thermiques a permis une véritable analyse des phénomènes hétérogènes dans les matériaux continus dans un cadre thermodynamique rigoureux. Jusqu'à présent, les matériaux granulaires ont été globalement exclus de cette approche dans la communauté de la mécanique expérimentale. Nous avons considéré que ce type de matériau pouvait être étudié de la même manière que les matériaux continus via des mesures de température durant un chargement mécanique. Cela permettrait de fournir des informations intéressantes pour la compréhension de leurs comportements mécaniques. Quelques travaux traitent de cette question dans la littérature. Les études réalisées dans le passé montrent que des variations de température significatives peuvent être facilement obtenues dans des particules souples présentant une élasticité entropique. L'objectif de l'étude ici est de distinguer les variations de température associées au couplage thermoélastiques (CTE) et à la dissipation mécanique (DM). Des particules cylindriques ont été fabriquées à partir d'un matériau caoutchoutique, à savoir du polyuréthane thermoplastique (TPU), afin de bénéficier du fort CTE associé à l'élasticité entropique

ainsi que d'une faible conductivité thermique. Des formes elliptiques ont été considérées pour les sections droites des cylindres constituant les particules. L'idée est d'ouvrir la voie à des études sur des géométries plus complexes dans le futur, afin de se rapprocher progressivement des formes de particules de milieux granulaires réels. Les cylindres différaient par la longueur de l'axe principal des sections elliptiques : 15 mm, 18 mm et 22,5 mm. La longueur de l'axe secondaire était la même pour toutes les particules, à savoir 10 mm. Les particules ont ensuite été empilées aléatoirement dans un cadre en métal pour créer trois configurations distinctes : monodisperse (16 petites particules) et bidisperse (7 petites et 7 grandes particules) pour des observations préliminaires, ainsi que tridisperse (32 petites, 31 moyennes et 30 grandes particules) pour une analyse statistique.

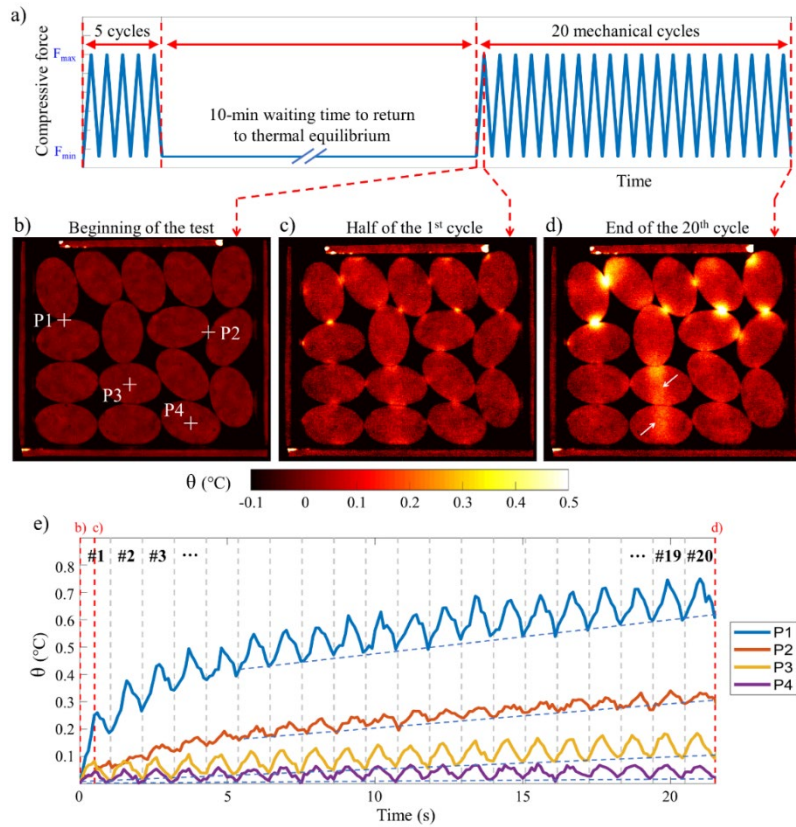


*Dispositif expérimental pour l'analyse thermomécanique de milieux granulaires souples en TPU via des mesures par thermographie infrarouge.*

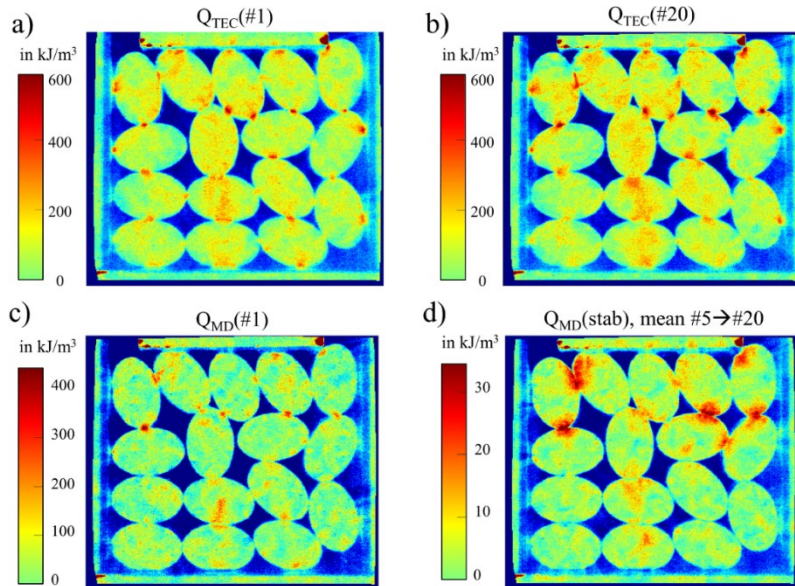
Les réponses thermiques des systèmes monodisperse et bidisperse ont d'abord été mesurées au cours d'une compression confinée cyclique. Différentes vitesses de sollicitation ont été testées afin d'évaluer l'impact d'une viscosité sur la DM. Une oscillation de la température à la même fréquence que le chargement a été observée.

Pendant les phases de compression, des points chauds ont été identifiés à tous les contacts interparticulaires. Ce phénomène s'explique par le CTE de type entropique activé par les concentrations de contraintes au niveau des contacts, avec une contribution potentielle de la DM associée à des phénomènes irréversibles tels que la viscosité et le frottement. Un auto-échauffement au cours des cycles a également été observé autour de contacts spécifiques, ainsi qu'à l'intérieur de certaines particules. Ce phénomène est associé à la DM en considérant que la chaleur associée au CTE s'annule au cours d'un cycle thermodynamique. Des taux d'auto-échauffement allant jusqu'à environ  $0,01^{\circ}\text{C}/\text{cycle}$  ont été mesurés en régime permanent. Une plus grande contribution de la DM a été observée au cours des premiers cycles mécaniques. Une comparaison entre les systèmes monodisperse et bidisperse à même niveau de chargement macroscopique a montré une signature thermique plus forte dans le premier cas, en accord avec les différences attendues dans l'intensité des forces de contact. Une approche calorimétrique nous a ensuite permis de calculer les chaleurs associées aux variations de température mesurées. On a estimé que l'intensité de la chaleur générée par le CTE entropique pouvait atteindre plus de  $600 \text{ kJ}/\text{m}^3/\text{compression}$  (chaleur produite sur la durée de la compression uniquement) dans les zones de contact, alors que celle associée à la DM était limitée à environ  $30 \text{ kJ}/\text{m}^3/\text{cycle}$  en régime permanent (et à environ  $300 \text{ kJ}/\text{m}^3/\text{cycle}$  dans le régime transitoire initial). Cela montre que le CTE est un couplage fort.





*Réponse thermique d'un matériau granulaire souple en TPU soumis à un chargement mécanique de compression confinée cyclique.*



*Analyse calorimétrique : a-b) chaleur produite par le couplage thermoélastique (CTE) durant la phase de compression ; c-d) chaleur produite par la dissipation mécanique (DM) sur un cycle charge-décharge.*



Ensuite, les données CTE ont été traitées pour le système tridisperse composé d'environ 600 contacts interparticulaires. Les informations statistiques sur la distribution de la chaleur associée au CTE (chaleur produite sur la durée de la compression uniquement) au niveau des contacts interparticulaires montrent un changement dans les distributions en fonction du niveau de compression appliqué. Plusieurs extensions de ce travail peuvent être proposées : réaliser des expériences avec beaucoup plus de particules ou des formes de section de cylindre plus complexes (angles vifs, géométrie non-convexe) ; réaliser des expériences en couplant *mesure dans le visible* (pour accéder aux champs de déformation) et *mesure dans l'infrarouge* (pour accéder aux chaleurs), ce qui permettrait de faire des bilans d'énergie. La comparaison entre résultats numériques et résultats expérimentaux de type thermodynamique est aussi une perspective. Une dernière étape consisterait à proposer un modèle thermodynamique macroscopique adapté au comportement des milieux granulaires souples. Cette approche nécessiterait des opérations de moyenne appropriées pour obtenir des données calorimétriques macroscopiques à mettre en relation avec des variables mécaniques moyennes (*fabric stress* ou *fabric strain*). Cela pourrait conduire à la proposition de techniques de mesure des contraintes macroscopiques/mésoscopiques en utilisant uniquement la température, de la même manière que cela se fait pour les matériaux continus par ATC.

## General Introduction

Granular materials are a type of material that can be found everywhere and used in everyday life. Everyone inevitably encounters granular materials, but not everyone can recognize their existence. This is quite surprising given how plentiful and ubiquitous they are. Let us cite some examples: sugar, salt and pepper are used for cooking; sand, pebbles and bricks are required for construction; powders are used in certain industrial manufacturing processes. A granular material is defined as a collection of solid particles. The latter consists of grains that come in a variety of shapes, materials and sizes. They can range from sand to rock, and even interplanetary aggregates (planet rings, asteroids). The behavior of granular materials is complicated and difficult to predict at the particle scale. This is a major issue for their modelling [2, 23]. Despite that, discrete materials can be considered as continuous matters at a macroscopic level. Granular materials can behave macroscopically like solids or liquids at a macroscopic level, depending on certain parameters. For instance, throwing a bowling ball into a pile of sand, the ball moves a short distance before stopping. The sand pile thus behaves like a solid. On the other hand, throwing the same bowling ball into a fluidized-bed pile of sand causes the ball to travel through the sand. The latter behaves here like a fluid. This example demonstrates that the behavior of granular materials is not only interesting but also complex. Researchers and scientists have primarily focused on studying continuous materials. Several decades ago, a few researchers and scientists paid attention to discrete materials, while continuum mechanics theory seemed to be rather completely developed. The reminded paper is the study published in 1944 by Casagrande and Carillo, who seem to be the pioneers for scientifically investigating discrete materials. They enhanced the understanding of the behavior of anisotropic granular materials through experiments and numerical simulations. They distinguished strength into two types, namely induced anisotropy and inherent anisotropy [24]. A few decades later, Dantu applied photoelasticity on two-dimensional (2D) piles of translucent disks and discovered a significant heterogeneity of the contact forces distribution in these 2D granular materials [25]. Biarez developed the concept of fabric anisotropy in connection with the distribution of contact orientations,

by studying 2D analogue materials (piles of disks) [26]. The stress-dilatancy relation, which is well-known and widely employed in soil mechanics, was proposed by Rowe, relying on the basis of the minimum energy principle [27]. In 1966, Weber presented a now-classic formula linking local contact forces in a granular material with a specific Cauchy-like stress tensor, namely an average stress tensor over a group of particles [28]. Other researchers attempted to connect the angle of friction measured at local scale with the classical internal angle of friction used in soil mechanics [29-32].

These effective outcomes and understanding of granular media during those decades were mainly obtained from experiments carried out on analogue materials and actual materials. Some theoretical attempts based on compositions of idealized particles were also developed. These kinds of materials were rather difficult to analyze experimentally at the local scale due to the techniques and instruments available at that time. At the end of the 1960s, it seems that the researchers confronted a dead-end due to the lack of experimental data at local scale. In 1971, Cundall developed a numerical approach named Distinct Element Method (DEM) that he employed to rock mechanics [33]. This approach considers the matter as a multi-contact system, in contrast to the classical Finite Element Method (FEM). Each grain in a granular material is regarded as an individual rigid body governed by the Newton's laws of motion and interacting with its neighbors through frictional contact laws. There are two widespread employed DEM approaches: the smooth DEM method known as molecular dynamics (MD); and the non-smooth DEM method known as non-smooth contact dynamic (NSCD) or contact dynamic (CD). The former approach is based on an explicit algorithm that takes the interaction between contacts into account as a function of relative displacements and velocities of particles. Furthermore, the interaction of contacts is governed by the generalized Coulomb's law of dry friction. The latter approach was established by J.J. Moreau [34]. It is based on Convex Analysis which proposes a consistent framework for the non-smooth laws involved in frictional contact, such as dry friction. Moreover, it is an implicit numerical algorithm which handles the equations of the Newton's law of motion and the non-smooth frictional contact laws. In terms of computational time, the CD method outperforms the MD method in some cases. The reason for this is that MD requires a fine time step (temporal resolution) for numerical integration of the Newton's second law

(equation of motion). The MD method appears to be less precise than the CD method in terms of friction handling. However, the CD method cannot be employed in some situations involving the deformation of the particles because it treats the particles as rigid (“undeformable”) bodies and disregards the elasticity of the contacts [8, 34, 35]. Since that time until now, numerical simulations have been a powerful, trustworthy and widely used research tool in the field of granular materials. In comparison, the experimentation is not so widely used due to the difficulties of preparation and instrumentation, as well as the often limited number of particles used in the tests.

Nowadays, non-contact measurement methods, also known as full-field measurement techniques, are becoming increasingly familiar and attractive to engineers and scientists working in the field of experimental mechanics. This is due to the rapid advances in equipment such as camera technology, sensors, computers and image processing software [36, 37]. Full-field measurements are non-destructive, meaning that they do not change or disturb the mechanical system under consideration. These methods give access to spatially distributed physical quantities such as temperatures (scalars), displacements (first-order tensors), strains (second-order tensors), depending on the type of sensor and after adequate calibration and suitable data processing [36]. Full-field measurement techniques are powerful and advantageous tools compared to traditional measurement techniques that rely on local measurement using common equipment such as thermocouples, displacement transducers or strain gauges. These traditional measurement techniques allow to characterize the material response at a small number of locations, whereas full-field measurement techniques can provide fields of local characterization that can lead to a better understanding of the global response of the material. It is interesting to note that full-field measurement techniques are actually not that new in the community of granular materials. In the 1950, photoelasticity was employed to granular materials by Dantu [25]. Since then, the amount of literature on granular materials investigated by full-field measurement techniques has increased. Some of them concentrate on kinematic information in the volume of the granular medium: digital speckle radiography [38-40], X-ray tomography [41-43], electrical capacitance tomography [44-46], magnetic resonance imaging [47-49] and positron emission particle tracking [50-52].

Certain full-field measurement techniques have been employed to measure strains or stresses in 2D granular systems composed of cylinders stacked in parallel. Note that these 2D systems are called Schneebeli materials [53]. The mechanical loading is applied perpendicularly to the axis of the cylinders while a camera acquires images of the free ends of the cylinders. These 2D techniques are:

- particle image velocimetry (PIV) — From the displacement of particles considered as rigid, it is possible to measure strain patterns within Schneebeli materials [15, 54, 55]. The pioneering works of Calvetti [56] and Misra [57] identified deformation patterns by using wood, aluminum and plastic rods under a variety of 2D loads (compression, shear, compression/shear; displacement-controlled boundaries, mixed stress-controlled/displacement-controlled boundaries);
- photoelasticimetry, using cylindrical particles (disks) made of a transparent birefringent material as mentioned above — The technique first allows to extract the fields of the difference of the principal stresses (i.e., the shear stress) in the disks using polarizing filters [4, 25, 58, 59]. From the photoelastic patterns, Majmudar and Behringer were able then to identify contact force networks in various 2D granular systems [4]. The limitation of this technique is that the particles must be made from a birefringent material;
- digital image correlation (DIC) — The technique first allows the measurement of the fields of the in-plane components of the strain tensor in deformable particles, see for instance Refs [60-62]. It was then possible to extract interparticle contact forces by combining experimental strain data with FEM [63-65];
- thermoelastic stress analysis (TSA), which relies on infrared (IR) thermography [66-68] — The idea is to measure first the fields of temperature amplitudes at the particle surface during a cyclic mechanical loading and to convert the quantities in terms of sums of the principal stresses (which are proportional to the hydrostatic stresses) from the thermoelastic coupling equation. This technique is rather new for granular community. It was employed in a few granular studies [21, 69]. It allowed to measure “stress networks” but, for the moment, it was not possible to use TSA data to identify interparticle contact force networks. Note that IR thermography was

also employed in the granular material community for the characterization of heat generation (mechanical dissipation) in granular flows [70] and in soil and sand under vibratory loading [20, 71, 72]. Let us cite observations at the micro-scale [73, 74].

In this context, this dissertation proposes other experimental routes for investigating the solid-like mechanical behavior 2D granular systems:

- using the **localized spectrum analysis (LSA)** and the **virtual fields method (VFM)**, which are a full-field strain measurement technique and an identification strategy respectively [14, 75, 76] — LSA relies on images of a periodic pattern placed at the material surface before testing, providing an interesting compromise between measurement resolution and spatial resolution [75, 76]. VFM, which relies on the weak form of the equation of equilibrium, is usually employed to identify material parameters knowing the mechanical loading. It was rarely used for the measurement of forces knowing the material response [14]. The objective for us is to identify interparticle force networks in 2D granular systems relying on strain data obtained by LSA;
- performing “**deformation calorimetry**” using **IR thermography (IRT)** — The objective is to distinguish thermoelastic effects (reversible mechanical response) and mechanical dissipation effects (irreversible mechanical response such as friction or damage) from the temperature evolution of a granular material subjected to cyclic mechanical loading at constant room temperature.

The outline of this dissertation is:

- Chapter 1 presents the concepts, theories and experimental techniques discussed in the dissertation. It provides a background on mechanics of granular materials, thermomechanics of continuous materials, full-field measurement and post-processing techniques used in this work (VFM, LSA and IRT), as well as a reminder of full-field techniques already applied to granular materials;
- Chapter 2 presents the principle to interparticle contact force identification by using synthetic strain fields provided by a finite element model. The robustness of the identification procedure, relying on VFM, will be assessed with respect to various sources of error in the strain data;
- Chapter 3 is dedicated to various experimental applications of the approach developed in the previous chapter by processing strain maps obtained using LSA for each particle. The number of particles used in the experiments will enable us a statistical processing;
- Chapter 4 is dedicated to the use of IRT for the analysis of thermomechanical couplings in soft granular systems. Let us note that it is independent from the previous two chapters, offering another point of view based on temperature measurement only.

# CHAPTER 1

## Theoretical Background

### 1.1 Introduction

The purpose of this chapter is to remind, review and summarize the concepts, theories and experimental techniques that are discussed in this dissertation. This bibliography is structured as follows:

- Section 1.2 provides an **overview of the granular materials**. Their behaviors are rather different from those of classical materials due to their discrete nature. Granular materials exhibit complex mechanical responses which can be assimilated to fluid-like or solid-like behavior depending on various parameters. This section is focused on the solid-like case at static equilibrium, which is the context of our research work. The granular texture will thus be used to discuss some interesting properties of a granular material in static condition in terms of compaction, solid fraction, coordination number, mechanical fabrication, force distribution, and stress tensor. Next, the molecular dynamics (MD) method is presented. It is one of the commonly used numerical simulations for granular media. The MD method employs the Newton's equation of motion and Gear predictor-corrector to identify the contact forces and kinematic quantities in the considered granular system. Finally, the thermal behavior of granular media is discussed from a numerical modeling of heat production and transmission.
- Section 1.3 presents the theory of **thermomechanics of continuous materials**, as a base to understand later the response within individual particles. It recalls the first and second principles of thermodynamics as well as the heat diffusion equation. A focus is on the calorific effects associated to reversible mechanical response



- (thermoelastic coupling) and irreversible mechanical response (intrinsic dissipation, also called mechanical dissipation).
- Section 1.4 presents the experimental measurement techniques and post-processing approaches that are applied in our work. First, **infrared (IR) thermography (IRT)** is described in broad terms, recalling the fundamentals of the IR radiation and the Stefan-Boltzmann law to measure temperatures. After that, the basic concepts of IR imaging systems are explained. Second, the full-field strain measurement technique called **localized spectrum analysis (LSA)** is presented, including details on the preparation of the periodic pattern to be placed preliminary at material surface. Finally, the **virtual fields method (VFM)** is presented in its usual application, i.e. the identification of material properties from measured strain fields and the knowledge of the external mechanical loading. The method will be used in Chapter 2 to identify interparticle contact forces.
  - Section 1.5 is dedicated to the use of **full-field measurements applied to granular materials in the literature**. It includes photoelasticimetry, particle image velocimetry (PIV), digital image correlation (DIC) and IRT.

## 1.2 Mechanics of granular material

Granular materials are omnipresent. They are all around us in our daily lives (salt, sand, snow and soil) and they can be found far away in asteroids and planet rings. They can be found in various fields, such as in agriculture for food products (rice and wheat), in civil engineering for constructions (rocks and cement), as well as in pharmaceuticals for medicine (drugs and pills). In addition, granular movements or granular flows are also involved in natural phenomena like avalanches and landslides. Examples of granular materials are illustrated in Figure 1.1.

Granular material is one kind of discrete material. It can then be defined in engineering terms as a collection of solid particles whose mechanical behavior at macroscopic level is governed by interparticle forces [23, 77]. They are typically composed of grains distributed in a variety of ways, with different shapes, materials and sizes. Granular media, as discussed here, typically has particle sizes larger than 100  $\mu\text{m}$ .

Despite their extreme diversity, all granular materials share fundamental characteristics. They can behave like a fluid or a solid at macroscopic level depending on a set of parameters. They exhibit phenomena such as avalanches, segregation and convection. Figure 1.2 illustrates the behavior of bead pile in different regions. However, granular media are disordered, unmanageable and unpredictable at microscopic level (grain level) [2]. More than with the classical materials like solids, liquids and gases, understanding and modelling of granular materials pose many complicated challenges.



Figure 1.1 Examples of granular materials.

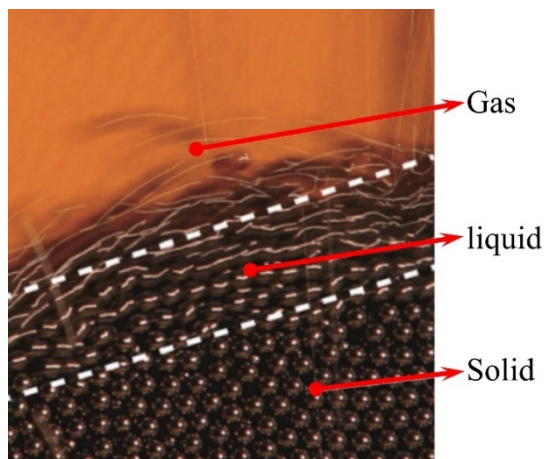


Figure 1.2 Gas, liquid, and solid region of a bead pile [1].

The interactions between particles are non-trivial and non-linear. They involve many phenomena such as friction, inelastic collision, adhesive force, and capillary

cohesion. These make the behavior complex and difficult to predict at the grain level. Other difficulties are that granular media easily dissipate energy due to friction and inelastic collision (although thermal agitation is negligible when the particle size is greater than 1  $\mu\text{m}$ ). These difficulties can thus be seen as a non-Brownian motion. Next, the lack of a clear separation of scales between the microscopic scale, i.e., grain size, and the macroscopic scale i.e., flow size, also complicates the continuum description of granular media. When sand flows down on a pile, the flow thickness is typically 10-20 particle diameters. Similarly, the breakdown of a granular soil is frequently localized in faults or shear bands a few tens of grain wide. This lack of scale separation calls into question the validity of the continuum approach.

This section will not deal with granular materials as a whole. It will only concern granular solids and the numerical simulation, including numerical modeling of heat production and transmission in static equilibrium conditions. In this frame, interesting and significant properties of granular media are described further below. The contact force between two dry grains is generally separated into two components: normal force and tangential force. Surface roughness, local mechanical properties, and physical and chemical properties all play a role in the physical origin of these forces at the microscopic level. So, we will focus also on the macroscopic laws of solid contact by Hertz contact and Coulomb's law. The granular texture, which refers to contact force and contact networks in multi-contact systems, is also discussed in this section. Heat production and transmission is a minor property of granular media, but they are also presented as an interesting topic which can be related to thermomechanics.

### 1.2.1 Elastic contact

Considering two spherical particles radius  $R$  squeezed together by an external force, the particles move toward each other by a distance  $2\delta$ . With the assumption of elastic and smooth spheres, the normal contact force can be then expressed as follows when  $\delta \ll R$  [78]:

$$F_N \approx E\sqrt{R}\delta^{\frac{3}{2}} \quad (1.1)$$

where  $E$  is the Young's modulus of material. It must be noted that the general equation depends on the geometries of the surfaces in contact (plane, sphere, cylinder, cone, etc.) and the material properties of each body [79].

### 1.2.2 Solid friction & Rolling friction

In addition to the normal component, a tangential component is commonly observed as a result of friction between the surfaces in contact. It is also called tangential force, friction force, sliding force, sliding friction, or solid friction [80]. Friction is an important factor at all the scales, from grain level to packing level in a granular medium. Solid friction is classically governed by the Coulomb-Amontons laws, which are expressed as follows:

- the friction force is directly proportional to normal force;
- the friction force is independent of the contact area;
- kinematic friction is independent of sliding velocity.

The Coulomb-Amontons laws are robust and widely used to explain many phenomena [80]. The tangential friction force can be written as follow:

$$F_T = \mu F_N \quad (1.2)$$

where  $\mu$  is a coefficient of friction. Furthermore, there are two types of coefficients of friction: dynamical coefficient of friction ( $\mu_d$ ) and static coefficient of friction ( $\mu_s$ ). These two coefficients are constant and depend on the materials in contact. Typically,  $0 < \mu_s < \mu_d < 1$ .

Sliding friction is well-known and primarily considered in general. It represents the resistance to translational motion between two solids in contact. Another type of friction occurs at the contact, known as "rolling friction". It is the resistance to rolling motion when one body rolls on a solid surface [80, 81]. Rolling friction is caused by the asymmetry of the contact area due to the presence of adhesive joints between the surfaces in contact. When the grain is rolling, force dissipation occurs in the contact zone, resulting in hysteresis between compression and extension forces at contact.

### 1.2.3 Granular packing

Granular packing is one of significant properties which characterizes the rigidity and flow of granular materials [77]. That is a reason why granular packing has been studied since the 1950s [82-84]. Engineers were interested in optimizing the storage of granular materials. This was an important issue for many industries at that time. Volume fraction, void fraction, and porosity are some of the variables that can be used to characterize the packing of granular materials. The volume fraction  $\eta$ , also known as the solid fraction, is the ratio of the volume  $V_{grains}$  occupied by the grains inside the representative elementary volume (REV) to the volume  $V_{REV}$  of the REV:

$$\eta = \frac{V_{grains}}{V_{REV}} \quad (1.3)$$

The maximum volume fraction is obviously equal to 1. This case indicates that the grains fill in the entire volume or REV. Literature has introduced other variables to measure the compacity of a granular material. The porosity  $\varepsilon$  is generally used in the porous media community. It indicates the ratio of the volume  $V_{voids}$  of voids to the entire volume. It can be expressed as:

$$\varepsilon = \frac{V_{voids}}{V_{REV}} = 1 - \eta \quad (1.4)$$

Another variable is the void fraction  $e_v$ , which is frequently used in soil mechanics. It represents the ratio of the volume of voids to the volume of grains. It can be written as:

$$e_v = \frac{V_{voids}}{V_{grains}} = \frac{1 - \eta}{\eta} \quad (1.5)$$

Since all these quantities are equivalent, we will only use the volume fraction  $\eta$  for the discussion in the rest of the dissertation. Stable packing normally exists in a finite range of volume fraction when the granular system is composed of frictional grains. Dense (high  $\eta$ ) or loose (low  $\eta$ ) packings can be obtained, depending on the packing technique used. The volume fraction is thus between a minimum value corresponding to the loosest packing and a maximum value corresponding to the densest packing. Vibration-induced compaction holds the potential to disturb the packing. It can make the packing evolve.

Now, let consider the simplest packing, i.e., an assembly of spheres of the same size. This granular assembly is not only the simplest model of a pile but it is also a useful model for discovering the molecular structure of liquids and glassy materials [85, 86]. It is generally called “monodisperse”. The densest packings of spheres for this system correspond to regular crystalline organizations, such as the face-centered cubic and the close-pack hexagonal lattices, which have the same volume fraction  $\eta = 0.74$  [2, 87, 88]. These regular packings were first discovered by Johannes Kepler in 1611, achieved with cannonballs. About four centuries later, Hales achieved the mathematical proof to support this conjecture [89]. Although crystalline packings correlate with the global minimum of potential energy, achieving them in practice is rather difficult. When a collection of spherical grains is shaken, the grains generally self-rearrange and settle into a stable random configuration. This packing is known as “the random close packing”. This stable random packing typically has a volume fraction that falls between two limits: the random close packing (RCP) limit and the random loose packing (RLP) limit. This random close packing is referred to as the densest configuration achieved by randomly packing [90]. It is well-known that the volume fraction in RCP limit is approximately 0.64 [87, 88, 91]. The definition of random loose packing, in contrast to RCP, is the loosest feasible random packing that still maintains mechanical stability [90, 92, 93]. The volume fraction of RLP limit is about 0.55. These packings of monodisperse spheres are simple and provide interesting models for initial investigation. However, many applications involve mixtures of grains of various sizes. Such systems are referred to as “polydisperse”. They are rather complex and still unclearly understood. The volume fraction is still used to describe the properties of these configurations. It was demonstrated that the packings of polydisperse systems are denser than those of monodisperse systems [88, 94]. This can be extended to an extreme case, namely a mixture composed of various sizes referred to as Apollonius packing. It completely fills the space with a series of smaller and smaller grains, as shown in Figure 1.3. This extreme case is employed to improve composite material, e.g., high-strength concretes. Practically, it is difficult to create a homogeneous pattern of Apollonius packing.

In general, granular packing depends on several influences such as the preparation method (dropping type, dropping height), material properties (coefficient of friction,

coefficient of restitution), grain size distribution (monodisperse, polydisperse), grain shape (sphere, ellipsoid, polyhedron), and absolute grain size (fine to coarse grains). These can significantly affect the interaction between particles [95-97]. These influences on granular packing were investigated in terms of influence of the volume fraction [93, 95, 96, 98-103].

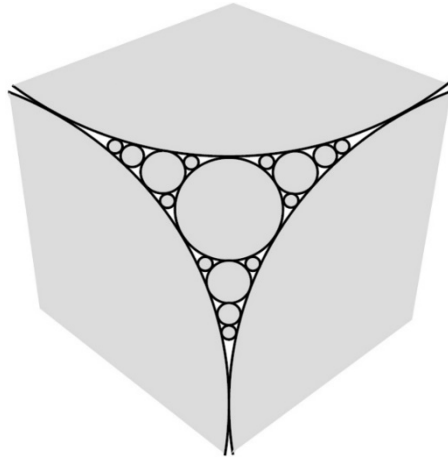


Figure 1.3 Schematic sketch of an Apollonius packing [2].

Another parameter related to compactness can be considered, given that all particles in a granular packing interact with each other at a finite number of contact points. This parameter is defined as the average number of contacts per particle, referred to as the **coordination number**  $z$  [2, 104]. It can be calculated by the total number of contacts  $2N_c$  in the granular packing divided by the total number of particles  $N$ , as expressed in following equation.

$$z = \frac{2N_c}{N} \quad (1.6)$$

It must be noted that the total number of contacts is multiplied by 2 because there are two particles at each contact point.

The coordination number is an important quantity because contacts between particles in a granular packing require a sufficient number of mechanical constraints to ensure the global stability. Considering a  $d$ -dimensional static granular packing (with  $d = 1, 2$  or  $3$ ) consisting of  $N$  frictionless particles, it needs  $d \times N$  equilibrium equations for determining the  $N_c$  contact forces between each particle. The coordination number in a

static granular packing to maintain the stability against the external disturbances is equal to 4 in the two-dimensional (2D) case and 6 for three-dimensional (3D) case. These packings are referred to as “isostatic”, indicating systems that are statically determinate [2, 104-106]. This isostatic packing implies that the total number of contacts equals the equations of equilibrium. It is worth noting that the isostatic granular packing is rather sensitive to external disturbances because even a single contact breaking can disrupt the stability of the system. In the case of a granular packing system with frictional particles, the number of contact forces in 2D and 3D is equal to  $2N_c$  and  $3N_c$ , respectively. Consequently, a static granular packing needs  $3N$  and  $6N$  equilibrium equations for the 2D and 3D cases, respectively. A dry granular packing consisting of frictional particles thus has a coordination number in the range of  $3 \leq z \leq 4$  in two dimensions and  $4 \leq z \leq 6$  in three dimensions. A static granular packing containing frictional particles might then be “hyperstatic” and the contact forces are undetermined [2]. However, despite that the concept of isostaticity based on spherical grains, its analysis helps to clarify the role of friction plays in granular systems. Investigating acoustic propagation and vibration modes in granular packings can also benefit from this approach [107-109].

#### 1.2.4 Forces in a granular packing

In the previous section, the equilibrium of static granular packings was discussed. The uniqueness of the contact forces in a random packing was discussed in terms of number of contacts. In this section, we present more in detail the statistics of the contact forces and the fundamental properties of their distribution. It is commonly understood that contact forces are transmitted from one particle to another through the contacts. First, the contact forces can be used to display the force network, which is a chain-like structure in the granular packing. The force network is the distribution of contact forces located at every single contact. Contact networks have specific features linked to the mechanical properties of the static granular matter. The mechanics of granular materials has the basic goal to improve the understanding of the contact forces and their spatial correlation, particularly the capability of bearing the external loading from the boundaries of the system. An example of a force network in a static granular system is presented in Figure



1.4. The black lines are referred to as contact forces, which the thickness represents the amplitude of contact force.

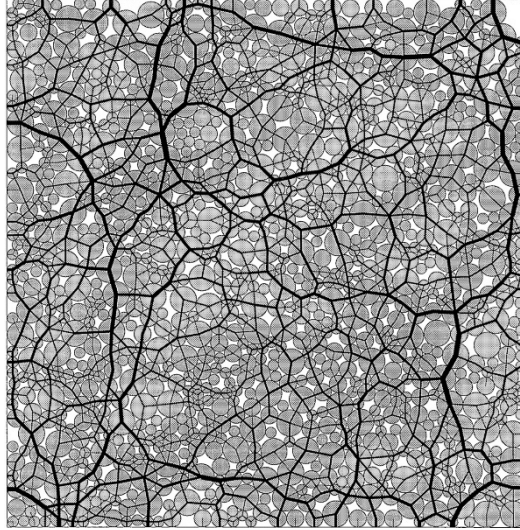


Figure 1.4 Example of normal force network obtained by simulation [3].

Contact forces in granular materials can be experimentally measured using a variety of techniques already indicated in the general introduction of this thesis. A first technique relies photoelasticimetry, which was employed for granular materials for the first time in 1957 by Dantu [25]. This technique relies on particles made of photoelastic materials, such as plexiglass, pyrex or polymer, which exhibit the property of a transient birefringence under strain. Figure 1.5-a shows an example of photoelastic image under a high-stress isotropically compressed state. However, it is rather complicated to extract the contact forces at each contact. Majmudar and Behringer were the first to successfully solve this issue in 2005 [4]. A second technique is the carbon paper method, which was employed to measure contact forces at the boundary of granular systems. This technique requires placing a piece of carbon paper on a wall of the container containing the particles. When applying an external force, the particles create spots on the carbon paper. The sizes of the spots are proportional to the normal forces exerted by the particles on the carbon paper [5]. An example of this technique is shown in Figure 1.5-b. This technique was first performed by Liu *et al* [110] in 1995. In practice, it can be employed to measure contact forces in the 2D and 3D cases. However, it is limited to measuring at the boundaries of the system and it requires a sufficiently high external loading to create visible spots on

the paper. Later, this measurement technique was improved by using geomembranes and contact papers for measuring contact forces [6, 7]. These two techniques can give better results than the carbon paper method due to a higher sensitivity to contact forces, as shown in Figures 1.5-c and -d. The discrete element method (DEM), which is numerical approach, enables to calculate all the contact forces in the bulk of three-dimension granular packings neglecting uncontrollable experimental parameters. Moreover, the simulations offer a higher measurement precision on the small contact forces. However, they are still not sufficiently realistic to represent experiments.

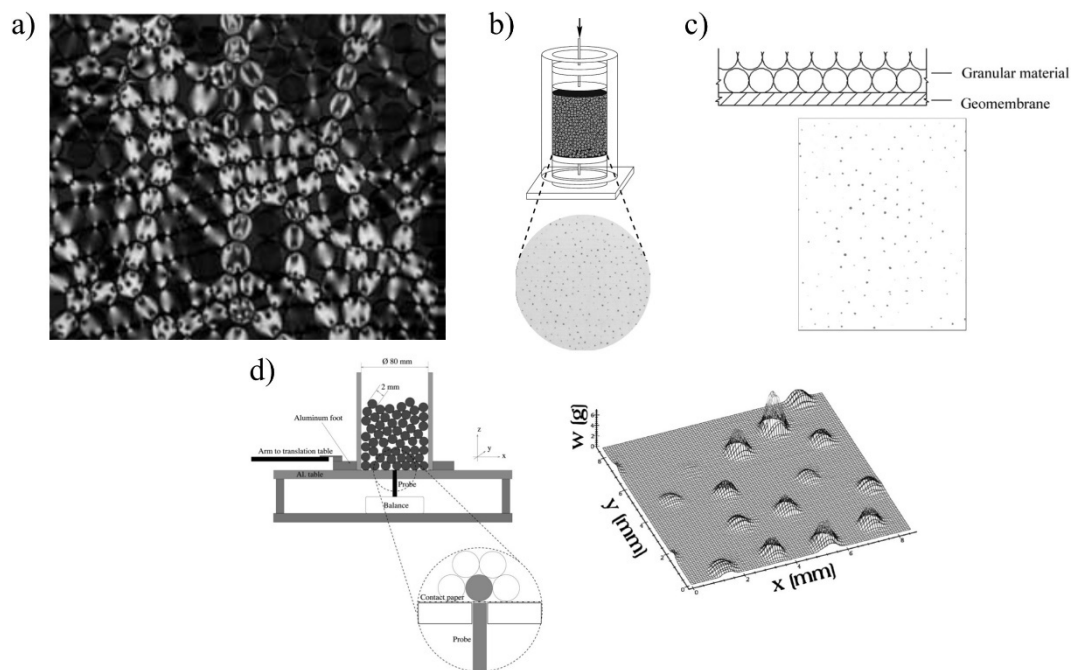


Figure 1.5 Contact force measurement in the literature: a) photoelastic image of a 2D system under isotropic compression [4], b) setup for the carbon paper method [5], c) setup and result using geomembranes [6], d) setup and result of the contact paper method [7].

In previous paragraphs, it was seen that contact forces can be measured by a few experimental methods, with the final objective to obtain force networks within granular systems. Despite this, it is difficult to compare at the local scale the results of one granular system with those of another system. The better way is to compare the results in terms of statistical properties at a macroscopic level. Probability density functions (PDFs) are thus classically employed to represent the macroscopic properties of a granular system. Figure

1.6 shows an example of PDF of normal contact forces obtained from 2D simulations [8]. Note that the graph shows a semi-logarithmic plot, with x- axis in logarithmic scale and y- axis in normal scale.

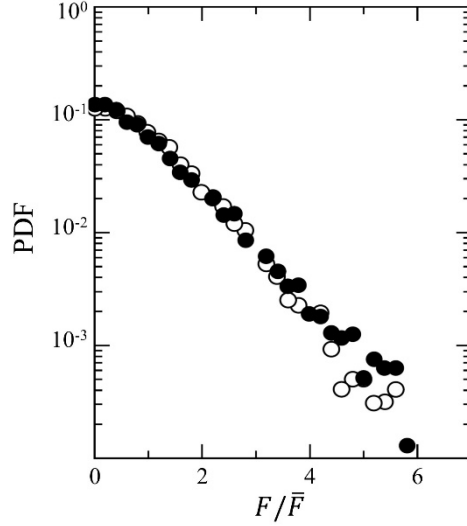


Figure 1.6 Probability density function (PDF) of the normal contact forces normalized by the mean normal contact force [8], for two values of the coefficient of friction between particles (white, 0.1 and black, 0.4).

On this graph, the first significant observation is that the range of force amplitude is wide. Strong heterogeneities are observed in the force network (not shown here). More precisely, it can be seen in the graph that large forces, up to six times the mean, can be found while near-zero forces also exist. The second observation is the shape of the PDF. It can be split into two complementary parts, above and below the mean contact force, defining the **strong and weak networks** respectively. The strong network is a set of contact forces which are greater than the mean contact force. On the contrary, the weak network is a set of contact forces which are lower than the mean contact force. The distribution of the strong network was well-found to be an exponential decay in all studies (revealed by the linear part of the PDF), while the weak network is very flat and can be approximately by a power law. These distributions can thus be expressed as [3, 111]:

$$P(F) = \begin{cases} k(F / \bar{F})^{-\alpha} & F / \bar{F} < 1 \\ ke^{\beta(1-F/\bar{F})} & F / \bar{F} > 1 \end{cases} \quad (1.7)$$

where  $k$  is the normalization coefficient given by:

$$\frac{1}{k} = \frac{1}{1-\alpha} + \frac{1}{\beta} \quad (1.8)$$

In addition, the relationship between the two coefficients of these two distribution functions is given by:

$$\beta^2 = (1-\alpha)(2-\alpha) \quad (1.9)$$

Several studies revealed such contact force distributions similarly in experiments, numerical simulations and theoretical models [4-6, 8, 18, 19, 112-115]. According to some of these studies, the exponential decrease of the strong forces is a robust characteristic of force distributions in both 2D and 3D granular materials. On the other hand, the initial state of the packing (experimental or numerical preparation of the granular sample) can affect the force distribution in the weak network. **The number of particles in a weak network is approximately 60% of all particles in the granular system. A strong network thus contains only 40% of the particles** [3, 8]. The difference in behavior between strong- and weak-force networks, as well as the existence of an exponential tail in the strong network, are both very robust characteristics. It can be noted that the force distribution has the same shape in the case of frictional and frictionless particles, regardless of whether the packing is regular or random.

Other researchers studied the micromechanics of granular packings at the jamming point. Figure 1.7 illustrates the PDF of normalized normal contact forces by using numerical simulation, namely the CD method, for frictionless pentagon packings in Figure 1.7-a and for frictionless disk packings in Figure 1.7-b, for various volume fractions of granular packings. It is clear that the **PDFs of strong network and weak network are governed by exponential decay and power law, respectively**. Even though increasing the volume fraction of granular packing until it reaches the jamming point, the number of extreme values of both strong and weak forces decreased because the force transmitted throughout the entire system [9].

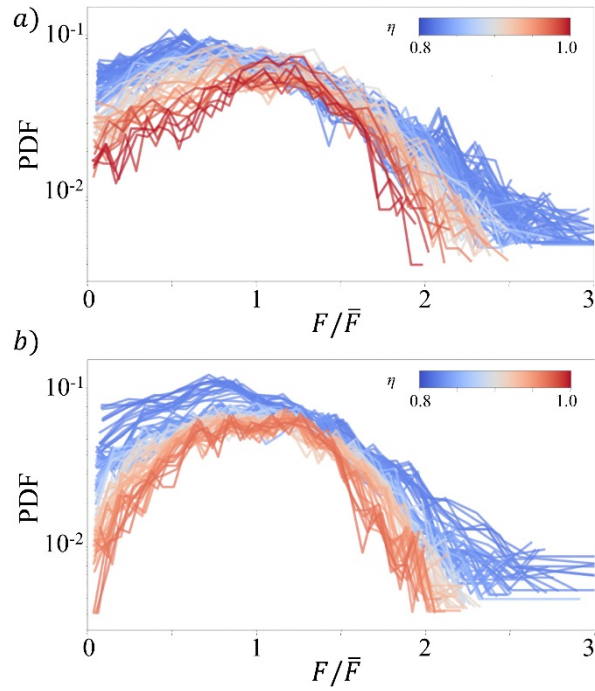


Figure 1.7 Probability density function of the normal forces normalized by the mean normal contact force, for frictionless contacts, for different volume fractions [9]: a) pentagon packings, b) disk packings.

In addition, numerical simulations based on CD method were employed to study the force transmission in highly polydisperse granular packings subjected to simple shear [10]. The particle size span (range of difference in particle size as given by the equation  $s = (d_{max} - d_{min}) / (d_{max} + d_{min})$ ) was varied from 0.2 to 0.96 in this study. The coefficient of friction between particles was set to 0.4. It was evidenced that strongest force chains are mainly transmitted by large particles while the force chains are absent in the majority of small particles. Therefore, inhomogeneous force distribution is more often observed when the particle size span widens. PDFs of normal contact forces normalized by the means of normal contact forces for various particle size spans are shown in Figure 1.8.

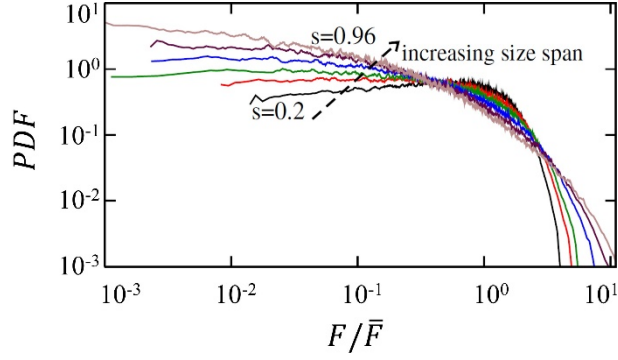


Figure 1.8 Probability density function of the normal contact forces normalized by the mean of normal contact force for different particle size spans [10].

In the previous paragraph, the contact force distributions appeared to be highly inhomogeneous due to the force transmission through the interparticle contacts. In the granular material community, two beneficial statistical quantities (relevant to the fabric tensor  $\phi$ ) are taken into account in order to clearly characterize the force network and to define the chance of contact occurrence in each direction of the space [2]. The first statistical quantity describes the angular distribution of contact directions, which is known as “geometrical fabric”. The second statistical quantity describes the angular distribution of contact forces, which is known as “mechanical fabric” [2]. The difference between these two statistical quantities is that the mechanical fabric takes the magnitude of the contact forces into account. The fabric tensors consider the geometrical structure of the particles, which contains all of the directional information of contact orientations in space [111, 116]. This fabric tensor is symmetric and can be expressed as:

$$\phi_{ij} = \frac{1}{N_c} \sum_{P \in N_c} n_i^P n_j^P \quad (1.10)$$

where  $N_c$  is the total number of contacts in the system. The  $i$  and  $j$  components of normal directional vector at contact point  $P$  are  $n_i^P$  and  $n_j^P$ , respectively.

In 2012, three micromechanical mechanisms were mentioned by Krut [116]. The first is known as “contact disruption”, which occurs when two particles that are in contact move apart and lose contact. The second is known as “contact creation” and refers to a new contact that is made when two particles come into contact. This is known as a contact

reorientation, which means that the orientation of the contact normal directions changes due to the movement of particles while they are still in contact with each other.

Considering the 2D case, the geometrical fabric in the normal direction can be simply given by function  $P(\theta)$  defined such that  $P(\theta)d(\theta)$  provides the total number of contacts in the normal direction between  $\theta - d\theta/2$  and  $\theta + d\theta/2$  [2]. The integration of  $P(\theta)$  over all angles is equal to the value of the coordination number  $z$  or the averaging number of contacts per particle. It is worth noting that the preparation method and the external loading applied to the granular packing significantly affect the angular distribution of contact directions. The packing of pile under gravity clearly exhibits four lobes whose peaks are approximately  $45^\circ$  from the vertical. This angular distribution can be understood by the fact that each particle finds an equilibrium position during the deposition process under gravity, resting on two particles below [117]. The isotropic angular distribution is clearly observed in the case of granular packings under isotropic compressive loading. Finally, a granular packing with a high vertical loading exhibits a slight anisotropy in the principal stress direction [11]. These three examples of angular distribution of contact forces are illustrated in Figure 1.9.

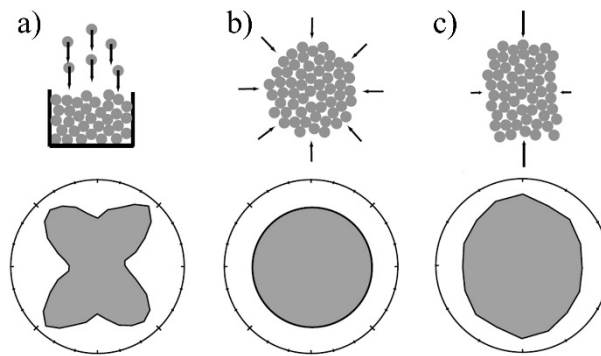


Figure 1.9 Angular distribution of contact directions for three granular packings [2]: a) under gravity, b) under isotropic compression, c) under vertical loading.

The **angular distribution of contact forces** can be split into two contact networks corresponding to the strong and weak networks, as discussed in the previous paragraph. The two cases can be plotted from the angular distribution of contact forces higher and lower than the mean of contact forces respectively. This is represented in Figure 1.10.

The two networks seem to have different angular anisotropies. **The angular distribution of the strong network is significantly more anisotropic than that of the weak network. Furthermore, the slight anisotropy of the weak network is oriented in the direction opposite from the direction of the compression. The angular distribution of the strong network is mainly aligned along the direction of the compression.** In order to determine the contributions of the strong network and the weak network to the stress tensor, it is possible to define a stress tensor by averaging over the interparticle forces, which will be discussed in next section. The strong network dominantly contributes to the deviatoric part of the stress tensor, i.e., the presence of shear stresses in the medium, whereas the weak network contributes to the hydrostatic pressure [2, 11, 111]. This indicates that **the strong network allows the granular materials to resist shearing, exhibiting thus a solid-like behavior.** Nevertheless, **the strong network is unstable in the absence of the weak network, i.e., lateral forces are necessary to prevent the buckling of the strong network.**

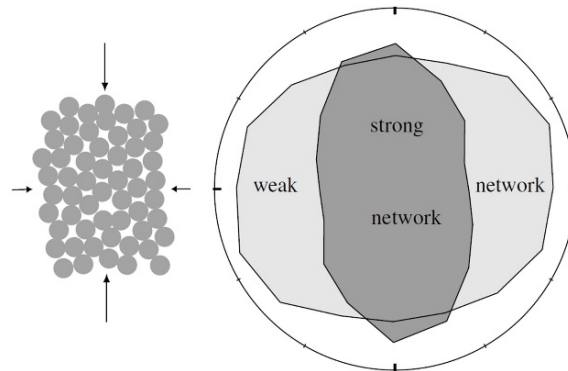


Figure 1.10 Angular distribution of contact forces in the strong and weak networks for a packing under vertical loading [11].

### 1.2.5 From forces to stresses

Granular materials are discrete materials, so the Cauchy stress tensor derived from continuous materials cannot be applied to define them. The previous section showed that the contact forces distributions within granular packings are highly heterogeneous. The question is how to define a stress tensor in the case of a discrete material. This section recalls the method for properly defining the stress tensor from the interparticle forces in a granular material by using concepts of continuum mechanics.



In order to relate the contact forces in discrete materials to the stress tensor in continuum materials, many researchers developed an averaging process with various theoretical considerations [4, 118-121]. The stress tensors that these researchers have suggested are equivalent to one another in equilibrium conditions. The stress tensor in this case is defined as the average stress of a collection of particles. The definition of the stress tensor at the continuum scale is briefly explained by using a grain by grain approach in the reference [111]. The concept behind this approach relies on the determination of the internal moment, such as the internal moment tensor efforts of a bounded mechanical system. The tensorial internal moment  $M_i$  of each particle  $p$  is taken into account when calculating the stress tensor [111]. It can be defined as follow:

$$M_{ij}^p = \sum_{c \in p} \mathbf{f}_i^c \mathbf{r}_j^c \quad (1.11)$$

where  $\mathbf{f}_i^c$  and  $\mathbf{r}_j^c$  are the  $i^{th}$  component of force vector exerted on the particle at contact point  $c$  and the  $j^{th}$  component of the radius vector through the contact point  $c$ , respectively. The summation in this equation takes into account all contact points of the considered particle. The stress tensor of a granular packing over the volume  $V$  can be simply defined by the tensorial internal moment as follow:

$$\sigma_{ij} = \frac{1}{V} \sum_{p \in V} M_{ij}^p = \frac{1}{V} \sum_{c \in V} \mathbf{f}_i^c \mathbf{l}_j^c \quad (1.12)$$

where  $\mathbf{l}_j^c$  is the  $j^{th}$  component of branch vector connecting the centroids of two contacting particles at contact point  $c$ .

Before identifying the hydrostatic stress in each particle, the definition of the stress tensor at grain scale should be first defined. The definition of stress tensor at grain scale  $\sigma^p$  for each individual particle is developed by using the stress tensor at continuum scale as follows:

$$\sigma_{ij}^p = \frac{1}{V_p} \sum_{c \in V_p} \mathbf{f}_i^c \mathbf{r}_j^c \quad (1.13)$$

where  $V_p$  is the volume of the particle. The summation of this equation is performed over the entire collection of contacts along the perimeter of the particle.

### 1.2.6 Molecular Dynamics (MD) method

By construction, numerical simulation techniques developed for continuous materials, such as the Finite Element (FE) method, cannot be easily applied to simulate discrete materials. The Discrete Element Method (DEM) was first introduced in 1971 by Cundall for rock mechanics [33]. In fact, molecular dynamics (MD) simulation has been widely used in the granular materials community. It is a powerful method which has been extensively employed to study the mechanical behavior of various types of granular media. The MD method relies on an explicit algorithm. Moreover, it considers the particles as rigid bodies with non-conforming surfaces [78]. Several integration schemes can be employed within the framework of the finite difference method to integrate the Newton's equations of motion. The MD method employed in this dissertation is based on a predictor-corrector scheme with Gear's correction of corrector coefficients [122, 123].

The MD method is simple and flexible as it applies only the Newton's second law for calculating kinematical quantities which can be written as follows:

$$m_i \frac{d^2 x_i}{dt^2} = \mathbf{F}_i, \quad i = 1, 2, 3, \dots, N \quad (1.14)$$

where  $N$  is the number of particles in the simulation,  $m_i$  is the mass of particles  $i$ ,  $x_i$  is the position of particles, and  $\mathbf{F}_i$  is the force exerted on that particle. The method consists of calculating the forces  $\mathbf{F}_i$  and solving ordinary differential equations (ODE). Integration of the Newton's equations of motion can be achieved by applying a predictor-corrector scheme with Gear's correction of corrector coefficients. Thus, positions, velocities, accelerations and third-order time derivatives are obtained for all the particles.

In order to estimate the motion of the particles to reach a new configuration, the integration of the Newton's equation of motion is applied. For the MD method, the finite difference methods are employed to estimate the motion of each particle in the granular system in the new configuration [111, 122]. The integration is divided into discrete summation with many interval times  $\delta t$ . When the kinematical quantities and the forces to each particle at time  $t$  are determined, they are applied as the input to estimate the quantities at the new configuration at time  $t + \delta t$  by Newton's second law. It is worth

noting that there are various algorithms for numerical integration schemes, such as Verlet algorithm, leap-frog algorithm, velocity Verlet algorithm, Beeman algorithm, as well as another higher-order algorithm [123-127]. In this dissertation, the kinematic quantities in MD method will be estimated as Taylor series, as follows:

$$\begin{aligned}
r(t+dt) &= r(t) + v(t)\delta t + \frac{1}{2}a(t)\delta t^2 + \frac{1}{6}b(t)\delta t^3 + \dots \\
v(t+dt) &= v(t) + a(t)\delta t + \frac{1}{2}b(t)\delta t^2 + \dots \\
a(t+dt) &= a(t) + b(t)\delta t.. \\
b(t+dt) &= b(t) + \dots
\end{aligned} \tag{1.15}$$

where  $r$ ,  $v$ ,  $a$  and  $b$  are the position, the velocity (first-order time derivative of position), the acceleration (second-order time derivative of position) and the third-order time derivative of position.

Since numerical integration schemes are effective, the algorithms can use large time steps while maintaining high precision. On the contrary, the higher-order algorithm can achieve a higher accuracy for a given time step. The higher-order algorithm used in MD method is the so-called ‘‘Gear Predictor-corrector’’ algorithm [128]. This is a powerful algorithm because it only requires one calculation of the interaction forces per time step. Actually, the evaluation of the contact forces between particles requires more computation time than the integration of the equations.

Gear predictor-corrector has three main steps: predictor, evaluation, and corrector. First, the predictor step estimates the kinematic quantities, which are the positions, the velocities, the accelerations, and other higher-order time derivatives at the next time step  $t + \delta t$  by using the Taylor series expansion in Equation 1.15. Second, the interaction forces between particles are evaluated by using a contact force model at predicted position at time  $t + \delta t$ . It must be noted that the contact force modelling can be any model that is related to a type of material. The interaction forces between particles are substituted into the Newton’s equations of motion to calculate the ‘‘evaluated’’ acceleration  $a^e(t + \delta t)$ . By subtracting between the evaluated and the predicted accelerations, it is possible to estimate the error in the predictor step:

$$\Delta a(t + \delta t) = a^e(t + \delta t) - a(t + \delta t) \quad (1.16)$$

Last, the corrector corrects all the predicted kinematic quantities from a coefficient which is proportional to the error in Equation 1.16. According to the degree of the order of the time derivative, this correction is applied with different weights:

$$\begin{aligned} r^c(t + \delta t) &= r(t + \delta t) + c_0 \Delta a(t + \delta t) \\ v^c(t + \delta t) &= v(t + \delta t) + c_1 \Delta a(t + \delta t) \\ a^c(t + \delta t) &= a(t + \delta t) + c_2 \Delta a(t + \delta t) \\ b^c(t + \delta t) &= b(t + \delta t) + c_3 \Delta a(t + \delta t) \end{aligned} \quad (1.17)$$

where  $c_0, c_1, c_2, \dots$  are the set of corrector coefficients proposed by Gear. These coefficients are dependent on both the order of the Taylor series expansion and the order of the differential equations [122, 129]. The corrector operates as a feedback control that reduces the error from the predictor. As a result, Gear predictor-corrector offers good stability and accuracy. It is worth noting that using more terms of higher-order of time derivative in Gear predictor-corrector can increase the accuracy of the algorithm while it requires more computation time. The MD algorithm based on Gear predictor-corrector can be summarized by the flowchart in Figure 1.11.

The MD algorithm was discussed in the paragraph above. Force calculation is one of the most important steps in this algorithm. Various contact force models can be employed for this step. The contact force model used in this dissertation is presented in the following paragraphs.

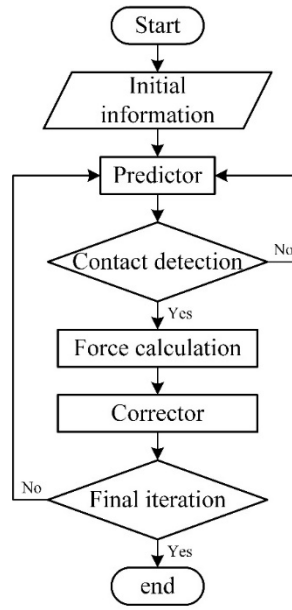


Figure 1.11 Flowchart of molecular dynamics algorithm.

The force  $F_i$  exerted on the particle  $i$  as written in Equation 1.14 above is the result of two influences. It is affected by the external forces as well as by the interaction forces between particles. The equation of this force can be written as:

$$F_i = \sum_{j \neq i} F_{ij} + F_i^{ext} \quad (1.18)$$

where  $F_{ij}$  is the interaction force exerted on particle  $i$  by particle  $j$ .  $F_i^{ext}$  denotes the external forces exerted on particle  $i$ .

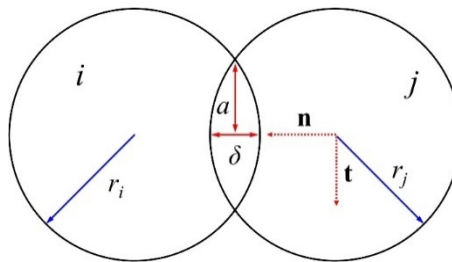


Figure 1.12 Schematic of two particles,  $i$  and  $j$ , in contact.

In the case of a 2D granular system, the contact force between particles has two components, namely the normal and tangential components as shown in Figure 1.12. The normal force  $F_n$  affects the translation of the particles, whereas the tangential force  $F_t$  affects their rotation and sliding. Thus, the interaction force can be written as:

$$F_{ij} = F_n \mathbf{n} + F_t \mathbf{t} \quad (1.19)$$

Furthermore, the normal interaction force can be split into three parts in the case of frictionless contact. The first part is a repulsive force  $F_n^e$ , which resists the deformation of particles. The second part is a viscous force  $F_n^d$ , which is relevant to energy dissipation. The third part is a cohesive force  $F_n^c$ , which is split into normal, shear, and rolling [130]. The normal force can be this written as:

$$F_n = F_n^e + F_n^d + F_n^c \quad (1.20)$$

It is worth noting that only repulsive and viscous forces are taken into account in the case of non-cohesive granular materials. On the contrary, all the terms are considered in the case of cohesive granular materials.

In the MD method, the deformation is simply modeled by considering the virtual overlap  $\delta$ , as illustrated in Figure 1.12. As the particle geometries do not change, the normal force can be calculated by a function of the virtual overlap, which is expressed in terms of vector position of the particle centers  $x_i$  and  $x_j$  and radius  $r_i$  and  $r_j$  of the two particles  $i$  and  $j$  in contact:

$$\delta = (r_i + r_j) - |x_i - x_j| \quad (1.21)$$

The “linear spring-dashpot” [131, 132] is a common model, which is applied in the present study for a calculation of the normal force between two particles. The normal force  $F_n$  is calculated by:

$$F_n = k_{eff} \delta + \alpha_n v_n \quad (1.22)$$

where  $k_{eff}$  is the effective contact stiffness,  $\alpha_n$  is the normal damping coefficient, and  $v_n$  is the normal velocity (the first-order time derivative of the virtual overlap). In fact, the integration of the Newton’s equations of motion requires a smooth friction law (mono-valued), i.e., the tangential force must be expressed as a linear function of the sliding velocity  $v_t$ . Note that the classical Coulomb’s law friction is a non-smooth function. Hence, the tangential force  $F_t$  in this study was classically defined as a “regularized” form of the exact Coulomb’s law, which can be expressed by this expression:

$$F_t = \min \{ |\gamma_t v_t|, \mu F_n \} \cdot \text{sign}(v_t) \quad (1.23)$$

where  $\gamma_t$  is the tangential viscosity coefficient and  $\mu$  is the coefficient of friction. In this study, the rotational motion due to the tangential force is assumed to be free because its value is very small compared to the normal force.

### 1.2.7 Thermal modeling in granular media

The phenomena of heat transfer consist of heat conduction, heat convection, heat radiation and heat generation (self-heating). They are complex, especially in the case of granular materials. In our research work, heat transfers were assumed limited to heat conduction, heat convection and heat generation only. When two particles move and come into contact, their relative motion creates a source of heat, denoted as  $Q_{ij}^s$  in the following. Heat generation can be computed by different methods. The heat generation model used in our research work is directly based on the first principle of thermodynamics, accounting for normal motions as well as tangential motions. The heat generation of each particle, which is related to the energy dissipation at the contact level [130], can be expressed as:

$$Q_i^s = \sum_{i=1}^N Q_{ij}^s; \quad Q_{ij}^s = \frac{1}{2} F_n^{ij} v_n^{ij} + \frac{1}{2} F_t^{ij} v_t^{ij} \quad (1.24)$$

Then, the heat conduction between particle  $i$  and its neighbors in contact is the sum of all heat exchanges as follows [133]:

$$Q_i^c = \sum_{i=1}^N Q_{ij}^c; \quad Q_{ij}^c = H_{ij}^c (T_i - T_j) \quad (1.25)$$

where  $H_{ij}^c$  is the heat conductance of contact and the term  $T_i - T_j$  is the temperature difference between particle  $i$  and particle  $j$ . This formula relies on two assumptions. The first assumption is that there is no temperature distribution inside the particle, i.e., each particle has only one temperature. The second assumption is that the temperature exchange between the particles is slow enough to prevent disrupting near particles in contact during each time step. This means that the variation of the temperature of particle over a time step is smaller than the difference temperature between particles and time step should be sufficiently small. The coefficient  $H_{ij}^c$ , which is a function of compression force,

depends on the particle properties which is explained below. Based on the Hertz theory, the coefficient  $H_{ij}^c$  can be determine from [133]:

$$\frac{H_{ij}^c}{k_{eff}^s} = 4 \left( \frac{F_n^{ij} R_{eff}}{\pi L E_{eff}} \right)^{\frac{1}{4}} \quad (1.26)$$

where  $R_{eff}$ ,  $E_{eff}$ ,  $k_{eff}^s$  and  $L$  are the effective contact radius, the effective Young's modulus, the effective thermal conductivity and the length of the cylinder, respectively.

Heat convection can be taken into account as follows:

$$Q_i^d = H_{air}^d (T_i - T_0) \quad (1.27)$$

where  $H_{air}^d$  and  $T_0$  are the heat convection coefficient and the temperature of surrounding medium (the ambient air), respectively.

For the evolution of the system, the Euler scheme can be applied to discretize the differential equation characterizing the evolution of temperature of each particle. Thus, the temperature at each time step  $dt$  can be discretized explicitly using a  $\theta$ -method over time  $t$  to time  $t+dt$  [18], which can be expressed as:

$$T_i^{t+dt} = T_i^t + (1-\theta)\dot{T}_i^t + \theta\dot{T}_i^{t+dt} \quad (1.28)$$

where  $\theta$  is a constant value between 0.5 to 1 for stability reasons. The term  $\dot{T}_i^{t+dt}$  is a function of the local thermal phenomena of particle  $i$  by accumulating from multi-contacts [134]. It can be thus calculated from:

$$\dot{T}_i^{t+dt} = \frac{dT_i^{t+dt}}{dt} = \frac{Q_i^{t+dt}}{(\rho_i c_i V_i)^{t+dt}} \quad (1.29)$$

where  $\rho_i$ ,  $c_i$ , and  $V_i$  are the bulk density, the specific heat capacity and the volume of particle respectively. In 2D simulations, the particle volume is replaced by an area. The term  $Q_i^{t+dt}$  in Equation 1.29 implies that the amount of heat is accumulated from all thermal phenomena of particle  $i$  at time  $t+dt$ . The total amount of heat in each particle can be thus split into two components:

$$Q_i = Q_i^c + Q_i^s + Q_i^d \quad (1.30)$$



where  $Q_i^c$  represents the heat exchange (heat conduction) between particle  $i$  and its neighbors in contact,  $Q_i^g$  corresponds to the heat generation by the relative motion between particle  $i$  and its neighbors, and  $Q_i^d$  corresponds to the heat exchange (heat convection) between particle  $i$  and surrounding medium (the ambient air).

### 1.3 Thermomechanics of continuous material

Thermomechanics is commonly described in terms of continuous material. In this thesis, thermomechanical phenomena in granular systems are analyzed within individual particles (“inside” the particles), allowing the continuum thermodynamics theory to be applied. Thermomechanics is a theory that generally describes the conversion between mechanical deformation and thermal energy in continuum bodies. When a body deforms, the energy of deformation may be converted into thermal energy which functions as an internal heat source of the considered body.

#### 1.3.1 Thermodynamics with internal variables

Any thermomechanical system out of equilibrium can be assumed to be the sum of subsystems at equilibrium. In the framework of this dissertation, a deformation process is considered as a quasi-static thermodynamic process. It is possibly a dissipative process. The equilibrium state of any material volume element (at equilibrium) is then characterized by set of  $n$  state variables [12, 135, 136]: the absolute temperature  $T$ , the strain tensor  $\boldsymbol{\varepsilon}$  and internal variables written as  $\boldsymbol{\alpha}$ , composed of  $n-2$  terms ( $\alpha_1, \dots, \alpha_{n-2}$ ). The free-energy function  $\psi$  is chosen as the Helmholtz free-energy function. It can be expressed in terms of internal energy  $e(\boldsymbol{\varepsilon}, \boldsymbol{\eta}, \boldsymbol{\alpha})$  and entropy  $\eta(\boldsymbol{\varepsilon}, T, \boldsymbol{\alpha})$  as follows:

$$\psi(\boldsymbol{\varepsilon}, T, \boldsymbol{\alpha}) = e(\boldsymbol{\varepsilon}, \boldsymbol{\eta}, \boldsymbol{\alpha}) - T\eta(\boldsymbol{\varepsilon}, T, \boldsymbol{\alpha}) \quad (1.31)$$

The local form of the second principle of thermodynamics is employed to derive the local form of the Clausius-Duhem inequality, defining the dissipation  $d$  [136]:

$$d = \underbrace{\boldsymbol{\sigma} : \mathbf{D} - \rho \psi_{,\varepsilon} : \dot{\boldsymbol{\varepsilon}} - \rho \psi_{,\alpha} \cdot \dot{\boldsymbol{\alpha}}}_{d_1} - \underbrace{\frac{\mathbf{q}}{T} \cdot \text{grad } T}_{d_2} \geq 0 \quad (1.32)$$

where  $\boldsymbol{\sigma}$  is the Cauchy stress tensor,  $\mathbf{D}$  is the Eulerian strain rate tensor and  $\rho$  is the mass density,  $\mathbf{q}$  is the heat flux vector. It must be noted that the dot symbol ( $\dot{\phantom{x}}$ ) means the material time derivative. The irreversible entropy source is frequently mentioned by the thermodynamics community as  $\sigma_s = d/T$ . And  $\sigma_s = 0$  means that the dissipation is null. This characterizes a reversible thermodynamic process. Usually, the dissipation can be split into two parts, which are the “intrinsic (mechanical) dissipation”  $d_1$  and the “thermal dissipation”  $d_2$  as follows:

$$d_1 = \boldsymbol{\sigma} : \mathbf{D} - \rho \psi_{,\epsilon} : \dot{\boldsymbol{\epsilon}} - \rho \psi_{,\alpha} \cdot \dot{\boldsymbol{\alpha}} \geq 0 \quad \text{and} \quad d_2 = -\frac{\mathbf{q}}{T} \cdot \text{grad } T \geq 0 \quad (1.33)$$

Furthermore, the intrinsic dissipation  $d_1$  can be distinguished into three parts as follows:

$$d_1 = \underbrace{\boldsymbol{\sigma} : \mathbf{D}}_{w_{def}^{\dot{}}} - \underbrace{\rho \psi_{,\epsilon} : \dot{\boldsymbol{\epsilon}}}_{w_e^{\dot{}}} - \underbrace{\rho \psi_{,\alpha} \cdot \dot{\boldsymbol{\alpha}}}_{w_s^{\dot{}}} \quad (1.34)$$

where  $w_{def}^{\dot{}}$ ,  $w_e^{\dot{}}$ , and  $w_s^{\dot{}}$  are the deformation energy rate, the elastic energy rate and the stored energy rate, respectively.

### 1.3.2 Heat diffusion equation

The first and second principles of thermodynamics can be written as follows, respectively [12, 135]:

$$\rho \dot{e} = \boldsymbol{\sigma} : \dot{\boldsymbol{\epsilon}} - \text{div } \mathbf{q} + r_e \quad (1.35)$$

$$\rho T \dot{\eta} = d_1 - \text{div } \mathbf{q} + r_e \quad (1.36)$$

where  $r_e$  is the external heat source (radiation).

From the constitutive state equations of the Helmholtz free-energy, Equation 1.35 can be rewritten as:

$$\rho T \dot{\eta} = \rho T \frac{\partial^2 \psi}{\partial T \partial t} = -\rho T \psi_{,s,TT} \dot{T} - \underbrace{\rho T \psi_{,T\epsilon} : \dot{\boldsymbol{\epsilon}}}_{w_{ihe}^{\dot{}}} - \underbrace{\rho T \psi_{,T\alpha} \cdot \dot{\boldsymbol{\alpha}}}_{w_{ihc}^{\dot{}}} \quad (1.37)$$

Considering Equations 1.34 and 1.35 and assuming the Fourier's law,  $q = k \text{ grad } T$ , the heat diffusion equation can be expressed as follows [135, 137]:

$$\underbrace{\rho C_{\varepsilon,\alpha} \dot{T}}_{(a)} - \underbrace{\text{div}(k \text{ grad} T)}_{(b)} = \underbrace{d_1}_{(c)} + \underbrace{\rho T \psi_{,T\varepsilon} : \dot{\boldsymbol{\varepsilon}} + \rho T \psi_{,T\alpha} \cdot \dot{\boldsymbol{\alpha}}}_{(d)} + \underbrace{r_e}_{(e)} \quad (1.38)$$

where  $C_{\varepsilon,\alpha}$  is the specific heat capacity at  $\varepsilon$  and  $\alpha$  constant. In Equation 1.34, the first term (a) is the heat power density associated to the change in temperature of the material (storage term). Heat exchanges by conduction are represented by the term (b). The term (c) is the heat power density  $d_1$  produced by the material due to irreversible mechanical phenomena. It is always positive and, as indicated above, it is called “**mechanical dissipation**” or “intrinsic dissipation”. It must be distinguished from the thermal dissipation  $d_2$  in the Clausius-Duhem inequality  $d_1 + d_2 \geq 0$ . The term (d) is associated with reversible mechanical phenomena and corresponds to thermomechanical coupling sources. It can be split into two parts. The first part corresponds to the “**thermoelastic coupling**” *with* due to thermoelasticity. They are two types of thermo-elastic coupling: one is governed by the change in internal energy (energetic elasticity) and the other is governed by the change in entropy (entropic elasticity) [138]. A simple tensile test enables us to distinguish between them: upon loading (unloading), energetic elasticity leads to a temperature decrease (increase) whereas entropic elasticity leads to a temperature increase (decrease). Actually, as both types of coupling exist in rubbery materials, a so-called *thermoelastic inversion* is observed upon loading, when the entropic contribution becomes preponderant [139]. On the contrary, compression loading (unloading) leads to a temperature increase (decrease) for both types of thermo-elastic couplings. The second part corresponds to other potential thermomechanical couplings, for instance due to solid-solid phase transformations. The last term (e) is the external heat rate  $r_e$  associated with radiation.

Some comments can be made here regarding thermoelastic couplings, depending on the type of elasticity (see page 310 of Ref [138] for more details about the comparison between the two types of elasticity):

- materials featuring **energetic elasticity** (these materials are sometimes called isentropic) have the thermal sensitivity with respect to the volume change. This sensitivity, expressed by the thermal expansion coefficient, is low for rigid materials;

- elastomeric materials feature **entropic elasticity**. Deformation-induced temperature variations in rubbers were initially discussed in the pioneering studies of Gough [140] and Joule [141] in the 19th century. The temperature changes caused by entropic elasticity are much higher than those resulting from energetic elasticity. In fact, both types of thermoelastic coupling exist in rubber-like materials, but that caused by entropic elasticity is rapidly predominant compared to that caused by energetic elasticity when the strain level increases [139].

It can be noted that **thermoelastic stress analysis (TSA)** relies on the thermal sensitivity of the volume change in materials featuring *energetic* elasticity. This sensitivity is low, but TSA succeeds in providing maps of hydrostatic stress amplitude from the temperature oscillations under cyclic loading. The method requires sufficiently high loading frequencies (to maximize the number of cycles over short times) and sufficiently high stress levels (when possible) to reach a sufficient thermal signal-to-noise ratio

### 1.3.3 Energy balance for a load-unload cycle

Let us consider a load-unload cycle, where  $A=(T_A, \varepsilon_A, \alpha_A)$  and  $B=(T_B, \varepsilon_B, \alpha_B)$  refer to the thermomechanical states of the material at the beginning and the end of the cycle respectively. Three cases can be considered [12]:

- case 1 ( $A \neq B$ ): the thermomechanical path does not correspond to a thermodynamic cycle;
- case 2 ( $A \neq B$  but  $\varepsilon_A = \varepsilon_B$ ): the stress-strain diagram shows a hysteresis loop, but it is not a thermodynamical cycle;
- case 3 ( $A = B$ ): the mechanical cycle is now a thermodynamic cycle.

The energy balance of these three situations can be discussed from the schematic diagrams in Figure 1.13.

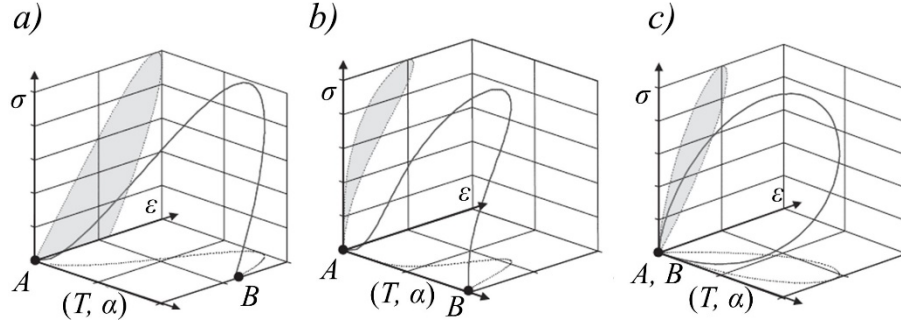


Figure 1.13 Three cases of thermomechanical evolution [12].

The two principles of thermodynamics give an alternative expression of the volume deformation energy  $w_{def}$  associated with the load-unload cycle (i.e. the area of the gray zones in the stress-strain plane in Figure 1.13) [12]:

$$w_{def} = \int_{t_A}^{t_B} d_1 dt + \int_{t_A}^{t_B} (w_e' + w_s') dt = \int_{t_A}^{t_B} d_1 dt + \int_{t_A}^{t_B} (\rho \dot{\epsilon} - \rho C_{\epsilon, \alpha} \dot{T} + w_{the}' + w_{thc}') dt \quad (1.39)$$

Equation 1.38 illustrates that:

- for case 1: it is clear that the area of the gray zones in the stress-strain plane in Figure 1.13-a is not only due to mechanical dissipation  $d_1$ . It involves stored energy and thermal dissipation as well as the effect of the thermoelastic coupling  $w_{the}$  and of other thermomechanical couplings  $w_{thc}$  if any;
- for case 2: the area of the hysteresis loop  $A_h$  in the stress-strain plane in Figure 1.13-b is due to mechanical dissipation  $d_1$  but also to the couplings.

$$w_{def} = A_h = \int_{t_A}^{t_B} d_1 dt + \int_{t_A}^{t_B} (w_{the}' + w_{thc}') dt \quad (1.40)$$

- for case 3: for a thermodynamic cycle, the area of the hysteresis loop  $A_h$  in the stress-strain plane in Figure 1.13-c is only due to mechanical dissipation.

The energy balance form then specifies the limited conditions under which the dissipated energy can be calculated by computing the hysteresis area of a load-unload cycle. This emphasizes the importance of analyzing thermal effects to determine whether a mechanical cycle is also a thermodynamic cycle, as well as determining the relative importance of coupling effects [12, 142].

## **1.4 Full-field measurement techniques and post-processing for thermomechanical analysis**

This section recalls the basis of the full-field measurement techniques that were used in our research work. Section 1.4.1 is dedicated to infrared (IR) thermography for measuring temperature fields, while Section 1.4.2 concerns the localized spectrum analysis (LSA) technique for measuring strain fields. Finally, Section 1.4.3 presents a post-processing method of the strain fields for identification purposes, namely the virtual fields methods (VFM).

### **1.4.1 Infrared thermography**

The basis for IR thermography is the measurement of the thermal radiation that is emitted from an object. Thermal radiation can be measured by the thermal sensors in an IR camera [143], offering thus various non-destructive testing and non-contact diagnostic technologies based on so-called thermal imaging, IR radiometry, IR imaging, and IR condition monitoring [144]. A wide variety of IR thermography applications exists in addition to the thermomechanics of materials, such as monitoring civil structures, microscale applications, postharvest quality control, industrial applications, medical science applications, monitoring electrical and electronic components, monitoring of the natural environment, monitoring of military applications, etc. [143-148].

Thermal radiation is an energy transmitted by electromagnetic waves. Such a phenomenon does not require a transportation medium. Thermal radiation is produced by the movement of charged particles (protons and electrons), which is caused by the temperature of matter [149]. Due to the fact that all objects with a temperature above absolute zero, they have a capability to emit electromagnetic radiation. The thermal radiation can actually originate from a solid, a liquid, and even a gas. The IR radiation was first discovered in 1800 by the experiments of Herschel [150]. In his experiments, Herschel measured the temperature of each color of sunlight passing through a prism. Herschel invented a simple monochromator from a thermometer dedicated to temperature measurement. He discovered that the highest temperature occurred at the region outside

the red of visible light spectrum, which was later referred to as “infrared”. The discovery of IR radiation opened new opportunities for applications of temperature measurement.

Figure 1.14 shows the spectrum of electromagnetic waves. Thermal radiation occupies the entire visible range, the entire IR range, and a part of the ultraviolet spectrum. Despite that, a body at room temperature only emits the majority of its energy in the IR spectrum. The IR wavelength range is defined between 0.7 to 1000  $\mu\text{m}$ . The IR radiation can be divided into 5 wavelength ranges based on the spectral band limits of frequently used IR detectors [151]:

- Near infrared (NIR), whose sensitivity is restricted to Si sensors and has a wavelength range of 0.75 to 1  $\mu\text{m}$ ;
- Short wavelength infrared (SWIR), whose sensitivity is restricted to PbS and InGaAs sensors and has a wavelength range of 1 to 3  $\mu\text{m}$ ;
- Middle wavelength infrared (MWIR), whose sensitivity is restricted to InSb, PbSe, PtSi, and HgCdTe sensors and has a wavelength range of 3 to 6  $\mu\text{m}$ ;
- Long wavelength infrared (LWIR), whose sensitivity is restricted to HgCdTe sensors and has a wavelength range of 6 to 15  $\mu\text{m}$ ;
- Very long wavelength infrared (VLWIR), with a wavelength range of 15 to 1000  $\mu\text{m}$ .

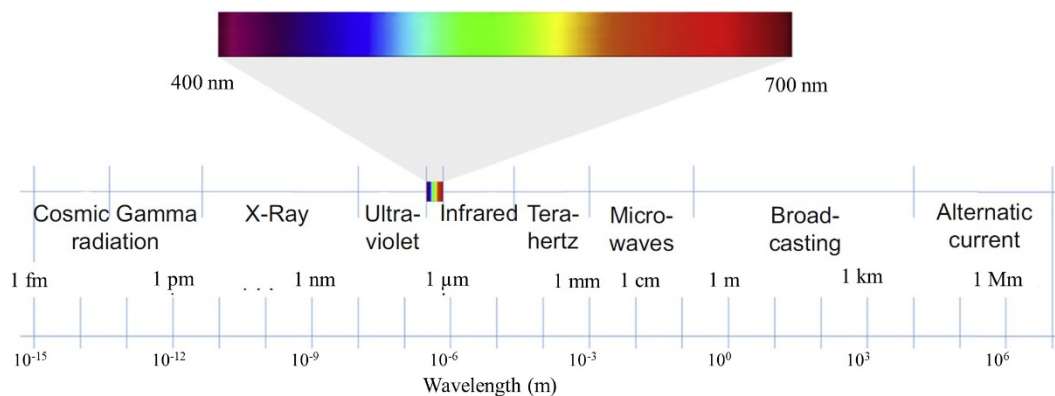


Figure 1.14 Spectrum of electromagnetic waves [13].

The most of currently in use IR cameras are primarily focused on the wavelength of two atmospheric windows: the middle (MWIR) and long (LWIR) wavelength IR spectral bands [143, 149, 151]. While the MWIR band has excellent contrast for working with

objects at high temperatures, the LWIR band is well suited for use with objects at ambient temperature. Usually, small temperature changes allow the LWIR and MWIR spectral bands to generate thermal images. Even though the LWIR band may be more sensitive to objects at ambient temperature, the MWIR band exhibits a better resolution. The LWIR spectral band performs better than the MWIR band under a variety of adverse weather conditions, such as fog, dust, and winter haze.

A hypothetical object called a "blackbody" is thought to be a perfect radiation emitter and absorber in the context of thermal radiation theory [145, 149, 152]. A blackbody is capable of absorbing all incident radiations of any wavelength and direction. Additionally, it can also emit the maximum feasible radiation at a given temperature and wavelength. The spectral hemispherical emissive power  $\phi_{\lambda,b}$  for a blackbody in terms of temperature and wavelength in accordance with Planck's law can be used to evaluate the energy flux (energy rate per unit surface area per wavelength) [143, 145, 152] as follows.

$$\phi_{\lambda,b} = \frac{C_1}{\lambda^5 (e^{C_2/\lambda T} - 1)} \quad (1.41)$$

$$C_1 = 2\pi c^2 h \quad \text{and} \quad C_2 = \frac{ch}{k_B} \quad (1.42)$$

where  $\lambda$  is the wavelength of the radiation,  $T$  is the absolute temperature,  $c$  is the speed of light,  $h$  is the Planck's constant, and  $k_B$  is the Boltzmann's constant.

The total hemispherical emissive power of blackbody at a given temperature is calculated by integrating the Planck's law in Equation 1.40 over all the wavelengths ( $0 \leq \lambda \leq \infty$ ). This equation is known as the Stefan-Boltzmann's law [143, 145, 152], which is written as follows:

$$\phi_b = \int_0^{\infty} \phi_{\lambda,b}(\lambda, T) d\lambda = BT^4 \quad (1.43)$$

where  $B$  is the Stefan-Boltzmann constant, which is function of constants  $C_1$  and  $C_2$ .

In general, the radiation of an actual body differs from the radiation of a blackbody. The former perfectly absorbs any incident radiation, also known as irradiation. On the



contrary, only a portion of the radiation is absorbed by actual bodies, with the remainder possibly being reflected or transmitted through them. Thus,

$$\tau + a + r = 1 \quad (1.44)$$

where  $\tau$  is the transmissibility coefficient,  $a$  is the absorptivity coefficient, and  $r$  is the reflectivity coefficient. All of these coefficients are typically functions of orientation (azimuth and altitude) and wavelength. Moreover, the absorptivity coefficient depends on temperature in addition to wavelength and direction [143, 152].

Most engineering materials are commonly opaque in the IR band, even if they are transparent to the visible light such as glass. It means that the transmitted radiation is equal to zero, thus:

$$a + r = 1 \quad (1.45)$$

The relationship between the emissivity and the absorptivity is given by Kirchoff's law of thermal radiation [152] as follow:

$$a = \varepsilon \quad (1.46)$$

where  $\varepsilon$  is the emissivity coefficient. The emissivity is a surface property which indicates its capability of energy emission. It is the ratio of the emitted radiation to the emitted radiation of blackbody at given temperature and given wavelength in a direction of azimuth and altitude [152]. The emissivity of the blackbody is thus equal to one, which is the maximum value for actual bodies. Practically, an IR camera not only detects energy emitted from the object but also energy reflected by the environment on the surface of the object. This surrounding reflectance effect can be solved by covering with stickers, paint, or tape on the reflecting surface. In order to improve emissivity, a general solution is to paint with a matt black color on the surface of the body, which mimics black body by decreasing the reflection [144].

Modern IR cameras can be split into two categories, depending on the type of sensor (detector) used. First, microbolometer cameras have semiconductors or metallic detectors operating at ambient temperature. The detectors respond to radiant energy with a change in resistance, leading to a change in voltage output. The latter is converted to digital level

(DL), which is calibrated into radiance or more commonly temperature. Their thermal sensitivity is around 50 mK. They are lightweight and have a relatively low cost. Second, quantum cameras, also called photon detector camera or cooled camera, have semiconductor detectors operating at cryogenic temperatures, using generally a sterling cooling engine embedded inside the camera. They incorporate an electronic shutter which controls the integration time (IT) defining how long the IR radiation is captured by the detectors. Their main advantages their excellent sensitivity, namely 20 mK after calibration and their high acquisition frequency.

For both types of cameras, a calibration must be carried out. The output from the detector is first converted into “uncalibrated” DLs. The latter must then be converted into a quantitative quantity, e.g., temperature. Currently, the sensor of both types of cameras is in the form of a matrix of detectors (pixels). These are nominally identical; but in reality, each detector reacts differently to the incoming IR radiation. Calibration laws are offered by manufacturers and are integrated into the camera system software (“factory” calibration). In the case of cooled cameras, these laws take into account the internal temperature of the camera in order to avoid thermal drifts which penalize the measurement. Calibration procedures offered by camera manufacturers consider the response of each detector to be approximately linear in terms of IR flux versus DL between two temperatures (lower and upper saturation levels) for fixed shooting conditions (IT, focus, lens, etc.). The principle of the two-point non-uniformity correction (NUC) operation consists of obtaining calibrated DLs by modifying the gain and the offset of the linear law of each pixel between two uniform thermal scenes so as to have the same linear law for all pixels. Optimal NUC calibration can be achieved over a temperature range extending from approximately 30% to 70% of the unsaturated range. Higher order polynomial functions or Planck-type functions can also be used as calibration laws, allowing the calibrated range to be extended to the vicinity of saturations. The one-point or single-point NUC consists of correcting only the offset values by considering one uniform thermal scene, generally at the ambient temperature. For more accurate measurement of the temperature fields, calibration can be performed in the laboratory using a dedicated blackbody system such as a precision extended blackbody. It is then possible to bypass the NUC operation and perform an individual

calibration for each pixel (“pixel by pixel” calibration) using polynomial functions as in ref. [153].

### 1.4.2 Localized spectrum analysis

LSA is a full-field measurement technique extracting full-field displacement and strain maps from a material surface on which a periodic pattern has previously been deposited. In the experimental application performed in this thesis, a checkerboard was employed because this pattern leads to the best metrological performance [76]. The checkerboard pattern features two periodicity directions, thus allowing displacement measurements in two directions. Processing images of a checkerboard pattern relies on the Windowed Fourier Transform (WFT) of the undeformed (reference) and deformed images of the pattern. Let  $f$  be the spatial frequency of the periodic pattern. The WFT can be written as follow [76]:

$$\hat{s}(x_1, x_2, \theta) = \int_{-\infty}^{+\infty} \int_{-\infty}^{+\infty} s(\eta_1, \eta_2) w(x_1 - \eta_1, x_2 - \eta_2) e^{-2i\pi f(\eta_1 \cos\theta + \eta_2 \sin\theta)} d\eta_1 d\eta_2 \quad (1.47)$$

where  $s$  is the gray level distribution of the checkerboard image. Angle  $\theta$  with respect to the  $x_1$ -direction (horizontal axis of the grid of the camera) defines the direction along which the displacement is measured. The checkerboard pattern features two periodicity directions, thus allowing 2D displacement measurement.  $w$  is a window centered on any pixel of coordinates  $(x_1, x_2)$  where the quantity  $\hat{s}(x_1, x_2, \theta)$  is calculated. A Gaussian function was used for this window. It represents the optimal trade-off between various constraints; see Ref [154]. It is written as:

$$w(x_1, x_2) = \frac{1}{2\pi\sigma^2} e^{-\left(\frac{x_1^2 + x_2^2}{2\sigma^2}\right)} \quad (1.48)$$

where  $\sigma$  is the standard deviation of the Gaussian function.  $\hat{s}$  is calculated for each pattern periodicity direction. Two distributions of complex numbers are thus obtained. Their arguments correspond to the phase modulation distributions along the pattern periodicity directions. By processing images in the undeformed and deformed configurations, it is possible to obtain the reference and current phase distributions  $\Phi^{\text{ref}}$  and  $\Phi^{\text{cur}}$ , respectively.

The sought displacement is proportional to the phase change between these two distributions as follows:

$$\mathbf{u}(x_1, x_2) = -\frac{p}{2\pi} \left( \Phi^{\text{cur}}(x_1 + u_1(x_1, x_2), x_2 + u_2(x_1, x_2)) - \Phi^{\text{ref}}(x_1, x_2) \right) \quad (1.49)$$

where  $p$  is the pitch of the checkerboard,  $\mathbf{u}$  the sought in-plane displacement vector, and  $u_1$  and  $u_2$  its components along  $x_1$  and  $x_2$  respectively. It should be noted that displacement is involved in both sides of the equation. A fixed-point algorithm is employed to retrieve  $u_1$  and  $u_2$  from Equation 1.48. Full details concerning the method used to process the images can be found in Refs [75, 76].

### 1.4.3 Virtual fields method

VFM is a technique which was first developed to identify the parameters governing the constitutive equations of various types of materials [14, 155]. It is based on the Principle of Virtual Work (PVW) [156]. This principle, which can be applied to any solid or portion of solid, can be regarded as the weak form of the local equations of equilibrium. It reads as follows:

$$-\int_V \boldsymbol{\sigma} : \boldsymbol{\varepsilon}^* dV + \int_{S_f} \mathbf{T} \cdot \mathbf{u}^* dS + \int_V \mathbf{b} \cdot \mathbf{u}^* dV = \int_V \rho \mathbf{a} \cdot \mathbf{u}^* dV \quad (1.50)$$

where  $\boldsymbol{\sigma}$  designates the stress tensor,  $\mathbf{T}$  the surface force,  $\mathbf{b}$  the volume force acting within the body,  $\rho$  the density, and  $\mathbf{a}$  the acceleration.  $V$  and  $S_f$  are respectively the volume of the body and its boundary.  $\mathbf{u}^*$  designates a virtual displacement field, while  $\boldsymbol{\varepsilon}^*$  is the associated virtual strain field. In the following, the different fields are functions of the  $x_1$ ,  $x_2$  and  $x_3$  Cartesian coordinates. The following quantities are generally introduced: the first term of the left-handed side refers to a virtual work done by the internal forces, the second and third terms of the left-handed side refer to a virtual work done by the external forces exerted on surface and volume, and the term of the right-handed side refers to a virtual work done by the acceleration forces. It must be noted that the term on the right-handed side can be thus neglected in case of static or quasi-static loading. The vectorial field  $\mathbf{u}^*$  must be  $C^0$ -continuous. In the case where unknown surface forces within  $S_f$  are involved in the equation, a **kinematically admissible (KA)** virtual displacement field is

used. This means that it takes zero values at all contact zones where the applied forces are not known. It is worth noting that the principle of virtual work should not be employed with discontinuous virtual displacement field. The reason is when discontinuous virtual displacement field is applied, there is a virtual tear on the surface, virtual displacement jump due to the discontinuity [14].

An important property is that Equation 1.49 is valid for an infinite number of virtual displacement fields  $\mathbf{u}^*$ . With VFM, the idea is to take advantage of this property by writing Equation 1.49 with as many independent virtual fields as necessary so that the resulting set of equations provides the parameters which are involved in the different integrals. When the parameters governing the constitutive equations of the material are the unknowns (*e.g.* Young's modulus and Poisson's ratio), the idea is to express the stress field  $\sigma$  as a function of these parameters and of the measured strain components. During a mechanical test on a continuous material, the loading  $\mathbf{T}$  applied to the specimen by the testing machine is known. All the quantities involved in Equation 1.49 can thus be expressed, the user defining suitable virtual fields. The automatic generation of virtual fields can be employed in some cases to identify the unknown material's constitutive parameters; see Ref [14] for instance. The known and unknown sets of parameters can also be switched. In this case, the constitutive equations and their governing parameters are known (so the stress field  $\sigma$  can be calculated from the measured strain field) and the loading becomes the unknown. The spirit of the method remains however the same, namely using Equation 1.49 with as many suitable virtual fields as necessary to identify the parameters defining the load.

The paragraph above dealt with quantities in the bulk of the body. The above equation involved volume integrals which can be considered as weighted averages of the stress component distributions, the weights being the virtual strain components. Stress components are related to actual strain components through the constitutive equations, so the volume integrals involve strain distributions in the bulk of the body [14]. However, the above equation is then adapted to consider in-plane problems. This is due to the fact that deformations are frequently measured over the specimen and instead of in bulk. In this case, a flat specimen or a thin body is considered as shown in Figure 1.15. The stress

components are thus assumed that in-plane stress components  $\sigma_{11}$ ,  $\sigma_{22}$ , and  $\sigma_{12}$  which are predominant over components  $\sigma_{33}$ ,  $\sigma_{13}$ , and  $\sigma_{23}$ , which can be neglected. This assumption is commonly used for thin solids, i.e., plates and shells [14].

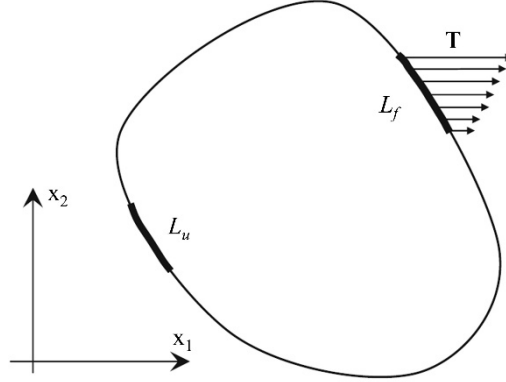


Figure 1.15 Plane stress problem [14].

The strain components on the surface of the body,  $\sigma_{11}$ ,  $\sigma_{22}$ ,  $\sigma_{12}$  as well as the acceleration  $\mathbf{a}$  and the volume force  $\mathbf{b}$  are supposed to distribute constantly through the thickness of the body. It is worth noting that the virtual fields are defined independently of  $x_3$  [14]. Therefore, the principal of virtual work becomes:

$$-t \int_S \boldsymbol{\sigma} : \boldsymbol{\varepsilon}^* dS + t \int_{L_f} \mathbf{T} \cdot \mathbf{u}^* dl + t \int_S \mathbf{b} \cdot \mathbf{u}^* dS = t \int_S \rho \mathbf{a} \cdot \mathbf{u}^* dS \quad (1.51)$$

This equation can be simplified by thickness  $t$ , thus:

$$-\int_S \boldsymbol{\sigma} : \boldsymbol{\varepsilon}^* dS + \int_{L_f} \mathbf{T} \cdot \mathbf{u}^* dl + \int_S \mathbf{b} \cdot \mathbf{u}^* dS = \int_S \rho \mathbf{a} \cdot \mathbf{u}^* dS \quad (1.52)$$

This equation represents the virtual work principle for what is commonly referred to as a plane stress problem. It is an important formulation in practice since several full-field measurement techniques available only provide measurements on the surface of the specimens under loading. As a result, strain or displacement measurements performed on the external surface can be assumed to be representative of through-thickness distributions [14].

As discussed in paragraph above, the VFM is frequently applied to identify the parameters governing constitutive equations of materials. But it has the capability to identify the forces exerted on the specimen. The constitutive equation and their governing

material parameters as well as the strain distribution should be known. The virtual displacement fields must be then defined. The virtual strain fields are then obtained by spatial differentiation. The acceleration remains in the dynamics case. This quantity can be obtained by time differentiation of the displacement fields [14]. For the sake of simplicity, the volume force acting on the body is generally supposed to be null. The principal of virtual work is reduced to:

$$-\int_V \boldsymbol{\sigma} : \boldsymbol{\varepsilon}^* dV + \int_{S_f} \mathbf{T} \cdot \mathbf{u}^* dS = \int_V \rho \mathbf{a} \cdot \mathbf{u}^* dV \quad (1.53)$$

The second integral term of the left-handed side is only the unknown, referred to surface force or traction. The virtual displacement  $\mathbf{u}^*$  in this term can be factorized when it is constant over  $S_f$ . The constant virtual displacement is then denoted as  $\mathbf{u}_s^*$ . Thus,

$$\mathbf{u}_s^* = u_s^* \mathbf{x}_1 \quad (1.54)$$

where  $\mathbf{n}_1$  is a unit vector. Equation 1.52 can be thus written as follows:

$$u_s^* \mathbf{x}_1 \cdot \mathbf{F} = u_s^* F_1 = \int_V \boldsymbol{\sigma} : \boldsymbol{\varepsilon}^* dV + \int_V \rho \mathbf{a} \cdot \mathbf{u}^* dV \quad (1.55)$$

where  $F_1$  is the projection of force vector  $\mathbf{F}$  on a unit vector  $\mathbf{x}_1$ . Thus,

$$F_1 = \frac{1}{u_s^*} \left( \int_V \boldsymbol{\sigma} : \boldsymbol{\varepsilon}^* dV + \int_V \rho \mathbf{a} \cdot \mathbf{u}^* dV \right) \quad (1.56)$$

The two other force components can be identified by repeating this procedure with two other virtual fields: the first field being constant along  $\mathbf{x}_2$ , and the second field along  $\mathbf{x}_3$ . It is necessary to select these two new unit vectors so that  $(\mathbf{x}_1, \mathbf{x}_2, \mathbf{x}_3)$  form a basis. Hence, consequently, two new projections  $F_2$  and  $F_3$  can be identified, and vector  $\mathbf{F}$  is thus fully obtained as follows:

$$\mathbf{F} = F_1 \mathbf{x}_1 + F_2 \mathbf{x}_2 + F_3 \mathbf{x}_3 \quad (1.57)$$

Hence,  $\mathbf{F}$  is composed of only two force components in a stress plane case. Only two virtual fields are required instead of three [14].

## 1.5 Full-field measurement techniques applied to granular materials

Numerical simulations and experiments have been used for many decades to study granular materials. Classical measurements are unable to investigate an entire granular system. Full-field measurement techniques are thus a solution to this issue. They are capable of providing complete spatial information about the granular system. Some examples of applying full-field measurement techniques to granular materials are presented below.

### 1.5.1 Photoelasticimetry

Photoelasticimetry is one of the classical optical full-field measurement techniques for stress and strain analysis based on a transparent non-crystalline material that is optically isotropic when free of stress to become optically anisotropic when stressed. These characteristics persist while loads are maintained but disappear when the loads are removed. When a photoelastic material is subjected to load and viewed with polarized light, colorful patterns are seen, which are directly proportional to the shear stresses and shear strains in a mechanically isotropic material. Photoelasticity was first employed in granular materials in 1957 by Dantu [25]. This technique supports particles made of photoelastic materials such as plexiglass, pyrex, polymer, which exhibit the property of transient birefringence under loading.

Majmudar and Behringer were the first to successfully identify contact forces by using photoelasticimetry [4]. The study investigated the inhomogeneous contact networks in dry granular materials under external load as shown in Figure 1.16-a, revealing different distributions of contact forces and force chain structures. The experimental system consisted in a two-dimensional array of 2,500 bidisperse photoelastic disks subjected to pure shear and isotropic compression. The researchers visualized internal stresses in each grain and by solving the inverse photoelastic problem for each disk, and they finally obtained normal and tangential force components for each contact between disks. The authors then investigated the differences in force distributions and force chain



structures between pure shear and isotropic compression states, as shown in Figure 1.16- b. The findings showed that contact forces have distinct angular distributions and spatial correlations depending on macroscopic preparation. Pure shear systems have long-range correlations in the direction of force chains, whereas isotropically compressed systems have shorter correlations.

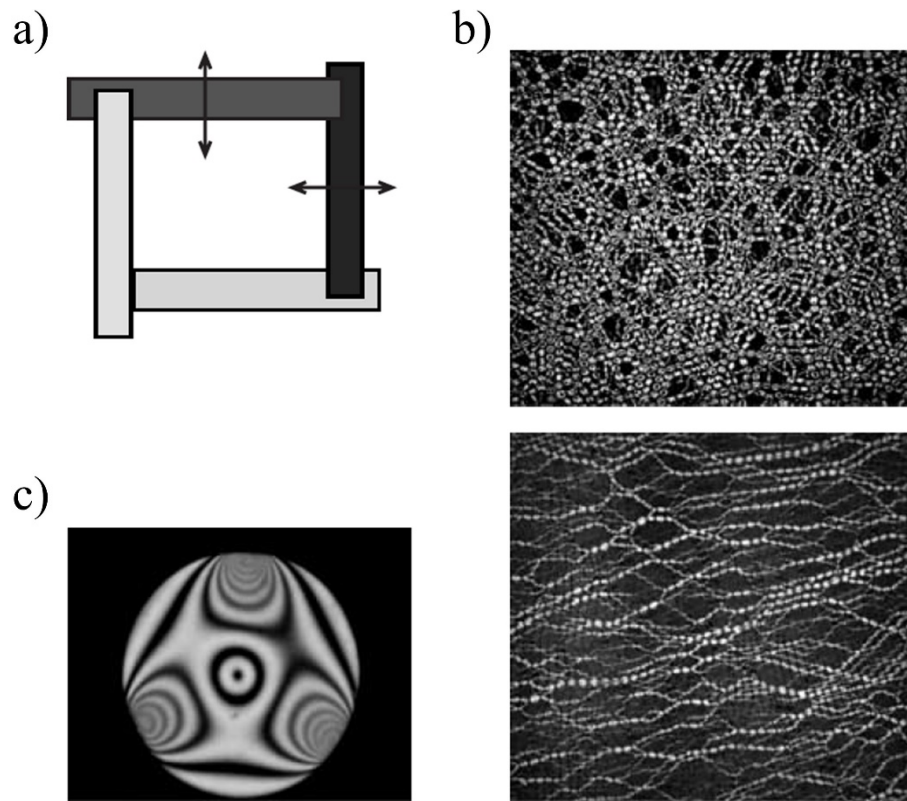


Figure 1.16 Use of photoelasticimetry to identify interparticle force networks: a) schematic of the experimental loading system; b) typical images for an isotropically compressed state (top) and a sheared state (bottom); c) example of photoelastic pattern in a single disk [4].

The study also investigated the role of friction in the system, examining the geometric anisotropy. The sheared system exhibited a strongly anisotropic distribution, with a large number of contacts aligned along the majority of force chains and a small number perpendicular to it. The isotropically compressed system showed a six-fold symmetry, indicating that the contacts are distributed evenly along these directions.

### 1.5.2 Particle image velocimetry

Particle image velocimetry (PIV) is a powerful optical surface velocity-measuring tool to visualize two-dimensional deformations of particles. It is worth noting that the technique considers each particle as being rigid. The image processing consists in identifying the translation of the particles and calculating strain patterns from these displacements. The technique was originally developed in the field of experimental fluid and gas mechanics. In contrast to fluids or gases, it does not need any intrusive markers to be installed in granulates since the grains themselves serve as tracers. Its advantage lies in the simplicity. A high-resolution monitoring can be obtained by processing successive digital images taken with a constant time between frames. There are two main steps for PIV, related to image field intensity and cross-correlation function respectively. The image intensity field assigns a scalar value to each point in the image plane, reflecting the light intensity of the corresponding point in the physical space. The area of interest (AOI) is divided into small interrogation cells, and a deformation pattern is detected by comparing two consecutive images. A search zone is extracted from the second image to find a local displacement. A cross-correlation function calculates possible displacements by correlating all gray values from the first and second images. The correlation plane is evaluated at single pixel intervals. The relative displacements are then converted into a Lagrangian deformation field with respect to the initial configuration by 2D linear interpolation. The strain tensor is calculated with a displacement matrix used in the FE method [15]. In 2007, Slominski and others employed PIV to investigate the deformation and stain field during the granular silo flow as shown in Figure 1.17-a. They studied the effect of the initial sand density and roughness of silo walls on the volumetric and deviatoric strain [15]. In 2009, Hermann and others studied the landslide impacted the water at high-speed generating a giant tsunami and the highest wave runup. They observed the kinematics of wave generation and runup by PIV. The results showed that high-speed granular landslide impacts can be divided into two main stages: landslide impact and penetration, with flow separation and cavity formation, and air cavity collapse, causing massive phase mixing [16]. The experiment is illustrated in Figure 1.17-b. In 2020, PIV was applied to investigate the dynamics and processes of rapid granular flow and the granular segregation mechanism in gravity-driven flow at the laboratory scale, which refers to granular avalanches [17]. The experiment is illustrated in Figure 1.17-c.

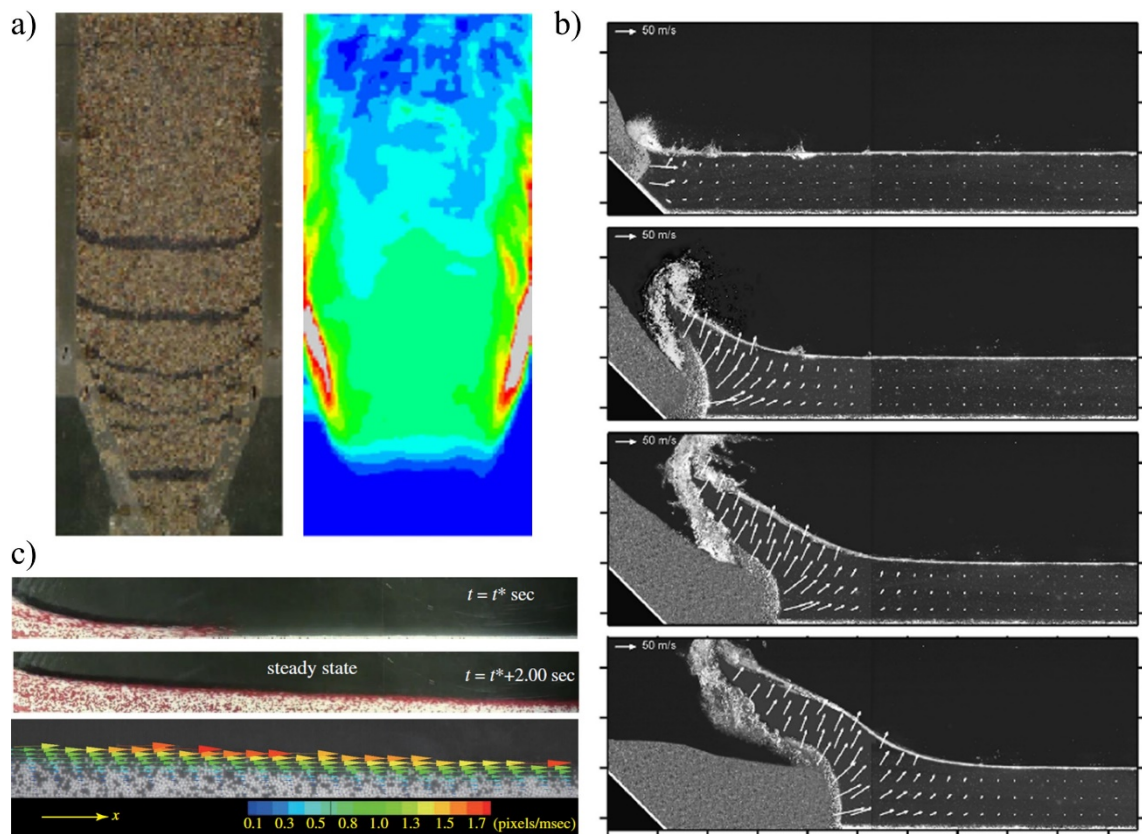


Figure 1.17 Examples of experiments using PIV: a) granular flow in silo [15], b) landslide and a giant tsunami [16], and c) granular flow under gravity [17].

### 1.5.3 Digital image correlation

Digital image correlation (DIC) is an optical technique that employs tracking movements across images. The technique is often applied to measure 2D full-field displacement and strain on the surface of a material specimen or mechanical part. It is widely employed in the science and engineering communities. Speckle patterns are applied by randomly spraying the specimen's or component's surface. There are two main types of speckle patterns, namely laser-light speckle pattern and white-light speckle pattern. In a 2D case, a white-light speckle is more robust and appealing. Indeed, it is easy to see that most of current DIC publications use white-light speckle patterns with a white light source or natural light illumination. The basic principle of DIC is to compare two consecutive images, referred to as at reference configuration and deformed configuration.

The reference image is used to track its corresponding modification in the deformed image in terms of displacement field using a cross-correlation criteria. The displacement field is then evaluated. Hence, the full-field strain field is computed by numerical differentiation. In 2017, Tolomeo proposed an approach to evaluate contact force in granular materials based on the combination of experimental measurements and numerical technique. Experimental measurement was performed by using DIC to track the displacement of the particles, as illustrated in Figure 1.18-a. A set of contact forces is then identified by a static elastoplastic computation (SEPC) or non-smooth contact dynamics (NSCD) [18]. Fanxiu employed DIC to measure mean displacement and mean strain fields. The average strain of each particle could be calculated using the DIC method, and the average stress could be calculated using the Hooke's law. The relationship between stress and particle force could be determined using basic Newtonian mechanics and the balance of linear momentum at the particle level [19]. The experiment and results are illustrated in Figure 1.18-b.

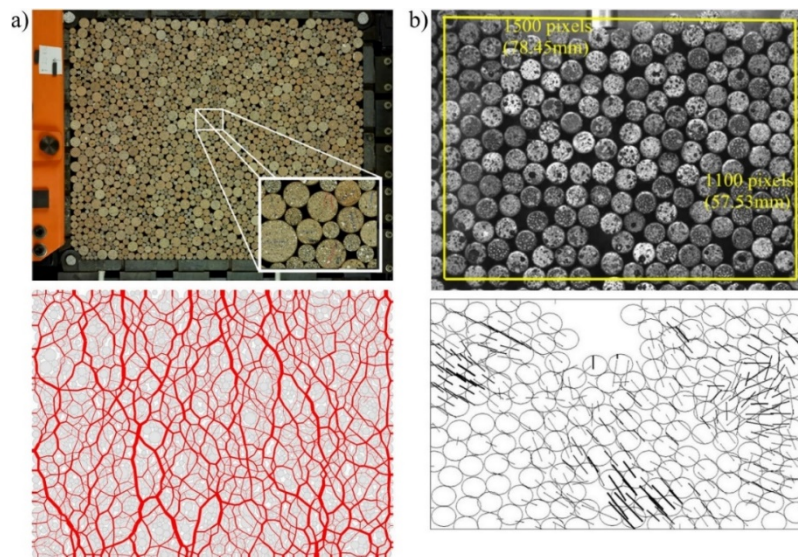


Figure 1.18 Experiment and contact force network: a) Tolomeo's study [18];  
b) Fanxiu's study [19].

#### 1.5.4 Infrared thermography

As discussed above, IR thermography is a full-field temperature measurement based on the thermal radiation that is emitted from an object. Luong employed this

experimental means on granular systems several times: see Refs [20, 71, 72]. In 2007, he employed it to soil dynamics. It allowed observation in real time of heat patterns produced by the energy dissipation caused by friction force between grains. Such dissipative heat occurred when soil was subjected to vibratory loading exceeding a characteristic threshold, evidencing the distortion mechanism [20]. The result is illustrated in Figure 1.19-a. In 2014, granular systems with about 1200 rigid particles made of polyoxymethylene (POM) and high-density polyethylene (HDPE) were analyzed by using TSA data averaged over each particle [69]. Temperature oscillations of more than  $0.1^{\circ}\text{C}$  in amplitude were measured under cyclic mechanical loading at 3 Hz. Note that the use of rapid and repeated cycles was required to obtain hydrostatic stress distributions with sufficient sensitivity. The latter was about  $0.015^{\circ}\text{C}/\text{MPa}$  and  $0.026^{\circ}\text{C}/\text{MPa}$  for POM and HDPE respectively. Then, in 2015, TSA was applied to granular systems made of a few hundred POM particles in order to analyze localizations within them [21]. It enabled us to evidence hydrostatic stress “paths” within the particles from temperature oscillations up to about  $0.2^{\circ}\text{C}$  in amplitude. Because of the need for numerous and rapid mechanical cycles (to ultimately obtain only a low thermal response), the suitability of the methodology was questioned in 2018 in Ref [22]. In this work, rigid and soft particles made of POM and thermoplastic polyurethane (TPU), respectively, were mixed. It was found that temperature variations of more than  $0.8^{\circ}\text{C}$  could be obtained in the soft particles without the need to average the values over several cycles. Typical results are illustrated in Figure 1.19.



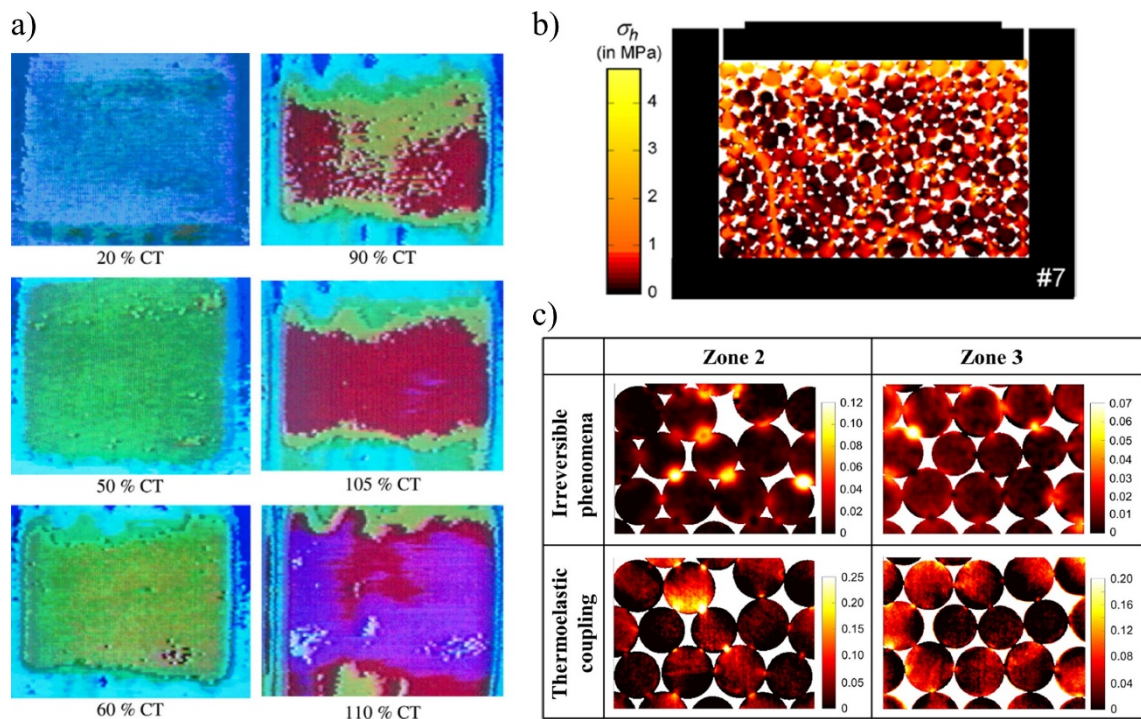


Figure 1.19 Application of infrared thermography to the analysis of the mechanics of granular materials: a) temperature patterns associated to mechanical dissipation in a dry siliceous sand under shearing [20]; b) temperature changes associated to thermoelastic coupling, converted in hydrostatic stress, in two-dimensional granular systems under cyclic confined compression [21]; c) evidence of differences in thermal response between particles made in energetic material and entropic material [22].

## 1.6 Conclusion

As can be seen in the literature, the mechanical behavior of granular media was mainly studied with numerical simulations, in particular using the molecular dynamics (MD) method. Thermal modeling of granular media was also concerned, including heat production (mechanical dissipation) and heat transmission between particles. Experimental studies are much fewer in number compared to the numerical studies. The available experimental methods are indeed complex to implement. However, it was noted in this chapter that there exist some approaches based on two-dimensional (2D) full-field measurements relying on cameras: i) photoelasticimetry, which was successfully used to

identify force contact networks in granular systems made of birefringent particles; ii) particle image velocimetry (PIV), which considers particles as rigid and allows measuring strain patterns in the granular systems; iii) digital image correlation (DIC), which enables the measurement of the particle deformations, and then to identify contact forces by coupling with suitable modelling. These three techniques, widely used in the granular material community, are not used in the following of the thesis. Let us indicate also the scarce use of infrared thermography (IRT) in the granular materials community, providing first elements to perform an experimental thermomechanical analysis of discrete materials.

The work described in the following chapters relies on two types of full-field measurement techniques:

- Localized spectrum analysis (LSA) with subsequent processing by the virtual fields method (VFM);
- IRT and subsequent deformation calorimetry on soft particles.

## CHAPTER 2

# Identification of contact forces from synthetic strain data

### 2.1 Introduction

Force measurement is a classical problem in engineering. However, it is difficult to measure forces in certain challenging situations, in particular within multi-contact systems. This chapter proposes to develop an approach for interparticle contact force identification in 2D granular materials by using the virtual fields method (VFM). See Section 1.4.3 in the bibliography and state-of-the-art chapter for a reminder about this identification method. VFM is generally applied to identify the parameters governing the constitutive equations of materials (for instance the Young modulus or the Poisson's ratio in the case of linear isotropic elasticity) assuming the external forces are known. It can be also applied to identify the external loading by switching between the sets of known and unknown. In this case, the constitutive equations and their governing parameters are known, and the loading becomes the unknown. **The purpose of this chapter is to apply this principle to interparticle contact force identification by using synthetic strain fields provided by a finite element (FE) model.** The next chapter deals with experimental data obtained by localized spectrum analysis (LSA). Specific questions concerns the choice of the *virtual* displacement fields in case of noisy *real* strain data (as in experiments) and the impact of potential bias in the *real* strain data, missing along the boundary of the cylinders, error in the particle locations, lack of spatial resolution due to strain concentration near the contacts, as in experiments.

Throughout this chapter, the following convention is used to represent quantities: scalars are written in *italics*; first-order tensors (vectors) are written in **bold**; second-order



tensors are written with straight symbols, neither italic nor bold; the contracted product between two matrices and the scalar product between two vectors are represented by symbols “:” and “·”, respectively; finally, virtual quantities are indicated by a star “\*” labeled in superscript.

## 2.2 Additional assumptions for contact force identification

In the present work, the goal is to apply VFM in order to identify contact forces in a 2D multi-contact system composed of cylindrical particles, assuming that the constitutive equations of the base material and their governing parameters are known. Equation 1.50 in previous chapter can be written for each cylindrical particle, and the unknowns are the contact forces. The following additional assumptions were considered in this work:

- the contribution of the volume force  $\mathbf{b}$  is neglected, considering that the effect of gravity is small compared to that of the applied external load;
- the material of the cylinders is assumed to be homogeneous and isotropic linear elastic. The constitutive equation is governed by Hooke’s law;
- the stress state is considered as a plane because measurement areas are free boundaries (the free ends of the cylinders). Three-dimensional FE simulations with friction were carried out in a preliminary study. The strain component fields at the free end of the cylinders were extracted for subsequent force identification by VFM. The obtained results (not reported here) showed that the plane stress hypothesis provides the fewest identification errors compared to plane strain and generalized plane strain hypotheses.
- the in-plane contact forces are assumed to act at points, meaning that for all particles, the second integral in Equation 1.50 is replaced, for a given virtual field, by a discrete sum of scalar products between forces and virtual displacements expressed at the contacts.

With these simplifications, Equation 1.50 from Section 1.4.3 reduces to:

$$\int_S \mathbb{Q} \boldsymbol{\varepsilon} : \boldsymbol{\varepsilon}^* dS = \sum_{i=1}^{N_{\text{cont}}} \mathbf{T}_i \cdot \mathbf{u}^*(P_i) \quad (2.1)$$

where  $\mathbb{Q}$  is the stiffness matrix of the material,  $\boldsymbol{\varepsilon}$  is the (*real*) strain field,  $S$  is the cross-section area of the 2D particle,  $N_{\text{cont}}$  the number of contacts, and  $\mathbf{T}_i$  the contact force at point  $P_i$ . Let us recall that  $\mathbf{u}^*$  designates a *virtual* displacement field, while  $\boldsymbol{\varepsilon}^*$  is the associated *virtual* strain field.

We consider first a simple example where the objective is to identify the two components  $F_1$  and  $F_2$  of the contact force  $\mathbf{F}$  acting at point  $P$  in Figure 2.1. Equation 2.1 can be rewritten by discretizing the integral, considering that the real strains are known over a pixel grid using a full-field measurement technique:

$$A \times \left[ Q_{11} \sum_{k=1}^{N_{\text{pix}}} \varepsilon_{1_k} \varepsilon_{1_k}^* + Q_{22} \sum_{k=1}^{N_{\text{pix}}} \varepsilon_{2_k} \varepsilon_{2_k}^* + Q_{12} \sum_{k=1}^{N_{\text{pix}}} \varepsilon_{1_k} \varepsilon_{2_k}^* + \right. \\ \left. Q_{21} \sum_{k=1}^{N_{\text{pix}}} \varepsilon_{2_k} \varepsilon_{1_k}^* + Q_{66} \sum_{k=1}^{N_{\text{pix}}} \varepsilon_{6_k} \varepsilon_{6_k}^* \right] = \frac{1}{t} \left[ F_1 u_1^*(P) + F_2 u_2^*(P) \right], \quad \forall \mathbf{u}^* \text{ KA} \quad (2.2)$$

where  $A$  is the area of the pixel,  $N_{\text{pix}}$  the number of pixels covering the area  $S$ , and  $t$  the thickness of the cylindrical particle. Quantities  $Q_{ij}$ ,  $\varepsilon_i$  and  $\varepsilon_i^*$  are respectively the stiffness components and the real and virtual strain components in Voigt notation ( $\varepsilon_1 = \varepsilon_{11}$ ,  $\varepsilon_2 = \varepsilon_{22}$  and  $\varepsilon_6 = 2 \varepsilon_{12}$ , same for the virtual quantities). On the right-hand side of the equation,  $u_1^*(P)$  and  $u_2^*(P)$  are the components of the virtual displacement  $\mathbf{u}^*$  expressed at the contact point  $P$ . Note that “ $\mathbf{u}^*$  KA” (kinematically admissible) means here that  $\mathbf{u}^*$  is equal to zero at all the contact points except point  $P$ .

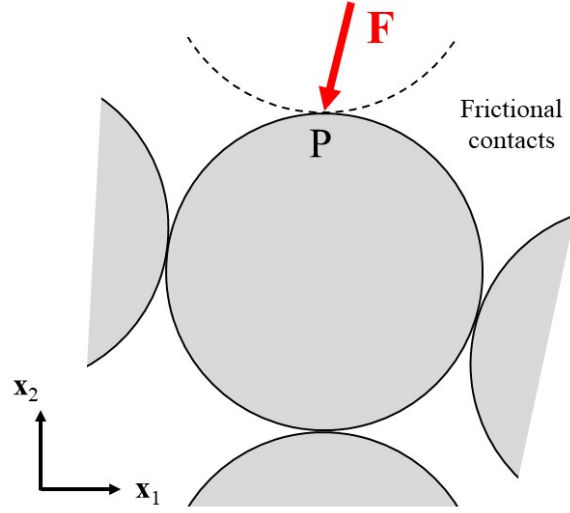


Figure 2.1 Cylindrical particle subjected to several contacts. The objective is to apply VFM to identify the two components of the in-plane interparticle force  $\mathbf{F}$  at point P.

Additional relations can be used in the case of linear isotropic elasticity:

$$\begin{cases} Q_{11} = Q_{22} = \frac{E}{1-\nu^2} \\ Q_{12} = Q_{21} = \frac{\nu E}{1-\nu^2} \end{cases} \quad (2.3)$$

where  $E$  and  $\nu$  are Young's modulus and Poisson's ratio, respectively. Equation 2.2 thus reduces to:

$$A \times \left[ Q_{11} \sum_{k=1}^{N_{\text{pix}}} (\varepsilon_{1_k} \varepsilon_{1_k}^* + \varepsilon_{2_k} \varepsilon_{2_k}^*) + Q_{12} \sum_{k=1}^{N_{\text{pix}}} (\varepsilon_{1_k} \varepsilon_{2_k}^* + \varepsilon_{2_k} \varepsilon_{1_k}^*) + Q_{66} \sum_{k=1}^{N_{\text{pix}}} \varepsilon_{6_k} \varepsilon_{6_k}^* \right] = \frac{1}{t} [F_1 u_1^*(\mathbf{P}) + F_2 u_2^*(\mathbf{P})], \quad \forall \mathbf{u}^* \text{ KA} \quad (2.4)$$

The two scalar unknowns  $F_1$  and  $F_2$  can be determined using the PVW twice with independent virtual fields, providing two linear equations. The system of two equations can be then written in matrix form as follows:

$$\mathbf{E}\mathbf{Q} = \mathbf{U}^*\mathbf{T} \quad (2.5)$$

where

$$\begin{aligned}
\mathbf{E} &= \begin{bmatrix} \sum_{k=1}^{N_{\text{pix}}} (\varepsilon_{1_k} \varepsilon_{1_k}^* + \varepsilon_{2_k} \varepsilon_{2_k}^*) & \sum_{k=1}^{N_{\text{pix}}} (\varepsilon_{1_k} \varepsilon_{2_k}^* + \varepsilon_{2_k} \varepsilon_{1_k}^*) & \sum_{k=1}^{N_{\text{pix}}} \varepsilon_{6_k} \varepsilon_{6_k}^* \\ \sum_{k=1}^{N_{\text{pix}}} (\varepsilon_{1_k} \varepsilon_{1_k}^* + \varepsilon_{2_k} \varepsilon_{2_k}^*) & \sum_{k=1}^{N_{\text{pix}}} (\varepsilon_{1_k} \varepsilon_{2_k}^* + \varepsilon_{2_k} \varepsilon_{1_k}^*) & \sum_{k=1}^{N_{\text{pix}}} \varepsilon_{6_k} \varepsilon_{6_k}^* \end{bmatrix} \\
\mathbf{Q} &= \begin{pmatrix} Q_{11} \\ Q_{12} \\ Q_{66} \end{pmatrix} \\
\mathbf{U}^* &= \begin{bmatrix} u_1^{*(1)}(\mathbf{P}) & u_2^{*(1)}(\mathbf{P}) \\ u_1^{*(2)}(\mathbf{P}) & u_2^{*(2)}(\mathbf{P}) \end{bmatrix} \\
\mathbf{T} &= \frac{1}{t} \begin{pmatrix} F_1 \\ F_2 \end{pmatrix}
\end{aligned} \tag{2.6}$$

where exponents (1) and (2) indicate the first and second virtual fields considered. Note that Equation 2.5 can be rewritten as a linear system  $\mathbf{A} \mathbf{X} = \mathbf{B}$  where  $\mathbf{X}$  is the vector gathering the two unknowns  $(F_1, F_2)$ . Vector  $\mathbf{B}$  is equal to  $\mathbf{E} \mathbf{Q}$ . By moving constant  $1/t$  from  $\mathbf{T}$  to  $\mathbf{U}^*$ , matrix  $\mathbf{A}$  is then equal to  $\mathbf{U}^*/t$ .

Choosing the best possible virtual fields  $\mathbf{u}^{*(1)}$  and  $\mathbf{u}^{*(2)}$  is a key point of the problem, since they directly influence the conditioning of the matrix of the linear system. In an experimental context, this choice therefore influences noise propagation from the images captured by the camera to the final identified forces. Various procedures were compared in the present study to elaborate these virtual fields.

Before considering the case of multiple contact points, a simple example is given here with only two opposite frictional contacts: see Figure 2.2-a. The objective is to define two virtual displacement fields  $\mathbf{u}^{*(1)}$  and  $\mathbf{u}^{*(2)}$  to identify the two components of the interparticle force  $\mathbf{F}$  at point P. A simple way to do this is to choose a virtual compression and a virtual shear to decouple the equations. Thus:

$$\begin{cases} u_1^{*(1)} = 0 \\ u_2^{*(1)} = -k_1 x_2 \end{cases} \quad \text{and} \quad \begin{cases} u_1^{*(2)} = -k_2 x_2 \\ u_2^{*(2)} = 0 \end{cases} \tag{2.7}$$

where  $k_1$  and  $k_2$  are two scalar constants. Figures 2.2-b and c show schematic views of these two virtual displacement fields.  $\mathbf{u}^{*(1)}$  and  $\mathbf{u}^{*(2)}$  are null at contact point O and non-null at contact point P. It should be noted that the virtual displacement fields can be

defined by any equation or field, the important point being that they must be  $C^0$  continuous and KA.

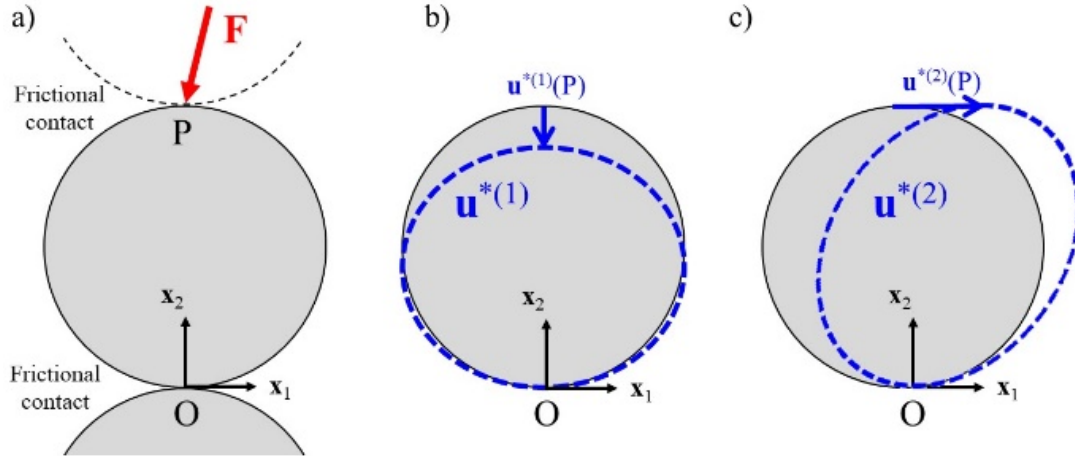


Figure 2.2 Illustration in the case of two opposite frictional contacts:  
 a) force  $\mathbf{F}$  at point P to be identified by VFM; b-c) shape of the particle subjected to two virtual displacement fields  $\mathbf{u}^{*(1)}$  and  $\mathbf{u}^{*(2)}$  enabling the identification of the two components of  $\mathbf{F}$ .

## 2.3 Defining virtual fields

The objective of this section is to define the best virtual fields to identify the contact forces. We rely for this on numerical simulations. A FE model is used to provide synthetic real strain fields ( $\epsilon$ ). The criterion for virtual field selection is the difference between identified and reference force values when noisy strain data are considered. The best type of virtual fields being chosen, we examine the sensitivity of the identification to sources of error other than noise in the images during experiments; these are the fact that the coordinate system used to perform the VFM calculation and the one where the experimental data are obtained can potentially be shifted; and the fact that experimental strain data are generally missing along the boundaries.

### 2.3.1 Creation of synthetic strain fields

The first step was to create 2D FE models with the Ansys package in order to have reliable synthetic fields of displacement  $\mathbf{u}$  and strain  $\epsilon$ . These fields were then processed

with VFM to retrieve the contact forces. Linear quadrilateral elements were used; see Figure 2.3. A convergence study (not reported here) showed that the mesh refinement was sufficient to obtain reliable data for the identification procedure.

Particles have a circular cross-section and a thickness  $t$  equal to 30 mm. They are made of a plastic material with a Young's modulus of the order of 1 GPa, chosen from the Ansys material database:  $E = 1.08$  GPa and  $\nu = 0.42$ . The frame containing the particles and the pusher applying a vertical force at the top of the granular system are made of steel (Young's modulus of 200 GPa and Poisson's ratio of 0.30). Two types of contact are considered in the study: *frictionless* and *with friction*. In the latter case, Coulomb's law is used with friction coefficients equal to 0.29 and 0.23 for the interparticle contacts and the particle-wall contacts, respectively [157, 158].

A vertical displacement was applied to the pusher to create a vertical compression force with an amplitude of  $-10$  kN. The values considered as input data for the identification procedure are the strain components  $\varepsilon_1 (= \varepsilon_{11})$ ,  $\varepsilon_2 (= \varepsilon_{22})$  and  $\varepsilon_6 (= 2 \varepsilon_{12})$  obtained from the FE calculation. Gaussian noise was added to these data in order to mimic actual noise affecting experimental strain fields. A standard deviation of  $2E-04$  was considered for the noise affecting the  $\varepsilon_1$  and  $\varepsilon_2$  strain maps. This is the order of magnitude which is classically considered with the measurement technique used in the following chapter, namely LSA [75, 159]. Note that this standard deviation value must be multiplied by  $\sqrt{2}$  for the engineering shear strain  $\varepsilon_6$ . Lower and higher levels of noise are compared in the following section to observe the influence of the noise on the identification results. Figure 2.3 shows the mesh of the three configurations considered in the following part of the study:

- Configuration C1: one particle 50 mm in diameter with four frictionless contacts — Various procedures for the construction of the virtual fields are compared to identify the vertical compression force  $\mathbf{F}$  at the top contact A;
- Configuration C2: same as Configuration C1, but with 6 contacts — The objective is to evaluate the influence of a larger number of contact points on the quality of the identification results. Note that the contact locations correspond to the situation of a particle within a compact monodisperse granular system;

- Configuration C3: three particles, 40 mm, 50 mm and 60 mm in diameter — VFM was applied to identify all the contact forces in the granular system. Frictionless and frictional contacts were considered.

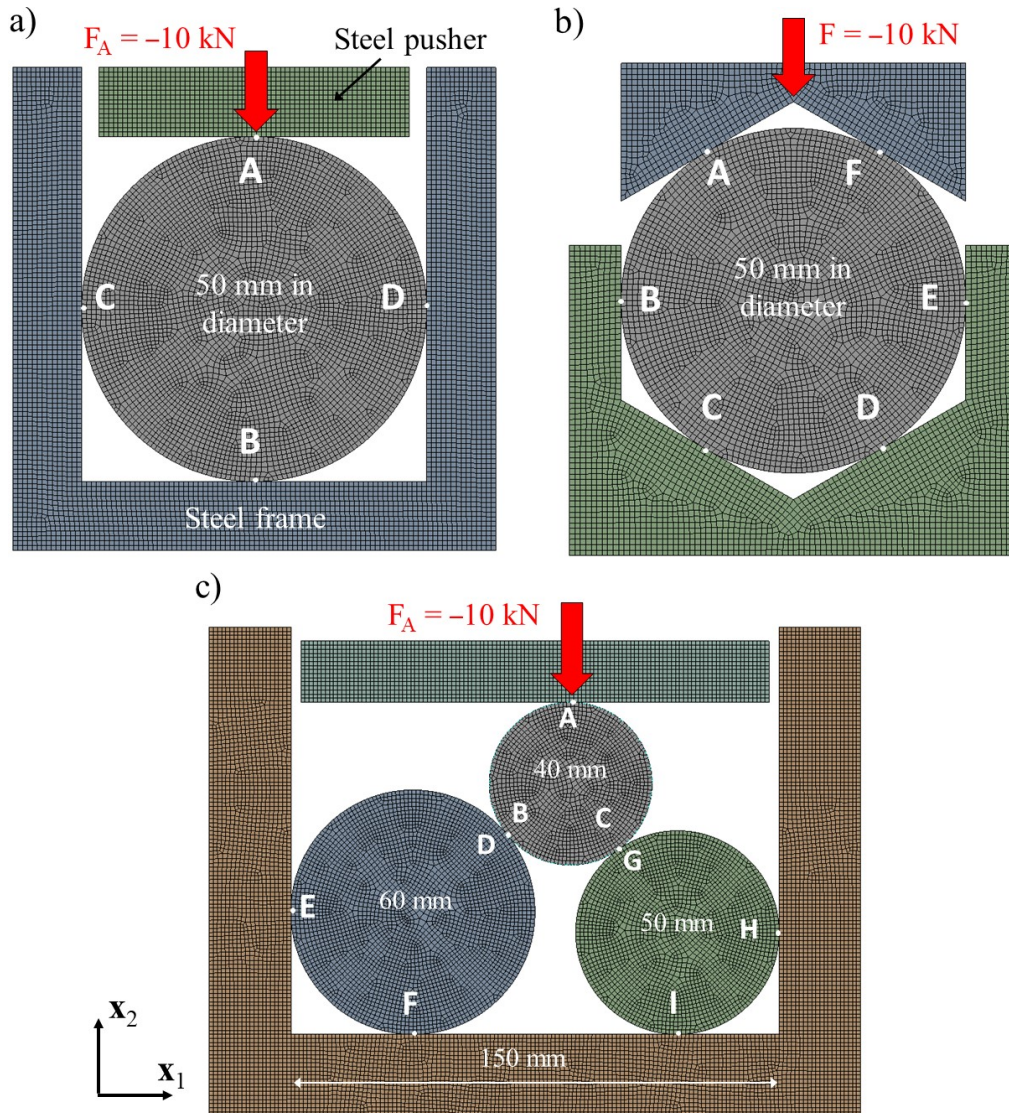


Figure 2.3 Finite element models to obtain real strain fields:

a) Configuration C1; b) Configuration C2; c) Configuration C3.

### 2.3.2 Several approaches to define virtual displacement fields

In the general case, a particle is surrounded by several other particles. The two components  $F_1$  and  $F_2$  of each contact force must be therefore identified. For a given

contact on a given particle, the idea is to define a pair of virtual displacement fields  $\mathbf{u}^{*(1)}$  and  $\mathbf{u}^{*(2)}$  which are null at all the contact points of the particle except at the one where the force components must be identified. The procedure shall be applied to all the contact points of a given particle so that the pairs of unknown force components are identified one by one at all the contact points. As the procedure above will be applied to all the particles and, for each particle, at several contact points, the definition of the virtual displacement fields has to be as versatile as possible.

There is an infinite number of virtual fields that can potentially lead to the sought contact force. The classic method for defining them consists in considering a closed-form equation, as in Equation 2.7 defining the virtual fields shown in Figure 2.2. Other routes can be investigated, namely using randomly defined functions or piecewise-defined functions or by interpolating data generated in a way which is suitably defined by the user. Configuration C1 in Figure 2.3-a is first considered for comparison between different procedures. The objective is to rank the different virtual fields investigated by comparing for each of them the value of the identified force component  $F_2$  at Point A to the reference force. The latter is the force introduced by the user in the FE model (here – 10 kN). The sensitivity to noise of the result as well as the robustness of the procedure must be accounted for in this ranking.

It is worth noting that the real strain field provided by the FE model in the zones close to the contact points is certainly not reliable. The same remark holds for the strain components in these zones measured in experiments. The idea was therefore to remove the influence of these zones from the equations. This can easily be done by defining suitable virtual fields. To this end, we consider a small zone around each of the contact points. These small zones are denoted  $Z_A$ ,  $Z_B$ ,  $Z_C$  and  $Z_D$  around points A, B, C or D respectively for Configuration C1. Virtual *rigid body* motion is imposed within these four small zones. Consequently, the virtual strain field is rigorously null within such zones. Since the integrands of the integrals involved in Equation 2.1 are mere products of real and virtual strain components calculated at any point, tailoring the virtual field in such a way that it is null over some zones is equivalent to saying that the influence of the real strain field is eliminated over these zones. Questionable data are therefore eliminated.



Four different procedures were defined for the identification of the force component  $F_2$  at Point A from the strain values obtained by the FE model. Figure 2.4-a shows the  $u_2^*$  displacement fields of the four procedures described below, the  $u_1^*$  components being null in all cases. Note that the pitch of the regular mesh used to discretize the different fields is  $25 \mu\text{m}$ . This value was chosen as it represents the size of one pixel of the camera sensor that will be used for the experiment with the three-particle system in following chapter:

- Procedure #1: virtual field defined by closed-form expressions — The idea is to define the virtual displacement field as the product of *linear* functions ensuring a zero value on lines located near the contact points, except the one where the force must be identified. Between each of these contact points and its associated line, the virtual displacement is set to zero. As indicated above, the underlying idea is to remove those zones where the real strain gradients are the highest, *i.e.*, where the measurement is the most prone to measurement errors. Far from the contacts, the real strain values are lower in amplitude, and thus more affected by measurement noise. However, the latter is expected to be averaged out when calculating the weighted sums of real strain components in Equation 2.4, the weight being the virtual strain components. In the four-contact case (Configuration C1), it gives the following “cubic” equation over the zone Z defined by  $a < x_1 < b$  and  $c < x_2$ ; see Figure 2.4-a column 1:

$$u_2^*(x_1, x_2) \begin{cases} (x_1 - a) \times (x_1 - b) \times (x_2 - c) & \text{over } Z \\ 0 & \text{if } x_1 < a \text{ or } x_1 > b \text{ or } x_2 < c \end{cases} \quad (2.8)$$

Here, constants  $a$ ,  $b$  and  $c$  are chosen in such a way that  $u_2^*$  is null along the vertical (for  $a$  and  $b$ ) or horizontal (for  $c$ ) lines that define the three zones  $Z_B$ ,  $Z_C$  and  $Z_D$ . Zone  $Z_B$  was chosen as a narrow horizontal band with a width of  $1.25 \text{ mm}$  (corresponding to 5% of the diameter of the cylinder).  $Z_C$  and  $Z_D$  were defined in the same way, except that both are vertical instead of horizontal. Then  $u_2^*$  is extended beyond domain Z with  $u_2^* = 0$ . Note that by using a cubic function over Z, it is not possible to define a zone  $Z_A$  around Point A where the virtual displacement would be rigid-body-like in the same spirit as for zones  $Z_B$ ,  $Z_C$  and  $Z_D$ . This means that the real strain field, which is probably not correctly estimated

in the vicinity of Point A, either with numerical simulations or with real measurements, cannot easily be eliminated with this first procedure. The three zones  $Z_B$ ,  $Z_C$  and  $Z_D$  are visible in the virtual strain field  $\varepsilon_2^*$  represented in Figure 2.4-b column 1, with small portions of the disk close to contact points B, C and D over which  $\varepsilon_2^*$  is rigorously null (yellow color in the maps). Note that, while  $u_2^*$  is  $C^0$  continuous,  $\varepsilon_2^*$  is not continuous since there is a “jump” at the line defining zone  $Z_B$ . However, this does not induce any approximation in the PVW equation.

- Procedure #2: randomly defined virtual field— Since there is an infinite number of KA  $u_2^*$  fields, an option can be to choose them randomly [160]. In this case,  $u_2^*$  can be defined piecewise by using a coarse mesh, randomly choosing the virtual nodal displacements lying between  $-1$  and  $0$ ; see Figure 2.4-a (column 2). Values are then calculated at the pixel level by using the shape functions of the elements. For the present four-contact case, the value prescribed for  $u_2^*$  is  $0$  within  $Z_B$ ,  $Z_C$  and  $Z_D$ , and  $-1$  within  $Z_A$ . The values of  $\varepsilon_2^*$  are thus rigorously equal to zero in the four zones; see Figure 2.4-b (column 2). Note that the identification was performed 1000 times, each time with different randomly-defined displacements at the virtual nodes. The objective was to find the best field among these 1000 virtual fields, *i.e.*, the one that minimizes the identification error caused by noise in the real strain field. The virtual displacement field displayed in Figure 2.4-a column 2 is the best one that was found. Long calculation times were however required to perform these 1000 calculations, which is a drawback of Procedure #2; see further comments below.
- Procedure #3: virtual field defined by triangulation-based linear interpolation — Triangulation-based linear interpolation can be performed between different zones using the built-in Matlab function named ‘griddata’. For the present application, the virtual displacements  $u_2^*$  were interpolated between the four zones  $Z_A$ ,  $Z_B$ ,  $Z_C$  and  $Z_D$ , with  $u_2^* = -1$  over  $Z_A$ , and  $u_2^* = 0$  over the other three zones. The spatial distribution of the corresponding virtual strain field  $\varepsilon_2^*$  was then deduced by differentiating the virtual displacement field with the ‘gradient’ function of Matlab. The four zones  $Z_A$ ,  $Z_B$ ,  $Z_C$  and  $Z_D$  are clearly visible in the virtual strain field  $\varepsilon_2^*$  in Figure 2.4-b column 3, since  $\varepsilon_2^*$  is rigorously null over these zones. Strain jumps

are visible along some inclined lines, which does not induce any approximation in the PVW equation, as indicated above.

- Procedure #4: virtual field defined by triangulation-based natural neighbor interpolation — VFM involving integrals whose integrands are products between real and virtual strain components over the particle, reducing the influence of this noise, can be obtained by considering virtual strain components with *smooth* spatial fluctuation, so that the influence of the noise affecting the measurements is equivalent at any point. Smoothly fluctuating virtual strain fields can be obtained by triangulation-based natural neighbor interpolation, which is a similar approach to the previous one except for the option in the Matlab command, which is ‘natural’. See Figure 2.4 column 4 showing the  $\varepsilon_2^*$  field with smooth fluctuations (compare with Procedure #3).

It can be observed that the different virtual displacement fields  $u_2^*$  shown in Figure 2.4-a are all continuous, whereas the associated virtual strain fields  $\varepsilon_2^*$  in Figure 2.4-b are not. In particular, Procedure #2 gives (by construction) the most fluctuating virtual strain field. It is worth remembering that  $u_1^*$  was considered as null, thus enabling us to retrieve the vertical component of the force  $F_2$  at Point A by using  $u_2^*$ . By switching  $u_1^*$  and  $u_2^*$ , it is possible to identify the horizontal component of the force  $F_1$  instead of  $F_2$ .

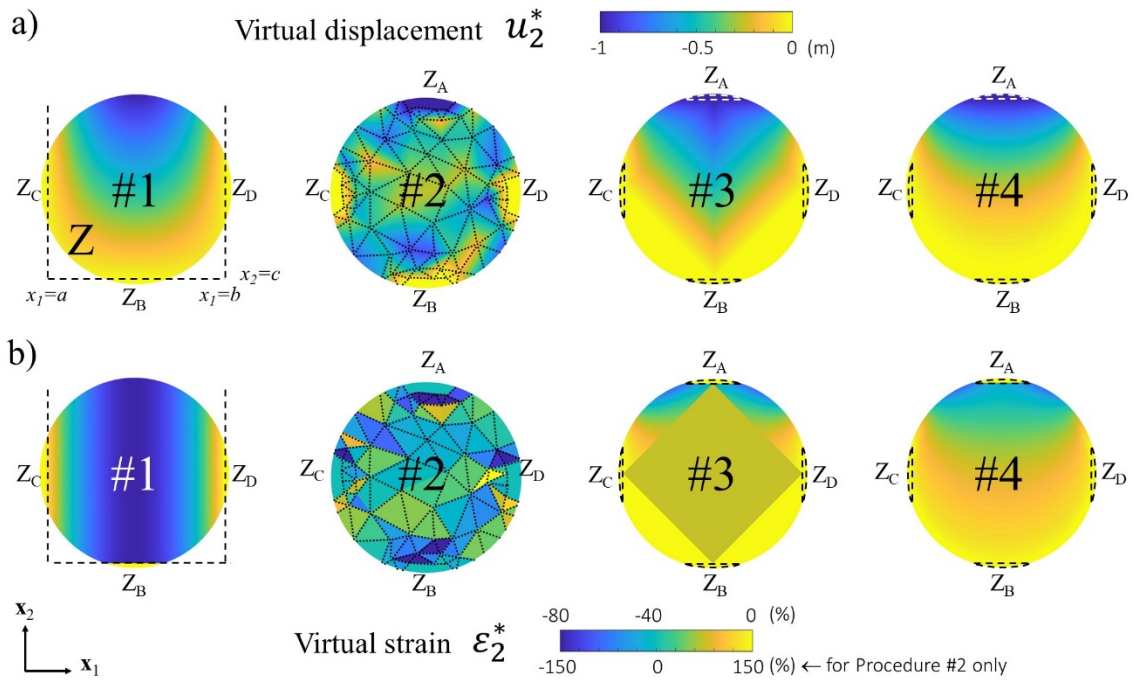


Figure 2.4 Different procedures for the identification of the force component  $F_2$  at Point A for Configuration C1 in Figure 2.3-a: a) field of the virtual displacement component  $u_2^*$ ; b) corresponding virtual strain fields  $\epsilon_2^*$ . First column: closed-form expressions (Procedure #1). Second column: randomly defined from a coarse mesh (Procedure #2). Third column: triangulation-based linear interpolation (Procedure #3). Fourth column: triangulation-based natural neighbor interpolation (Procedure #4).

### 2.3.3 Application of the four procedures and selection of the most relevant

The objective here is to assess the quality of the results provided by the four different virtual fields described above, and to select the most relevant procedure. The criterion for selection is to obtain the lowest sensitivity to noise in the real strain fields when applying the force identification procedure with VFM.

The four procedures were applied to identify the value of the force component  $F_2$  at Point A of Configuration C1. The force retrieved with each procedure was compared to the reference value ( $-10$  kN). For this, noise with a standard deviation of  $2E-04$  as discussed in the following section was first added to the strain values given by the FE

model. For each strain component, 100 different copies of the noise were considered. Figure 2.5 gives the mean and standard deviation (SD) of the relative errors that were obtained for  $F_2$ . It can be seen that all the mean relative errors are very small (less than or equal to 0.12 %), except with Procedure #2 (1.20%). The highest error is certainly due to the fact that the integrand in the integral of the left-hand side of Equation 2.1, *i.e.*, the internal virtual work, has a strong fluctuating sign over the integration domain with Procedure #2 since it can potentially change from one element to another, which amplifies the effect of the errors caused by the noise. When VFM is used to identify constitutive parameters, it has been observed that the smoother the expression of the virtual strain fields (for instance with the lowest possible degree if a polynomial expression is employed to express the virtual field), the lower the sensitivity to noise of the identified parameters [75]. This is also what is observed here for the identification of the applied force, since the case of virtual strain changing erratically (Procedure #2) gives the highest error, followed by Procedure #1, which corresponds to cubic interpolation. As a general remark, calculating weighted averages is a good option to attenuate the effect of noise affecting measurements; and the higher the number of points to discretize the integral used to calculate the internal virtual work, *i.e.*,  $N_{\text{pix}}$  in Equation 2.2 or 2.3, the better the noise attenuation. This number is directly the number of pixels covering the particle. For instance, in the present case, the diameter of the particle is 50 mm. With the pixel size indicated above (25  $\mu\text{m}$ ), the particle surface is covered by 3,056,280 pixels. Such a large number leads to a strong “averaging effect”, and therefore minimizes the effect of noise. The best results on the mean relative errors are obtained with Procedure #4 (0.01%), followed by Procedure #3 (0.09%).

Figure 2.4-b shows that the  $\varepsilon_2^*$  field of Procedure #4 is the smoothest among the four virtual strain fields, which lends credence to the argument discussed above. This claims that the virtual fields should be the smoothest possible. It can also be seen in Figure 2.5 that the SD of the relative errors is also small (less or equal to 1.29%), but the ranking of the procedures is different: Procedure #1 is here the best (0.42%), followed by #2 (0.94%) and finally Procedures #4 and #3 (1.20% and 1.29% respectively), making the former a

*a priori* advantageous in an experimental case for which one set of real strain data is generally available at a given loading level.

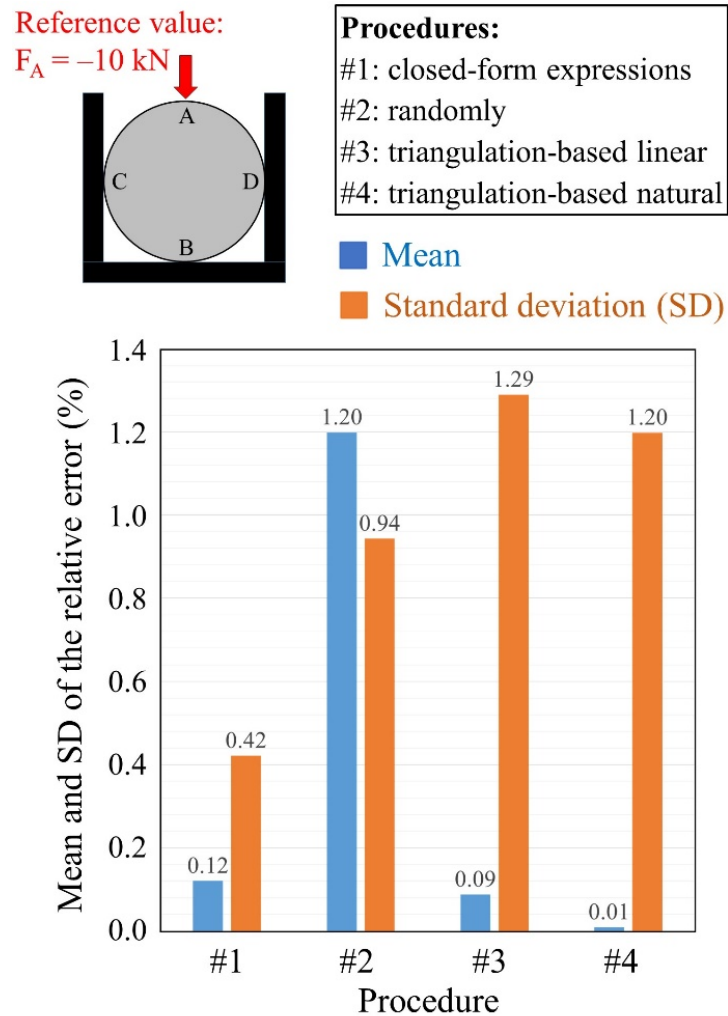


Figure 2.5 Four-contact system: comparison between the four procedures for the identification of the force component  $F_2$  at Point A with respect to the reference value ( $-10 \text{ kN}$ ).

It is worth remembering that the previous results were obtained with the four-contact system. As mentioned above, smooth virtual deformation fields are beneficial for reducing the effect of noise. An increase in the number of contacts should *a priori* make the virtual strain field more fluctuating, thus *a priori* increasing the influence of noise. Figure 2.6 gives the mean and SD of the relative errors obtained with the four procedures for the six-contact system (Configuration C2 in Figure 2.3-b). All the relative errors

obtained here (quantified by both the mean and the SD) are greater than those obtained with the four-contact system. Procedure #2 leads to the worst results in terms of mean (4.52%) and SD (3.27%). Procedure #1 is now ranked third. The fact that the virtual displacement field in Zone Z is now a five-degree polynomial function (compared with the cubic expression used in Equation 2.8s for the four-contact system) may explain the loss in performance of Procedure #1. Procedure #4 gives the best result (SD = 0.43%), closely followed by Procedure #3 (SD = 0.49%).

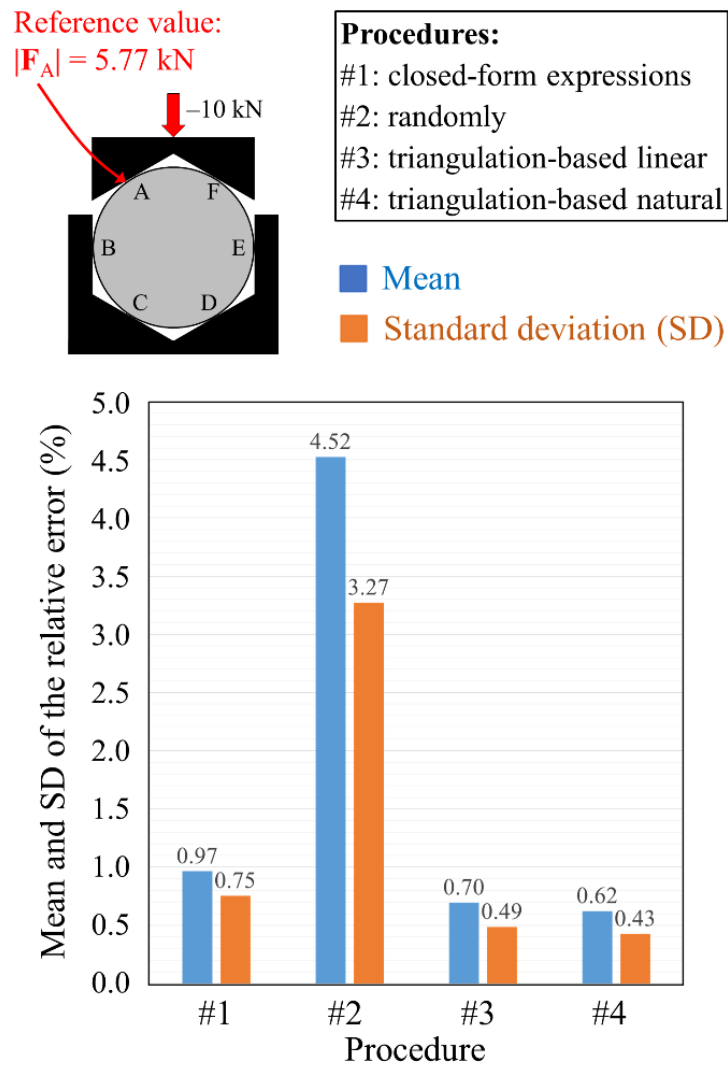


Figure 2.6 Six-contact system (Configuration C2): comparison between the four procedures for the identification of the force component  $F_2$  at Point A with respect to the reference value (−10 kN).

Based on these results and considering that the identification procedure should be applicable to any number of contacts, Procedure #4 was chosen for the calculations performed in the rest of the paper. Additional information can be provided concerning calculation times. The computer used for these calculations was equipped with an Intel Core i7-7700HQ @ 2.8GHz CPU and 16 GB RAM. Table 2.1 gives the calculation time needed to build one virtual displacement field  $\mathbf{u}^*$  and the associated virtual strain field  $\varepsilon^*$  (Step 1) for each procedure. The calculation time to identify one contact force with VFM with 100 different noisy strain fields (Step 2) was about 530 s for the four procedures. Since 1000 random virtual fields were processed to find an optimal virtual displacement field with Procedure #2, the total duration of Step 1 was more than 3 hours in this case. It should be emphasized that Procedure #3 requires less than 10 minutes, and Procedure #4 less than 14 minutes. Consequently, calculation time may also become a criterion if the system under study contains numerous particles. Since the errors obtained with Procedure #3 are very close to those obtained with Procedure #4, Procedure #3 may be preferred to Procedure #4 if calculation time is an issue. Procedure #4 is nevertheless considered in the following study.

Table 2.1 Calculation time for each procedure. Durations were measured for the six-contact system (Configuration C2).

Procedure	Time needed to build one virtual displacement field $\mathbf{u}^*$ and the associated virtual strain field $\varepsilon^*$
#1	6.8 s
#2	11.3 s (to be multiplied by the number of random virtual displacement fields to find an optimal one)
#3	11.6 s
#4	322.1 s

## 2.4 Influence of the noise magnitude

In this section, the robustness of the identification technique is briefly investigated by changing the standard deviation (SD) of the noise in the real strain field corresponding to Configuration C1, the virtual displacement field defined by Procedure #4 being used



in the calculations. Six SD values were considered, namely 0 (images are noiseless in this case),  $1\text{E-}05$ ,  $1\text{E-}04$ ,  $2\text{E-}04$ ,  $5\text{E-}04$  and  $1\text{E-}03$ . The third value ( $2\text{E-}04$ ) corresponds to the actual noise measured with the technique employed in the following chapter, namely LSA, but other measurement techniques characterized by different levels of the noise could also be used to obtain the experimental data. Consequently, we briefly examine here the sensitivity to noise of the identification technique.

Figure 2.7 shows the  $\varepsilon_2$  fields obtained with simulated data in each of these cases. For each component, 100 different copies of noise were added to the synthetic strain data. Figure 2.8 shows the mean and SD of the relative error on the force component  $F_2$  at Point A identified for each noise level affecting the strain maps. It is observed that VFM still provides reasonable force values for the highest noise level, illustrating the benefit of the averaging effect discussed above. On close inspection, it is observed that the noise affecting the force identified with VFM is roughly proportional to the noise affecting the strain maps, which is logical since the force is identified with a weighted average of the strain distribution throughout the surface of the particle.

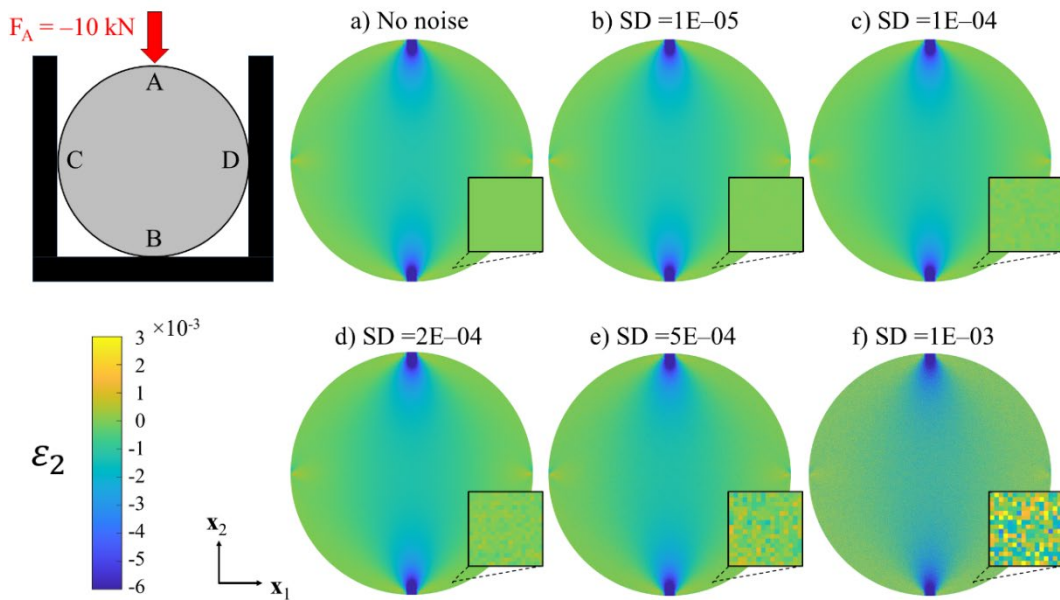


Figure 2.7 Real strain fields  $\varepsilon_2$  obtained by the FE model for Configuration C1. Gaussian noise with different standard deviations (SDs) is added. Pixel size is equal to  $25\ \mu\text{m}$ , as in the experiment with the three-particle system in the Chapter 3.

In the following section, simulated data corrupted by noise featuring a standard deviation of  $2E-04$  will be considered. 100 different copies of noise will be used to calculate means and standard deviations. Furthermore, the three-particle system described in Configuration C3 in Figure 2.3-c is considered for the analyses in the following, since it represents a granular system, for which it possible for instance to compare the forces identified on both sides of an interparticle contact.

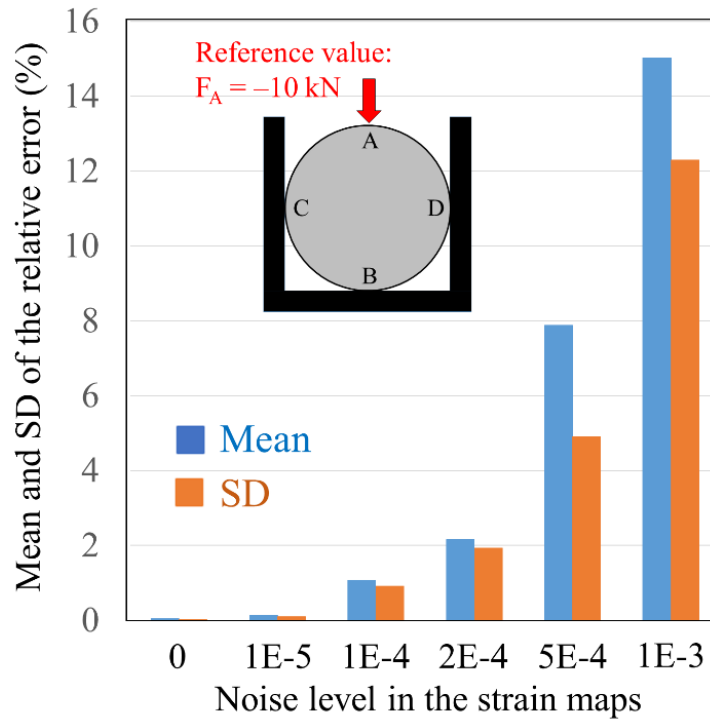


Figure 2.8 Influence of the noise level on the mean and standard deviation (SD) of the relative error on force  $F_2$  identified at Point A.

## 2.5 Sensitivity of the identification technique to other sources of error

Noise in the images is not the only source of error. We examine here first the influence of a shift between the coordinate system where real strain data is collected and the one used to perform the VFM calculation. Since experimental data are generally missing near the boundaries, we then assess the influence of missing real strain data on the value of the identified force and propose a procedure to limit this effect.

### 2.5.1 Effect of a shift between virtual and real strain fields

In real experiments on 2D granular systems, it may be difficult to find the exact boundaries of the particles. This potentially induces a shift between virtual and measured strain fields. We examine here the sensitivity of the identified force to this shift. The top particle of the three-particle system was considered for the analysis: see Figure 2.9-a. VFM was applied to identify the contact forces at points A, B and C. As schematically illustrated in this figure, the virtual strain fields were deliberately shifted when applying VFM in order to mimic an error in the location of the center of the cylinder when defining the virtual fields. Three cases were considered: +50 pixels along the  $x_1$ -axis, +50 pixels along the  $x_2$ -axis, and +50 pixels along both the  $x_1$ - and  $x_2$ -direction. *50 pixels* represents a significant shifting amplitude, since the diameter of the top particle is equal to 1973 pixels with the setting given above: the shift corresponds to 2.5% of the diameter along each direction. Hence *50 pixels* certainly represents an upper bound of what can occur in real experiments. Figure 9-b shows a diagram with the mean force components identified in each of these three cases as well as the reference ones (without shifting). It can be seen that the error induced by this shifting is acceptable, since its absolute value is lower than 2%.

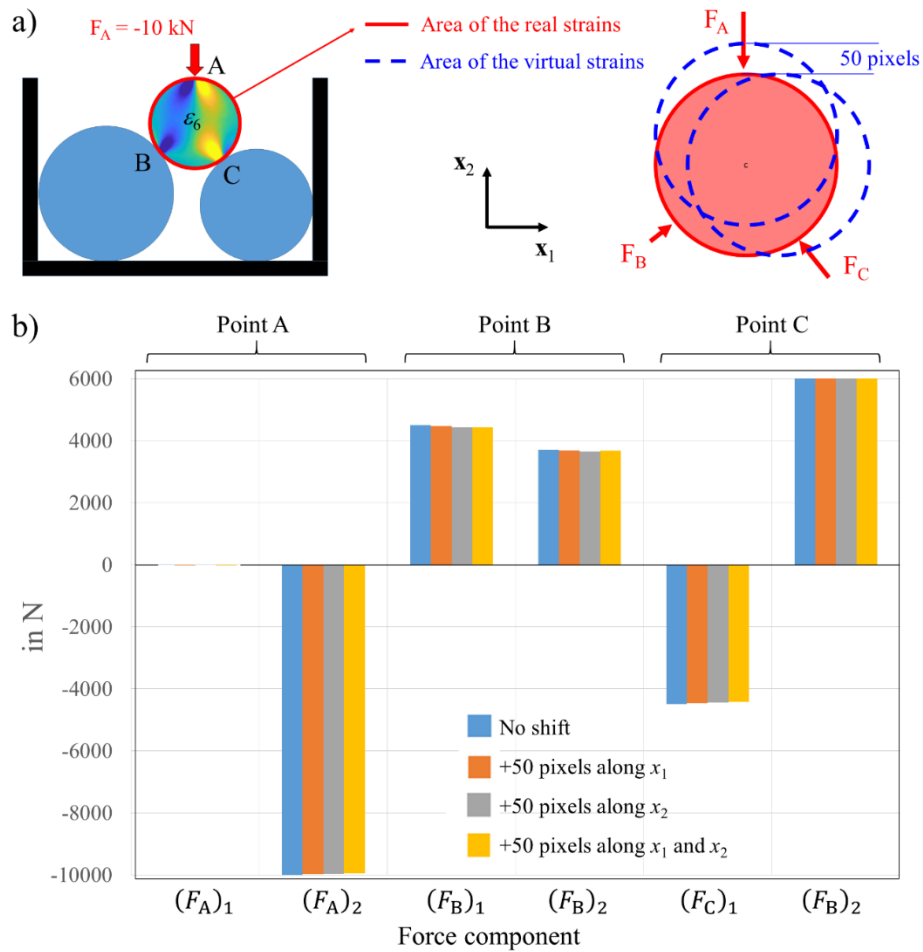


Figure 2.9 Effect of a shift between virtual and real strain fields:

- a) schematic representation for the top particle for Configuration C3;
- b) mean force components identified at points A, B and C.

### 2.5.2 Effect of missing data along particle boundaries

In real experiments using localized spectrum analysis, strain data are missing along the boundary of the cylinders. A majorant of the width of the zone where these data are not measured is half the size of the window used in the windowed Fourier transform employed; see below the explanation about image processing that provides the final strain maps. As in the previous section, the study was performed on the top particle of Configuration C3. Figure 2.10-a shows a schematic view of the ring over which measurements are not available. This particle is the smallest one, thus the one for which losing a ring of data has potentially the highest impact. Two values were chosen for the width of the ring, namely 2.5% and 5% of the radius of this particle. 2.5% corresponds to

about one-half the apparent size of the standard deviation of the Gaussian window used when processing real images of regular patterns, and 5% represents the apparent width of the Gaussian window. The missing data is on a ring whose width lies between these two bounds. For the top cylinder under investigation, considering its diameter is equal to 1579 pixels, 5% represents 79 pixels, while the size of the Gaussian window is 42 pixels according to the so-called “3-sigma” rule [161].

Two strategies were considered to reduce the impact of this missing information. A first and very simple strategy consists in merely stretching the data available within the red area in Figure 2.10-a. This can be done using the ‘imresize’ function of Matlab. A second and more logical one is to extrapolate the data available. This can be done using the ‘scatteredinterpolant’ function of Matlab with the ‘linear’ option.

VFM was applied to the two types of completed data and the results are reported in Figure 2.10-b for comparison purposes. As above, 100 different copies of the noise were considered in order to calculate the mean and SD of the relative error in the force component identification. Following comments can be made concerning this figure:

- The different curves show that the mean value of the relative error (compared to the values given by the FE model) remains reasonable, since 0.7% and 3.6% are majorants of the errors when the width of the missing band of data is equal to 2.5% and 5% of the diameter of the particle, respectively.
- With the first type of correction (stretching), the error affecting the mean values increases compared to the results obtained without any correction, which is certainly due to the fact that strain concentrations near the contacts cannot be created by mere stretching. With the second type of correction (extrapolation), the majorants of the errors reduce from 0.7% to 0.2% and from 3.6% to 0.5%, respectively, which notably improves the quality of the results.
- The SDs of the relative error are also given in the figure. No clear effect of the two correction strategies can be observed in the histograms. The main result is certainly the fact that whatever strategy is used to identify the force, noisy data only slightly

influences the scattering of the final result, since the SDs of the relative error are lower than 4.5%.

As a conclusion of this section, the second type of correction (extrapolation) is used in the remainder of the dissertation.

## **2.6 Accounting for friction at the contacts**

### **2.6.1 Estimating the whole set of normal and tangential forces with VFM**

Configuration C3 is considered again, but this time considering friction at the contact points. The contact forces are defined by their normal and tangential components, respectively denoted  $F_n$  and  $F_t$ . Figure 2.11 shows the mean and the SD of the relative errors of the contact forces identified with VFM. The corresponding reference values given by the FE model are also reported for comparison purposes. The error on the mean values is very small, since it is lower than 1%. The SDs are also low, at less than 1.4%. Consequently, VFM returns values which are very close to the reference ones. It can be noted that the errors for the normal forces are smaller than those for the tangential ones. This is because normal forces are dominant in any dry granular system (better signal-to-noise ratio).

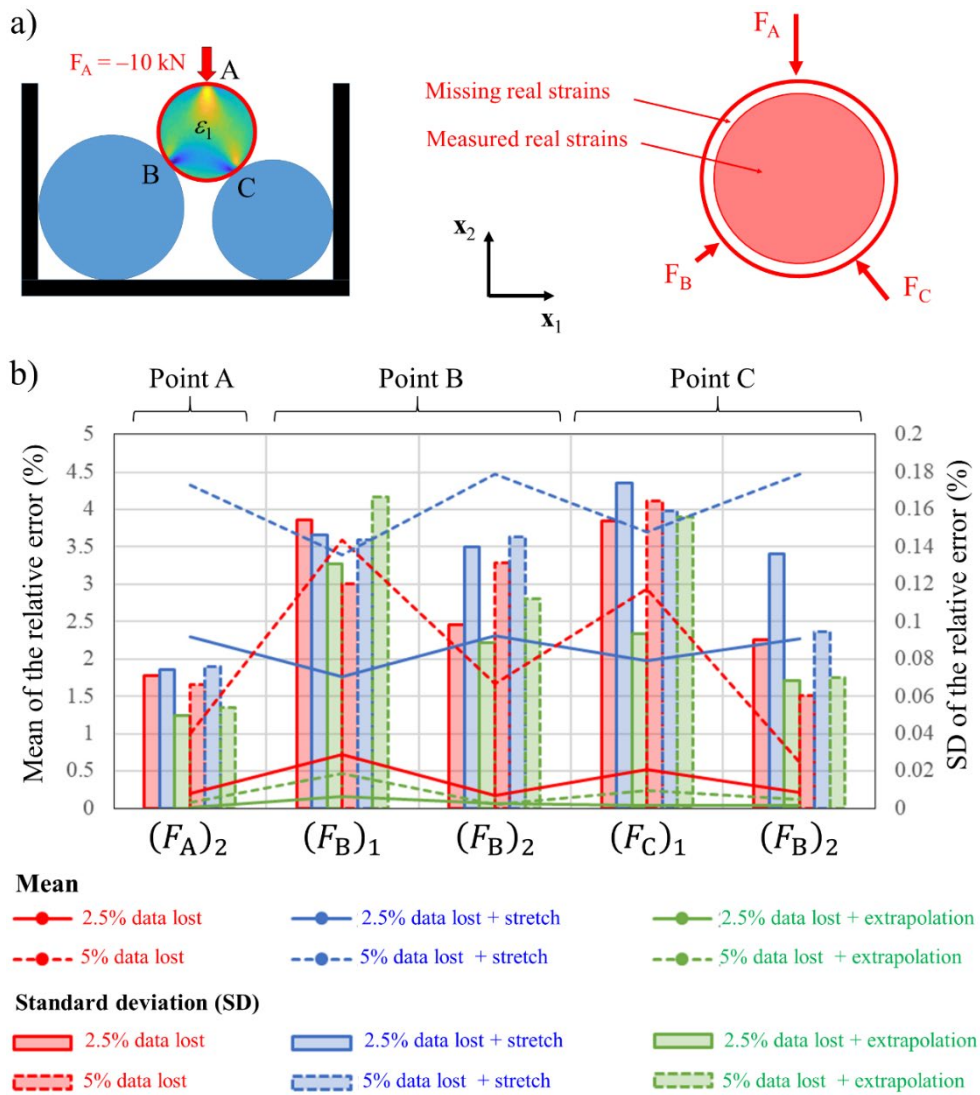


Figure 2.10 Effect of data missing along the boundary of a particle:

a) schematic representation for the top particle in Configuration C3; b) mean and standard deviation of the relative error compared to the data provided by the FE model.

## 2.6.2 Hybrid approach: estimating the normal and tangential forces with VFM and Newton's third law of motion

Newton's third law of motion allows us to state that the force applied by any particle P1 to a neighboring particle P2 is the opposite of the force applied by P2 to P1. Since all the particles are considered in turn in the procedure, all interparticle contact force components are thus identified twice. This enables us to assess the quality of the

identification by comparing the two solutions at each interparticle contact. It can be noted that points B and D correspond to the same contact but belong to two different particles. The same holds for points C and G. Table 2.2 gives the norm of the normal and tangential forces at these points obtained by the VFM procedure and by the FE model. The Newton's third law of motion is rigorously verified with the data given by the FE model. With VFM, the values are very close for both pairs of points, showing a relative difference lower than 0.2%. These values are also close to the reference ones given by the FE model, with a relative error lower than 0.1% even though noisy data were considered in this simulation. As a conclusion, the interparticle forces are correctly identified using VFM.

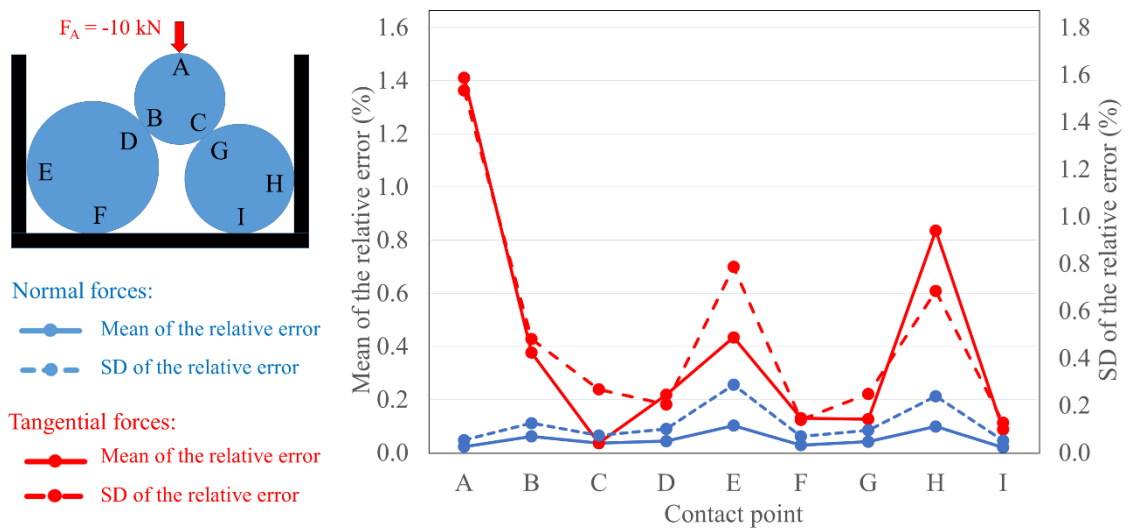


Figure 2.11 Comparison of the contact forces identified with VFM and their reference counterparts obtained by the FE model: mean and standard deviation (SD) of the relative error at each contact for Configuration C3.



Table 2.2 Normal and tangential forces,  $F_n$  and  $F_t$  respectively, at points B/D and C/G of Configuration C3 in Figure 2.3-c. Comparison between points B and D and between C and G enables us to verify that Newton's third law of motion is respected.

Contact point	VFM		FE model	
	$F_n$ (N)	$F_t$ (N)	$F_n$ (N)	$F_t$ (N)
B	4717.54	1394.12	4714.61	1388.89
D	4716.69	1391.91	4714.61	1388.89
C	6399.83	1275.76	6402.16	1276.23
G	6399.47	1274.62	6402.16	1276.23

## 2.7 Estimating contact forces with fewer pixels

The previous section concerned the application of VFM to the case of three particles, which is not representative of a real granular material. We investigate here the impact of an increase in the number of particles on the quality of the results. The size of the camera sensor and the size of the field of view of the camera are considered as constant data for the numerical analysis. As a result, increasing the number of particles in the medium causes the number of pixels  $N_{\text{pix}}$  used to encode the surface  $S$  of any of the particles to decrease as the number of particles increases. Two phenomena are expected to negatively impact the quality of the interparticle forces measured with VFM in this case:

- first, the number of data points being lower for each particle as their size decreases, the impact of the noise corrupting the images is expected to increase. The reason is that the averaging effect which occurs when calculating the integrals involved in the PVW becomes lower;
- second, the width of the band of pixels located along the boundary of each cylinder, and for which no data are available (see the section above), remains the same, since this quantity is only driven by the period of the periodic pattern that is used for the

measurement; see the following chapter. This period does not change when increasing the number of particles. A consequence is that the influence of the missing information is expected to increase as the size of the particles decreases.

These two issues were tackled by considering again Configuration C3, this time by reducing the number  $N_{\text{pix}}$  of data points in Equation 2.6. For instance, considering a particle of diameter 10 mm instead of 40 mm was simply modeled by keeping the same FE simulation as that described in the section above, but by dividing by 4 the number of data points in both directions, *i.e.*, by 16. As in the previous simulations, 100 different copies of the noise were added to the FE results, thus giving 100 different noisy strain fields. The mean and SD of the relative errors compared to the values provided by the FE model are reported in Figure 2.12. The maximum relative errors are about 6% for the mean and 7% for the SD, which is higher than in Figure 2.11 (for which the number of pixels  $N_{\text{pix}}$  was greater by a factor of 16). For the sake of comparison, Figure 2.13 gathers the results on the mean values only, confirming the trend. Increasing the number of particles is thus *a priori* possible.

Considering the experimental setting indicated in the following chapter (size of the camera sensor, size of the camera field of view, pitch of the checkerboard pattern deposited on the surface of the particles), it would be possible to identify contact forces for up to 150 particles of diameter 10 mm (compactly organized) with a relative error of the order of 6% for the mean and 4% for the SD. The experimental application of such a configuration would, however, require some implementation difficulties; see prospects in the conclusion section.

The next chapter is dedicated to experimental applications. It will appear that the use of VFM equations alone to process experimental strain data may not be sufficient. Additional equations will be taken into account.

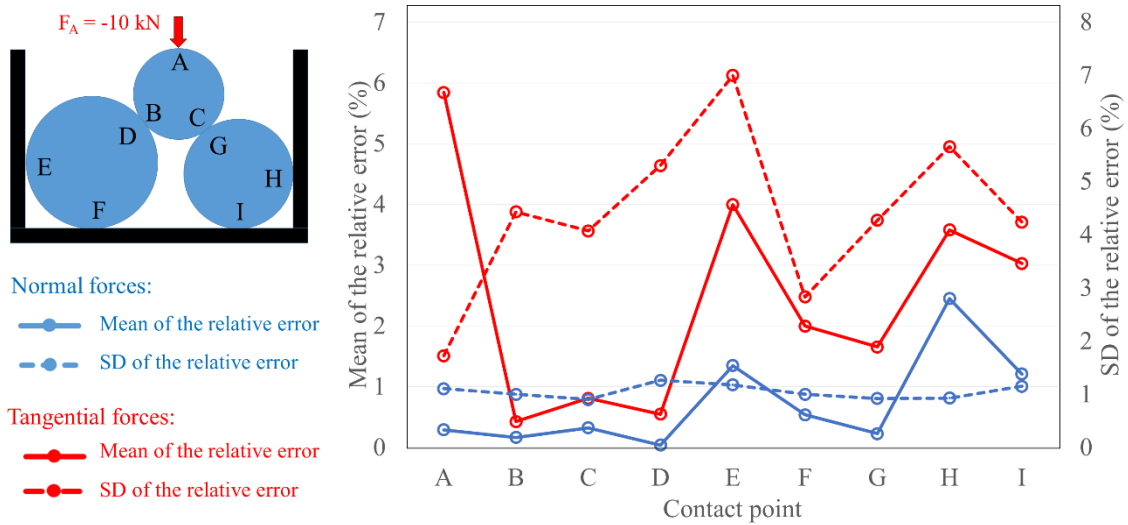


Figure 2.12 Comparison of the contact forces identified with VFM, and their reference counterparts obtained by the FE model (with a number of pixels reduced by 4 in both directions): mean and standard deviation (SD) of the relative error at each contact for Configuration C3.

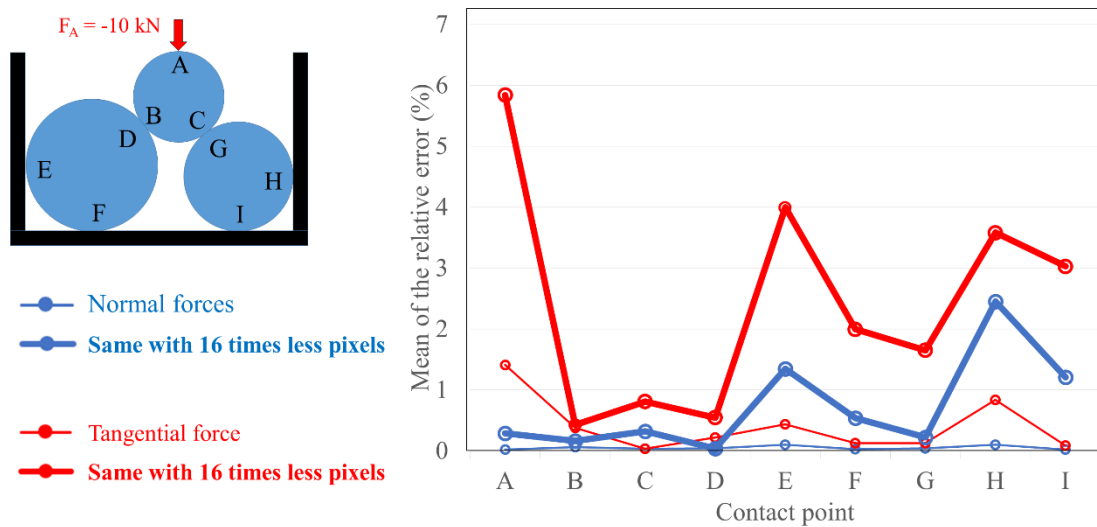


Figure 2.13 Comparison of the contact forces identified with VFM, and their reference counterparts obtained by the FE model (with and without a number of pixels reduced by 4 in both directions): mean deviation (SD) of the relative error at each contact for Configuration C3.

## 2.8 Conclusion

The objective of this chapter was to propose an experimental approach to measure interparticle contact forces in a 2D granular system using VFM. This identification method relies on the measurement of the strain distribution in the particles. Synthetic strain data provided by a finite element model (with added noise) were here used as input data for the identification procedure. It was shown that if the mechanical response of the constitutive material is known, the contact forces applied to a particle can be identified since they are proportional to a weighted average of the strain components, the weights being the virtual strain components. In short, each particle can be regarded as a multi-directional cell force, which directly provides the sought contact forces applied to it by suitably processing the strain distribution with the principle of virtual work. Various strategies were tested to propose kinematically admissible (KA) virtual displacement fields. It was shown that a relevant choice for the KA virtual displacement fields consists in using a triangulation-based natural interpolation between the contact points. Various simulations illustrated the impact of the choice of the virtual fields and the robustness of this identification technique, opening perspectives to its application to granular materials in real experiments. This study was submitted to the *European Journal of Mechanics A/Solids* [162] and is currently under review. The next chapter deals with experimental applications to various granular systems.



## **CHAPTER 3**

# **Application of VFM to experimental strain data obtained by LSA**

### **3.1 Introduction**

The objective of this chapter is to perform experimental applications of the approach developed in the previous chapter by processing strain maps obtained using localized spectrum analysis (LSA) for each particle. See Section 1.4.2 in the bibliography and state-of-the-art chapter for a reminder about this full-field measurement method:

- Section 3.2 is dedicated to a three-particle system similar to Configuration C3 in Figure 2.3-c. It will appear that the use of VFM equations alone to process experimental strain data may not be sufficient. Additional equations will be introduced, relying on the equilibrium of each particle and the Newton's third law of motion (principle of action-reaction);
- Section 3.3 is dedicated to bigger granular systems allowing various analyses of the interparticle force networks identified, including angular force distributions and probably density functions of normal forces in the weak and strong networks.

### **3.2 Application to a three-particle system**

The objective of this section is to apply the approach proposed in Chapter 2 by processing experimental strain data obtained by LSA, in the case of a multi-contact system comprising three cylindrical particles.

#### **3.2.1 Experimental setup**

The configuration considered for the experiment is shown in Figure 3.1-a. Similar to Configuration C3 in Figure 2.3-c, the particles are 40, 50 and 60 mm in diameter. The

latter are referred to as “small”, “medium” and “large”, respectively, in the following. Several plastic materials were tested for the particles. Polyamide 66 (PA66) was finally selected as it has a low viscosity, which enabled us to apply (reasonably slow) loadings without inducing viscous strains. For the VFM identification, Young’s modulus  $E$  was fixed to 3 GPa and Poisson’s ratio  $\nu$  to 0.42 [157, 158]. Particles were cut from long bars and slightly polished to obtain cylinder lengths of 30 mm.

The camera used for the experiments was a Prosilica GT 6600 featuring a CCD sensor of size  $6576 \times 4384 = 28.8$  Megapixels, with an 8-bit gray depth equal to 256 gray level. It was equipped with the AF Micro NIKKOR 200mm f/4D IF-ED lens. Considering that about 90% of the pixels cover the scene to be observed, the pixel size projected on the measurement plane was adjusted to be equal to about  $25 \mu\text{m}$  ( $150 \text{ mm}/0.9/6576 = 0.025 \text{ mm}$ ). The reason for using 90% of the pixel is to ensure that all the particles are always captured by a camera, despite the deformation or translation of particles. According to Ref [163], the squares of the checkerboard should be encoded with at least 3 pixels. For this reason, the width of the checkerboard squares was set to at least  $75 \mu\text{m}$ . This value enabled us to capture the whole granular system with our camera while maintaining an acceptable value for the number of pixels per period used to sample the information contained in the images.

A checkerboard pattern was deposited on the surface of the three particles using a Keyence MDU1000C laser engraving machine. This machine engraves dots as small as  $32 \mu\text{m}$  in diameter. The shape of each black square forming the checkerboard was approached by engraving  $3 \times 3 = 9$  circles. The shifting distance between these circles was  $21.5 \mu\text{m}$  in both the vertical and horizontal directions, which means that an overlap occurred between the dots. The laser engraving machine was set to the following parameters: 100% laser power, 0 mm spot variable offset, 25 repetitions, 6000 mm/s scan speed and 40 kHz pulse frequency. Printing a cylinder of diameter equal to 40 mm took about 40 minutes; see Ref [159] for more details concerning this printing procedure. Note that a small angle was deliberately applied with respect to the  $x_1$ -axis (horizontal axis of the grid of the camera) to avoid aliasing effects in the images [164].

Figure 3.1-b shows the experimental setup. A  $\pm 15$  kN uniaxial hydraulic MTS testing machine (858 Elastomer Test System) was used to apply the vertical force at Point A. The steel pusher was attached to the top grip of the machine. The steel frame containing the granular system was attached to the (fixed) bottom grip. Two LED sources were used to enhance the contrast of the checkerboard pattern. Before starting the experiments, three preliminary compression cycles were applied to ensure that the system was mechanically stabilized. Then the compressive loading was maintained at  $-30$  N to keep the contacts between the cylinders. The mechanical loading for the test then consisted of four stages:

- Stage 1 (reference state): waiting at  $-30$  N for a 60 s time period during which the camera captured images at an acquisition frequency of 0.1 Hz;
- Stage 2: vertical compressive loading up to  $-10$  kN with a constant loading rate of  $-328.7$  N/min (about 30 min). The benefit of such a slow loading rate is to avoid the appearance of viscous strains. After some preliminary tests (not reported here), this loading rate did not cause creep to occur in the third phase.
- Stage 3: compressive force maintained at  $-10$  kN for a 60 s period during which the camera captured images at an acquisition frequency of 0.1 Hz;
- Stage 4: the system was unloaded to the minimum loading,  $-30$  N, with a loading rate of  $-328.7$  N/min (about 30 minutes).

Stage 1 enabled us to process a stack of 100 images and to deduce an averaged reference phase map with limited noise. Note that the phase maps and not directly the photos must be averaged to avoid the effect of microvibrations, as shown in Ref [165].

The objective is now to identify the contact forces between the minimum ( $-30$  N, stage 1) and maximum ( $-10$  kN, stage 3) loads from the images of the checkerboard in the reference and deformed states respectively.

Figure 3.2 shows the in-plane strain maps obtained with LSA. From the images captured in the reference state (stage 1), the standard deviations of the noise in the  $\varepsilon_1$  ( $= \varepsilon_{11}$ ) and  $\varepsilon_2$  ( $= \varepsilon_{22}$ ) maps were estimated to be  $2.11\text{E}-04$  and  $2.25\text{E}-04$  respectively. The standard deviation of the noise in the  $\varepsilon_6$  ( $= 2 \varepsilon_{12}$ ) map was estimated to be  $2.84\text{E}-04$ , which is about  $\sqrt{2}$  times greater than the values for  $\varepsilon_1$  and  $\varepsilon_2$ . The small red circle



superimposed on the map on the bottom left particle has a diameter equal to 42 pixels = 1.05 mm. This is the apparent size of the Gaussian envelope used in LSA according to the “3-sigma” rule. Roughly speaking, this is the size of the optical gage used to obtain the strain maps. The three maps in Figure 3.2 are the inputs of the contact force identification procedure in the next section.

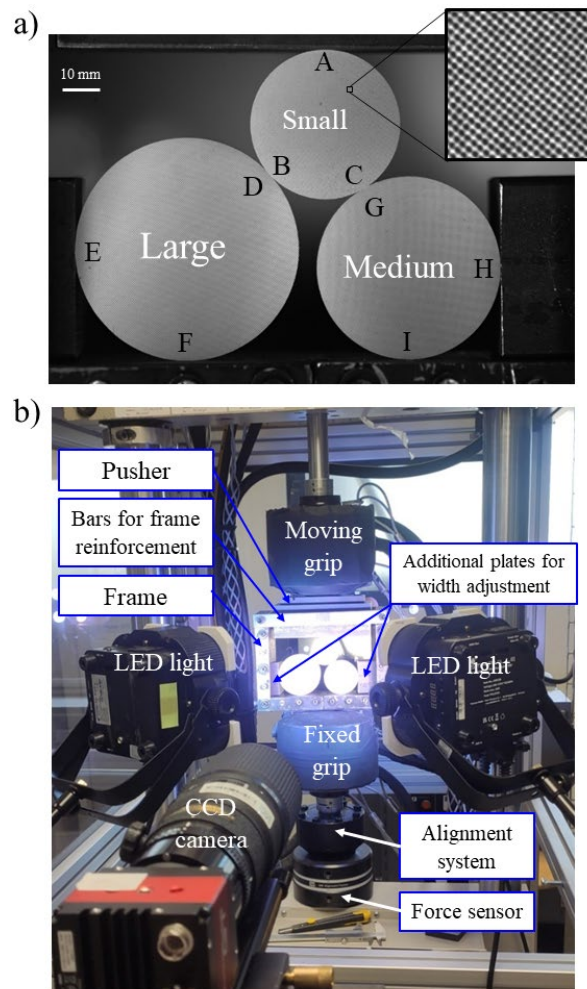


Figure 3.1 Experiment on a three-particle system: a) cylindrical particles;  
b) experimental set-up.

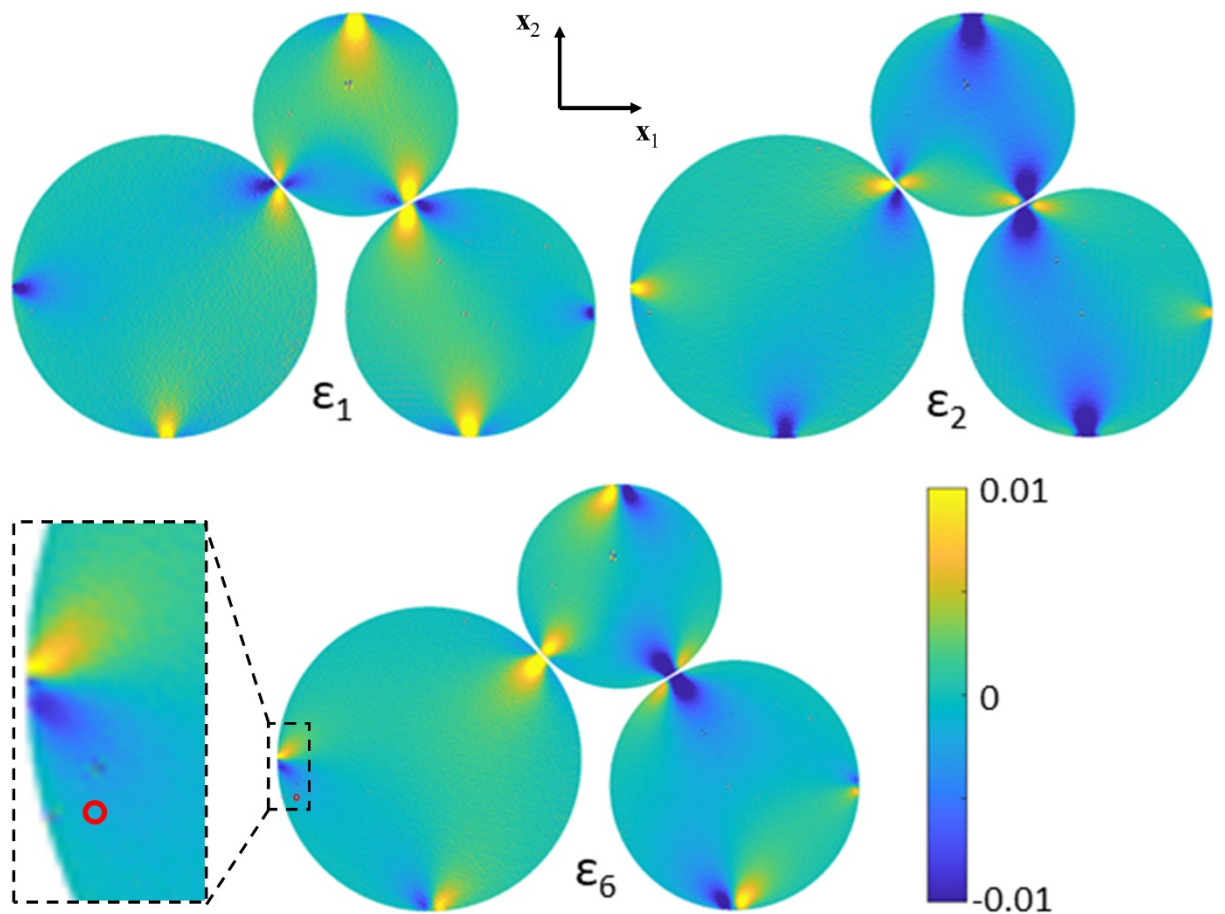


Figure 3.2 Experimental strain maps used as inputs for the contact force identification procedure.

### 3.2.2 Definition of contact force identification strategies

VFM was then applied to each particle to identify the contact forces using Procedure #4 described in Section 2.3.2 in previous chapter. It appeared that the use of VFM equations alone to process experimental strain data may not be sufficient (see results of Strategy S1 below). This can be due to: 1) imperfect 2D framework with potential non-uniform force distributions along the linear contacts between the cylinders; 2) out-of-plane movements; 3) error in the elastic parameters of the particle material. These factors cannot be fully controlled, so various alternative approaches for force identification are proposed in this section. The purpose is to find which of them are the most suitable.

The idea is to consider how the contact forces should simultaneously satisfy:

- local equilibrium: for each particle, static equilibrium should be respected. The sum of the contact forces applied to each particle should be equal to zero. The same holds for the moments, calculated for instance at the center of the particle;
- Newton's third law of motion: for each pair of forces identified on both sides of a contact, the action-reaction principle should be respected, *i.e.* forces should be opposite.

It is worth noting that achieving both local equilibrium and Newton's third law of motion leads to the global equilibrium being satisfied, *i.e.*, both the sums of all the contact forces and their moments in the granular system are then equal to zero.

Let us now enumerate the unknowns of the problem and of the equations at our disposal. The number of unknown force components is designated by  $n$  in the following. For the three-particle system in Figure 3.1-a, there are three contacts for each particle, making a total of nine contacts: see points A to I. There are two force components (along the  $x_1$  and  $x_2$  directions) at each contact. Thus there are  $n = 18$  unknowns. Let us see now the number of equations. Denoting  $n_{\text{part}}$  the number of particles and  $n_{\text{inter}}$  the number of interparticle contacts, we have  $n_{\text{part}} = 3$  (small, medium and large) and  $n_{\text{inter}} = 2$  ("small-large" contact at B-D, and "small-medium" contact at C-G). Therefore:

- VFM provides  $n = 18$  scalar equations;
- the local equilibrium provides three scalar equations per particle (two for the forces and one for the moments), which gives  $3n_{\text{part}} = 9$  scalar equations;
- the Newton's third law of motion gives two scalar equations per interparticle contact (one for each direction  $x_1$  and  $x_2$ ), which gives  $2n_{\text{inter}} = 4$  scalar equations.

This leads to a total of  $n + 3n_{\text{part}} + 2n_{\text{inter}} = 31$  scalar equations, which are potentially available to find  $n = 18$  unknowns. Note that considering the last two sets of equations only is not sufficient to resolve the problem, which underlines the fact that the problem is hyperstatic. The main objective of the developments below is to determine how best to handle these 31 equations for contact force identification.

Five strategies were defined (see the flowchart for each strategy in Figure 3.3:

- Strategy S1: application of VFM only — The  $n$  unknown force components are directly identified using  $n$  KA virtual displacement fields. The latter therefore give  $n$  independent linear scalar equations, allowing a direct resolution.
- Strategy S2: use of VFM equations and all the additional equations — In this strategy, all the  $3n_{\text{part}} + 2n_{\text{inter}}$  additional equations are used in addition to the  $n$  VFM equations. As there are more equations than unknowns, the linear system is solved in the least-square sense by using the ‘mldivide’ Matlab function.

Note that some equations need to be normalized beforehand so that all equations have the same “weight” before solving. The equations associated with the local force equilibrium and with Newton’s third law of motion have the same coefficient +1 in front of the unknowns: *e.g.*  $1 \times F_{A1} + 1 \times F_{B1} + 1 \times F_{C1} = 0$  for the force equilibrium of the small particle in the  $x_1$ - direction; or  $1 \times F_{B1} + 1 \times F_{D1} = 0$  for Newton’s third law of motion at the contact between the small particle and the large particle. The normalization of the VFM equations consists therefore in applying a multiplication factor so that the +1 value also appears in front of the unknowns. Regarding local moment equilibrium, the coefficients in front of the unknowns depend on the distance between the force vector and the calculation point of the moments; they can have different signs. Thus, the normalization of each local moment equilibrium equation consists in applying a multiplication factor so that the average of the absolute values of the coefficients in front of the unknowns is equal to +1. This normalization procedure enables us to give the same importance to all the equations before solving.

- Strategy S3: use of VFM equations with substitution of unknowns from the local force equilibrium and Newton’s third law of motion — For each particle, one of the contact forces can be substituted by the opposite of the sum of the other forces applied to the particle (local force equilibrium). For instance, in the three-particle system the two components of  $\mathbf{F}_A$  can be replaced by the two components of  $-\mathbf{F}_B - \mathbf{F}_C$ . Additional substitutions can be made using Newton’s third law of motion. For example, the two components of  $\mathbf{F}_B$  can be replaced by the two components of  $-\mathbf{F}_D$ . This reduces the number of unknowns, which is now equal to  $n - 2n_{\text{part}} -$

$2n_{\text{inter}} = 8$ , for  $n = 18$  scalar equations derived from VFM. As there are more equations than unknowns, solving the linear system is performed in the least-square sense.

- Strategy S4: use of VFM equations, then the average of the forces at each interparticle contact to respect the Newton's third law of motion, and finally correction of the forces to respect the local force equilibrium — This strategy is actually an incremental three-step approach. In the first step, VFM is applied to calculate preliminary values for all the contact forces, as with Strategy S1. In the second step, the forces at the interparticle contact points (here the small-large contact at B-D and the small-medium contact at C-G) are replaced by the averages of the two forces identified in the first step on each side, obviously taking into account the opposite signs on each side. The third step relies on the local force equilibrium: for each particle and each direction (along  $x_1$  and along  $x_2$ ), the value of the lowest component is replaced by the opposite of the sum of the components of the other forces applied to the particle. This may modify the component values at the interparticle contacts. Therefore, Newton's third law of motion is examined again for each interparticle contact. If it is not satisfied, steps 2 and 3 are performed again, iteratively, until Newton's third law is satisfied at each interparticle contact. By construction, the contact forces obtained at the end of the procedure verify both Newton's third law of motion (due to the second step) and the local force equilibrium (due to the third step).
- Strategy S5: use of VFM equations with Lagrange multipliers to respect all the additional equations — Strategy S5 consists in minimizing the sum of the squared errors deriving from Equation 3.1 at all the contacts, while strictly respecting the local equilibrium and Newton's third law of motion. The constraints of the minimization problem can be written as  $\mathbf{g}(\mathbf{F}) = \mathbf{0}$ , where  $\mathbf{F}$  gathers all the components of all the contact forces to be identified and the vector function  $\mathbf{g}$  is expressed from the  $3n_{\text{part}} + 2n_{\text{inter}}$  additional scalar equations. The Lagrange function  $\mathcal{L}$  is then expressed as follows:

$$\mathcal{L}(\mathbf{F}, \boldsymbol{\lambda}) = f(\mathbf{F}) - \boldsymbol{\lambda} \cdot \mathbf{g}(\mathbf{F})$$

with 
$$f(\mathbf{F}) = \sum_{i=1}^{N_{\text{cont}}} (\mathbf{U}^* \mathbf{T} - \mathbf{E} \mathbf{Q})_i^2 \quad (3.1)$$

and 
$$\boldsymbol{\lambda} \cdot \mathbf{g}(\mathbf{F}) = \sum_{i=1}^{N_{\text{const}}} \lambda_i \times g_i(\mathbf{F})$$

where  $N_{\text{cont}}$  is the number of contact forces in the granular system (so  $N_{\text{cont}} = n/2 = 9$ ),  $N_{\text{const}}$  is the number of constraints (so  $N_{\text{const}} = 3n_{\text{part}} + 2n_{\text{inter}} = 13$ ) and the vector  $\boldsymbol{\lambda}$  is composed of the Lagrange multipliers  $\lambda_i$ . The objective is to find a stationary point, *i.e.* all the partial derivatives of the Lagrange function are equal to zero:

$$\frac{\partial \mathcal{L}}{\partial \mathbf{F}} = \mathbf{0} \quad \text{and} \quad \frac{\partial \mathcal{L}}{\partial \boldsymbol{\lambda}} = \mathbf{0} \quad (3.2)$$

This gives  $2N_{\text{cont}} + N_{\text{const}}$  scalar equations, *i.e.*, 31 equations composed of  $2N_{\text{cont}} = 18$  equations for the force components and  $N_{\text{const}} = 13$  equations for the Lagrange multipliers. It gives a system of 31 equations for 31 unknowns. The latter are the 18 force components and the 13 Lagrange multipliers. In practice, this calculation was performed with Matlab using symbolic solving and the ‘jacobian’ function for the derivatives. It is worth noting that the force components obtained from this strategy respect local equilibrium for all the particles and Newton’s third law of motion at all the contacts.

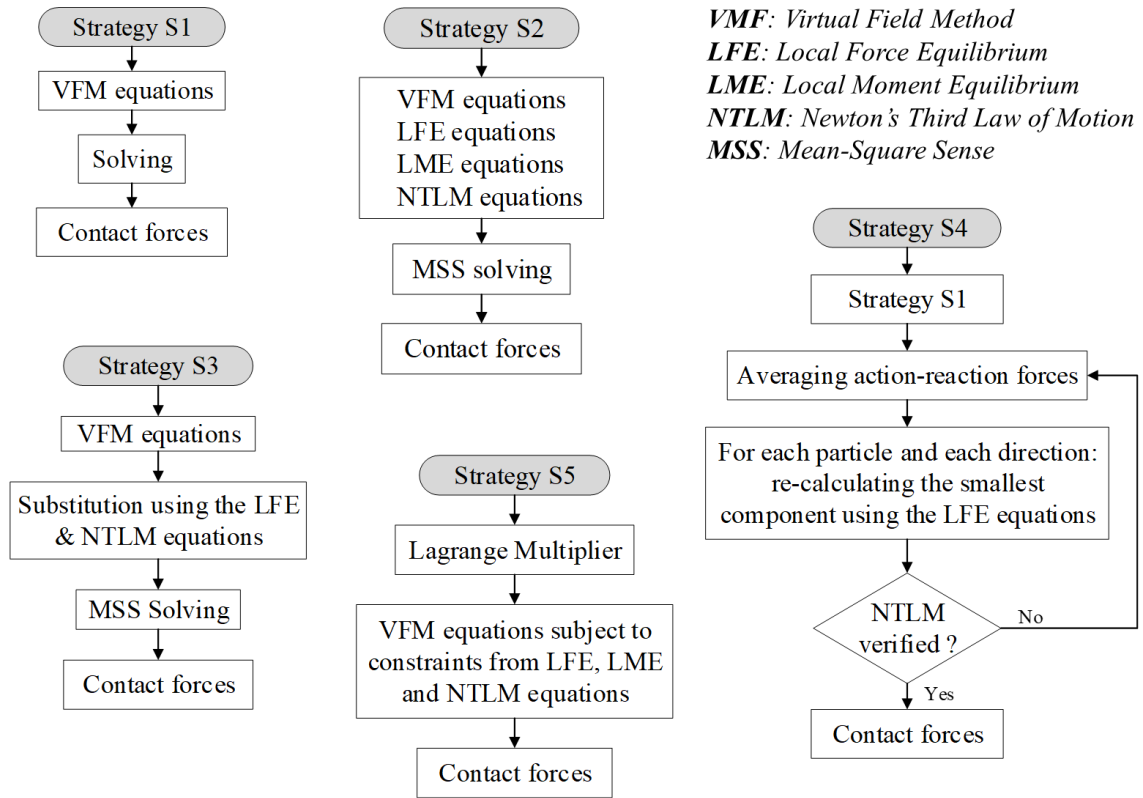


Figure 3.3 Flowchart of the five strategies to identify the contact force components in the case of experimental strain data.

### 3.2.3 Experimental results

The results of the different contact force identification strategies were compared using the strain maps in Figure 3.2 as input data. The quality of the identification was estimated through three error indicators:

- the norm of the residual force for each particle (small, medium and large):

$$F_{\text{resid}}(\text{particle}) = \left\| \sum_{3 \text{ contacts}} \mathbf{F} \right\| \quad (3.3)$$

- the absolute value of the residual moment for each particle (small, medium and large):

$$M_{\text{resid}}(\text{particle}) = \left\| \sum_{3 \text{ contacts}} \mathbf{M} \right\| \quad (3.4)$$

- the norm of the residual force at each internal contact (small-large and small-medium):

$$F_{\text{resid}}(\text{internal contact}) = \left\| \sum_{2 \text{ internal contacts}} \mathbf{F} \right\| \quad (3.5)$$

By construction, some strategies provide null values for these indicators. The values of  $F_{\text{resid}}(\text{particle})$  and  $F_{\text{resid}}(\text{internal contact})$  are always null for Strategies S3, S4 and S5 because local force equilibrium and Newton's third law of motion are "enforced" in these procedures. The values of  $M_{\text{resid}}(\text{particle})$  are always null for Strategy S5 because local moment equilibrium is enforced in the procedure.

Figure 3.4 gives the three error indicators obtained with the five strategies. Figure 3.5 shows the contact force vectors, as well as the direction of these forces with thin dashed lines. Note that, as each particle is subjected to three force contacts, the condition  $M_{\text{resid}}(\text{particle}) = 0$  is obtained when the three force directions cross at the same point. The following comments can be made concerning this figure:

- it can be observed that Strategy S1 globally leads to the worst results: see for instance the value of  $F_{\text{resid}}(\text{medium})$  at about 250 N and the value of  $F_{\text{resid}}(\text{small} - \text{large})$  at about 1000 N. Applying Strategy S2 decreases these values: about 100 N and 650 N respectively;
- by construction, Strategies S3 and S4 give zero values for  $F_{\text{resid}}(\text{particle})$  and  $F_{\text{resid}}(\text{contact})$ . However, the  $M_{\text{resid}}(\text{particle})$  values for these two strategies are not globally better than for Strategies S1 and S2. The values for  $M_{\text{resid}}(\text{medium})$  are even worse: see the crossing of the force directions in Figures 3.5-c and -d;
- as expected, the error indicators for Strategy S5 are all equal to zero, making this strategy the best of the five. This choice is also confirmed by comparing the errors made on the vertical component of the force at point A, which should be equal to the vertical force applied by the testing machine (-10 kN): see Table 3.1. The



relative error is equal to 1.3% with Strategy S5, about double that with strategy S1, S2 and S3, and 8.4% for Strategy S4.

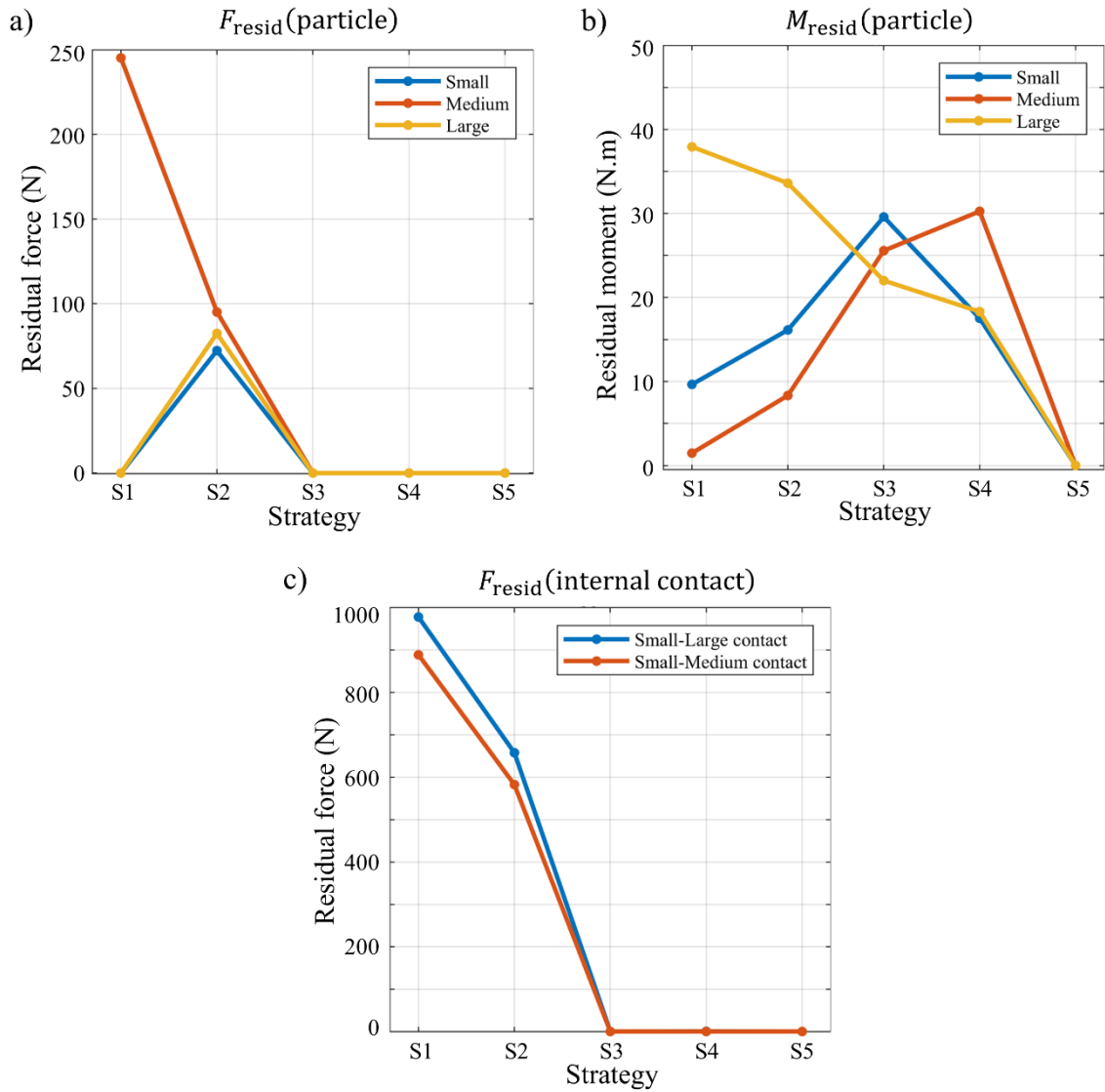


Figure 3.4 Comparison of the different strategies for contact force identification from experimental data: a) deviation from the local force equilibrium; b) deviation from the local moment equilibrium; c) deviation from Newton's third law of motion.

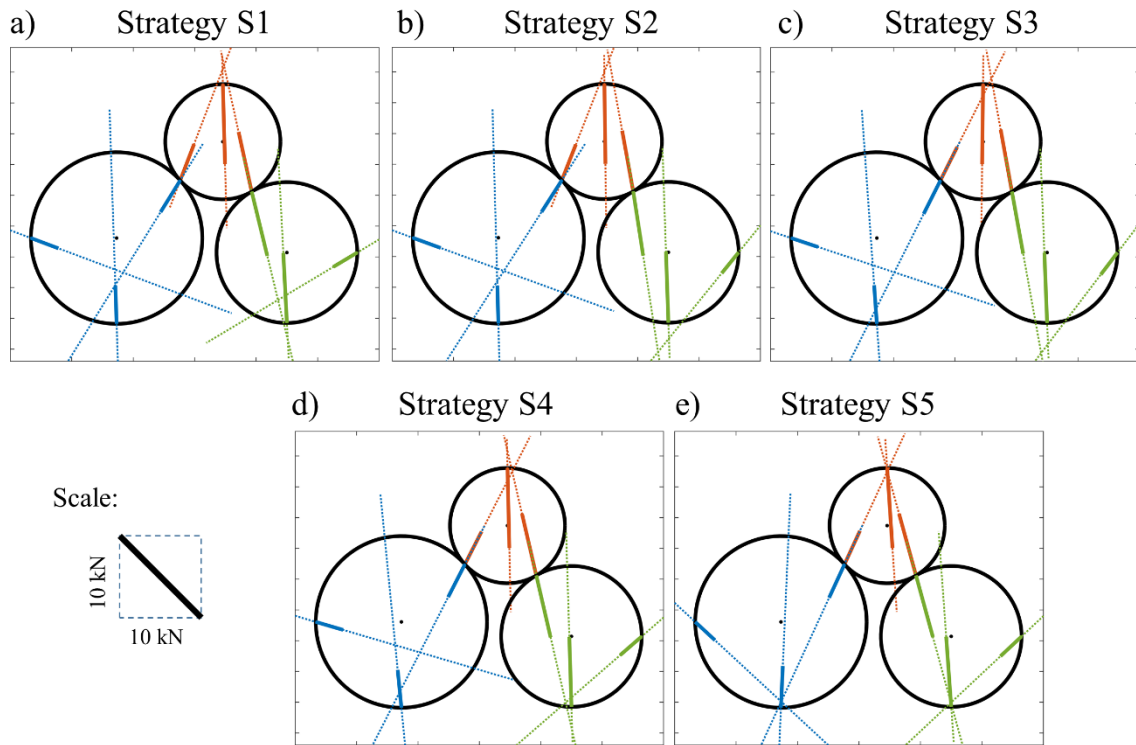


Figure 3.5 Contact force at each contact identified using the five strategies.

Table 3.1 Vertical component  $F_{A2}$  of the force at point A (in contact with the pusher) identified using the five strategies. Relative errors are calculated with respect to the vertical force applied by the testing machine ( $-10$  kN).

Strategy	$F_{A2}$ (N)	Relative error
S1	-10235	2.4%
S2	-10274	2.7%
S3	-10251	2.5%
S4	-10841	8.4%
S5	-10127	1.3%

### 3.2.4 Conclusion of the application to a three-particle system

An experimental application was performed on a three-particle system by processing strain maps obtained in each particle using LSA. VFM failed to identify consistent force

components, and in particular failed to verify the Newton's third law of motion (principle of action-reaction at the interparticle contacts). This can be explained by an imperfect 2D assumption, out-of-plane movements or errors in the elastic parameters of the particle material. Alternative force identification approaches were proposed by adding equations derived from the local equilibrium of each particle, and Newton's third law of motion at each interparticle contact. Since the number of available equations becomes higher than the number of unknowns (the contact force components), several strategies were compared to determine how best to handle these equations for contact force identification. The best solution was obtained using the VFM equations with Lagrange multipliers to strictly respect force and moment equilibrium for each particle and Newton's third law of motion at each interparticle contact. The application to higher numbers of particles is presented in the next section.

### **3.3 Application to bigger granular systems**

Experiments with greater numbers of particles were carried out to analyze three cases: monodisperse, bidisperse and tridisperse configurations. LSA was applied using the same checkerboard pattern on the cylindrical particles as in the three-particle system; and Strategy S5 was used to identify the contact forces. The objective is to analyze the interparticle force networks in terms of angular force distribution and probably density functions of forces in the weak and strong networks.

#### **3.3.1 Experimental setup**

Three diameters of cylindrical particles were used to prepare the granular systems: 12 mm, 15 mm and 20 mm, referred to as "small", "medium" and "large" in the rest of the chapter respectively. The particles were made of PA66 as in the previous section. The length of the cylinders was approximately equal to 20 mm. Three configurations were considered: monodisperse, bidisperse and tridisperse, as illustrated in Figure 3.6. The numbers of particles for each configuration is indicated in Table 3.2. The monodisperse configuration was composed only of small particles: 108. The bidisperse configuration consisted of small and medium particles: 56 and 29 respectively. The tridisperse configuration consisted of the three types of particles: 54 small particles, 22 medium

particles, and 4 large particles. For each configuration, the particles were randomly placed on the rectangular steel frame, 150 mm in width.

Table 3.2 Number of particles for the three configurations tested.

Configurations	Particles		
	Small	Medium	Large
Monodisperse	108	-	-
Bidisperse	56	29	-
Tridisperse	54	22	4

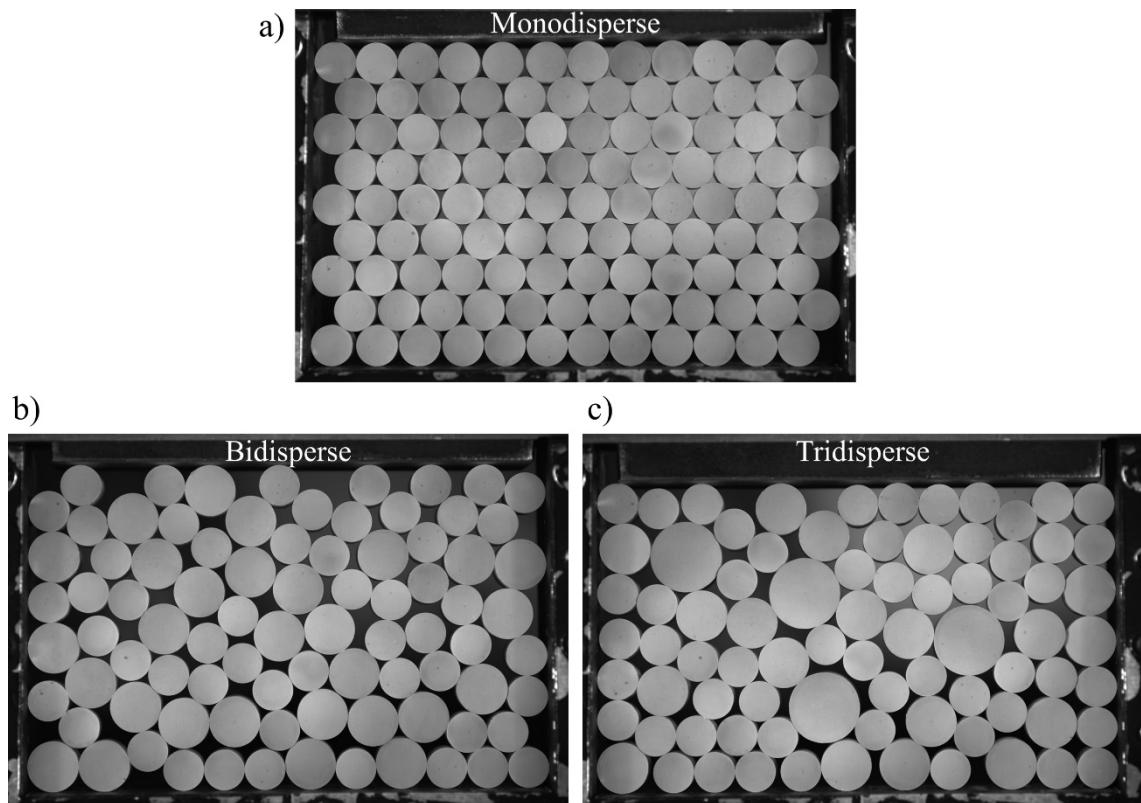


Figure 3.6 Photo of the three experimental configurations tested:

a) monodisperse; b) bidisperse; c) tridisperse.

The surface preparation of the particles was similar to the case of the three-particle system in Section 3.2.1: the width of the checkerboard squares was equal to  $75\ \mu\text{m}$ ; see Figure 3.7-a. The loading system, the lighting and the measurement setup by camera were

also similar to the case of the three-particle system; see Figure 3.7-b. The pixel size on the free-end of the cylinders was also equal to 25  $\mu\text{m}$ .

It is worth noting that the placement of the particles in the frame was long and complex:

- First, the particles were placed randomly with an orientation of checkerboard of about 10 degrees with respect to the horizontal axis. The objective is to prevent the aliasing effect during the mechanical tests, causing fringes that disturb the measurement of the strain fields [164]. Moreover, a transparent cover lid was used to ensure that the ends of all the cylinders in front of the camera were in-plane;
- Second, three preliminary compression cycles between  $-0.1$  kN and  $-14.5$  kN were applied to compact the granular system. The compressive load was then kept at  $-0.1$  kN to ensure the mechanical stability of the particles. The consequence of this second step was that the particles have moved and rotated, making the orientation of the checkerboards sometimes far from 10 degrees;
- Third, the particles were rotated manually one by one, still under the compressive load of  $-0.1$  kN and using the transparent cover lid, in order to have the orientation of all the checkerboards equal to about 10 degrees. Friction between particles makes this procedure possible, i.e., it was possible to rotate each cylinder nearly independently;
- The second and third steps were repeated several times until the orientation of all the checkerboards was about 10 degrees at the end of the second step; see Figure 3.7-a.

This procedure was found after numerous preliminary tests. It is worth noting that the duration to prepare one configuration was about half a day.

Similar to the test on the three-particle system, the mechanical loading consisted in four steps while the camera captured the images at an acquisition frequency of 0.1 Hz:

- Step 1 (reference state): capturing images at  $-0.1$  kN state for 50 seconds;
- Step 2 (loading): compressive loading up to  $-14.5$  kN at a constant rate of  $-5.56$  N/s. It took about 40 minutes to reach the maximum load. As indicated for the three-particle configuration, the advantage of such a slow loading is that potential viscous strains are avoided or very low. This loading rate did not cause creep in the third step, according to preliminary tests (not reported here);
- Step 3 (constant load): compressive load maintained at  $-14.5$  kN for 5 minutes;
- Step 4 (unloading): compressive loading decreasing to  $-0.1$  kN at a constant rate of  $+240$  N/s (about 1 minute).

The testing procedures were the same for the three configurations. Preliminary tests were actually performed, enabling us to progressively improve the quality of the experiments. The objective is now to identify the contact forces between the minimum stage ( $-0.1$  kN) and the maximum stage ( $-14.5$  kN) by using the images of the checkboard in the reference and deformed states respectively. It is worth recalling again that all particles in the granular systems should have been oriented properly before performing the tests. This is a critical point of the experimental setup, enabling us to obtain the highest possible quality of strain fields.

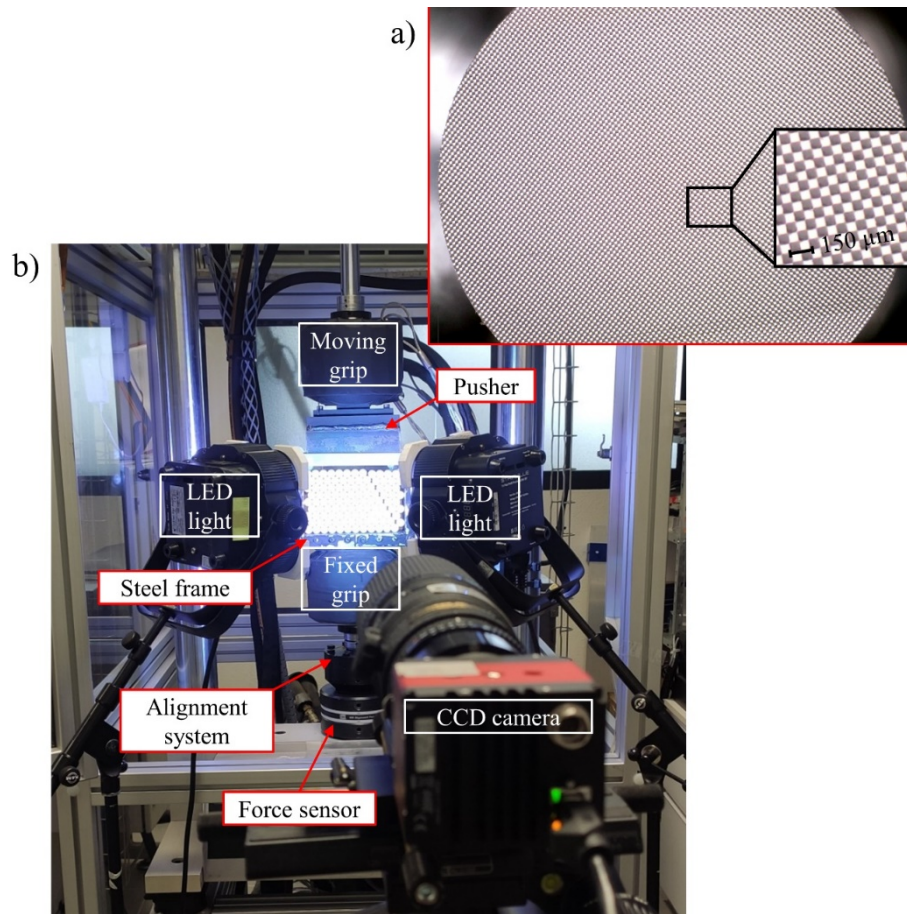


Figure 3.7 Experimental setup for the big granular systems: a) checkerboard on a particle, exhibiting an angle of about 10 degrees with respect to the horizontal direction; b) experimental equipment.

### 3.3.2 Experimental results

#### 1) Strain fields

LSA was applied to each configuration for each particle between the images in the reference state ( $-0.1$  kN) and at the maximum compressed state ( $-14.5$  kN). The fields of the in-plane strain components  $\varepsilon_{xx}$ ,  $\varepsilon_{yy}$ , and  $\varepsilon_{xy}$  are displayed in Figures 3.8, 3.9 and 3.10 for the monodisperse, bidisperse and tridisperse cases respectively. Note that the display is made in the reference configuration, i.e., with the location of the particles under the loading of  $-0.1$  kN. These strain fields are the inputs for the contact force identification procedure which was presented in the previous chapter.



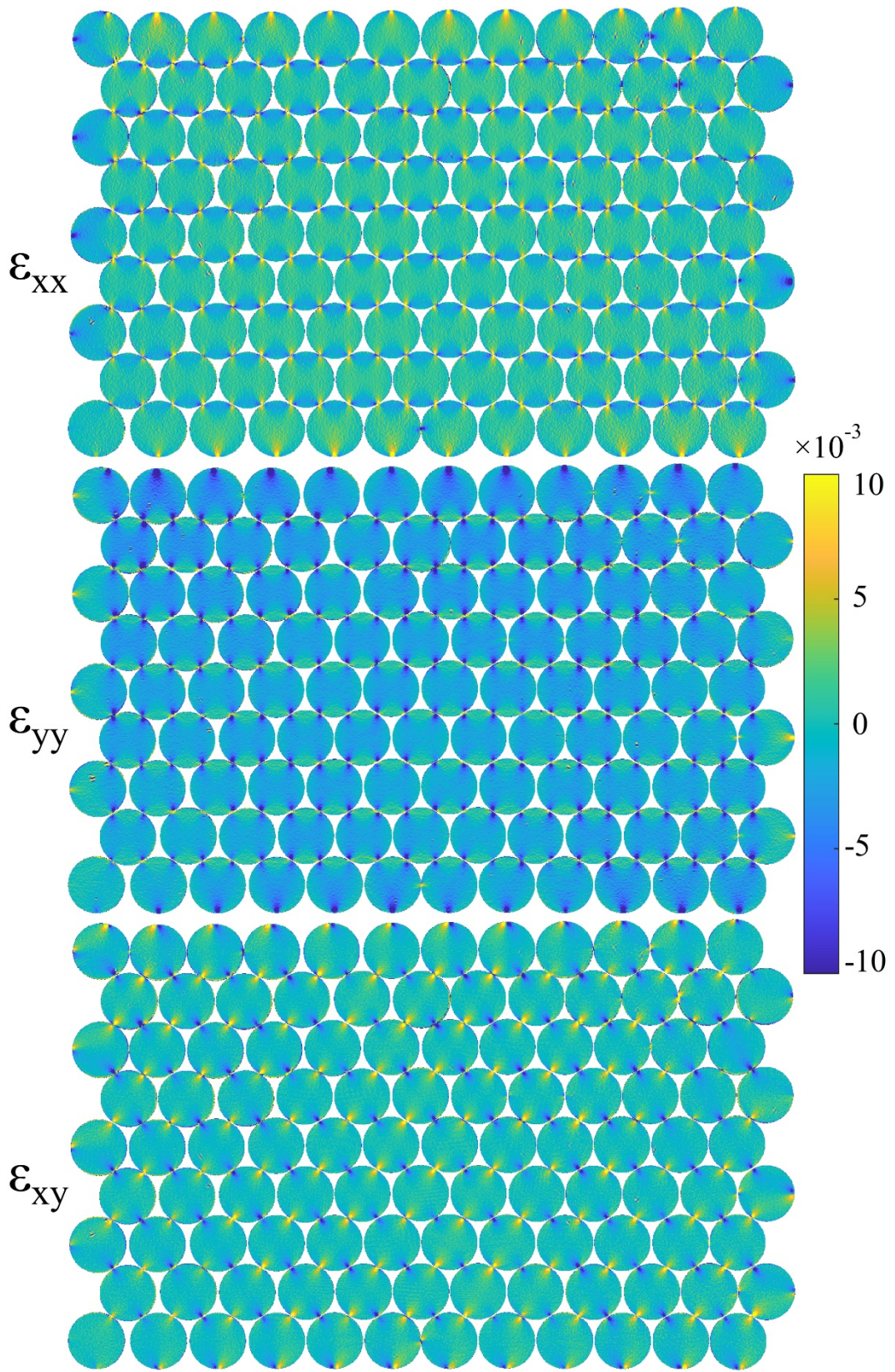


Figure 3.8 In-plane strain components for the monodisperse case.



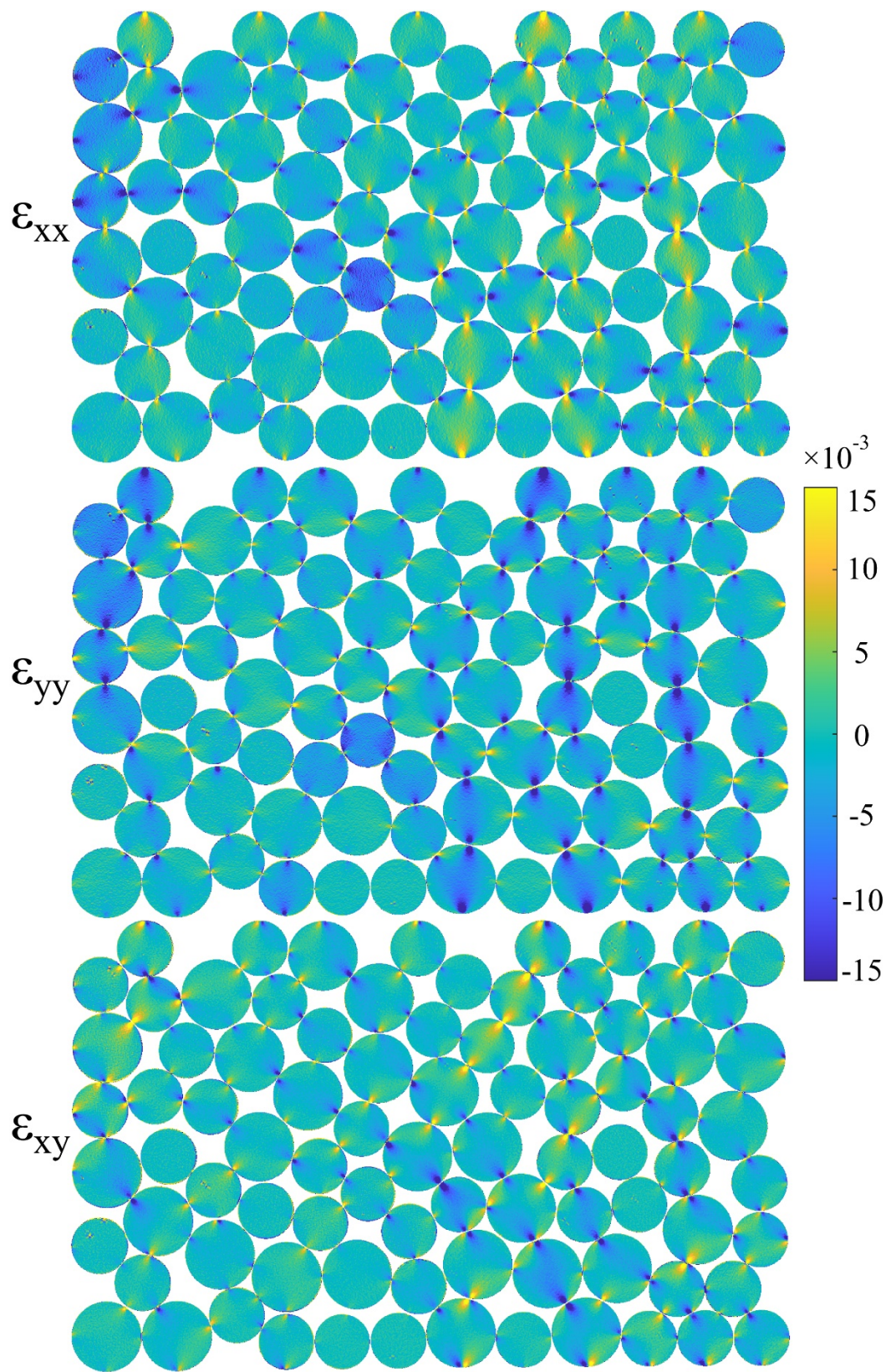


Figure 3.9 In-plane strain components for the bidisperse case.



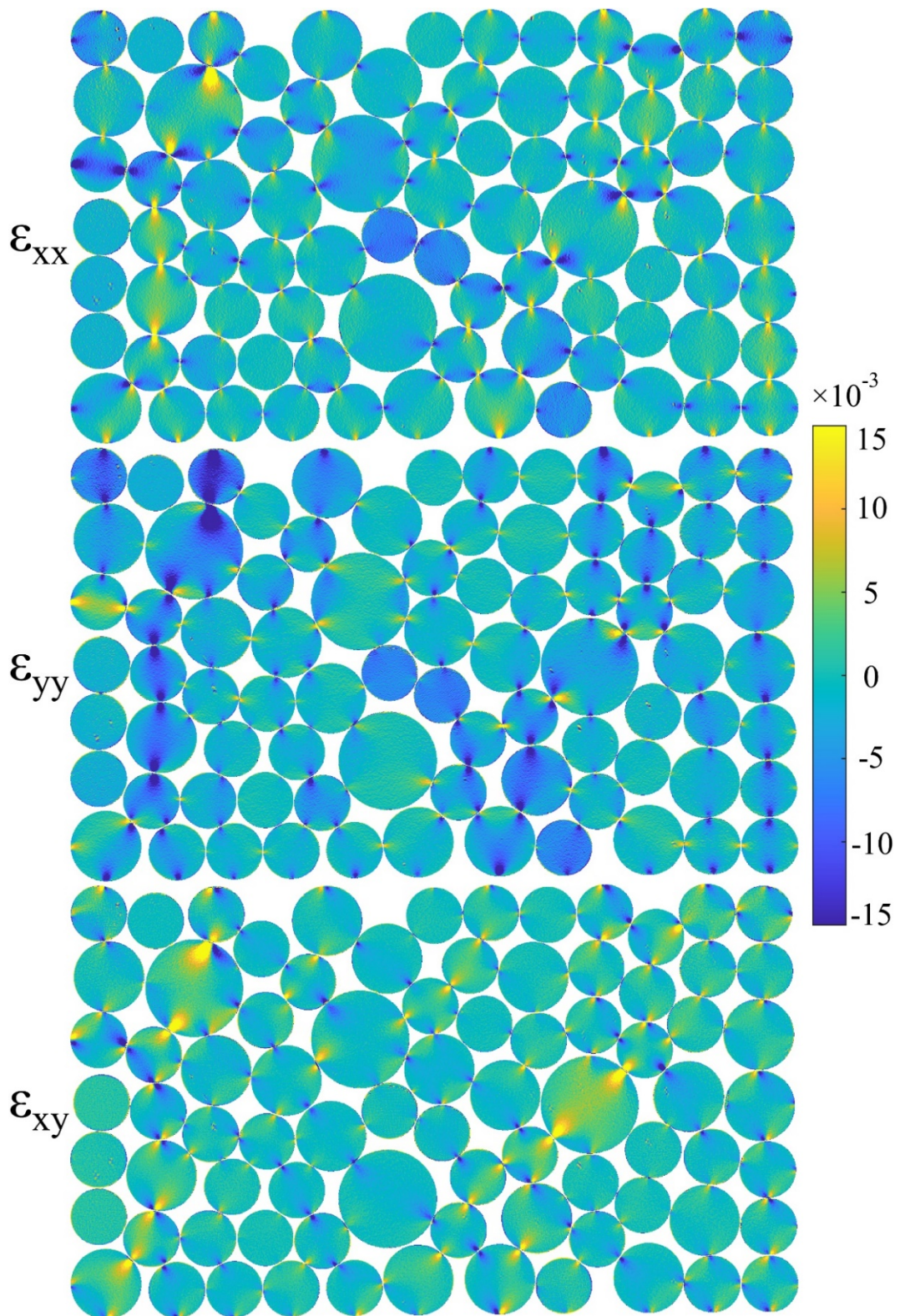


Figure 3.10 In-plane strain components for the tridisperse case.

2) Force networks and angular force distributions

Using the Strategy S5 described in Chapter 2 and still considering a Young's modulus of 3 GPa and a Poisson's ratio of 0.42 for the PA66 material, the **contact forces** were identified from the strain data for each configuration: see Figures 3.11-a, 3.12-a and 3.13-a for the monodisperse, bidisperse and tridisperse cases respectively. Contact forces are represented by red arrows. The same scale is used for the length of the vectors (referring to the force magnitude) in the three cases. The discussion below is the core of the mechanical analysis of the work, before considering thermo-mechanical aspects in the next chapter. The analysis below is based on two types of representation:

- Figures 3.11-b, 3.12-b and 3.13-b shows the **angular force distributions** using bin intervals of  $15^\circ$  and moving every  $1^\circ$  to create continuous distributions, for the monodisperse, bidisperse and tridisperse cases respectively, excluding the contacts with the four walls at the boundary of the granular system. Such graphs concern the directions of the *normal* forces;
- each contact force can be split in a normal component and a tangential component. Let us recall that normal forces are crucial for a granular system due to their dominance. It has a significant impact on the macroscopic behavior of the granular system, particularly in a quasi-static situation. Figures 3.11-c, 3.12-c and 3.13-c display the **normal force** network for the monodisperse, bidisperse and tridisperse cases respectively. These efforts transmitted to contact is represented by red line which join the particle's center in contact whose the thickness is proportional to the normal force magnitude. Note that the thickness scale is the different between the three configurations;

Note that the distinction of the normal forces between strong and weak networks will be discussed in the following subsection 3).

Let us start by the analysis of the monodisperse configuration. The coordination number in this case is approximately 4.4. It can be seen in Figure 3.11-a that, as expected, horizontal contact forces between particles are rare. Most of the particles (except obviously those in contact with the four walls) are subjected to four interparticle contact forces forming an X-pattern. However, almost horizontal interparticle contact forces are visible in the right-hand part of the granular system, particularly in the upper right-hand

zone. The angular force distribution in Figure 3.11-b shows that most of the interparticle forces are transmitted globally in the  $\pm 60^\circ$  and  $\pm 120^\circ$  directions with respect to the horizontal direction, while the remainders are transmitted nearly horizontally.

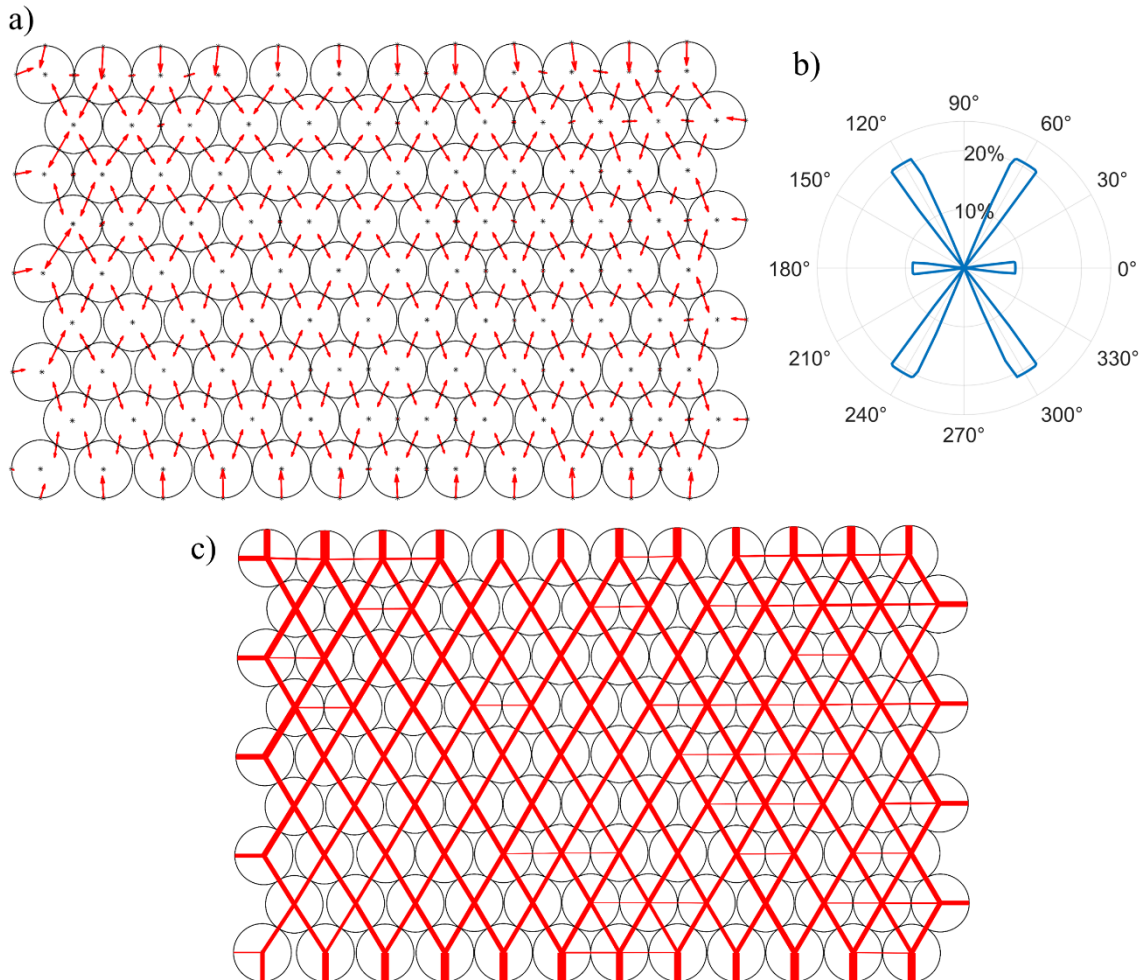


Figure 3.11 Results for the monodisperse configuration: a) contact force network; b) angular force distribution; c) normal force network.

The normal force network in Figure 3.11-c shows a strongly homogeneous distribution over the whole granular system. However, it was calculated that the total normal force at the top of the granular system (in contact with the pusher) is higher than that at the bottom of the granular system (in contact with the bottom wall): 15.66 kN vs. 14.71 kN. It can be noted that the total vertical force applied to the granular system (15.66 kN) is higher than the theoretical value (applied by the testing machine). It should be equal to the

difference between the maximum force (14.5 kN) minus the minimum force used to define the reference state (0.1 kN), i.e., 14.4 kN. The relative error, equal to 8.8%, could be explained by various sources of error. Anyway, this is not a problem for the rest of the study. Indeed, the analysis is based on the distinction between the strong network and the weak network, depending on if the normal force is higher or lower to the mean value, respectively.

The coordination number of the bidisperse configuration is approximately 4.0. The contact force network in Figure 3.12-a is heterogeneous. The highest magnitudes are located in the upper-left and lower-middle zones of the granular system. The angular force distribution in Figure 3.12-b shows that normal forces are transmitted in all directions except around  $30^\circ$  (and therefore also  $210^\circ$ ). Low occurrences are also visible at  $0^\circ$  (and therefore also  $270^\circ$ ). Normal forces are mostly oriented approximately between  $40^\circ$  and  $80^\circ$ , and between  $95^\circ$  and  $180^\circ$  (and therefore also in the opposite directions). The normal force network in Figure 3.12-c exhibits some “paths” of high magnitudes. The normal forces can be distinguished into two groups. The first one corresponds to normal forces transmitted globally along vertical direction when the particles are globally vertically aligned: see for instance the thick red lines in four particles in contact with the left wall, but such lines can be found in many places in the granular system. They are related to high values of the yy-component of the strain,  $\varepsilon_{yy}$ , in Figure 3.9. The second group of forces corresponds to normal forces transmitted globally along diagonal directions: see in particular in the middle-bottom zone. These forces are related to the high values of  $\varepsilon_{xy}$  in Figure 3.9. In addition, there are two “idle particles”, namely in the middle of the third column from the right wall and the fifth particle from the right in the bottom row. These particles have a very low strain level as shown in Figure 3.9. The very low thickness of the red lines in these two idle particles in Figure 3.12-c means that the corresponding contacts are caused by very low normal forces, but these particles are still in contact with their neighborhood. It must be noted that these idle particles may or may not be necessary for maintaining the system stability depending on the granular packing. In the present configuration, it seems that they are not required to maintain stability. Furthermore, the fifth particle from the left in the bottom row appears to be out of contact with the above neighbor but transmits (very small) normal forces with the bottom wall and with the left



and right particles. Actually, these three contacts come into and out of contact during the compressive loading.

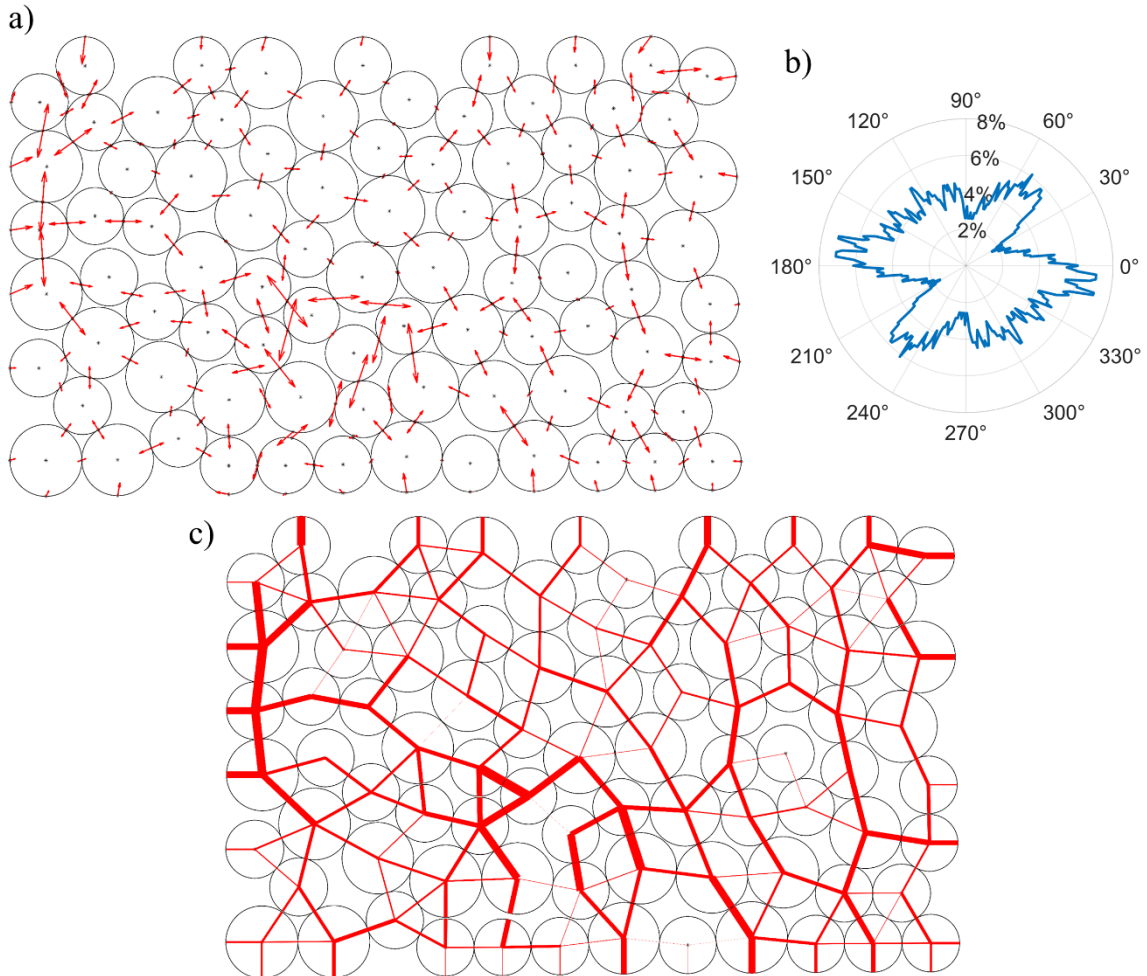


Figure 3.12 Results for the bidisperse configuration: a) contact force network; b) angular force distribution; c) normal force network.

The coordination number of the tridisperse configuration is approximately 3.9. The contact force network in Figure 3.13-a shows that the directions of the forces are mostly normal to each contact, i.e., the tangential forces are very low compared to the normal forces. Several idle particles can be found in the middle of the first column (in contact with the left wall). These three particles exhibit very low strain levels, as illustrated in Figure 3.10. However, they seem to be required for maintaining the stability of the system. Furthermore, another interesting phenomenon known as “jamming state” can also

be found near the big particle at the middle-bottom zone. Three small particles can be seen hovering above the big particle, without touching it. The normal force network in Figure 3.13-c illustrates that the force is transmitted from top to bottom through the big particles. The angular force distribution in Figure 3.13-b shows that most of the normal forces are oriented vertically and horizontally. In addition, some other normal forces are approximately at  $\pm 60^\circ$  and  $\pm 120^\circ$  from the horizontal.

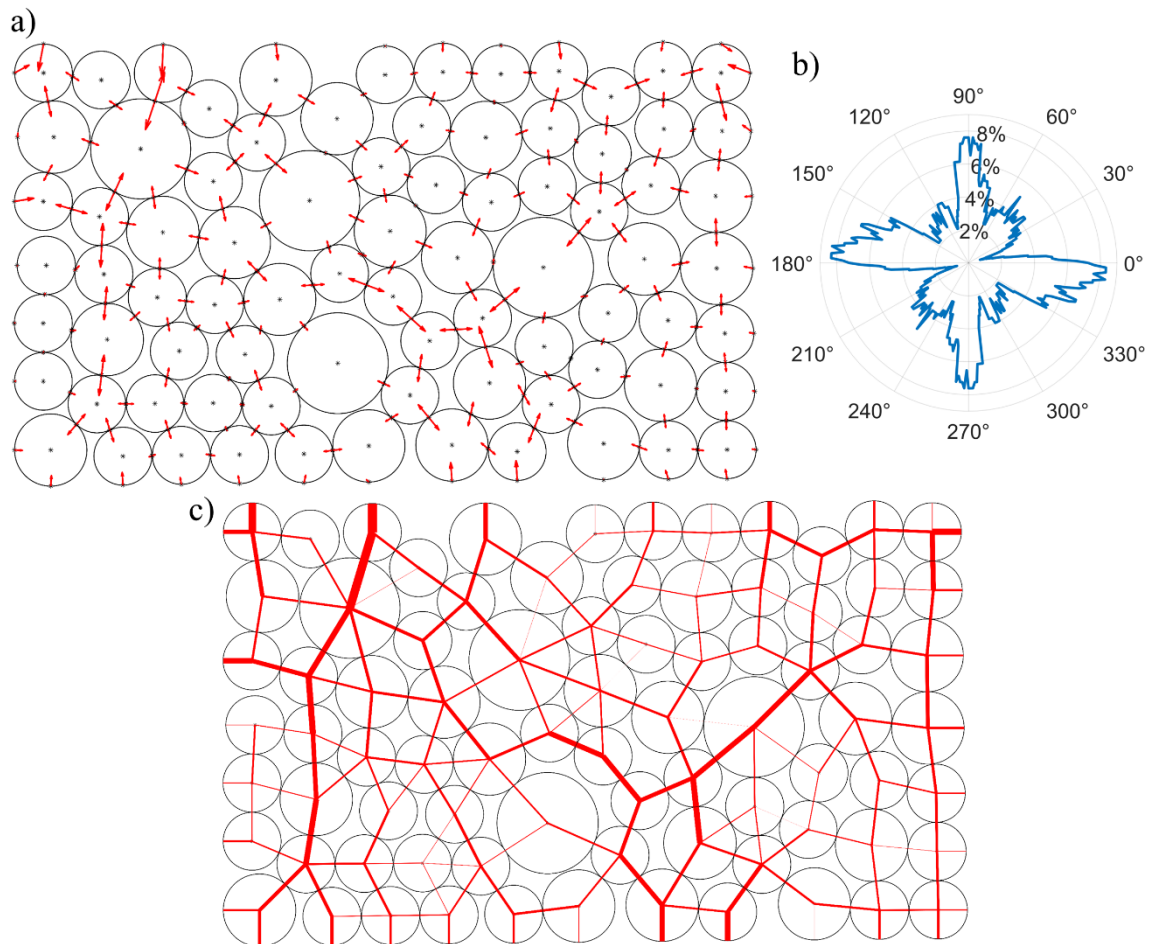


Figure 3.13 Results for the tridisperse configuration: a) contact force network; b) angular force distribution; c) normal force network.

### 3) *Strong forces and weak forces*

Due to the inhomogeneity and the anisotropy of the contact forces, the latter can be distinguished into two classes, referred to as **strong forces** and **weak forces** [11]. The strong network is defined by the normal forces higher than the mean of the normal forces over all the contacts. On the contrary, the weak network is defined by the normal forces lower than the mean. The strong forces generally transmit the mechanical loading throughout the system in the direction parallel to the compression direction, while the stability of the system requires the lateral forces in the complementary network (which are preferred by the weak forces). It is worth noting that the contact forces with the walls are not taken into account because they are not representative of the granular system. Another reason is that their orientations are always either vertical or horizontal (in the case of a rectangular frame), which may alter the analysis. Figure 3.14 presents the force networks and the angular force distribution of monodisperse, bidisperse, and tridisperse in the first and second columns, respectively, distinguishing strong, weak, and wall-particle forces. The latter are shown in the red, blue, and gray colors, respectively. The strong and weak forces are separately displayed in the angular force distributions using red and blue colors, respectively.

The normal force network of monodisperse case in the first column of Figure 3.14-a shows that the strong forces are entirely oriented in the diagonal “X” direction of the particles, whereas the weak forces are mainly oriented in the vertical direction (and also slightly in the diagonal direction). The normal force networks of the bidisperse and tridisperse cases in the first column of Figures 3.14-b and 3.14-c, respectively show that the strong forces are mainly oriented in the vertical direction, i.e., parallel to the external compressive loading. The weak forces are mainly oriented in the perpendicular direction of the external compressive loading.

For the angular force distribution of the monodisperse case in the second column of Figure 3.14-a, the orientation of the strong network is clearly seen having four spikes, which are all in the diagonal direction. The orientation of the weak network has six spikes. Two big spikes are mostly in the horizontal direction, which is perpendicular to the external compressive loading. The other four spikes are in diagonal direction. For the



bidisperse case, the angular force distribution of the strong forces is mostly oriented in the vertical direction. The angular distribution of the weak forces is mostly oriented along the angles  $0^\circ$ ,  $60^\circ$ ,  $180^\circ$  and  $240^\circ$ . For the tridisperse case, the angular force distribution of the strong forces is clearly seen in the vertical direction and the angular force distribution of the weak forces is mainly oriented in the horizontal direction.

In overall, the strong network of the polydisperse configurations is generally oriented in the direction parallel to the compression and the weak network is oriented in the direction perpendicular to the compression. In the monodisperse system, the strong network is entirely in the diagonal directions due to the triangular force pattern. The weak network is in the vertical direction and slightly in the diagonal directions. Furthermore, the strong and weak networks have 4-6 spikes due to the coordination number, which is greater than 4.

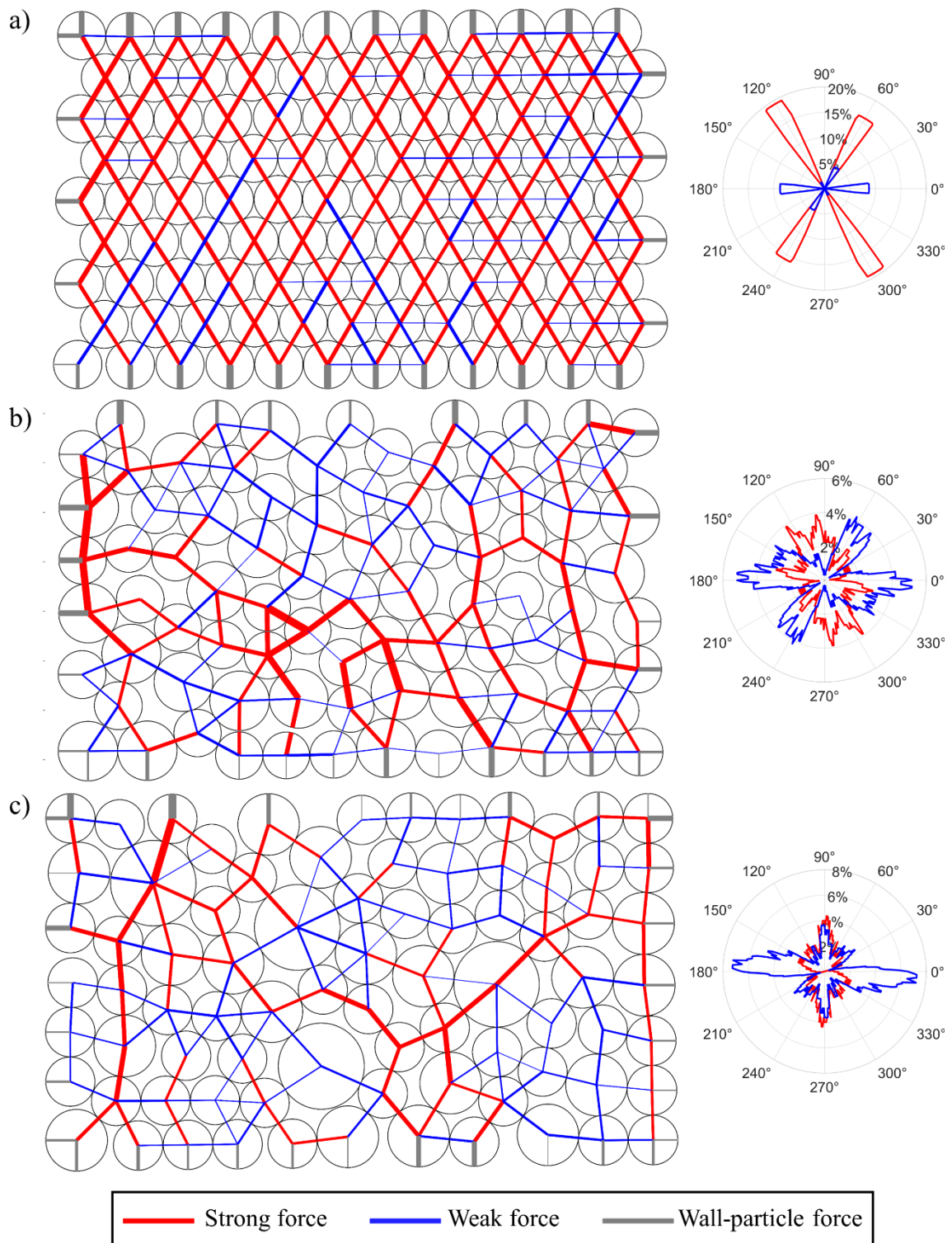


Figure 3.14 Normal force network and angular force distribution distinguishing between strong forces and weak forces: a) monodisperse configuration; b) bidisperse configuration; c) tridisperse configuration.

#### 4) Probability density function of the normal force magnitudes

A statistical analysis of the normal forces is now performed using probability density functions (PDFs). The PDF for the three configurations is first presented in Figure 3.15-a. The x-axis in the graph corresponds to the normalized normal force  $F/\bar{F}$ , the normal forces divided by the mean normal force of each configuration. The trend of the distribution is slightly left-skewed for the monodisperse case, and right-skewed for the bidisperse and tridisperse cases. Distinct PDFs are then calculated for the weak and strong networks: see Figures 3.15-b and -c respectively. The x-axis in these graphs corresponds to the normalized normal force  $F/\bar{F}$  between 0 and 1 for the weak network, and above 1 for the strong network. The same PDFs are displayed in semi-natural logarithmic scale in Figures 3.15-d and -e, respectively. The PDFs of weak forces in polydisperse systems are generally known to be characterized by power laws (see Section 1.2.4 for more information), leading to slightly curved plots as shown in Figure 3.15-d. Moreover, the distributions of the weak forces in the bidisperse and tridisperse configurations appear to be similar to each other. The situation is different for the monodisperse case, which has a lower percentage of weak forces compared to that of the strong forces. The percentages of strong forces in monodisperse, bidisperse and tridisperse configurations are approximately 67, 42% and 38%, respectively. On the other hand, the percentages of weak forces are about 33%, 58% and 62%, respectively. These results are consistent with previous papers that found that the percentages of strong forces and weak forces in polydisperse configurations are typically around 40% and 60%, respectively [11]. In polydisperse systems, the PDFs of strong forces are generally characterized by an exponential decay, which can be written by:

$$P \propto e^{\beta(1-F/\bar{F})} \quad (3.6)$$

where  $\beta$  is the decay coefficient. It is clearly seen that the distribution trends of the three configurations exhibit an exponential decay, as shown in Figure 3.15-c. Indeed, the PDFs in semi-logarithmic scale in Figure 3.15-e feature reasonably linear trends. The maximum normalized normal forces of the monodisperse, bidisperse and tridisperse configurations are approximately 1.8, 3.2 and 3.5, respectively. This emphasizes that in a polydisperse configuration, the largest particles would primarily transmit higher forces, as evidenced

in previous studies [10]. Concerning the compacted monodisperse configuration, the fact that the contact forces are almost homogeneously distributed in diagonal directions explains why the range of normalized normal forces is rather narrow, and the percentage of strong forces rather high compared to the others configuration.

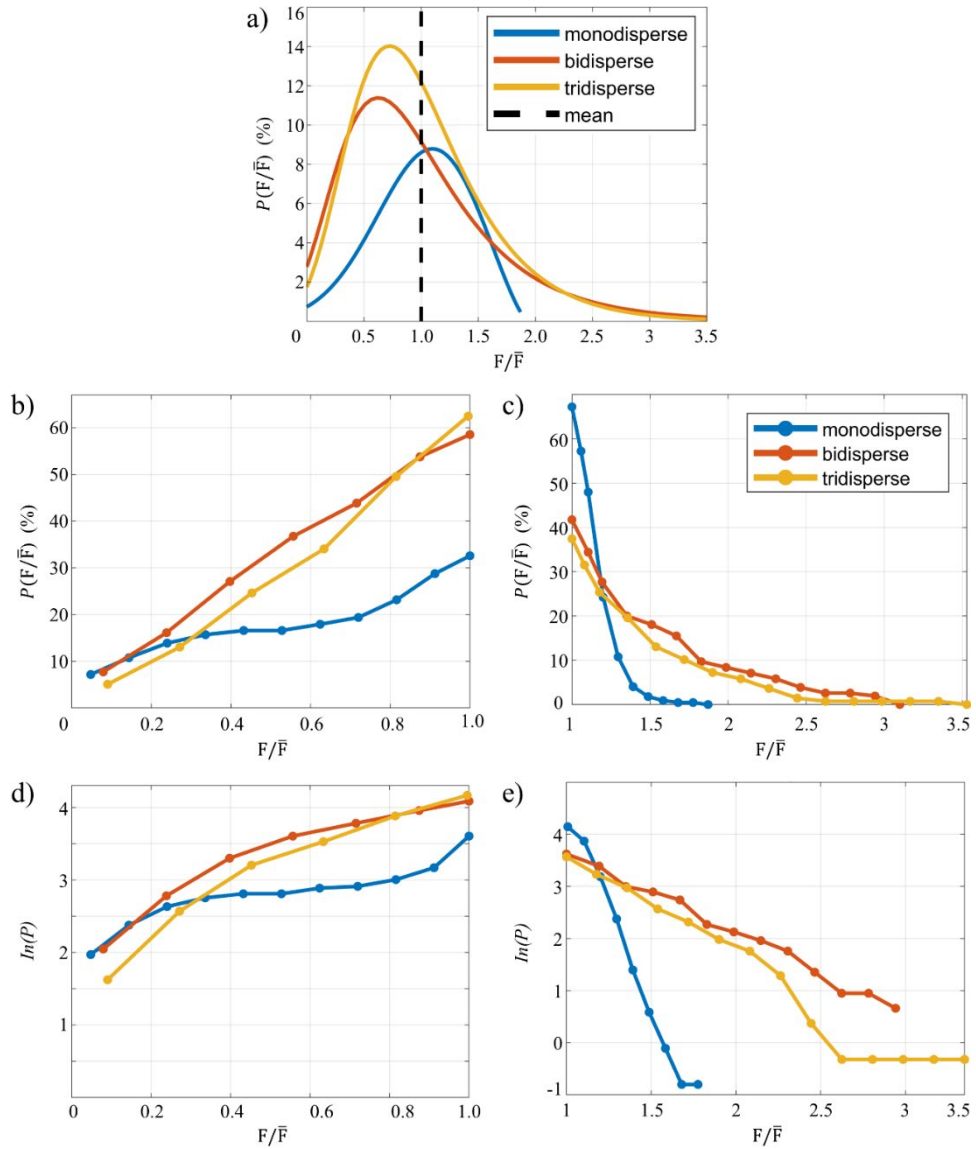


Figure 3.15 Probability density function (PDF) of the normalized normal forces: a) in the force network b) in the weak network; c) in the strong network; d) in the weak network in semi-natural logarithmic scale; e) in the strong network in semi-natural logarithmic scale.

### *5) Distribution of ratios between tangential and normal forces*

The tangential forces at all the contacts are presented in Figure 3.16. They are represented by red double-headed arrows that are tangential to the contacts and all of the same length. The arrow thickness is proportional to the tangential force magnitude. Note that single-headed arrows are used for the contacts with the walls because the measurements were made only on the side of the particle. Note that the thickness scale is different between the three configurations in Figures 3.16-a, -b and -c, corresponding to the monodisperse, bidisperse and tridisperse cases respectively.

The tangential force network of the monodisperse case in Figure 3.16-a shows that the high tangential forces are located along the two rows of particles near the bottom, left and right walls. The tangential force network of the bidisperse case in Figure 3.16-b shows that the high tangential forces are located in the middle-bottom zone of the granular system, as well as at the top-left and top-right corners. The tangential force network of the tridisperse case in Figure 3.16-c shows that the high tangential forces occur in the top-right zone of the granular system.

It is worth noting that tangential forces are rarely identified from experiments in the literature. Let us cite Ref [4] from photoelastic data and Refs [63-65] from strain data obtained by DIC in combination with FEM simulations. The present research work demonstrates that VFM and LSA enable to successfully measure both normal and tangential forces using a procedure which was carefully validated in Chapter 2 and Section 3.2.

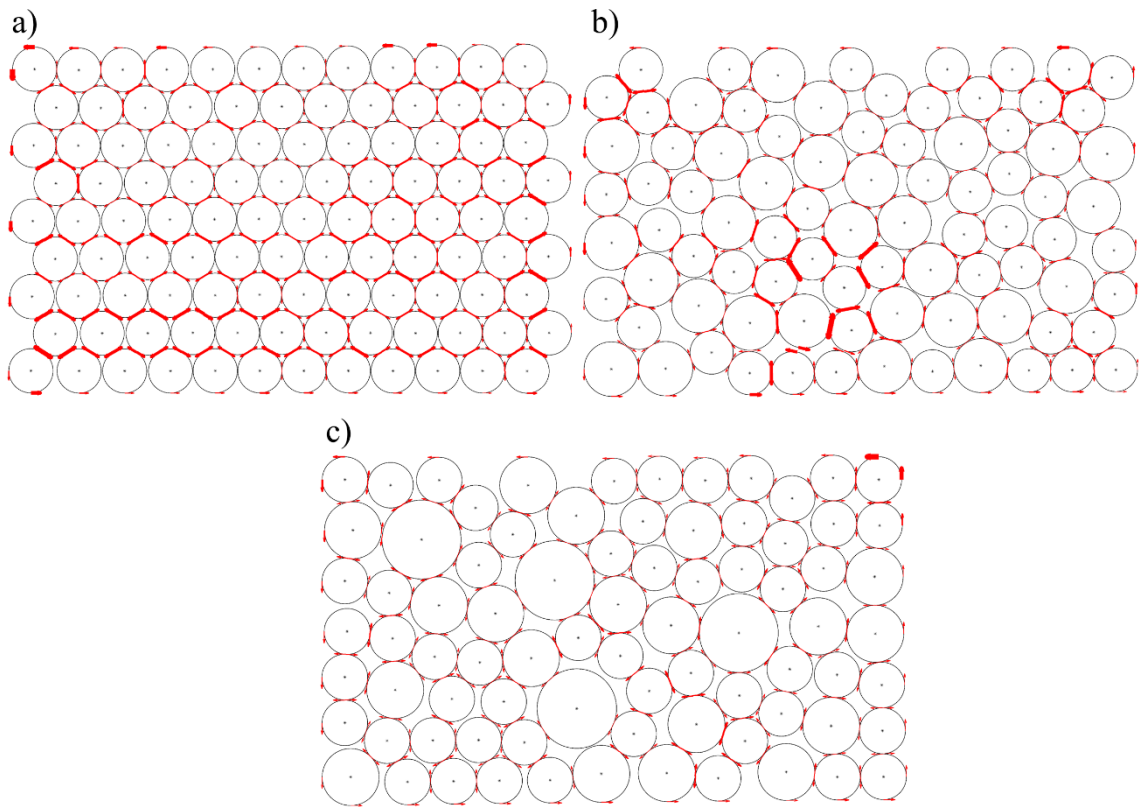


Figure 3.16 Tangential force network: a) monodisperse configuration;  
 b) bidisperse configuration; c) tridisperse configuration.

The histograms of the ratios between tangential and normal forces for the monodisperse, bidisperse and tridisperse cases are presented in Figures 3.17-a, -b and -c respectively. Reference [166] indicates that coefficient of friction  $\mu$  for PA66 ranges from 0.2 to 0.65. The maximum values ratios between tangential and normal forces are found to be approximately equal to 0.65, 0.8 and 0.7 respectively in the three graphs, which is slightly higher than the maximum value expected for PA66 (0.65). The percentages of the contacts with ratios between tangential and normal forces greater than 0.65 for the bidisperse and tridisperse cases is approximately 5% and 1%, respectively. The reason is probably because the particles are made in polymer, which can cause cohesive contacts.

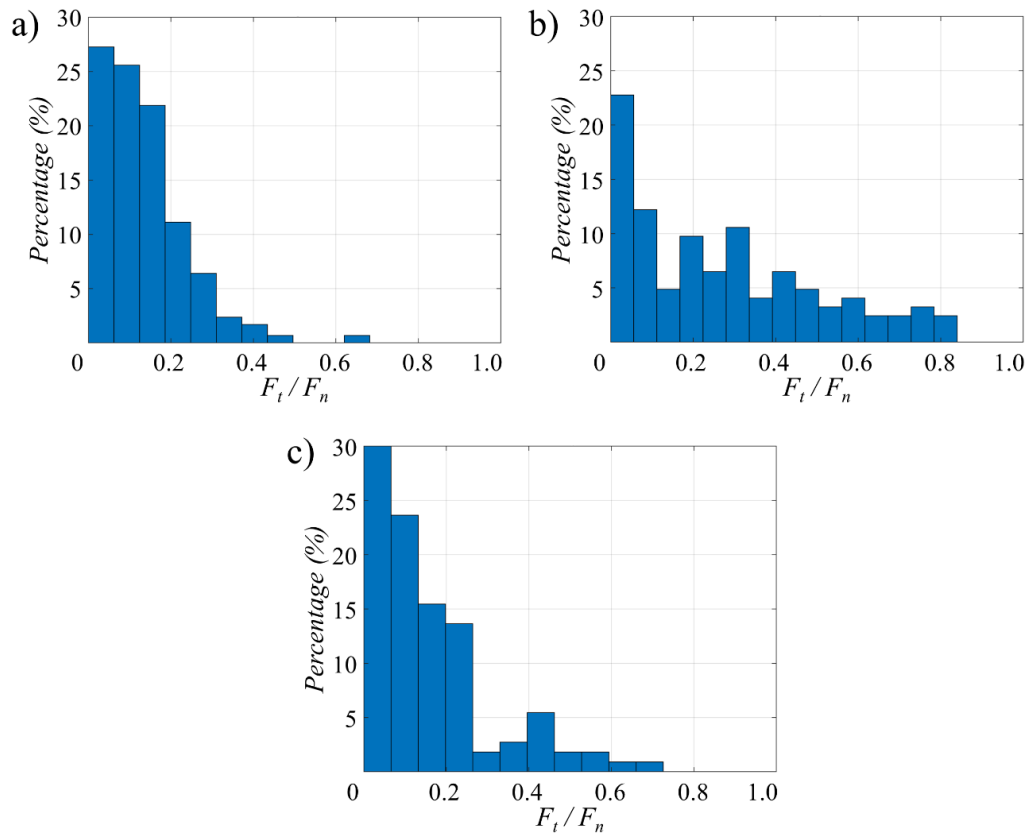


Figure 3.17 Histogram of ratio between tangential and normal forces:  
a) monodisperse configuration; b) bidisperse configuration; c) tridisperse configuration.

### 3.3.3 Limitation of the experiments

The objective of this section is to discuss some limitations or difficulties when performing the experiments for contact force identification with LSA and VFM.

#### 1) *Surface smoothness of particles*

To realize perfect checkerboard patterns on the particle surfaces, proper smoothness and flatness of the cylinder ends are required. The checkerboard pattern can be distorted if the smoothness and flatness are improper. A surface finishing is then required before engraving the pattern. However, it is worth noting that it is not necessary to have a “perfect” checkerboard pattern, but it should be sufficiently good to prevent errors in LSA technique.

## 2) Orientation of checkerboard pattern

LSA does not require only a good checkerboard pattern, but it also requires a proper orientation of the pattern when performing an experiment. The angle of checkerboard with respect to the horizontal axis of the camera should be approximately  $10^\circ$ . The reason is that some ranges of orientation angle can cause an aliasing effect, which creates fringes on the captured images [164]. These fringes disturb the retrieved strain maps. In our experiments, we needed to pay attention to placing all the particles in the proper angle before starting the tests. Figure 3.18 shows an example of fringes appearing in strain fields due to improper orientation of checkerboard. Vertical fringes are clearly visible in strain fields  $\varepsilon_{xx}$  and  $\varepsilon_{xy}$ , while horizontal fringes are slightly visible in strain field  $\varepsilon_{yy}$ .

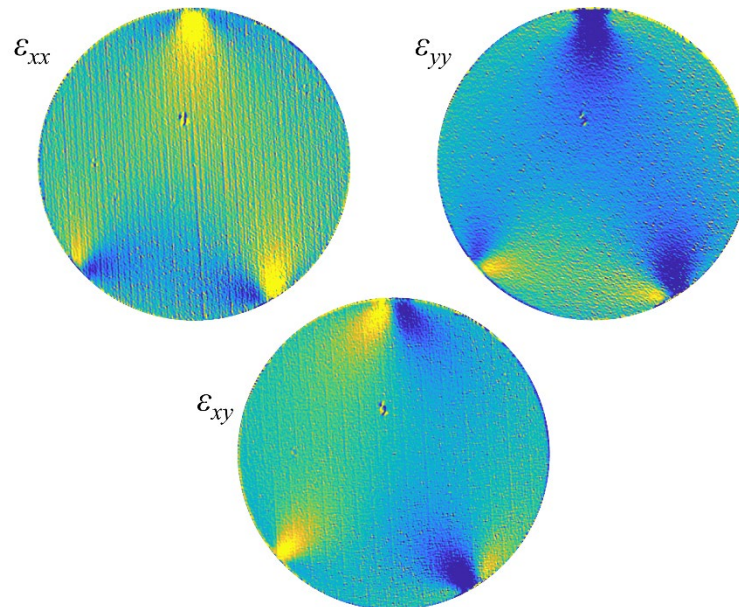


Figure 3.18 Example of fringes appearing in the strain fields in the case of an incorrect angular orientation of the checkerboard.

## 3) Out-of-plane particles

This is a common problem in 2D full-field measurement techniques. In our experiment, we attempted to deal with this problem by placing a transparent cover lid in front of the cylindrical particles and pushing them until they touched the cover lid. This procedure enables to have all the cylinders in-plane. However, it is difficult to manage while maintaining the proper orientation angle of the checkerboard of each particle. This



out-of-plane problem can cause the appearance of shadows on the surface of nearby particles. This may have an impact on the quality of the strain maps, leading to potential errors in the force distributions obtained at the end of the processing by VFM. Additionally, if the number of particles in the system increases, the management of the system becomes more and more challenging.

#### *4) Insufficient number of contacts*

In our experiments, the number of contacts may not be enough for statistical analysis, potentially leading to incorrect trends in the distributions of contact forces and the appearance of the angular force distribution. To get rid of this issue, increasing the number of particles in the system is necessary to obtain correct distribution trends. However, a larger number of contacts would require a higher external loading to maintain the sufficient strain level measurable by LSA. This means that a more powerful testing machine is then required.

### **3.4 Comparison between experiments and numerical simulations**

In this section, numerical simulation and experimental results are compared in terms of the contact force network, angular force distribution and probability density function (PDF) of normal forces. The MD approach was then employed to provide the numerical simulation results; see Section 1.2.6 for a reminder about this approach. The objective is to validate the experimental results by comparison with the numerical simulation results.

#### **3.4.1 Numerical simulation preparation**

Similar to the experiments, three cases of the numerical simulations were performed: monodisperse, bidisperse, and tridisperse configurations. First, the initial states were created from the extraction of the positions and radii of all the particles in the three experimental configurations. These data were employed to generate the particles in the numerical simulations at the same positions as in the experiments. It must be noted that it is not possible to get the perfect positions and radii. The generated particles were placed inside a rectangular box made of four rigid plane walls. The box has the same size

as in the experiments. The incremental compressive loading was then applied on the top wall up to 14.4 kN under quasi-static condition. The other walls were fixed. The gravitational force was taken into account despite the fact that its magnitude is rather small compared to the compressive loading. The contact stiffness of the PA66 was set to 11.33 MN/m. This value was obtained from experiments, not reported here, involving the compression of a single particle. The coefficient of friction of PA66 was set to the maximum value indicated in reference [166], i.e., 0.65.

In addition, three simulations were performed for each granular configuration (monodisperse, bidisperse and tridisperse) placing randomly the particles in the rectangular box. Hence, there are four simulations (one with same position of the particles and three with random positions) for each of the three granular configurations.

### 3.4.2 Comparison between experiments and simulations in terms of strong and weak forces

Figure 3.19 shows the comparison of the normal force networks between numerical simulations and experiments, with the particles in the same locations. The strong forces, weak forces and wall-particle forces are shown in red, blue and gray colors, respectively, with line thickness proportional to the normal force magnitude. The two force networks of the monodisperse case show the same patterns, where the forces are mainly transmitted in diagonal directions, as illustrated in Figure 3.19-a. The comparison for the bidisperse and tridisperse cases are presented in Figures 3.19-b and 3.19-c respectively. The experimental and simulated force patterns are clearly not the same. However, the force transmission patterns from left to right are still observed at the middle in both the experiment and the simulation in the bidisperse case. In the tridisperse case, the force transmission patterns for both the experiment and the simulation are in the vertical direction around the left and the right of the walls. As expected, it is not possible to compare the forces between numerical simulations and experiments at each contact location, but the results can be compared through a statistical analysis, which is discussed in the following section.

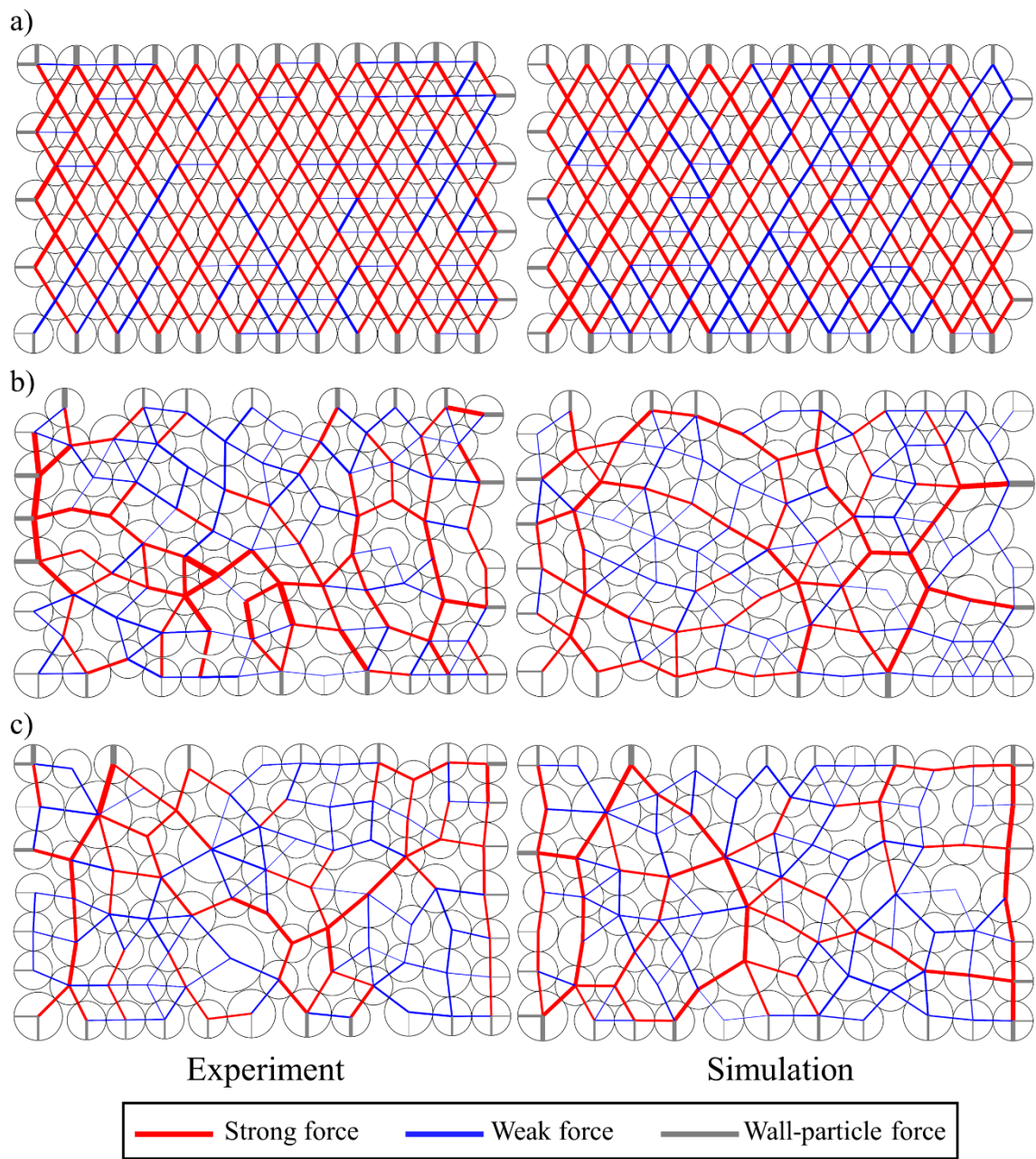


Figure 3.19 Comparison between the normal force networks obtained by experiment and by simulation, with the particles in the same locations: a) monodisperse configuration; b) bidisperse configuration; c) tridisperse configuration.

### 3.4.3 Comparison between experiments and simulations in terms of angular force distribution

Figure 3.20 shows the comparison of the angular force distributions between experiments and simulations, with the particles in the same locations. In the monodisperse case, the graphs of the experiment and the simulation shows four large spikes and two small spikes. They are in diagonal and horizontal directions, respectively. The four large spikes correspond to the strong forces while the two small spikes correspond to the weak forces. In the bidisperse case, the angular force distributions of both the strong and weak forces of the experiment and the simulation seem to have six spikes. The strong force directions of the experiment are mainly along the  $120^\circ$  and  $300^\circ$  directions, while the weak force directions correspond to the other angles. On the contrary, the strong and weak forces numerically obtained seem to be equally distributed along the  $\pm 60^\circ$ ,  $\pm 120^\circ$ ,  $0^\circ$ , and  $180^\circ$  directions. The trends of angular force distributions between the experiment and the simulation are similar. In the tridisperse case, the angular force distribution has eight spikes for both the experiment and simulation. The strong forces are mainly in the vertical direction, while the weak forces are mainly in the horizontal direction. The others are located in the diagonal directions. The comparisons between the experiment and the simulation thus show that the trends of angular force distribution of both approaches are similar. This emphasizes the reliability of the proposed contact force identification strategy.

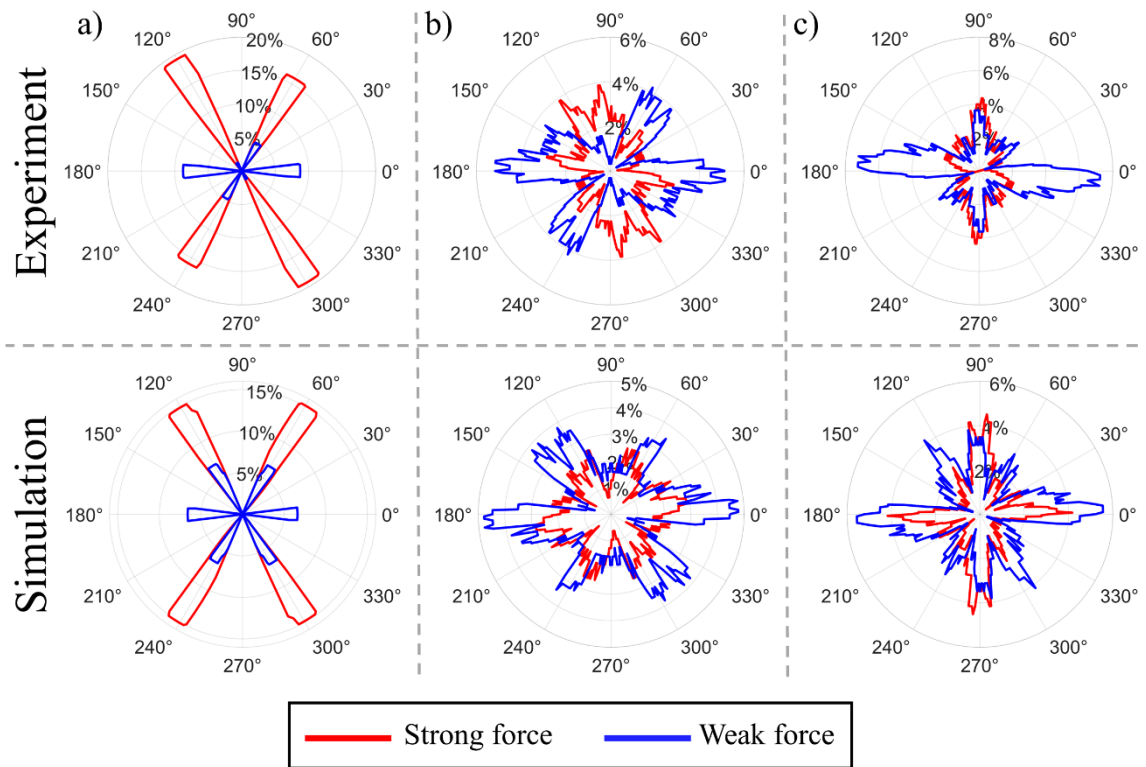


Figure 3.20 Comparison between the angular force distributions obtained by experiment and by simulation, with the particles in the same locations: a) monodisperse configuration; b) bidisperse configuration; c) tridisperse configuration.

### 3.4.4 Comparison between experiments and simulations in terms of probability density function of normal forces

Figure 3.21 presents the comparison of the probability density functions (PDFs) of the normalized normal forces between experiments and simulations with the particles in the same locations as in the experiments. The experimental curves are shown with thick solid lines, while the simulated curves are shown by using thin dotted lines. The blue, red and yellow colors correspond to the monodisperse, bidisperse and tridisperse cases respectively. All subfigures in Figure 3.21 show that the PDFs of experiments and simulations have nearly the same trends. This validates that the results obtained from the proposed experimental strategy for contact force identification are consistent with the results of simulations, and with the past studies.

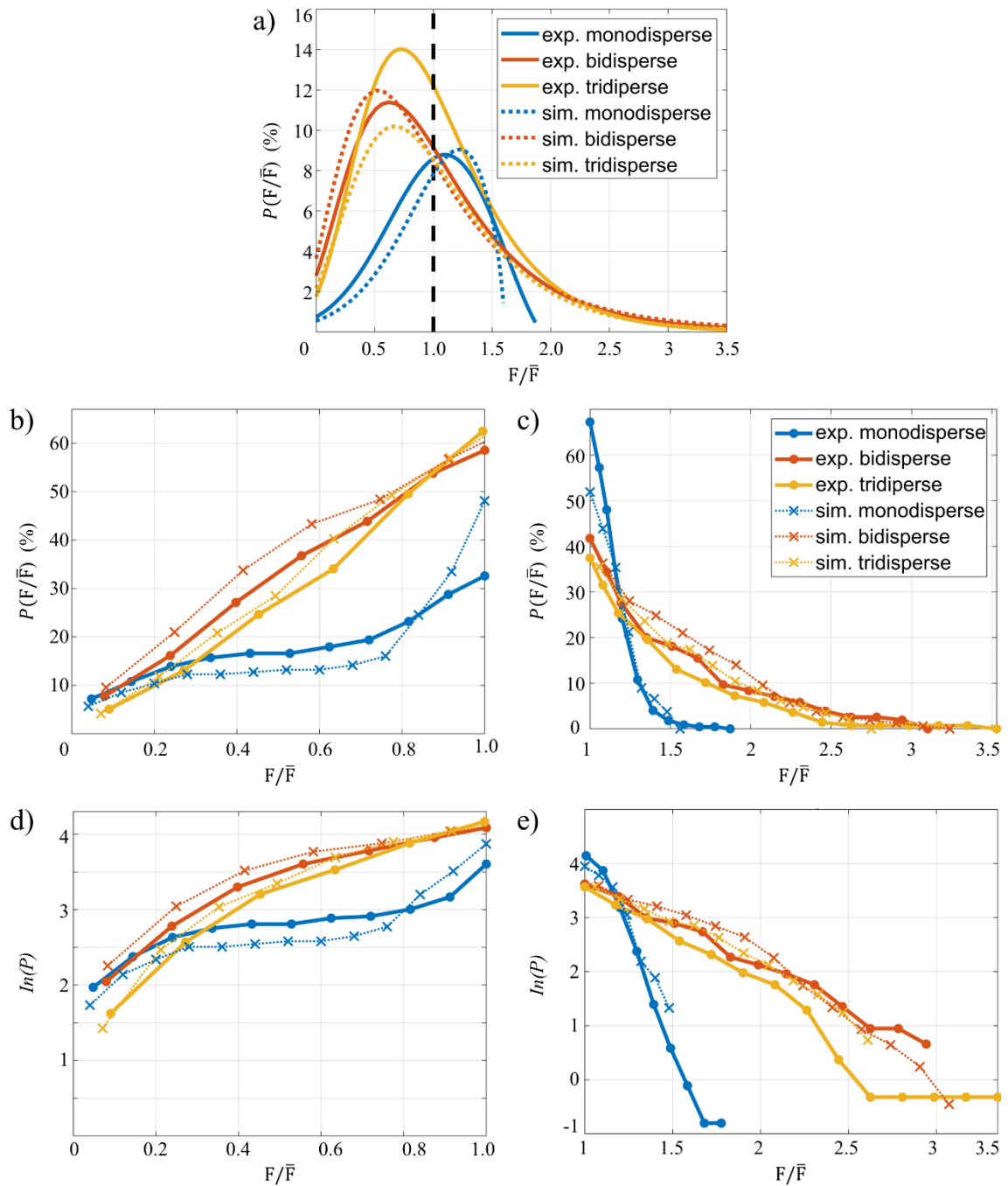


Figure 3.21 Comparison between the probability density functions (PDFs) of normalized normal forces obtained by experiment and by simulation, with the particles in the same locations: a) in the force network; b) in the weak network; c) in the strong network; d) in the weak network in semi-natural logarithmic scale; e) in the strong network in semi-natural logarithmic scale.

Finally, Figure 3.22 shows the same graphs as those in Figure 3.21 but adding results with random locations of the particles for the simulations. As indicated above, four simulations (one same position and three random locations) were performed for each configuration (monodisperse, bidisperse and tridisperse). For the monodisperse case (Figure 3.22-a), the trends of the PDFs for the weak network and the strong network of the simulations are similar to those of the experiment, except that the spans of distribution of the strong forces are wider in the simulation with random locations. For the bidisperse case (Figure 3.22-b), all the trends of the PDFs for the weak network and the strong network of the simulations are similar to those of the experiment. In the tridisperse case (Figure 3.22-c), the trends of the PDFs for the weak network of the simulations are similar to those of the experiment, with a higher probability. The trends of the PDFs for the strong network of the simulations are similar to those of the experiment, except their spans are wider than in the experiment. As a conclusion, it can be seen that all the distribution trends of the strong forces and the weak forces of all the three experimental configurations are consistent with the distribution trends of the simulations both with same location and random location.

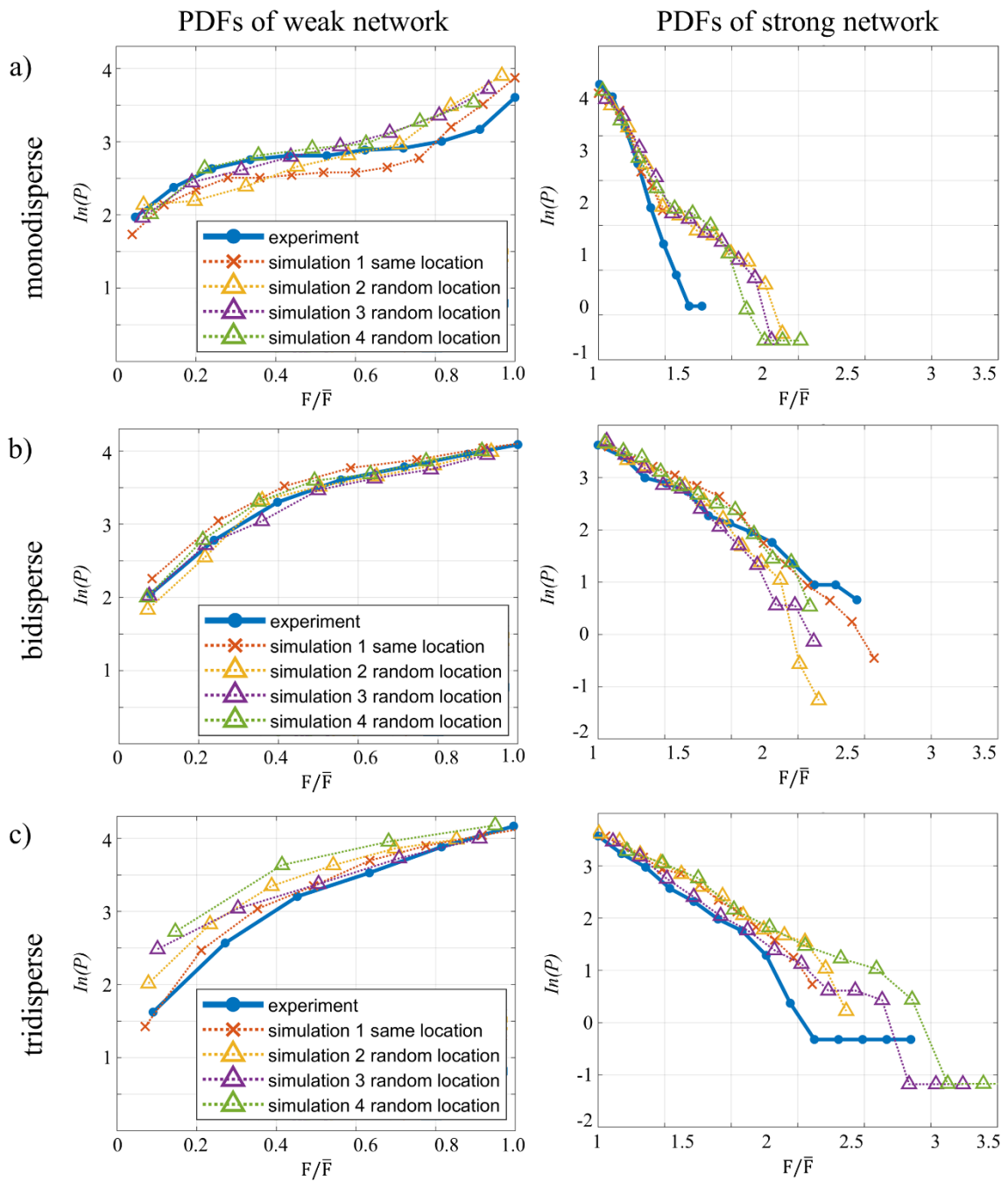


Figure 3.22 Same as Figure 3.21 but adding results with random locations of the particles for the simulations: a) monodisperse configuration; b) bidisperse configuration; c) tridisperse configuration. For each configuration, three simulations were performed for the random location case. Left column: in the weak network. Right: in the strong network.



### 3.5 Conclusion

An experimental application was first performed on a three-particle system by processing strain maps obtained in each particle using localized spectrum analysis (LSA). As indicated in the intermediate conclusion in Section 3.2.4, the virtual fields method (VFM) alone failed to identify consistent force components. This is potentially due to an imperfect 2D assumption, out-of-plane movements or errors in the elastic parameters of the particle material. Alternative approaches were then proposed by adding equations derived from the local equilibrium of each particle, and Newton's third law of motion at each interparticle contact. As the number of equations becomes higher than the number of unknowns (the contact force components), different strategies were compared for contact force identification. The best solution was obtained using the VFM equations with Lagrange multipliers to enforce force and moment equilibrium for each particle and Newton's third law of motion at each interparticle contact.

The experiments with a larger number of particles demonstrated that the contact force identification strategy has the capability to be employed for 2D multi-contact granular systems to identify the normal force and the tangential force at each contact. The identified contact forces were then statistically analyzed at a macroscopic level. The results appear to be consistent with the results of simulations performed relying on molecular dynamics (MD) as with the past studies. This thus validates the proposed contact force identification strategy. However, some limitations or difficulties were highlighted concerning the preparation of the experiments. These difficulties must be taken into the account when performing future experiments. It can be noted that the procedure has actually the benefit of being applicable to any full-field measurement techniques that measure in-plane strains with specimens made of any material, for instance digital image correlation (DIC).

## CHAPTER 4

# Towards a thermo-mechanical analysis of granular materials

### 4.1 Introduction

Infrared thermography (IRT) techniques and full-field deformation calorimetry approaches have profoundly impacted the experimental mechanics community. The way in which granular materials are tested is currently excluded from this trend, as evidenced by the small number of papers in the literature mentioning the use of thermographic cameras. Basically, the approach consists of analyzing the thermal response of a material subjected to a mechanical loading at constant room temperature. Under some mild assumptions, it is possible to assess the heat produced or absorbed by the material due to the change in its mechanical state [167]. Under cyclic loading, it is possible to deduce the field of hydrostatic stress amplitudes from the temperature oscillations using the so-called Thermoelastic Stress Analysis (TSA) technique [168], which is applicable to *energetic* materials (see Section 1.3.2 in the bibliography and state-of-the-art chapter). The processing relies on thermoelastic coupling, which exists in all materials featuring a non-null thermal expansion coefficient. Other approaches enable the identification of the calorific signature beyond thermoelastic coupling, for example related to plasticity, fatigue damage, viscosity, solid-solid phase change or cracking, depending on the type of material and loading conditions. More generally, the use of IR thermography and the framework of the thermodynamics of irreversible processes [169, 170] makes it possible to perform full-field “deformation calorimetry”. IR thermography techniques applied to mechanics of materials are now mature, but granular materials are currently absent from this trend.

The study of granular materials containing soft particles has only been addressed very recently [171, 172], despite the fact that they are commonly found in nature and in industry (e.g. pharmaceutical and food fields). This can be explained by the experimental difficulties associated with the large displacements/strains of the particles, which complicate the data processing and analysis. Experimental studies are still rare in the literature. Let us mention the study of the compressive behavior of 2D bidisperse granular assemblies made of soft and hard grains using DIC in Ref [173]. IRT was also used in Ref [22] to observe the thermal response of granular systems consisting of rigid and soft particles, namely made of polyoxymethylene (POM) and thermoplastic polyurethane (TPU). As indicated in Section 1.5.4, it was shown that significant temperature variations could be obtained in the soft particles without the need to average the values over several cycles. This is an advantage of the *entropic* elasticity.

In this context, the aim of this chapter is to take advantage of the strong thermal signature of entropic elasticity to analyze the thermomechanical response of granular materials entirely composed of elastomeric particles. An objective is to distinguish temperature changes associated with thermoelastic coupling (TEC) and mechanical dissipation (MD). Furthermore, studying soft granular systems is a topical issue (see Refs [171, 172]) for which there is a lack of full-field experimental measurements. Elliptical shapes for the particles are considered in the present study. This paves the way to studies on more complex geometries in the future, to progressively approach the particle shapes of real granular media. It should be noted that we have not sought to identify contact forces or stress fields.

The chapter is organized as follows:

- The second section presents the granular materials and the experimental devices used in the study;
- The third section presents some preliminary observations for a given test in order to illustrate a typical thermal response;
- The fourth section describes the procedure employed to extract calorific data from thermal measurements obtained by IR thermography;

- The fifth section aims at analyzing small-size granular systems (about 15 particles) at the local scale, using various spatial resolutions for comparison purposes;
- In order to approach real granular media, the sixth section is devoted to a statistical analysis on a larger granular system comprising about 100 particles.

Note that the particles for this thermomechanical analysis were prepared at the Institute of Physics Rennes (IPR). Some experiments were also performed at the IPR under the supervision of Prof. Jean-Benoit Le Cam.

## 4.2 Material and Methods

### 4.2.1 Particle Preparation

Figure 4.1 illustrates the preparation of the TPU particles employed in the experiments. Particles were prepared from a commercial biresin grade from Axson Technologies, composed of U1419-II isocyanate and U1458 polyol. To manufacture cylinders with elliptical cross-sections, the biresin was mixed and poured in molds. A vacuum chamber was used to remove bubbles from the mixture (see Figure 4.1-a). Twenty minutes were necessary for the complete solidification of the cylinders (see Figure 4.1-b), all of which were 26 mm long. Three dimensions were considered for the cross-sections, simply referred to as “small”, “medium” and “large” in the following of the paper for the sake of simplicity, see Figure 4.1-c. The cylinders differed in the length of the major axis of the elliptical section, which was equal to 15 mm, 18 mm and 22.5 mm, respectively. The length of the minor axis was the same for all the particles: 10 mm. The cylinders were slightly polished on one end and coated with a thin matte black paint to maximize the thermal emissivity of the surface. Finally, two material parameters are reported here for the subsequent calorific analysis of the thermal response of the granular systems made from the particles. The density of TPU was  $1,040 \text{ kg/m}^3$  according to the datasheet of the supplier. A value of  $1,700 \text{ J/(kg}\cdot\text{K)}$  was considered for the specific heat [174].

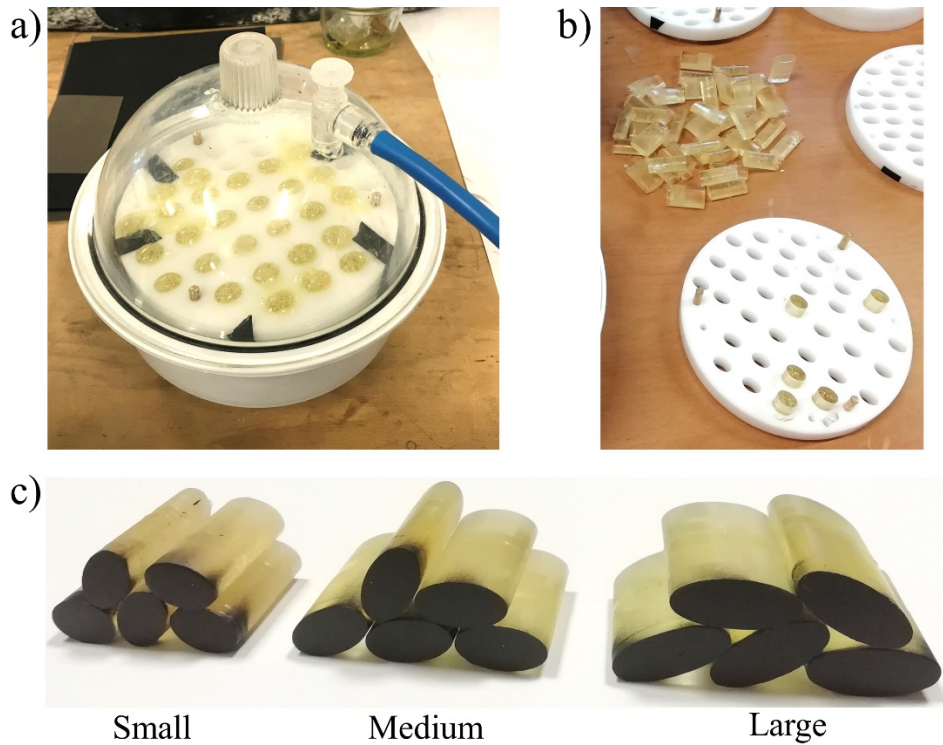


Figure 4.1 Material elaboration and elliptical particles.

#### 4.2.2 Experimental setup

Figure 4.2 shows the two types of thermomechanical setup used during this study. The difference is the size of the rectangular metal frame containing the particles for confined compressive loads, which are 50 mm and 150 mm in width (see Figure 4.2-a and Figure 4.2-c respectively). A pusher was employed to apply a vertical load at the top of the granular systems by a linear actuator. Two uniaxial testing machines were used: an Intron ElectroPuls E3000 machine and a Zwick/Roell Zmart Pro machine. The former allows cyclic loadings with a maximum compression force of 5 kN, enabling us to study the influence of the loading rate on small granular systems (about 15 particles). The latter allows quasi-static loadings up to 15 kN, enabling us to study the influence of the loading level on a large granular system (about 100 particles).

As mentioned above, all the particles were painted in black to maximize their thermal emissivity. As can be seen in Figure 4.2-d, the metallic frames were also spray-painted to limit parasitic reflections in the IR range. In addition, thick black fabrics were placed all around the granular systems as shown in Figure 4.2-b. A cardboard tunnel (not

visible in the pictures) was also placed from the IR camera to the granular material to minimize parasitic radiation caused by the close environment.

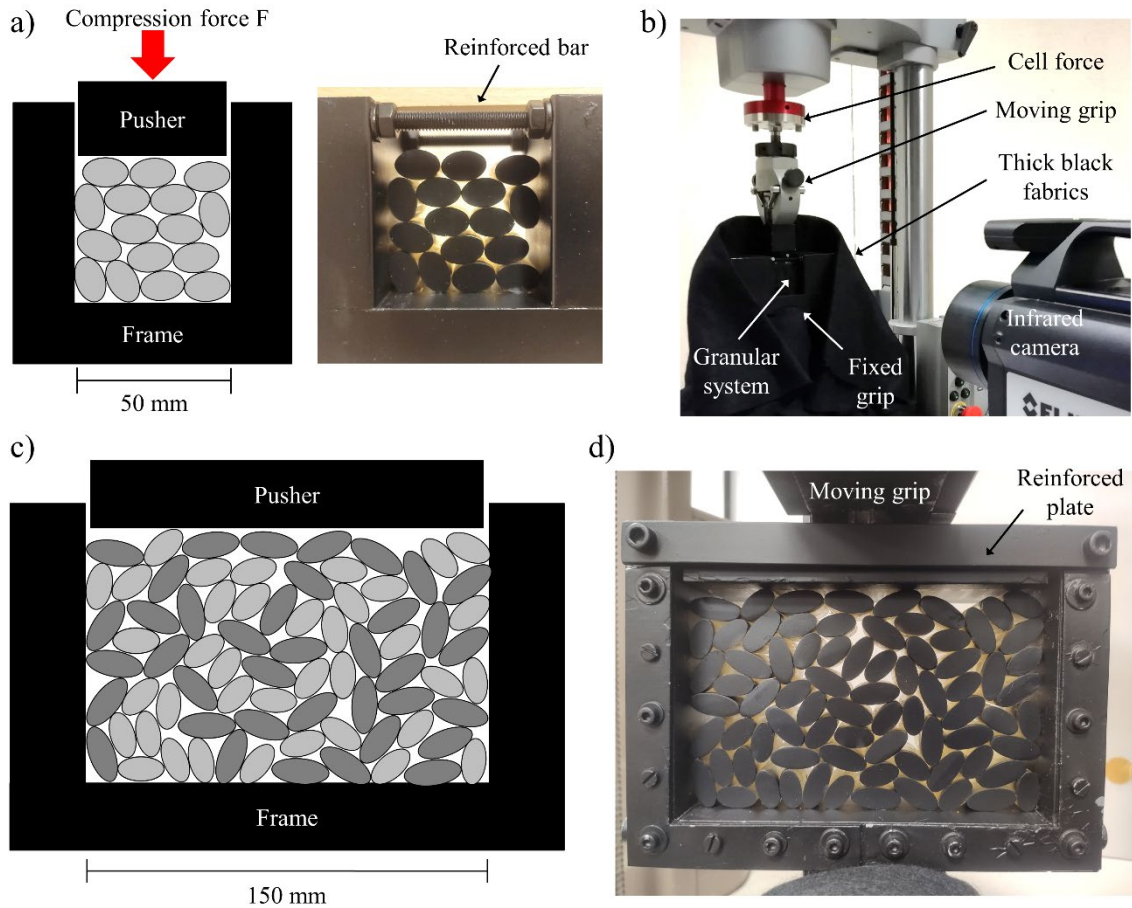


Figure 4.2 Experimental setup: a), b) a small granular system and c), d) a large granular system.

#### 4.2.3 Mechanical loading and thermal measurement

the granular systems were subjected to force-controlled cyclic loadings with a triangular profile. In all the tests, the minimum vertical compression force was set at 10% of the maximum force to avoid any loss of contact during unloading. Various tests were performed. Table 4.1 gives the list of the tests discussed in detail in the study:

- Tests T1 to T8 were dedicated to small granular systems (about 15 particles). The maximum compression force was set to 3 kN. For the monodisperse case (T1 to T6), the loading rate changed from one test to the next:  $\pm 0.5$  kN/s,  $\pm 1$  kN/s,  $\pm 1.5$  kN/s,  $\pm 2$  kN/s,  $\pm 2.5$  kN/s and  $\pm 5$  kN/s respectively. The objective here is to discuss the influence of the loading rate in terms of viscosity and heat diffusion time (since, by construction, the shorter the mechanical cycle, the more adiabatic the thermodynamical response over the cycle). For the bidisperse case (T7 and T8), two loading rates were applied ( $\pm 2$  kN/s and  $\pm 5$  kN/s respectively), the objective being to compare the results obtained with those of the monodisperse case.
- Tests T9 to T11 were devoted to a large granular system, with nearly 100 particles. The loading rate was fixed at  $\pm 1$  kN/s for the three tests, but the maximum force was set to 6 kN, 9 kN and 12 kN respectively. The objective here is to discuss the influence of the applied load level.

It should be noted that five preliminary mechanical cycles were applied to compact the granular systems (see Figure 4.3-a). Afterwards, the minimum force (10% of the maximum force) was held constant for about 10 minutes to ensure that the granular system had returned to thermal equilibrium with the environment before the beginning of the cyclic mechanical loading to be considered for the analysis. It can be noted in Table 4.1 that 20 cycles were applied to the small granular materials (T1 to T8) whereas only 5 cycles were applied to the large ones (T9 to T11). This is because the high force levels applied in the latter case make the mechanical cycle long. To limit heat exchanges between the large granular system and its environment during the measurements, the number of cycles was limited to 5.

Table 4.1 List and details of the tests presented in the paper. The asterisk symbol \* indicates that the test was repeated with different spatial resolutions for the temperature fields (obtained in practice by using different optical conditions for the infrared camera).

Test #	Type of granular material	Particle number	Content of the granular material	Maximum force (kN)	Force rate (kN/s)	Cycle duration (s)	Number of cycles
T1	Monodisperse	16	16 small	3	±0.5	12	20
T2					±1	6	
T3					±1.5	4	
T4					±2	3	
T5*					±2.5	2.4	
T6					±5	1.2	
T7*	Bidisperse	14	7 small	3	±2.5	2.4	20
T8			7 large		±5	1.2	
T9	Tridisperse	93	32 small	6	±1	12	5
T10			31 medium	9		18	
T11			30 large	12 kN		24	



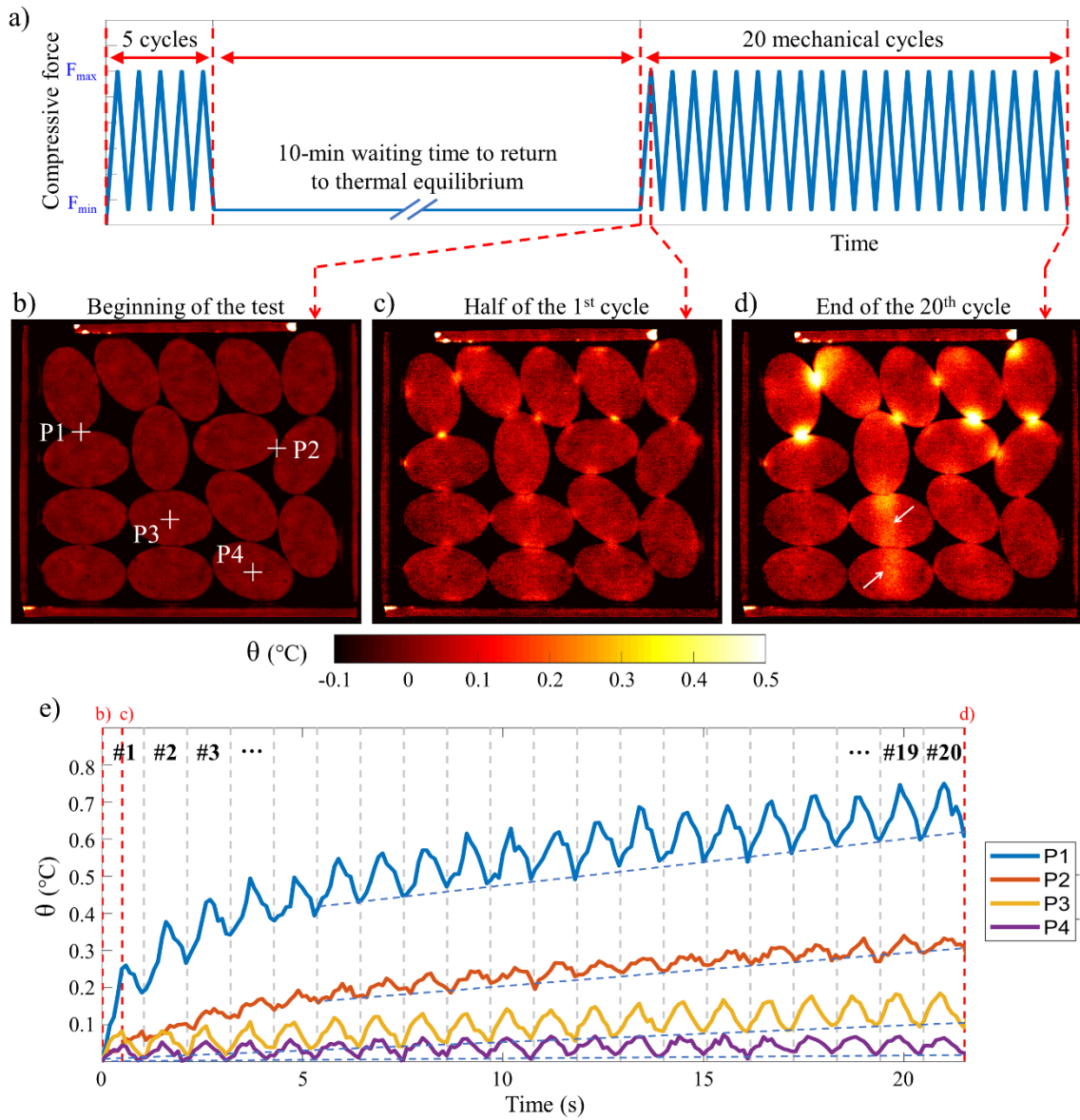


Figure 4.3 a) Schematic representation of the mechanical loading and b-e) temperature changes during test T6 (monodisperse configuration, force rate  $\pm 5$  kN/s, maximum 3 kN). The spatial resolution of the thermal maps is equal to  $131.6 \mu\text{m}$ .

Two IR cameras featuring a similar Noise Equivalent Thermal Difference of 20 mK around ambient temperature were used to capture the temperature fields at the surface of the particles: a FLIR X6540sc camera ( $640 \times 512$  pixels) and a Cedip Jade III-MWIR camera ( $320 \times 240$  pixels). The former camera was used to study small granular systems

in order to better understand the thermal response by “zooming in” on a few particles. The latter camera was used to study the large granular system in order to perform a macroscopic (*i.e.*, statistical) analysis. The acquisition frequency was set to 10 Hz in both cases. Note however that with the Cedip camera, the base acquisition frequency was 100 Hz with a real-time averaging operation every 10 thermal images (leading to a recording frequency of 10 Hz), which enabled us to improve the thermal measurement resolution. Different spatial resolutions were considered during the test campaign. It is worth recalling here that granular materials under mechanical loading were subjected to stress concentrations at the interparticle contacts, thus leading by construction to differences in the full-field measurements as a function of the spatial resolution used. The spatial resolution value, defined here as the size of the IR pixel projected onto the measurement plane, is provided for each temperature map displayed below. Some tests were duplicated with different spatial resolutions (in practice by varying the distance between the camera and the granular material): mechanical conditions T5 and T7 were both performed twice, by using in each case a different spatial resolution.

Finally, for each test, a reference thermal image was captured just before starting the cyclic mechanical loading, in order to identify the temperature *changes*. This quantity is denoted  $\theta$  in the following. Note that despite the fact that TPU was in the rubbery state, particle deformations were actually “small” due to the limited magnitude of the external loading, as well as the confined nature of the compression. Before presenting the results of all the tests, the next section provides some preliminary observations concerning one of them in order to highlight the key points of the study.

### **4.3 Preliminary observations**

Before comparing the results of the tests described in Table 4.1, Figure 4.3 shows a typical thermal response during a mechanical test, here test T6 (small granular system, monodisperse configuration, force rate  $\pm 5$  kN/s, maximum force 3 kN), with a spatial resolution of 131.6  $\mu\text{m}$  for the temperature maps. The profile of the mechanical loading is recalled in Figure 4.3-a. Several comments can be made about the thermal response:

- Figures 4.3-b to -d show the thermal fields at three times during the loading: beginning, half of the 1<sup>st</sup> cycle and end of the 20<sup>th</sup> cycle, respectively. Figure 4.3-c highlights “hot” spots at nearly all the contacts. Figure 4.3-d shows larger temperature changes at some interparticle contacts (especially in the upper part of the granular material) as well as a “hot path” through two particles (see white arrows).
- Four points of interest are selected in Figure 4.3-b to illustrate typical thermal responses *vs.* time. Points P1 and P2 are located at interparticle contacts, while P3 and P4 are at the center of particles. Figure 4.3-e presents the thermal variation  $\theta(t)$  *vs.* time  $t$  for these four material points. Oscillation at the same frequency as the loading is observed. Loading is accompanied by a temperature increase, whereas unloading is accompanied by a temperature decrease. Furthermore, a global increase is observed for the four points. A linear trend is obtained after the fifth cycle for points P1 and P2: see dashed lines. For P3 and P4, linearity is observed from the beginning of the test. It can also be noted that these four points exhibit distinct thermal responses in terms of *oscillation amplitude* (which can be *a priori* associated with the stress oscillation amplitude) and *average rate of increase* (which may be associated with mechanical irreversibility, such as damage, viscosity and friction). It is interesting to note that these two quantities are not always correlated. For example, point P2 is associated with a small oscillation amplitude and a high mean rate of increase, in contrast to point P3. The distinction between the calorific responses associated with thermoelastic behavior and anelastic behavior is the focus of the discussion proposed in the following sections.
- The thermal variation at point P4 shows an interesting property: a cyclic oscillation with nearly no overall increase, and a minimum value of  $\theta$  remaining close to zero over the 20 cycles. It can be assumed that the response is here adiabatic and nearly reversible (we can guess that the strain and strain rate levels are low enough not to create much heat by viscosity or damage). Indeed, in this situation the amount of heat produced and absorbed (during loading and unloading

respectively) by thermoelasticity is the same over a thermodynamical cycle. Thus  $\theta$  returns then to nearly zero at the end of each cycle if the latter is adiabatic.

Some thermomechanical properties have been presented here to anticipate the discussion in the next sections. Before analyzing the results of the tests listed in Table 4.1, the next section provides the thermomechanics of materials background used for the analysis. It also presents the approach used for calorific data extraction.

## 4.4 Data processing

### 4.4.1 Thermomechanics of materials background

The calorific response of materials subjected to mechanical loading was described in section 1.3.2. It is worth to remind that it can be split into two parts [136, 175]:

- The first part is associated with reversible thermomechanical phenomena, *i.e.*, thermoelasticity only in most cases. As mentioned above in the introduction, two types of *thermoelastic coupling* (TEC) exist: one is governed by the change in internal energy (energetic elasticity) and the other is governed by the change in entropy (entropic elasticity) [138]. A simple tensile test enables us to distinguish between them: upon loading (resp. unloading), energetic elasticity leads to a temperature decrease (resp. increase) whereas entropic elasticity leads to a temperature increase (resp. decrease). Actually, as both types of coupling exist in rubbery materials, a so-called *thermoelastic inversion* is observed upon loading, when the entropic contribution becomes preponderant [139]. On the contrary, compression loading (resp. unloading) leads to a temperature increase (resp. decrease) for both types of TEC.
- The second part is associated with irreversible mechanical phenomena, which can be of different origins since they depend on the material and the loading conditions. The associated heat power density is called *mechanical dissipation* (MD) or *intrinsic dissipation*. This calorific quantity is always positive. It is for instance at the origin of the so-called *self-heating* of the material during cyclic loading due to fatigue damage and/or viscosity.

Figure 4.4 schematically illustrates the thermal variation in a rubbery material subjected to compression cycles assuming an adiabatic evolution. Figure 4.4-a corresponds to the case of a purely thermoelastic response, *i.e.*, without MD. The temperature change  $\theta$  oscillates in phase with the mechanical loading between zero and a maximum value designated by  $\theta_{TEC}$  in the following. The return to zero at the end of each cycle is due to the fact that the heat released during loading is equal in magnitude to that absorbed during unloading. This response may correspond for instance to the thermal changes at point P4 in Figure 4.3-e. Figure 4.4-b corresponds to a case involving MD, assuming that the mechanical response of the rubbery matter is “accommodated” (stabilized mechanical response): the global temperature increase is linear, since the same amount of MD is produced at each cycle. This response may correspond to the thermal variation of point P3 in Figure 4.3-e. Figure 4.4-c corresponds to a general case for which material accommodation occurs during the first cycles. For the experiments performed in the present study, such a transient effect is expected to be minimized due to the five preliminary compaction cycles (see Figure 4.3-a). However, this response is observed for points P1 and P2 in Figure 4.3-e. Transient viscosity probably explains this observation. This could be due to two causes: variations in the material during the waiting time between preliminary compaction and the beginning of the test, or an insufficient number of preliminary compaction cycles, at least in terms of heat signature. Finally, we can recall that adiabaticity (“short” tests) is assumed in the temperature variations shown in Figure 4.6. After a certain time, the red dashed lines on the figure obviously tend to stabilize horizontally because of the balance between the heat produced by the MD and the heat exchanged with the environment.

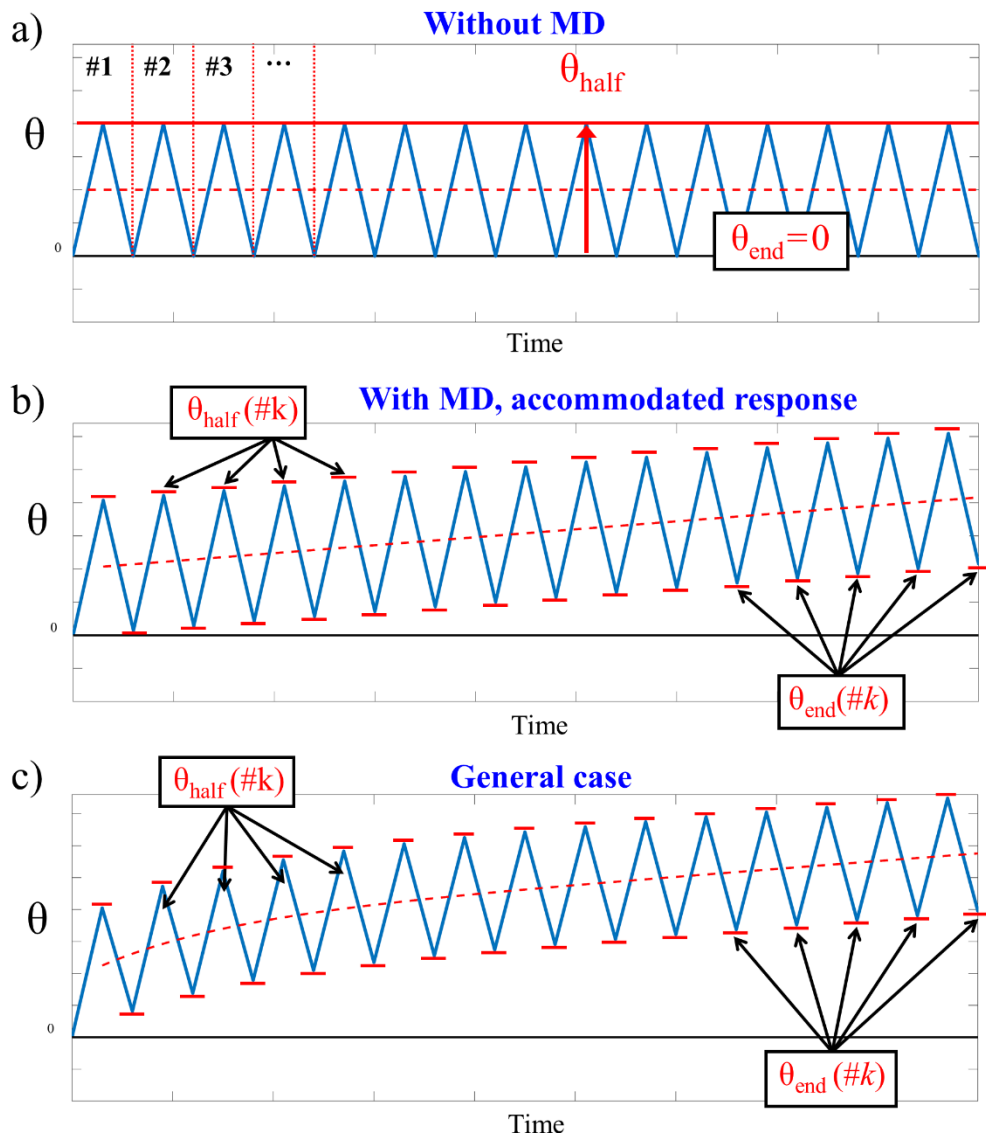


Figure 4.4 Schematic temperature variations reflecting thermoelastic coupling (TEC) and mechanical dissipation (MD) contributions assuming adiabatic conditions.

For the further processing of thermal data in the rest of the study, two parameters are pointed out:

- the temperature change  $\theta_{\text{MD}}(\#k)$  at the end of the  $k^{\text{th}}$  cycle, which is directly related to mechanical dissipation, assuming that the heat absorbed and released due to TEC vanishes over a mechanical cycle. Due to the accumulation of heat

released by irreversible mechanical phenomena,  $\theta_{\text{MD}}(\#k)$  increases along an adiabatic test (“self-heating”);

- the temperature change  $\theta_{\text{half}}(\#k)$  at the middle of the  $k^{\text{th}}$  cycle, when the force level is maximum. The value of  $\theta_{\text{half}}(\#k)$  is due to both TEC and MD.

The following section develops some practical aspects of the image processing and the conversion into calorific quantities associated with TEC and MD.

#### 4.4.2 Extracting calorific data

The basic idea of the subsequent processing is that the heat associated with TEC is null over an entire number of cycles and that the change is adiabatic. From a calorific point of view, the magnitude of the MD can therefore be quantified by the heat density  $Q_{\text{MD}}$  (in  $\text{J/m}^3$ ) over *each cycle* as follows:

$$Q_{\text{MD}}(\#k) = \rho C [\theta_{\text{MD}}(\#k) - \theta_{\text{MD}}(\#k - 1)] \quad (4.1)$$

where  $\rho$  and  $C$  are the density and the specific heat of the material, respectively. By construction, the total heat produced by the material over each adiabatic loading phase is given by:

$$Q_{\text{half}}(\#k) = \rho C [\theta_{\text{half}}(\#k) - \theta_{\text{MD}}(\#k - 1)] \quad (4.2)$$

This quantity implies a contribution from both TEC and MD. We propose to identify that of TEC by the heat density  $Q_{\text{TEC}}$  (in  $\text{J/m}^3$ ) over each *half* a cycle as follows:

$$Q_{\text{TEC}}(\#k) = Q_{\text{half}}(\#k) - \frac{1}{2} Q_{\text{MD}}(\#k) \quad (4.3)$$

By nature, mechanical dissipation is always a positive calorific quantity (whatever the loading “direction”, *i.e.*, loading or unloading). Equation 4.3 assumes implicitly that MD is produced equally during loading and unloading within each cycle, leading to the ratio of  $\frac{1}{2}$  applied to the quantity  $Q_{\text{MD}}(\#k)$ . This hypothesis is strong but remains reasonable as a first approach. Making a distinction between loading and unloading would be a relevant approach to be adopted in the future, in a similar way to the developments

proposed in Ref. [139] which deal with a rubbery (non-granular) material in uniaxial tension.

**Remark 1** — Because of the motion of the particles, it is tricky to deduce maps of  $Q_{\text{half}}(\#k)$  and  $Q_{\text{TEC}}(\#k)$ . Indeed, particle locations are different at the lower and higher force levels. Since the particles slightly deformed, rigid-body movements were considered for the processing in the present study. Coupling IR thermography with measurements of displacement/strain fields by DIC in the visible range is a perspective of the present work to completely overcome this hurdle in a precise manner. The situation is simpler for the MD effect. Indeed, as the granular materials were previously compacted (see Figure 4.3-a), the particles returned to their positions at the end of each cycle, making it easy to obtain maps of  $\theta_{\text{MD}}(\#k)$  and  $Q_{\text{MD}}(\#k)$  by simple image subtraction.

**Remark 2** — TEC is considered as a “strong” coupling in the sense that its magnitude is much higher than that of MD in most cases:  $Q_{\text{MD}} \ll Q_{\text{TEC}}$ . For instance, in the case of fatigue in steels, the ratio is of about three or four orders of magnitude [176]. For rubbers, the trend is the same, but MD may not be negligible due to viscosity or when the strain level increases: see Ref. [139] dealing with uniaxial tensile tests of rubbers. This situation may make the measurement resolution of  $Q_{\text{MD}}(\#k)$  disadvantageous compared to that of  $Q_{\text{TEC}}(\#k)$ . In order to improve the measurement resolution of the heat associated with MD in a steady-state cyclic regime, we decided to calculate also the *mean* value over several cycles, starting from the fifth one (*i.e.*, when the global temperature increases linearly, see the red dashed lines in Figure 4.3-e). This quantity is denoted  $Q_{\text{MD}}(\text{stab})$  in the following.

## 4.5 Application to small granular system

This section presents the results obtained for the “small” granular materials (16 particles in monodisperse configuration for tests T1 to T6; 14 particles in bidisperse configuration for tests T7 and T8) before applying the methodology to a larger system. The first part is dedicated to the analysis of the *thermal* responses ( $\theta$ ), in order to examine different aspects: influence of the loading rate; difference between the monodisperse and bidisperse systems; additional information on the influence of the spatial resolution used



to measure the temperature fields. The analysis of the *calorific* response ( $Q_{\text{TEC}}$  and  $Q_{\text{MD}}$ ) for a given test, namely test T6, is finally presented, before applying our approach to a more realistic granular system with more particles at the end of the paper.

#### 4.5.1 Influence of loading rate

Figure 4.5 shows the influence of the loading rate on the small monodisperse granular system for the same maximum force, equal to 3 kN (tests T1 to T6). The spatial resolution of the thermal maps is equal to 131.6  $\mu\text{m}$ . The following comments can be made concerning these maps:

- Figures 4.3-a to -f show the maps of  $\theta_{\text{half}}$  (see Figure 4.4-b and c) in the middle of the 1<sup>st</sup> cycle for a loading rate of  $\pm 0.5$  kN/s,  $\pm 1$  kN/s,  $\pm 1.5$  kN/s,  $\pm 2$  kN/s,  $\pm 2.5$  kN/s and  $\pm 5$  kN/s respectively. Temperature concentrations are visible at nearly all the contacts, including those with the metallic frame. The presence of these “hot” spots at the contacts can be related to stress concentrations, leading to stronger TEC and MD in these zones. The hot spots are slightly more intense and concentrated when the loading rate increases. This can be explained by an increase in viscosity (MD) and increasingly adiabatic behavior when the period of the cycle decreases (the heat has less and less time to diffuse).
- Figures 4.3-g to -l show the maps of  $\theta_{\text{MD}}$  measured at the end of the 20<sup>th</sup> cycle. MD is visible at specific contacts in the upper part of the granular system, as well as inside two particles at the bottom part (see black arrows). It appears to become stronger as the loading rate increases. At the lowest rate ( $\pm 0.5$  kN/s, see Figure 4.5-g), the field of  $\theta_{\text{MD}}(\#20)$  is nearly homogeneous and null. This is *a priori* the consequence of the heat exchanges with the environment during the 240 seconds required to complete the 20 cycles (non-adiabaticity). Concentrations of  $\theta_{\text{MD}}(\#20)$  identified at higher loading rates (mainly above  $\pm 1.5$  kN/s) at specific contacts can be explained by friction and material viscosity. As small interparticle movements mainly occur at the top of the granular system (see later), friction could *a priori* be the main cause of the MD effect here. However, material self-

heating is also clearly evidenced along the “hot path” through the two particles in contact marked by the black arrows.

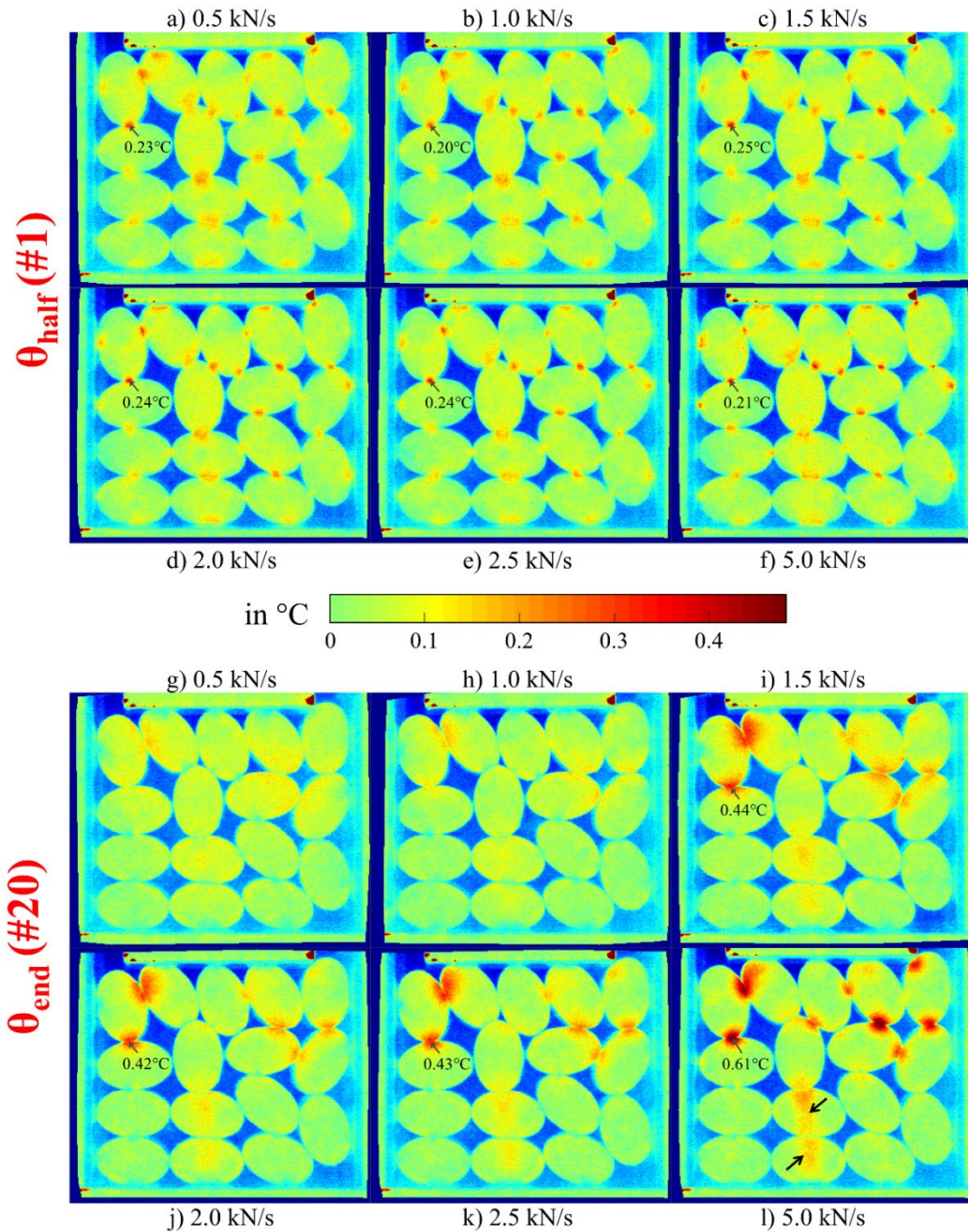


Figure 4.5 Influence of the loading rate (monodisperse configuration, maximum 3 kN, tests T1 to T6).  $\theta_{\text{half}}(\#1)$  and  $\theta_{\text{MD}}(\#20)$  are the temperature changes in the middle of the 1<sup>st</sup> cycle and at the end of the 20<sup>th</sup> cycle, respectively. The spatial resolution of the maps is equal to 131.6  $\mu\text{m}$ .

The orders of magnitude of the maximum values of  $\theta_{\text{half}}(\#1)$  and  $\theta_{\text{MD}}(\#20)$  appear to be similar. However, it must be recalled that the values were measured at the first half cycle and the end of the 20<sup>th</sup> cycle respectively. A “calorific” comparison between the two heat sources (TEC and MD) within one cycle will be presented later.

#### 4.5.2 Comparison between monodisperse and bidisperse systems

Figure 4.6 presents a comparison between a monodisperse configuration (test T6) and a bidisperse configuration (test T8) for the same loading conditions (loading rate =  $\pm 5$  kN/s, maximum force = 3 kN). The spatial resolution of the maps is again equal to 131.6  $\mu\text{m}$ . It is confirmed in the bidisperse case that concentrations of  $\theta_{\text{half}}(\#1)$  exist at each contact, whereas concentrations of  $\theta_{\text{MD}}(\#20)$  are only at some contacts in the upper part of the granular system. The magnitude of  $\theta_{\text{half}}(\#1)$  appears to be greater in the bidisperse case than in the monodisperse one (compare the red zones). Although two tests are not sufficient to draw general conclusions, this observation would seem to be logical, since the void ratio of the granular medium is higher in the bidisperse configuration than in the monodisperse one. Indeed, by construction, monodisperse granular materials are denser than bidisperse ones. Thus, for the same loading level, the stress level is *a priori* higher in the bidisperse configuration than in the monodisperse one. The same comment can be made for the MD effect through the maps of  $\theta_{\text{MD}}(\#20)$ . Although local responses are highly dependent on the location and orientation of particles relative to each other in the granular material, the comparisons here are consistent with previous studies on granular materials, which state that larger particles in polydisperse systems contribute more to strong forces than smaller ones do [3, 177].

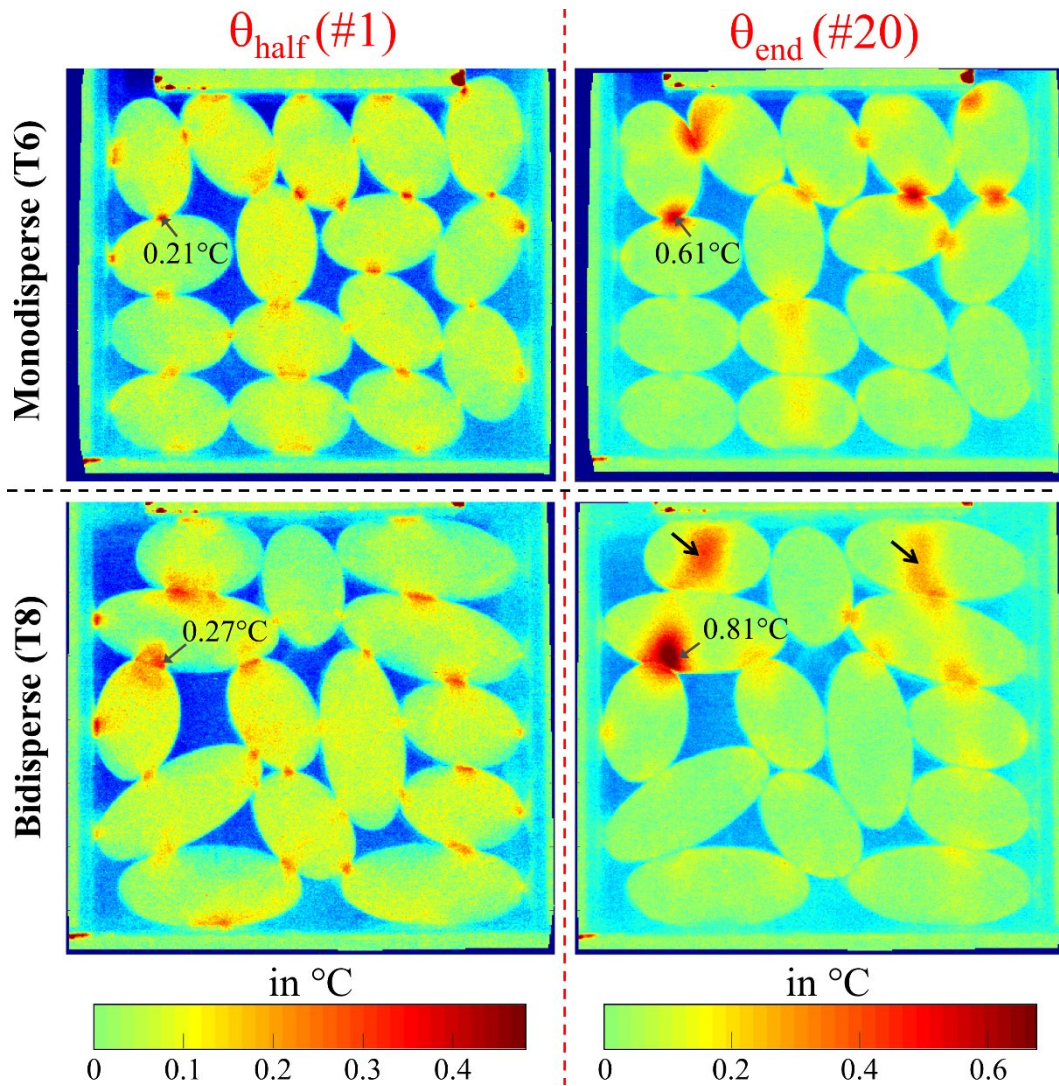


Figure 4.6 Comparison between monodisperse configuration (test T6) and bidisperse configuration (test T8) with same loading conditions (force rate  $\pm 5$  kN/s, maximum 3 kN). The spatial resolution of the thermal maps is equal to  $131.6 \mu\text{m}$ .

### 4.5.3 Improved spatial resolution

Figures 4.5-a and -b show thermal maps for the monodisperse and bidisperse configurations respectively, and for the same loading conditions (loading rate =  $2.5$  kN/s, maximum force =  $3$  kN, tests T5 and T7 respectively), but the spatial resolution is different from that used in the previous figures. The spatial resolutions were equal to  $41.0 \mu\text{m}$  and  $66.3 \mu\text{m}$ , respectively, thus enabling us to zoom in on small zones in the granular



systems. The locations of the enlarged zones Z1 and Z2 are indicated in the schematic views. For zone Z1, a comparison with previous maps at 131.6  $\mu\text{m}$  is also presented in Figure 4.8 by using five color yields. It can be seen that the distributions are globally the same for both maps  $\theta_{\text{half}}(\#1)$  and  $\theta_{\text{MD}}(\#20)$ , whatever the spatial resolution. The same conclusion was obtained for zone Z2 (color yield images not presented here). Some points of interest are indicated in Figure 4.7 for comparison purposes: P5 to P9 in zone Z1; P10 to P13 in zone Z2. It can be seen that the maximum contact temperatures are not exactly located at the boundary between the particles (see in particular P10). In practice, the values of  $\theta_{\text{half}}(\#1)$  and  $\theta_{\text{MD}}(\#20)$  that are reported in Table 4.2 are the maximum ones in the contact zones. It can be seen that certain extracted maximum values significantly depend on the spatial resolution used. The graph in Figure 4.9 shows the variation of the extracted values as a function of the pixel size projected on the measurement surface. It can be seen that, except for the smallest values (no temperature concentration), the better (*i.e.*, the lower) the spatial resolution, the higher the maximum temperature which is measured. This situation is inherent to the use of a full-field measurement technique in the case of localized phenomena. This could be a problem for the estimation of spatial gradients (for estimating heat diffusion). By nature, localizations take place in granular materials, thus making a calorific analysis of this type of material difficult to perform in non-adiabatic conditions. In any case, for a thermomechanical analysis, any comparison between different maps should be made using the same spatial resolution.

Table 4.2 Comparison of results depending on the spatial resolution for the same loading conditions (force rate  $\pm 2.5$  kN/s, maximum 3 kN, minimum 0.3 kN).

Zone	Point	Test T5 for Z1 and test T7 for Z2 (1 px = 131.6 $\mu\text{m}$ )		Same loading conditions with another spatial resolution (41.0 $\mu\text{m}$ for Z1 and 66.3 $\mu\text{m}$ for Z2)	
		$\theta_{\text{half}}(\#1)$ in $^{\circ}\text{C}$	$\theta_{\text{end}}(\#20)$ in $^{\circ}\text{C}$	$\theta_{\text{half}}(\#1)$ in $^{\circ}\text{C}$	$\theta_{\text{end}}(\#20)$ in $^{\circ}\text{C}$
Z1	P5	0.20	0.06	0.29	0.12
	P6	0.27	0.24	0.37	0.32
	P7	0.07	0.16	0.14	0.20
	P8	0.21	0.02	0.21	0.00
	P9	0.18	No contact	0.22	No contact
Z2	P10	0.34	0.67	0.38	0.69
	P11	0.22	0.08	0.23	0.08
	P12	0.18	0.02	0.20	-0.01
	P13	0.21	0.00	0.22	-0.01

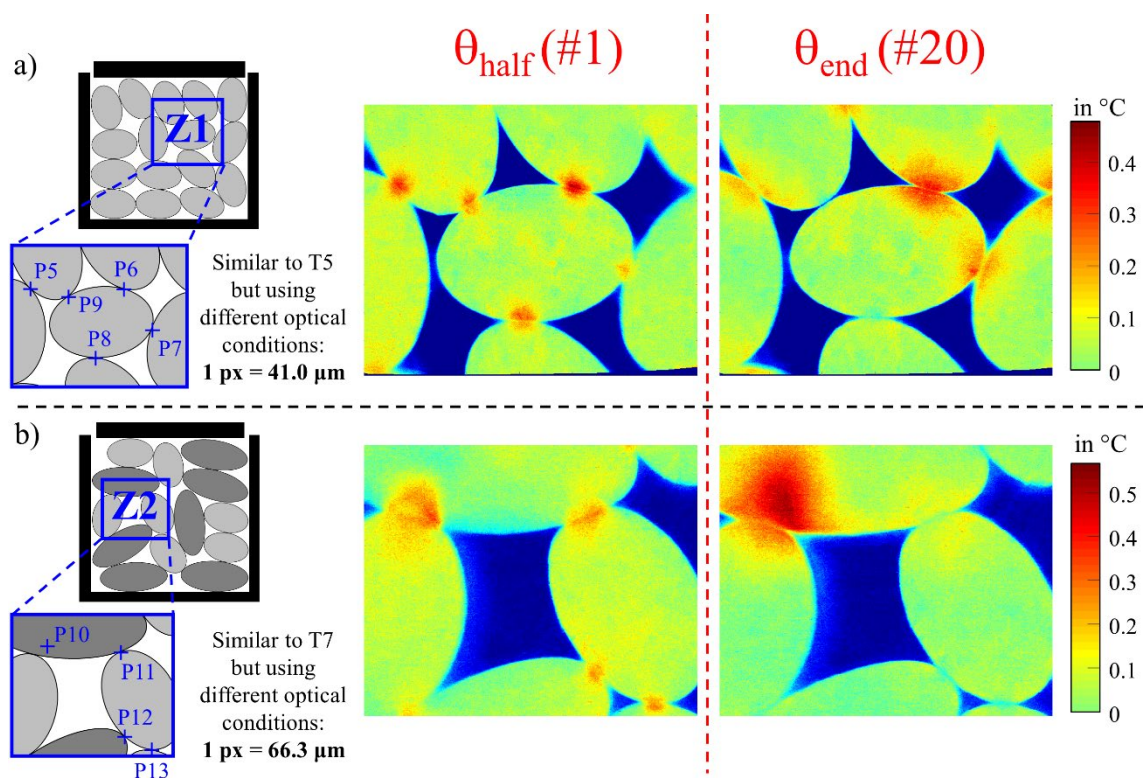


Figure 4.7 Comparison between monodisperse and bidisperse configurations with the same loading conditions (force rate  $\pm 2.5 \text{ kN/s}$ , maximum  $3 \text{ kN}$ ) but using smaller spatial resolution compared to tests T5 and T7, respectively. See Table 4.2 and Figure 4.6 for comparison with measurements at  $131.6 \mu\text{m}$  spatial resolution.

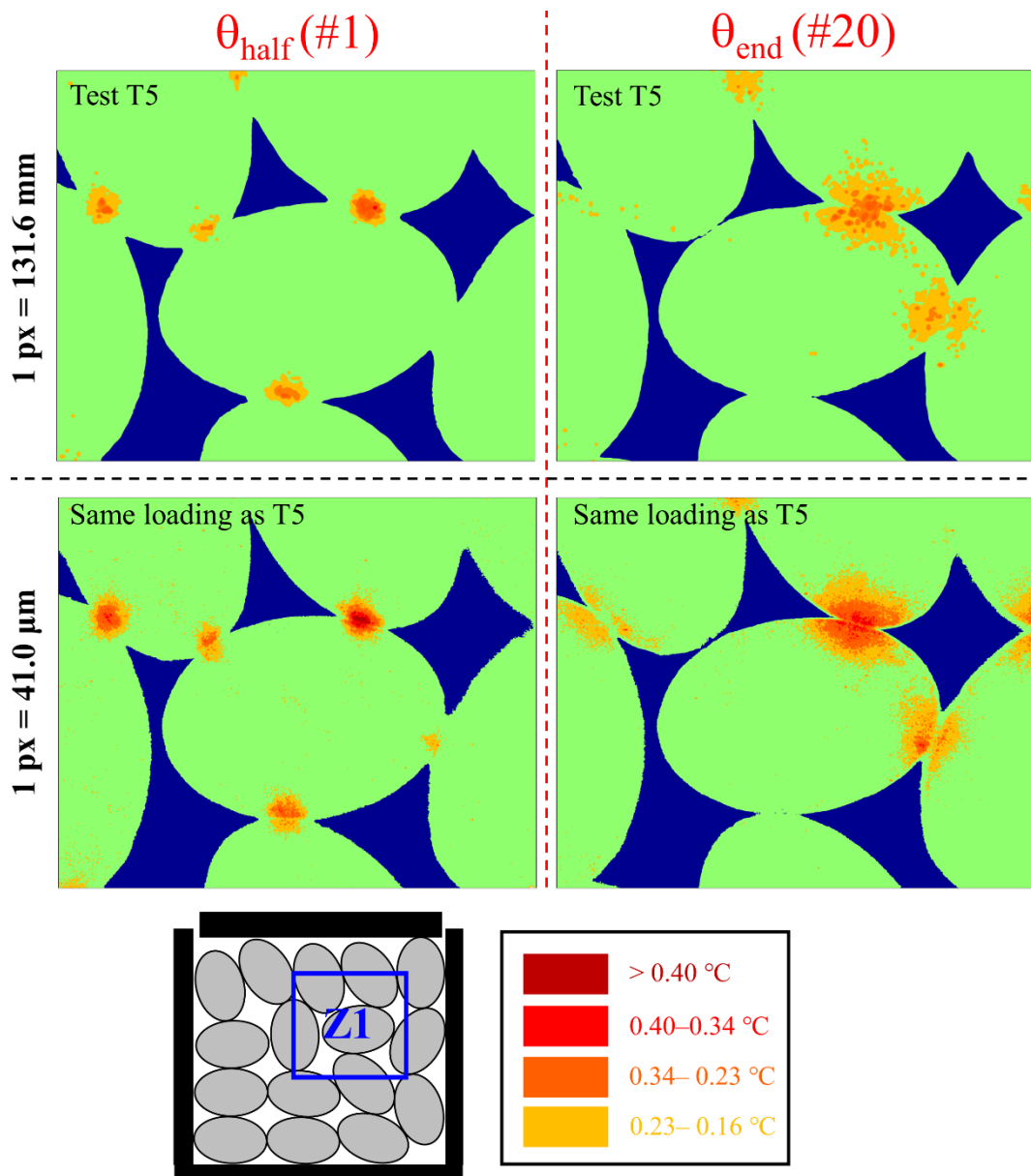


Figure 4.8 Comparison of results depending on the spatial resolution in zone Z1 for two similar tests (monodisperse configuration, force rate  $\pm 2.5$  kN/s, maximum 3 kN, minimum 0.3 kN).



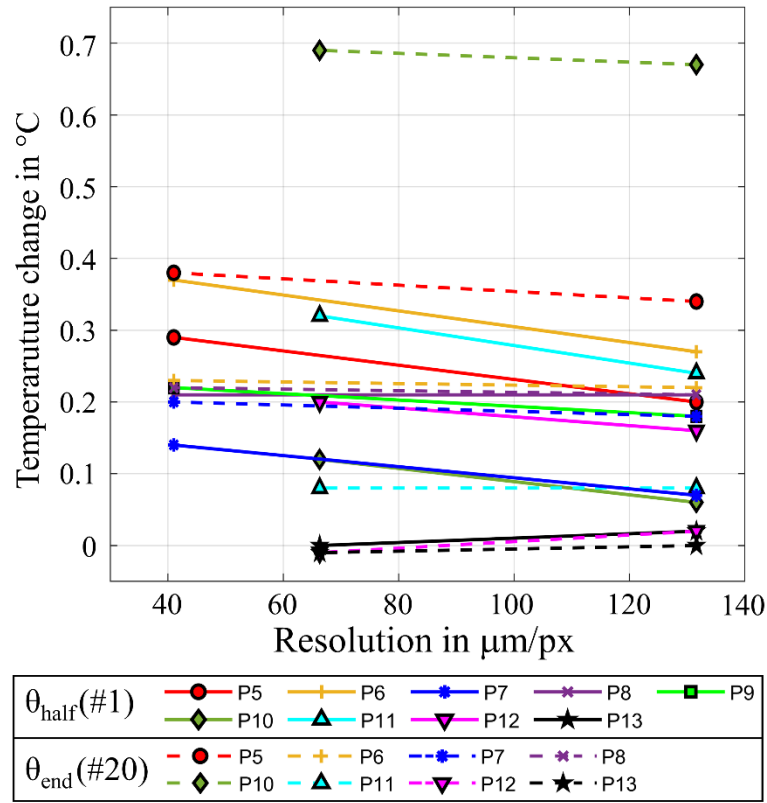


Figure 4.9 Temperature changes at various points in the two small granular systems (see locations in Figure 4.7) as a function of a pixel size projected on the measurement surface, and for the same loading conditions (force rate  $\pm 2.5$  kN/s, maximum 3 kN, minimum 0.3 kN).

#### 4.5.4 Calorific analysis

The objective here is to validate the data processing providing calorific data for one test, namely T6 (monodisperse configuration, force rate  $\pm 5$  kN/s, maximum 3 kN). In particular, it is a question of comparing the heat produced by the mechanical dissipation  $Q_{MD}(\#k)$  at each cycle (see Equation 4.1) and the heat produced by the thermoelastic coupling at each half-cycle  $Q_{TEC}(\#k)$  (see Equation 4.3):

Figure 4.10-a shows the variation in  $Q_{MD}(\#k)$  at four points in the granular system. It can be seen that the values for points P1 and P2 rapidly decrease along the first five cycles. The maximum values measured for the first cycle (more than  $300 \text{ kJ/m}^3$ ) appear to be more than half those of  $Q_{TEC}$  (more than  $600 \text{ kJ/m}^3$ ); compare the map of  $Q_{MD}(\#1)$

in Figure 4.10-b with the map of  $Q_{\text{TEC}}(\#1)$  in Figure 4.11-a. Thus, MD plays an important role in the temperature variations during the first five cycles. This result can be explained by a continuation of material accommodation during the five first cycles, as already discussed from the temperature variations. From the fifth cycle on, the value of  $Q_{\text{MD}}(\#k)$  at the four points seems to fluctuate around zero. However, they are positive on average: see Figure 4.10-b showing the maps of  $Q_{\text{MD}}(\text{stab})$ , which is the average of  $Q_{\text{MD}}(\#k)$  over cycles #5 to #20. Maximum values reach about  $30 \text{ kJ/m}^3$ . These small values for  $Q_{\text{MD}}(\text{stab})$  are also not negligible as they are at the origin of the global temperature increase represented by the dashed lines in Figure 4.3-e. A final remark can be made about the maps of  $Q_{\text{TEC}}(\#k)$ . The value does not really change over the cycles: compare cycle #1 (Figure 4.11-a) and cycle #20 (Figure 4.11-b). This can be explained by a stabilized elastic response due to the preliminary five cycles which compacted the granular material before performing the test. It can also be noted that high values are not only observed in the contact zones. Significant TEC is also revealed inside some particles. Finally, it is confirmed that TEC is a strong coupling in the steady-state cyclic regime. Indeed, the maximum values of  $Q_{\text{TEC}}$  exceed  $600 \text{ kJ/m}^3$ , whereas those of  $Q_{\text{MD}}(\text{stab})$  only exceed  $30 \text{ kJ/m}^3$ .

Various observations were made here on small discrete systems. They show that it is possible to obtain thermal and calorific information based on the proposed methodology. The next section is dedicated to a more realistic granular material case, since it comprises nearly 100 particles, thus enabling us to perform a statistical analysis.

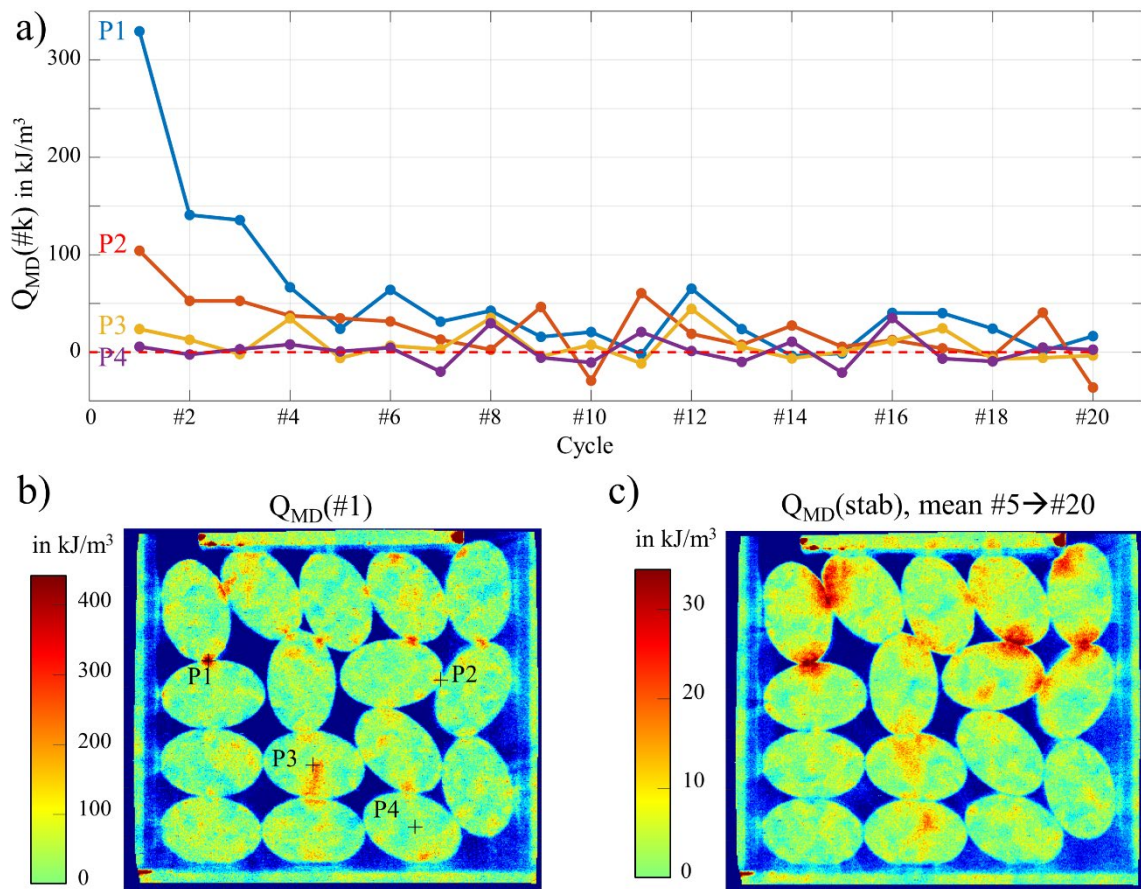


Figure 4.10 Heat produced by mechanical dissipation (MD) during each mechanical cycle during test T6 (monodisperse configuration, force rate  $\pm 5$  kN/s, maximum 3 kN): a) variations along the cycles at four points in the granular system; b) over the first cycle; c) average over the fifth to twentieth cycles. The spatial resolution of the maps is equal to  $131.6 \mu\text{m}$ .

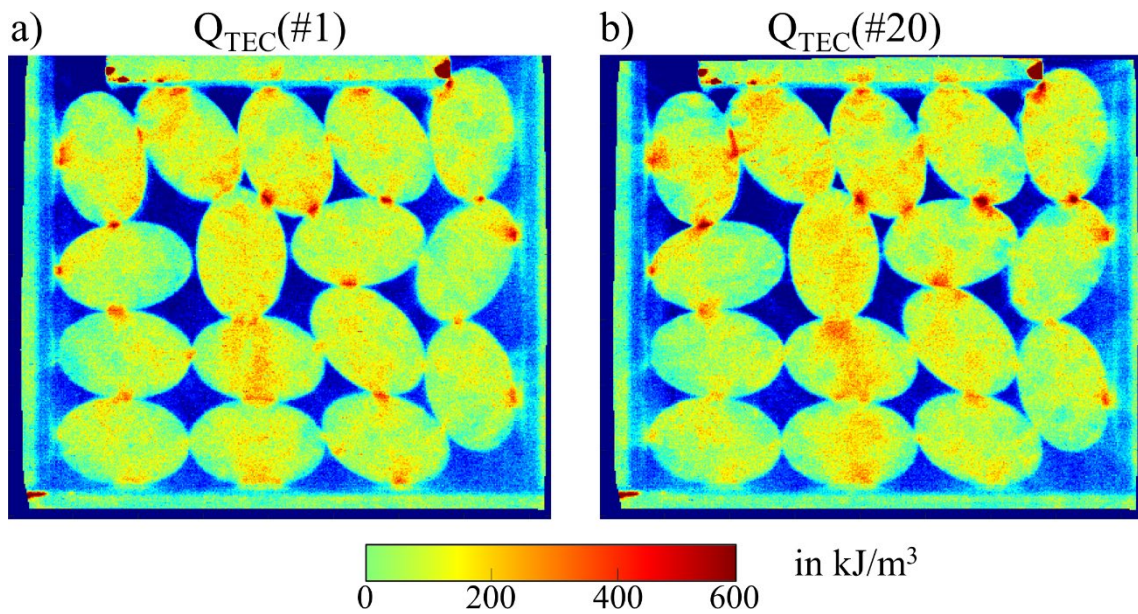


Figure 4.11 Heat produced by thermoelastic coupling (TEC) over the loading phase during test T6 (monodisperse configuration, force rate  $\pm 5$  kN/s, maximum 3 kN): a) in the first cycle; b) in the twentieth cycle. The spatial resolution of the maps is equal to  $131.6 \mu\text{m}$ .

#### 4.6 Thermomechanical behavior of a larger granular system

This section presents an analysis of the thermomechanical response of the “large” tridisperse granular material made with about 30 particles of each type (see Table 4.1). The spatial resolution is now equal to  $496 \mu\text{m}$ . The following three points are successively discussed:

- influence of the force level reached, namely 6 kN, 9 kN and 12 kN (tests T9, T10 and T11 respectively), at the same loading rate  $\pm 1$  kN/s;
- analysis of a potential correlation between calorific response and interparticle movements;
- statistical analysis from the nearly 600 interparticle contacts in the granular system.

#### 4.6.1 Influence of the force level reached

Figure 4.12 shows maps related to the thermoelastic coupling contribution for the three tested loading levels during the first half cycle. Results are first displayed in terms of  $Q_{\text{TEC}}(\#1)$  *heat* density: see the left-hand side of this figure. Logically, the higher the force level reached, the higher the values due to the increased stresses in the granular system. The results are also presented in terms of *mean heat rate* density, corresponding to the value of  $Q_{\text{TEC}}(\#1)$  divided by the duration of half a cycle: see the right-hand side of the figure. It can be observed that these maps now in  $\text{kW/m}^3$  are quite similar for the three loading levels. This result may appear surprising for a material featuring non-linear elasticity such as TPU. It can be explained by an operating loading range in the linear part of the TPU's mechanical response (low deformation of the particles during the test). Hot zones are observed at nearly all the interparticle contacts. It can be noted that the highest values are located at the upper left and right corners of the granular system. The lowest and least diffuse concentrations are in the bottom left- and right-hand zones of the granular system (see dashed triangular zones). This observation is quite similar to a previous result obtained on another type of granular material, namely a monodisperse system made of rigid particles, see Figure 4.8 in Ref [21]. This phenomenon is *a priori* related to the boundary conditions. The number of particles is probably not sufficient to limit these boundary effects.



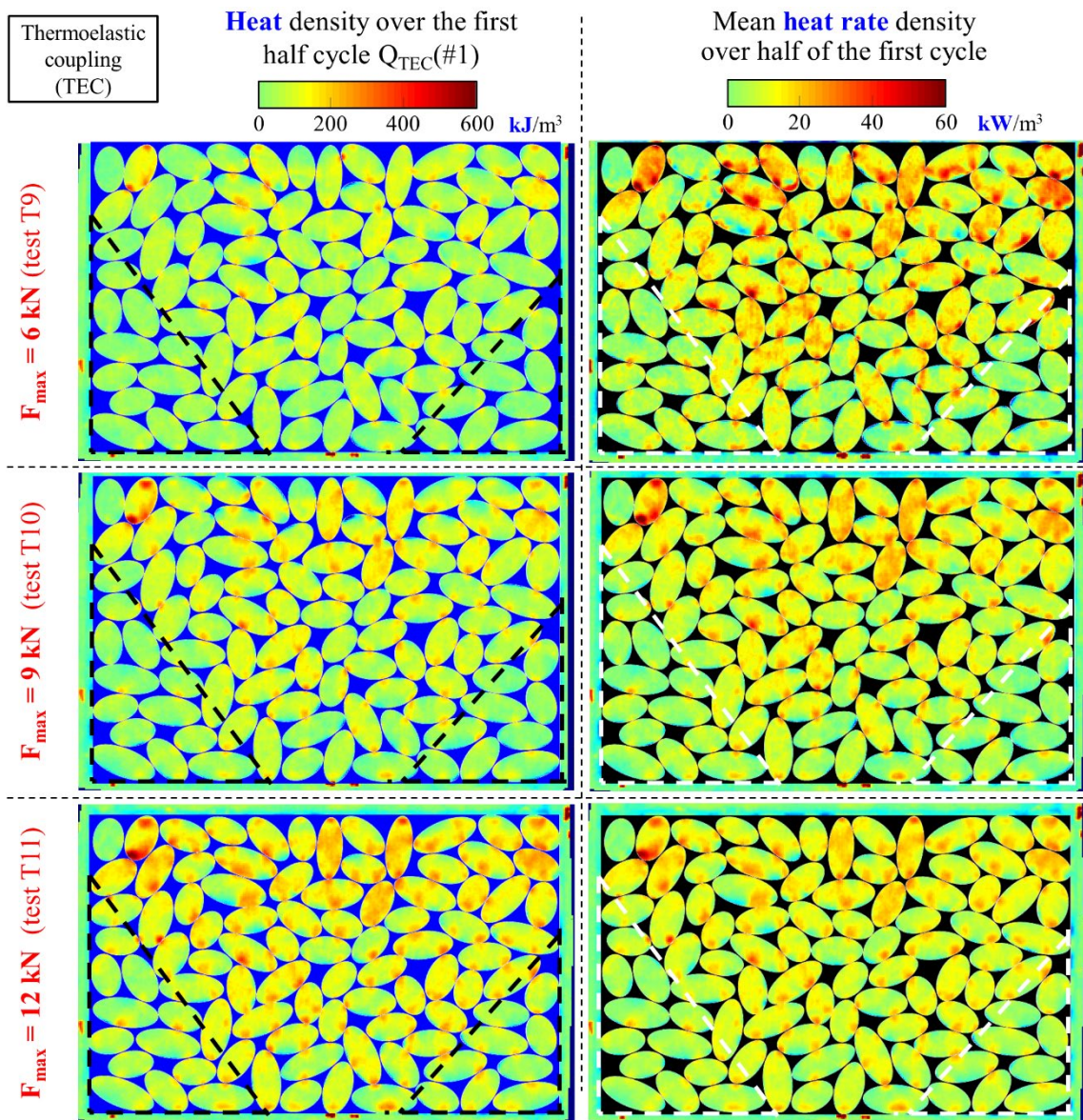


Figure 4.12 Thermoelastic coupling in the tridisperse granular material during the first half cycle. Left column: heat density over half a cycle; right column: corresponding mean heat rate density.

Figure 4.13 shows maps related to the mechanical dissipation contribution for the three loading levels that were tested. The results are displayed in terms of heat density over the first cycle  $Q_{MD}(\#1)$ . Note that the adiabaticity of the tests is questionable due to the long duration of the mechanical cycles (12 s, 18 s and 24 s for tests T9, T10 and T11 respectively, see Table 4.1). Moreover, maps of  $Q_{MD}(\text{stab})$  cannot be calculated due to the number of mechanical cycles, limited to 5. In any case, some results can be extracted.

As expected, the higher the force level, the higher the anelasticity level. The highest values are located at the upper left and right corners of the granular system. On the one hand, this is logical because high stress levels (revealed by strong TEC in Figure 4.12) are expected to be also *a priori* associated with high mechanical irreversibility levels (strong MD). On the other hand, tangential interparticle forces may create high friction without necessarily creating high stress concentrations, which may partially explain the difference between the TEC and MD responses. The next section aims to propose a potential correlation between calorific response and interparticle movements.

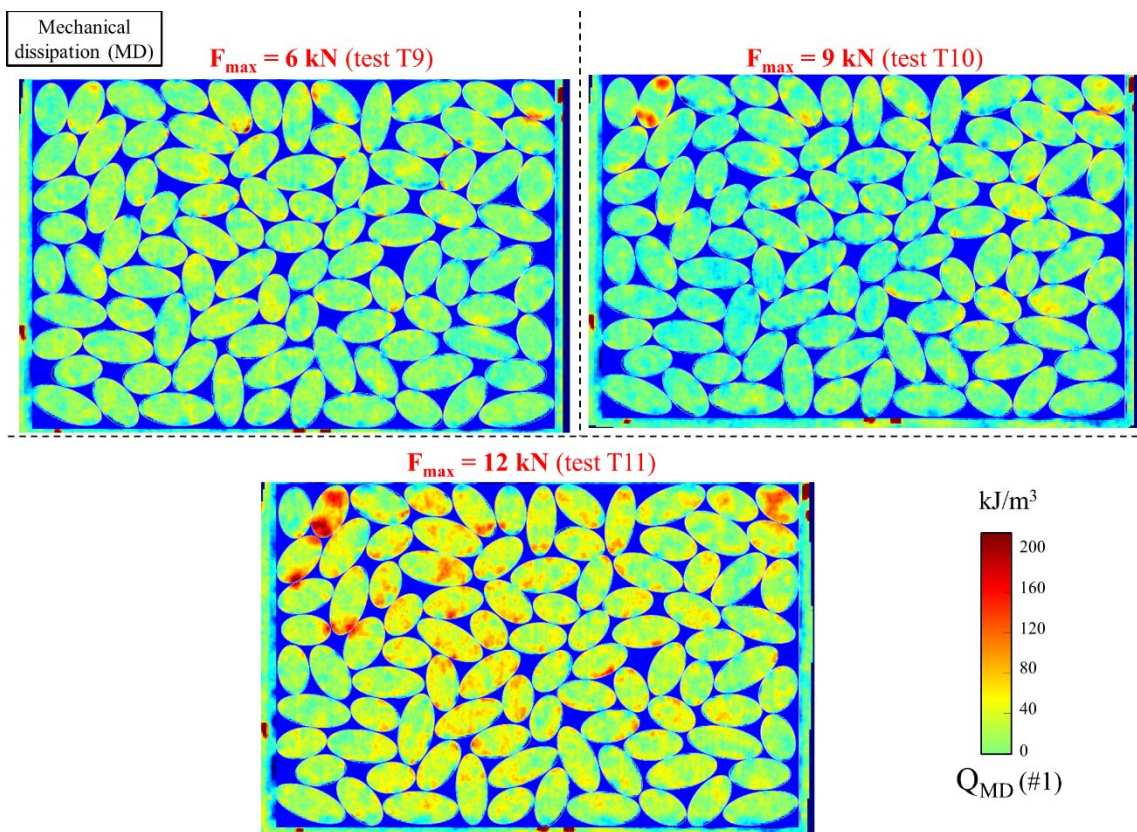


Figure 4.13 Mechanical dissipation in the tridisperse granular material: heat density over the first cycle.

## 4.6.2 Interparticle movements and calorific responses

For illustration purposes, the interparticle movements in the tridisperse granular system for the maximum force 12 kN (test T11) are shown in Figure 4.14-a, distinguishing between translation and rotation. It was necessary to measure these latter quantities in order to subsequently calculate relative movement at all the contacts, described in next section. The objective is then to compare kinematic quantities (whose calculation involves these translations and rotations) with calorific quantities (whose calculation involves temperature changes). The coordinates of the interparticle contacts and ellipse centers, as well as the orientation of the ellipses, were extracted at the minimum and maximum loads by hand, which is feasible for less than 100 particles. The translation field is displayed by arrows whose length is proportional to the magnitude of the translation of the particle center. As expected, the magnitude decreases from the pusher to the bottom of the fixed frame. In the lower part of the granular system, the directions are globally symmetrical with respect to the vertical median plane. The rigid-body rotation field is displayed by colors. It can be observed that the angles are mainly positive (trigonometric sense). Negative values are only observed in the upper part, especially near the top left corner. More importantly, interparticle motions deserve to be analyzed, as they are directly related to potential thermomechanical effects. This was performed via two interparticle movement indicators: *interpenetration* and *sliding*: see Figure 4.14-b. The calculation of these two parameters requires the knowledge of the normal and tangential directions at each contact: see the small white and red lines, respectively, in Figure 4.14-c. Their identification was performed by manually extracting geometric data directly from the thermal maps: inclination and location of the center of each ellipsoidal particle; location of each contact. In addition, the procedure was performed for both sides of each contact, which justifies the pair of normal forces (small white lines) and the pair of tangents (small red lines) displayed at each contact in the image. Slight differences are sometimes observed between the two sides, due to the difficulty in manually extracting geometric information with the low spatial resolution of an IR camera (compared to visible range cameras). An averaging operation was therefore performed between the two sides of each contact to determine one single normal direction



and one single tangential direction each time. From the translation and rotation data, it is then possible to calculate the interpenetration (*Int*) and the sliding (*Sld*) at each contact. The complete mathematical procedure used to calculate the interpenetration and the sliding are described in Appendix B.

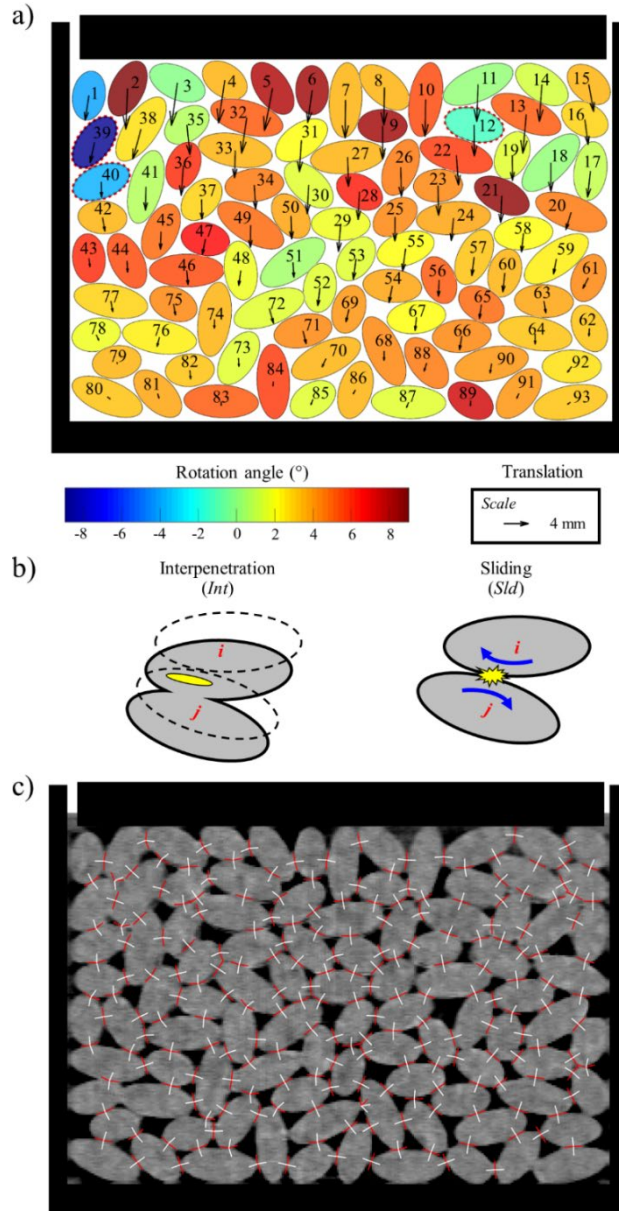


Figure 4.14 Movement of the particles: a) example for test T11; b) illustration of interparticle movement indicators; c) identification of normal (small white lines) and tangential (small red lines) directions at each contact.

Figure 4.15 shows the distributions of  $Int$  and  $Int \times Sld$ , whose values have been normalized by dividing them by their respective maximum values. The distributions are presented through a matrix whose row  $i$  and column  $j$  correspond the numbers of the particles in contact (see these numbers in the schematic view in the upper right corner of the figure). The objective is to compare them with the values of  $Q_{half}(\#1)$  and  $Q_{MD}(\#1)$  respectively, at the contacts. Indeed, it is expected that the higher the interpenetration, the greater the heat produced by the material  $Q_{half}(\#1)$ , which involves both TEC and MD contributions. It is also expected that MD at the contacts is strongly related to friction, which is here “mechanically” expressed by the product  $Int \times Sld$ . Indeed, the contact normal force is proportional to the interpenetration  $Int$  in the case of a contact between two elastic cylinders (see equation 5.34 in Page 63 in Ref. [178]). Moreover, the curvature radii do not appear at all in the relationship between force and interpenetration [178]. Assuming also that the tangential force is proportional to the normal force during sliding (Coulomb’s law), the product  $Int \times Sld$  is therefore representative of the mechanical work associated with friction. The calorific indicators  $Q_{half}(\#1)$  and  $Q_{MD}(\#1)$ , were manually extracted at all couples of particles  $i$  and  $j$  in contact. It is worth noting that, due to the large spatial resolution (496  $\mu\text{m}$ ) compared to the measurements in the small granular materials in the previous sections, the extracted values are actually strongly averaged. Normalization of  $Q_{half}(\#1)$  and  $Q_{MD}(\#1)$  by their maximum values over all the contacts was also performed. It is certainly illusory to try to find a precise correlation between these mechanical ( $Int$  and  $Int \times Sld$ ) and calorific ( $Q_{half}(\#1)$  and  $Q_{MD}(\#1)$ ) indicators. However, some agreements can be found at certain contacts: see for example the two insets in Figure. 4.13. The higher values are fairly well correlated: see black squares at contacts 48/49 and 51/52 for the comparison between  $Int$  and  $Q_{half}(\#1)$ , and at contacts 41/42 and 41/45 for the comparison between  $Int \times Sld$  and  $Q_{MD}(\#1)$ . Various approaches can be proposed to improve results in the future, such as defining other mechanical indicators and using measurements of displacement/strain fields by DIC in the visible range. Nevertheless, a statistical analysis is presented in the next section concerning the TEC interparticle data. The analysis is not pursued for the MD interparticle data because most of them are low and affected by noise (the highest values are mainly located in the upper left and right corners of the granular material). Higher

loading rates and averaging over multiple steady-state cycles could result in a better signal-to-noise ratio for the MD response in the future.

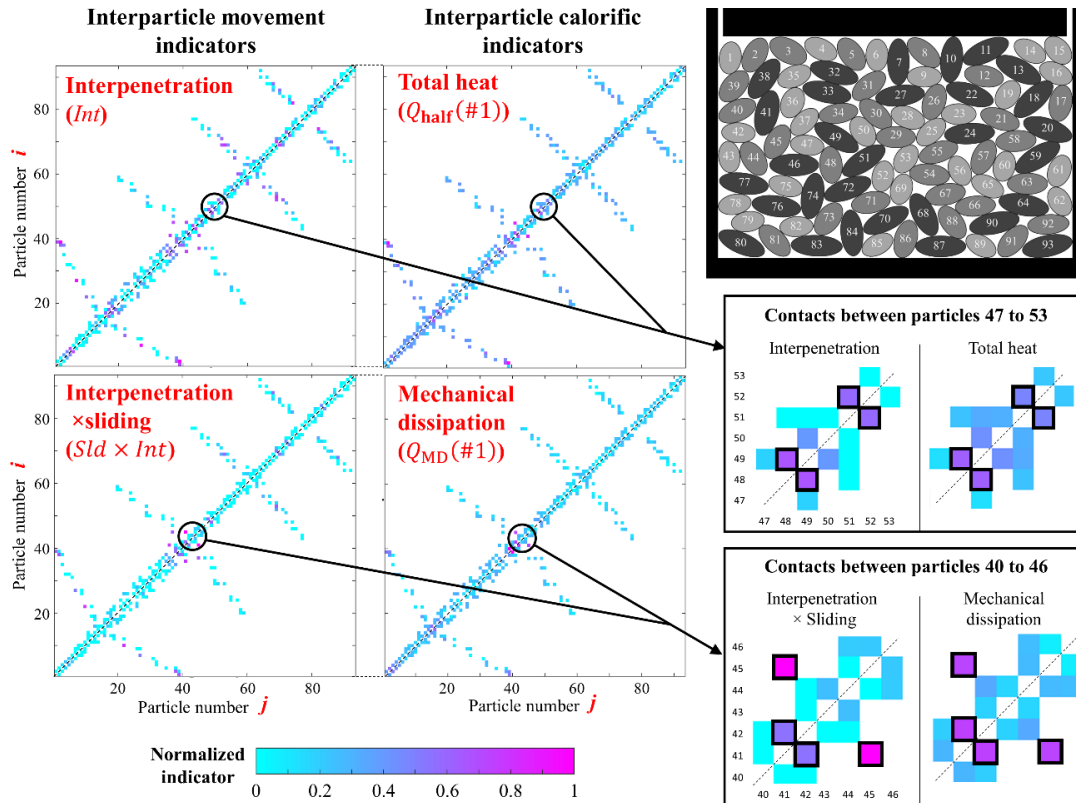


Figure 4.15 Comparison between interparticle movement indicators and contact calorific indicators for test T11.

### 4.6.3 Statistical analysis of the thermoelastic coupling signature at the interparticle contacts

Figure 4.16-a shows the distribution of the calorific signatures  $Q_{TEC}(\#1)$  associated with TEC at the interparticle contacts in the tridisperse system for the maximum force, 12 kN. The mean value is also indicated (see vertical dashed line), as well as the corresponding probability density function (PDF) that was fitted using a generalized extreme value distribution. This type of function was chosen due to the asymmetric distribution between low and high values. The comparison between the three force levels tested (6 kN, 9 kN and 12 kN) is presented in Fig. 4.16-b. Logically, an increase in the average value is observed with the maximum force level. The PDFs are indeed shifted to

the right in the graph and are wider when the maximum force increases. These results are quite logical but show that IR thermography and subsequent calorific analysis provide interesting/complementary data for the analysis of the thermomechanical behavior of granular materials, as discussed in the conclusion section.

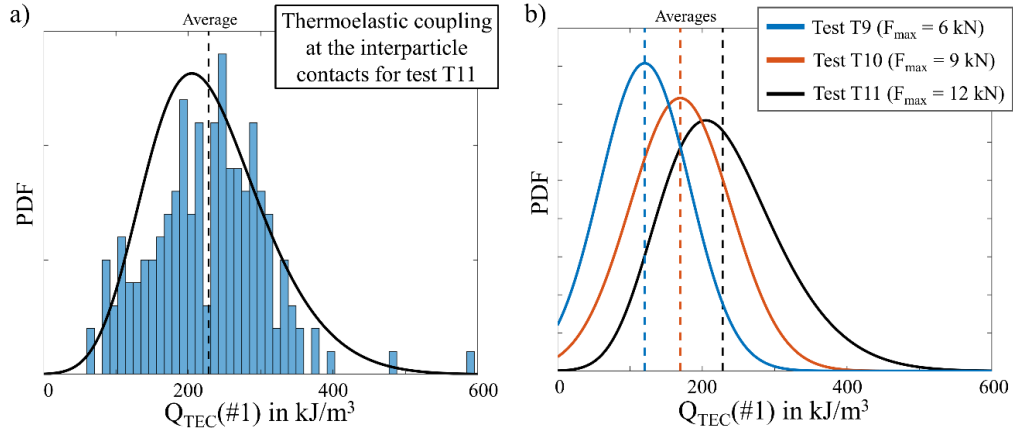


Figure 4.16 Calorific signature associated with thermoelastic coupling at the interparticle contacts in the tridisperse system: a) example of histogram and corresponding probability density function (PDF) using a generalized extreme value distribution; b) comparison of the PDFs for the three loading levels.

## 4.7 Conclusion

For several decades, the analysis of the mechanical behavior of continuous solids has benefited from full-field measurement techniques relying on infrared thermography and subsequent calorimetry processing. Indeed, the experimental evidence of the local couplings between mechanical and thermal responses has enabled a real analysis of heterogeneous phenomena in continuous materials within a rigorous thermodynamic framework. Until now, granular materials have been virtually excluded from this approach in the experimental mechanics community. We believe that such an experimental procedure can also provide information of interest for the understanding of the mechanical behavior of granular materials, which is potentially complementary to full-field strain measurements and numerical methods.

In the present study, soft granular systems composed of elastomeric particles were selected to take advantage of the thermoelastic coupling (TEC) associated with entropic elasticity. Centimeter-sized cylinders with ellipsoidal cross sections were elaborated to form the particles. The thermal response of monodisperse, bidisperse and tridisperse systems was measured by infrared camera under confined cyclic compression. A temperature oscillation featuring the same frequency as that of the load was observed. During the compression phases, hot spots were identified at all interparticle contacts. This was explained by the entropic TEC activated by stress concentrations at the contacts, with a potential contribution of mechanical dissipation (MD) associated with irreversible phenomena such as viscosity and friction. The importance of the spatial resolution used for the thermal measurements was highlighted. Local temperature changes of up to nearly 0.5 °C were measured with a spatial resolution of about 0.1 mm. The temperature change value is halved for a spatial resolution of about 1 mm. Self-heating over the cycles was also observed around specific contacts, as well as inside some particles. This is caused by MD, considering that the heat associated with TEC vanishes over a mechanical cycle. Self-heating rates up to about 0.01 °C/ cycle were measured in the steady-state regime. A greater contribution of MD was observed during the first cycles. A comparison between monodisperse and bidisperse systems at the same macroscopic loading level showed a stronger thermal response in the former case, in agreement with the expected differences in the intensity of interparticle contact forces. Calorimetric treatment allowed us to calculate the corresponding heat values. It was estimated that the intensity of the heat generated by entropic TEC could reach more than 600 kJ/m<sup>3</sup> in the contact zones during the compression phases, while that associated with MD was limited to about 30 kJ/m<sup>3</sup>/cycle in the steady-state regime (and about 300 kJ/m<sup>3</sup>/cycle in the transient regime). This shows that TEC is a strong coupling. TEC data were processed for a tridisperse system consisting of about 600 interparticle contacts. Statistical information on the TEC heat distribution at the interparticle contacts shows a change in the distributions with the level of compression that is applied. This paves the way for thermomechanical models based on such calorimetric data. This study was published in the *Experimental Mechanics* journal [179].

## CHAPTER 5

### Conclusion and Perspectives

Granular materials are collections of solid particles of various shapes, materials and sizes, making their mechanical behavior complex. In the past, effective understanding was mainly derived from experiments, which were limited by the equipment available at the time. Numerical approaches based on the Discrete Element Method were then developed. These are powerful, reliable and widely used as efficient tools for studying granular media. In comparison, experimentation was not as widespread due to difficulties of preparation and instrumentation. In recent decades, non-contact full-field measurement techniques based on cameras have become increasingly familiar and attractive in the experimental mechanics community. This is due to rapid advances in equipment and image processing techniques. Some of these were used to study two-dimensional (2D) granular media under mechanical loading: particle image velocimetry (PIV) to measure strain patterns; digital image correlation (DIC) to measure strains within deformable particles; photoelasticimetry to measure shear stresses in particles made of birefringent material; and thermoelastic stress analysis (TSA) based on infrared thermography (IRT) to measure hydrostatic stresses in particles. Some of these techniques enabled identifying the interparticle forces using appropriate image processing. However, there are certain limitations due to the specifications of each technique. Besides, soft granular materials have rarely been studied with these techniques. In this context, the aim of this thesis was to develop other full-field techniques for two purposes: 1) to identify contact forces using the virtual fields method (VFM) from knowledge of the strain distribution obtained by localized spectrum analysis (LSA); 2) to identify thermomechanical couplings in soft particles using IRT.

A contact force identification strategy using VFM was defined in this work relying on measurements of the strain fields on the particle surfaces. The approach was 2D as the granular systems under study were made of cylinders stacked in parallel. Synthetic strain data provided by a finite element model were first used as input data for the identification procedure. It was shown that kinematically admissible (KA) virtual displacement fields can be advantageously defined (with respect to limitation of the effect of noise in the real strain fields) using a triangulation-based natural interpolation between the contact points. Various simulations illustrated the impact of the choice of the virtual fields and the robustness of the identification technique, namely the influence of magnitude of noise, shift between the virtual and real strain fields, and missing data along particle boundaries. Various multi-contact systems were considered for this study. An experiment was then performed on a system made of three particles in PA66 under confined compression relying on strain distributions obtained by LSA. It was shown that the contact forces obtained by VFM failed to verify Newton's third law of motion. This can be due to out-of-plane movements or errors in elastic parameters of the particle material. Alternative force identification strategies were then proposed by considering equilibrium equation of each particle and Newton's third law of motion at each interparticle contact. The identification results were compared to determine which best handled the set of equations for contact force identification. The best strategy was obtained when using VFM equations with Lagrange multipliers to enforce equilibrium and Newton's third law of motion. This strategy was subsequently employed on three experimental multi-contact granular media. Using monodisperse, bidisperse and tridisperse systems composed of 108, 85 and 80 cylinders in PA66, respectively, it was shown that statistical results were consistent with those of numerical and experimental studies performed in the past. Some difficulties of preparation and implementation were described. However, it can be noted that the proposed contact force identification is applicable in theory to any type of materials if the constitutive equation is known. Note also that the procedure enables to completely identify all the contact forces in a 2D granular system: normal forces and tangential forces are simultaneously identified directly from the strain fields measured on the surface of each particle. Molecular Dynamics simulations were then performed to validate the experimental results in terms of contact force networks, angular force

distributions and probability density functions (PDFs) of the normal forces. It was concluded that the experimental procedure based on VFM and LSA is operational for statistical analysis of actual granular systems. This experimental approach can be employed for further work:

- performing experiments on bigger granular systems (with many more contacts) to improve the accuracy of the statistical results;
- performing experiments on granular systems composed of particles with more complex shape, e.g. non-convex;
- identifying contact forces in soft granular systems, e.g. using rubber-like materials for the particles. The constitutive model of material employed in the VFM should be modified. The large deformations will be also an issue to extract the strain fields using LSA. Large out-of-plane movements could be also a problem. The measurement techniques should be appropriately adapted for these issues.

Next, thermomechanical couplings were identified in soft granular systems using IRT. Particles were made in a rubber-like material, namely TPU, in order to benefit from the strong thermoelastic coupling (TEC) associated with entropic elasticity and a low thermal conductivity. The thermal response of monodisperse, bidisperse and tridisperse systems was measured under confined cyclic compression. A temperature oscillation at the same frequency as the loading was observed. Hot spots were discovered at all interparticle contacts during the compression phases. This was explained by the entropic TEC activated by stress concentrations at the contacts, with a potential contribution of mechanical dissipation (MD) associated with irreversible phenomena such as viscosity and friction. Self-heating over the cycles was also observed around specific contacts, as well as inside some particles. This is caused by MD, while the heat associated with TEC vanishes over a mechanical cycle. The comparison between the monodisperse and bidisperse systems showed a stronger thermal response in the former case, in agreement with the expected differences in the intensity of interparticle contact forces. Calorimetric treatment allowed us to calculate the corresponding heat values. It was estimated that the intensity of the heat generated by entropic TEC could reach more than  $600 \text{ kJ/m}^3$  in the contact zones during the compression phases, while that associated with MD was limited



to about 30 kJ/m<sup>3</sup>/cycle in the steady-state regime (and about 300 kJ/m<sup>3</sup>/cycle in the transient regime). This shows that TEC is a strong coupling. TEC data were processed for a tridisperse system consisting of about 600 interparticle contacts. Statistical information on the TEC heat distribution at the interparticle contacts shows a change in the distributions with the level of compression that is applied. Several extensions of this work can be proposed:

- increasing the number of particles; the objective would be to provide statistical calorific data on both reversible and irreversible mechanical phenomena excluding boundary effects;
- coupling IRT with visible-range measurements to measure the strain fields at the same time as the temperature maps; this should enable us to calculate energy balance;
- increasing the complexity of the shapes of the cylinder cross-sections, including for example sharp edges and non-convex geometries;
- modeling and simulating the thermomechanical experiments; this would require a coupling of discrete and finite element methods. The comparison between numerical and experimental methods for soft granular media is a further step of our work;
- proposing a macroscopic thermodynamical model; this approach would require appropriate averaging operations to obtain calorimetric data (TEC, MD) to be related to mean mechanical variables (fabric stress and/or strain). This could lead to the proposition of macroscopic/mesosopic stress measurement techniques by using only temperature data;
- applying the proposed approach to sand; the design of the experimental device would however be an issue. Indeed, the box containing the sand should simultaneously sustain the stress induced by the load and be infrared transparent, so that the IR camera could observe and capture the temperature field over one of the walls during the tests. The application of the proposed thermodynamical methodology to sand would therefore require significant implementation efforts.

## References

- [1] Y. Forterre and O. Pouliquen, *Flows of dense granular media*, in *Annual Review of Fluid Mechanics*. 2008, Annual Reviews. p. 1-24.
- [2] B. Andreotti, Y. Forterre, and O. Pouliquen, *Granular media: between fluid and solid*. 2013: Cambridge University Press.
- [3] F. Radjaï, et al., *Force distributions in dense two-dimensional granular systems*. *Physical Review Letters*, 1996. 77(2): p. 274-277.
- [4] T.S. Majmudar and R.P. Behringer, *Contact force measurements and stress-induced anisotropy in granular materials*. *Nature*, 2005. 435: p. 1079-1082.
- [5] D.M. Mueth, H.M. Jaeger, and S.R. Nagel, *Force distribution in a granular medium*. *Physical Review E*, 1998. 57(3): p. 3164-3169.
- [6] X.Z. Jiang and Y.M. Shu, *Probabilistic analysis of random contact force between geomembrane and granular material*. *Journal of Central South University*, 2014. 21(8): p. 3309-3315.
- [7] G. Løvoll, K.J. Måløy, and E.G. Flekkøy, *Force measurements on static granular materials*. *Physical Review E*, 1999. 60(5): p. 5872-5878.
- [8] F. Radjaï, S. Roux, and J.J. Moreau, *Contact forces in a granular packing*. *Chaos*, 1999. 9(3): p. 544-550.
- [9] M. Cardenas-Barrantes, et al., *Micromechanical description of the compaction of soft pentagon assemblies*. *physical Review E*, 2021. 103(6).
- [10] C. Voivret, et al., *Multiscale force networks in highly polydisperse granular media*. *Physical Review Letters*, 2009. 102.
- [11] F. Radjaï, et al., *Bimodal character of stress transmission in granular packings*. *Physical Review Letters*, 1998. 80(1): p. 61-64.
- [12] A. Chrysochoos, et al., *Use of Full-Field Digital Image Correlation and Infrared Thermography Measurements for the Thermomechanical Analysis of Material Behaviour*. *Strain*, 2010. 46(1): p. 117-130.
- [13] C.-A. Bunge, M. Beckers, and T. Gries, *Polymer Optical Fibres: Fibre Types, Materials, Fabrication, Characterisation and Applications*. 2017: Woodhead Publishing.
- [14] M. Grédiac and F. Pierron, *The Virtual Fields Method: Extracting Constitutive Mechanical Parameters from Full-field Deformation Measurements*. 1st ed. 2012, New York: Springer.
- [15] C. Słomiński, M. Niedostatkiewicz, and J. Tejchman, *Application of particle image velocimetry (PIV) for deformation measurement during granular silo flow*. *Powder Technology*, 2007. 173: p. 1-18.

- [16] H.M. Frtiz, F. Mohammed, and J. Yoo, *Lituya bay landslide impact generated mega-tsunami 50th anniversary*. Pure and Applied Geophysics, 2009. 166(1-2): p. 153-175.
- [17] L.T. Sheng, S.S. Hsiau, and N.W. Hsu, *Experimental study of the dynamic behavior and segregation of density-bidisperse granular sliding masses at the laboratory scale*. Landslides, 2021. 18(6): p. 2095-2110.
- [18] M. Tolomeo, et al., *Assessing contact forces in granular materials from experimental measurements of kinematics*. EPJ Web of Conferences, 2017. 140.
- [19] C. Fanxiu, Q. Zhuang, and H. Zhang, *Mechanical analysis and force chain determination in granular materials using digital image correlation*. Applied Optics, 2016. 55(18): p. 4776-4783.
- [20] M.P. Luong, *Introducing infrared thermography in soil dynamics*. Infrared Physics and Technology, 2007. 49: p. 306-311.
- [21] C. Chaiamarit, et al., *Stress network analysis of 2D non-cohesive polydisperse granular materials using infrared thermography*. Experimental Mechanics, 2015. 55(4): p. 761-769.
- [22] P. Jongchansitto, et al., *Thermoelastic couplings and interparticle friction evidenced by infrared thermography in granular materials*. Experimental Mechanics, 2018. 58(1469-1478).
- [23] H.M. Jaeger and S.R. Nagel, *Granular solids, liquids, and gases*. Reviews of Modern Physics, 1996. 68(4): p. 1259-1272.
- [24] A. Casagrande and N. Carillo, *Shear failure of anisotropic materials*. Journal of Boston Society of Civil Engineers, 1944. 31: p. 122-135.
- [25] P. Dantu. *Contribution à l'étude mécanique et géométrique des milieux pulvérulents*. In. *the 4th International Conference on Soil Mechanics and Foundation Engineering*, 1957: Butterworths Scientific Publications, p. 144-148
- [26] J. Biarez and K. Wiendieck, *La comparaison qualitative entre l'anisotropie mécanique et l'anisotropie de structure*. Comptes Rendus de l'Académie des Sciences, 1963. 254: p. 2712-2714.
- [27] P.W. Rowe, *The stress-dilatancy relation for static equilibrium of an assembly of particles in contact*. Proceedings of the Royal Society of London A, 1962. 269: p. 500-527.
- [28] J. Weber, *Recherches concernant les contraintes intergranulaires dans les milieux pulvérulents*. Bulletin de Liaison des Ponts-et-Chaussées, 1966. 20: p. 1-20.
- [29] J. Kakalios, *Resource Letter GP-1: Granular physics or nonlinear dynamics in a sandbox*. American Journal of Physics, 2005. 73: p. 8-22.
- [30] R.T. Fowler and W.B. Chodziesner, *The influence of variables upon the angle of friction of granular materials*. Chemical Engineering Science, 1959. 10(3): p. 157-162.

- [31] K. Hutter and K. T., *Motion of a granular avalanche in an exponentially curved chute: experiments and theoretical predictions*. Physical and Engineering Sciences, 1991. 334(1633): p. 93-138.
- [32] P. Evesque, *Analysis of Processes Governing Sandpile Avalanches Using Triaxial Test Results and "Critical State" of Soil Mechanics*. Europhysics Letters, 1991. 14(5): p. 427-432.
- [33] P.A. Cundall. *A computer model for simulating progressive large scale movements in blocky rock systems*. In. *the International Symposium on Rock Fracture*, 1971, p. 47-65
- [34] F. Radjaï and V. Richefeu, *Contact dynamics as a nonsmooth discrete element method*. Mechanics of Materials, 2009. 41: p. 715-728.
- [35] F. Radjaï, *Multicontact dynamics of granular systems*. Computer Physics Communications, 1999. 121 - 122: p. 294-298.
- [36] G. Viggiani and S.A. Hall. *Full-field measurements, a new tool for laboratory experimental geomechanics*. In: S.E. Burns, P.W. Mayne, and J.C. Santamarina. *Deformational Characteristics of Geomaterials*, 2008: IOS Press, p. 3-26
- [37] M. Grédiac, *The use of full-field measurement methods in composite material characterization: interest and limitations*. Composite: Part A, 2004. 35: p. 751-761.
- [38] S.G. Grantham and F. Forsberg, *Measurement of granular flow in a silo using digital speckle radiography*. Powder Technology, 2004. 146: p. 56-65.
- [39] B. Pan, et al., *Two-dimensional digital image correlation for in-plane displacement and strain measurement: a review*. Measurement Science and Technology, 2009. 20(6).
- [40] J.W. Addiss, A. Collins, and W.G. Proud, *Optimisation and use of a digital speckle radiography algorithm for investigation of long rod penetration of granular media*. AIP Conference Proceedings, 2009. 1195: p. 1313-1316.
- [41] P. Richards, et al., *Analysis by X-ray microtomography of a granular packing undergoing compaction*. Phys. Rev. E, 2003. 68.
- [42] J. Doreau-Malioche, et al., *Characterising processes at sand-pile interface using digital image analysis and X-ray CT*. Geotechnique Letters, 2019. 9(4): p. 254-262.
- [43] B. Chevalier, Y. Tsutsumi, and J. Otani, *Direct Shear Behavior of a Mixture of Sand and Tire Chips Using X-ray Computed Tomography and Discrete Element Method*. International Journal of Geosynthetics and Ground Engineering, 2019. 5(2).
- [44] K. Zhu, et al., *Electrical capacitance tomography measurements on vertical and inclined pneumatic conveying of granular solids*. Chemical Engineering Science, 2003. 58: p. 4225-4245.

- [45] Z. Chaniecki, et al., *Application of electrical capacitance tomography for bulk solids flow analysis in silos*. Particle and Particle Systems Characterization, 2006. 23: p. 306-312.
- [46] H. Zhou, Q.Y. Tu, and H.G. Wang, *Investigation of the complex gas-solids flow characteristics in a fluidized bed with a Wurster tube by process tomography and CFD simulation*. Powder Technology, 2019. 357: p. 117-133.
- [47] K.M. Hill, A. Caprihan, and J. Kakalios, *Bulk segregation in rotated granular material measured by magnetic resonance imaging*. Physical Review Letters, 1997. 78(1): p. 50-53.
- [48] T.T.M. Nguyễn, et al., *Segregation in horizontal rotating cylinders using magnetic resonance imaging*. Physical Review E, 2011. 84.
- [49] M. Danczyk, et al., *Influence of contact parameters on Discrete Element method (DEM) simulations of flow from a hopper: Comparison with magnetic resonance imaging (MRI) measurements*. Powder Technology, 2020. 372: p. 671-684.
- [50] D.J. Parker, *Positron emission particle tracking and its application to granular media*. Review of Scientific Instruments, 2017. 88(5). Article no. 051803.
- [51] C.R.K. Windows-Yule, et al., *Positron Emission Particle Tracking of Granular Flows*. Annual Review of Chemical and Biomolecular Engineering, 2020. 11: p. 367-396.
- [52] M. Al-Shemmeri, et al., *Coffee bean particle motion in a spouted bed measured using Positron Emission Particle Tracking (PEPT)*. Journal of Food Engineering, 2021. 311. Article no. 110709.
- [53] G. Schneebeli, *Une analogie mécanique pour les terres sans cohésion*. Comptes Rendus de l'Académie des Sciences, 1956. 243: p. 125-126.
- [54] S.A. Hall, et al., *Localised deformation patterning in 2D granular materials revealed by digital image correlation*. Granular Matter, 2010. 12: p. 1-14.
- [55] V. Richefeu, G. Combe, and G. Viggiani, *An experimental assessment of displacement fluctuations in a 2D granular material subjected to shear*. Géotechnique Letters, 2012. 2: p. 113-118.
- [56] F. Calvetti, G. Combe, and J. Lanier, *Experimental micromechanical analysis of a 2D granular material: relation between structure evolution and loading path*. Mechanics of Cohesive-Frictional Materials, 1997. 2: p. 121-163.
- [57] A. Misra and H. Jiang, *Measured kinematic fields in the biaxial shear of granular materials*. Computers and Geotechnics, 1997. 20: p. 267-285.
- [58] A. Drescher and G. De Josselin De Jong, *Photoelastic verification of a mechanical model for the flow of a granular material*. Journal of the Mechanics and Physics of Solids, 1972. 20: p. 337-351.
- [59] M.P. Hariprasad and K. Ramesh, *Analysis of contact zones from whole field isochromatics using reflection photoelasticity*. Optics and Lasers in Engineering, 2018. 105: p. 86-92.

- [60] N. Karanjaokar and G. Ravichandran. (2015) *Experimental Inference of Inter-Particle Forces in Granular Systems Using Digital Image Correlation*. In: H. Jin, et al. *Advancement of optical methods in experimental mechanics, Vol 3. Conference Proceedings of the Society for Experimental Mechanics Series*, Greenville, SC, USA, Jun 02-05, 2014: Springer, Berlin, p. 379-385
- [61] N. Karanjaokar and G. Ravichandran. (2016) *Study of Energy Contributions in Granular Materials During Impact*. In: DYNAMIC BEHAVIOR OF MATERIALS, VOL 1. *Conference Proceedings of the Society for Experimental Mechanics Series*, Costa Mesa, CA, USA, Jun 08-11, 2015: Springer, New York, p. 199-204
- [62] E. Marteau and J.E. Andrade, *A novel experimental device for investigating the multiscale behavior of granular materials under shear*. *Granular Matter*, 2017. 19(4). Article no. 77.
- [63] R.C. Hurley, et al., *Dynamic Inter-Particle Force Inference in Granular Materials: Method and Application*. *Experimental Mechanics*, 2016. 56(2): p. 217-229.
- [64] R. Hurley, et al., *Extracting inter-particle forces in opaque granular materials: Beyond photoelasticity*. *Journal of the Mechanics and Physics of Solids*, 2014. 63(1): p. 154-166.
- [65] N. Karanjaokar, *Evaluation of energy contributions using inter-particle forces in granular materials under impact loading*. *Granular Matter*, 2017. 19(2). Article no. 36.
- [66] J.M. Dulieu-Barton and P. Stanley, *Development and applications of thermoelastic stress analysis*. *Journal of Strain Analysis for Engineering Design*, 1998. 33(2): p. 93-104.
- [67] G. Pitarresi and E.A. Patterson, *A review of general theory of thermoelastic stress analysis*. *Journal of Strain Analysis for Engineering Design*, 2003. 38(5): p. 405-417.
- [68] R.J. Greene, E.A. Patterson, and R.E. Rowlands, *Thermoelastic stress analysis*, in *Springer Handbook of Experimental Solid Mechanics*, W. Sharpe Jr, Editor. 2008, Springer. p. 743-768.
- [69] P. Jongchansitto, et al., *Using infrared thermography to study hydrostatic stress networks in granular materials*. *Soft Matter*, 2014. 10: p. 8603-8607.
- [70] R.L. Rangel, et al., *Experimental investigation of heat generation during granular flow in a rotating drum using infrared thermography*. *Powder Technology*, 2023. 426. Article no. 118619.
- [71] M.P. Luong, *Charateristic threshold and infrared vibrothermography of sand*. *Geotechnical Testing Journal*, 1986. 9(2): p. 80-86.
- [72] M.P. Luong, *Infrared thermography of the dissipative behaviour of sand*. *Proceedings of the Fifteenth International Conference on Soil Mechanics and Geotechnical Engineering vols 1-3*, 2001.

- [73] J.H. Lever, et al., *The mechanics of snow friction as revealed by micro-scale interface observations*. Journal of Glaciology, 2018. 64(243): p. 27-36.
- [74] J.L.M.P. de Lima and J.R.C.B. Abrantes, *Can infrared thermography be used to estimate soil surface microrelief and rill morphology?* Catena, 2014. 113: p. 314-322.
- [75] M. Grédiac, B. Blaysat, and F. Sur, *Extracting displacement and strain fields from checkerboard images with the localized spectrum analysis*. Experimental Mechanics, 2019. 59(2): p. 207-218.
- [76] M. Grédiac, B. Blaysat, and F. Sur, *On the Optimal Pattern for Displacement Field Measurement: Random Speckle and DIC, or Checkerboard and LSA?* Experimental Mechanics, 2020. 60(4): p. 509-534.
- [77] H.M. Jaeger and S.R. Nagel, *Physics of the granular state*. Science, 1992. 255(5051): p. 1523-1531.
- [78] K.L. Johnson, *Contact mechanics*. 1985: Cambridge University Press.
- [79] H. Hertz, *Miscellaneous Papers*. On the contact of elastic solids. 1896, London: Macmillan.
- [80] C.A. Coulomb, *Royale des Sciences*. Mémoire des mathématiques et de la physique présentes à l'académie. 1785, Paris: Imprimerie Royale.
- [81] F.P. Bowden and D. Tabor, *The Friction and Lubrication of Solids*. Vol. 1. 1950, Oxford: Clarendon Press.
- [82] J.C. Macrae, P.C. Finlayson, and W.A. Gray, *Vibration Packing of Dry Granular Solids*. Nature, 1957. 179(4574): p. 1365-1366.
- [83] R. Aoki and M. Suzuki, *Effect of particle shape on the flow and packing properties of non-cohesive granular materials*. Powder Technology, 1971. 4(2): p. 102-104.
- [84] M. Shahinpoor, *Statistical Mechanical Considerations on the Random Packing of Granular Materials*. Powder Technology, 1980. 25(2): p. 163-176.
- [85] A.J. Liu and S.R. Nagel, *Jamming and Rheology: Constrained Dynamics on Microscopic and Macroscopic Scales*. 2001, London: Taylor and Francis.
- [86] J.D. Bernal, *The Bakerian Lecture, 1962: The Structure of Liquids*. Proceedings of the Royal Society of London Series A-Mathematical and Physical Sciences, 1964. 280(1380): p. 299-322.
- [87] J.G. Berryman, *Random close packing of hard spheres and disks*. Physical Review A, 1983. 27(2): p. 1053-1061.
- [88] V. Baranau and U. Tallarek, *Random-close packing limits for monodisperse and polydisperse hard spheres*. Soft Matter, 2014. 10: p. 3826-3841.
- [89] T.C. Hales, *A proof of the Kepler conjecture*. Annals of Mathematics, 2005. 162: p. 1065-1185.
- [90] K.J. Dong, et al., *Role of interparticle forces in the formation of random loose packing*. Physical Review Letters, 2006. 96.

- [91] Z. Gazzillo, S. Franklin, and S.L. Alarcon, *Using Quantum Computers to Study Random Close Packing of Granular Discs*. 2019 Tenth International Green and Sustainable Computing Conference, 2019. Article no. 8957200.
- [92] G.Y. Onoda and E.G. Liniger, *Random loose packing of uniform spheres and the dilatancy onset*. Physical Review Letters, 1990. 64(22): p. 2727-2730.
- [93] L.F. Liu, et al., *Uniform and decoupled shape effects on the maximally dense random packings of hard superellipsoids*. Powder Technology, 2018. 338: p. 67-78.
- [94] C. Voivret, et al., *Space-filling properties of polydisperse granular media*. Phys. Rev. E, 2007. 76(021301).
- [95] R.Y. Yang, R.P. Zou, and A.B. Yu, *Computer simulation of the packing of fine particles*. Physical Review E, 2000. 62(3): p. 3900-3908.
- [96] A.B. Yu, et al., *On the relationship between porosity and interparticle forces*. Powder Technology, 2003. 130: p. 70-76.
- [97] D. He, N.N. Ekere, and L. Cai, *Computer simulation of random packing of unequal particles*. Physical Review E, 1999. 60(6): p. 7098-7104.
- [98] Y. Jin, J.G. Puckett, and H.A. Makse, *Statistical theory of correlations in random packings of hard particles*. Physical Review E, 2014. 89.
- [99] C.X. Li, et al., *Experimental and numerical investigation on the packing of binary mixtures of spheres and ellipsoids*. Powder Technology, 2020. 360: p. 1210-1219.
- [100] L.F. Liu, et al., *Determining random packing density and equivalent packing size of superballs via binary mixtures with spheres*. Chemical Engineering Science, 2019. 202: p. 270-281.
- [101] S.R. Williams and A.P. Philipse, *Random packings of spheres and spherocylinders simulated by mechanical contraction*. Physical Review E, 2003. 67.
- [102] J.M. Valverde and A. Castellanos, *Random loose packing of cohesive granular materials*. Europhysics letters, 2006. 75(6): p. 985-991.
- [103] G.W. Delaney, J.E. Hilton, and P.W. Cleary, *Defining random loose packing for nonspherical grains*. Physical Review E, 2011. 83.
- [104] I. Preechawuttipong, et al., *Static states of cohesive granular media*. Journal of Mechanical Science and Technology, 2007. 21: p. 1957-1963.
- [105] J. Blouwolff and S. Fraden, *The coordination number of granular cylinders*. Europhysics Letters, 2006. 76(6): p. 1095-1101.
- [106] N.W. Krapf, *Force propagation in isostatic granular packs*. Physical Review E, 2012. 86.
- [107] C. Insecca, V. Tournat, and V. Gusev, *Characterization of granular compaction by nonlinear acoustic resonance method*. Applied Physics Letters, 2008. 92(19). Article no. 191916.



- [108] K. Tell, et al., *Acoustic waves in granular packings at low confinement pressure*. Review of Scientific Instruments, 2020. 91(3). Article no. 033906.
- [109] E. Clemet, L. Bonneau, and B. Andreotti, *Surface wave acoustics of granular packing under gravity*. Powders and Grains 2009: Proceedings of the 6th International Conference on Micromechanics of Granular Media, 2009. 1145: p. 3-8.
- [110] C.H. Liu, et al., *Force fluctuations in bead packs*. Science, 1995. 269: p. 513-515.
- [111] B. Cambou, M. Jean, and F. Radjaï, *Micromechanics of Granular Materials*. 2009: John Wiley & Sons.
- [112] S.J. Antony, *Evolution of force distribution in three-dimensional granular media*. Physical Review E, 2000. 63.
- [113] J.M. Erikson, et al., *Force distributions in three-dimensional compressible granular packs*. Physical Review E, 2002. 66.
- [114] K. Bagi, *Statistical analysis of contact force components in random granular assemblies*. Granular Matter, 2003. 5: p. 45-54.
- [115] M. Tolomeo, et al., *An assessment of discrete element approaches to infer intergranular forces from experiments on 2D granular media*. International Journal of Solids and Structures, 2020. 187: p. 48-57.
- [116] N.P. Kruyt, *Micromechanical study of fabric evolution in quasi-static deformation of granular materials*. Mechanics of Materials, 2012. 44: p. 120-129.
- [117] F. Radjaï, H. Troadec, and S. Roux, *Micro-statistical features of cohesionless granular media*. Italian Geotechnical Journal, 2003. 3: p. 39-49.
- [118] J. Christoffersen, M.M. Mehrabadi, and S. Nemat-Nasser, *A micromechanical description of granular material behavior*. Journal of Applied Mechanics, 1981. 48: p. 339-344.
- [119] L. Rothenburg and A.P.S. Selvadurai. *A micromechanical definition of the Cauchy stress tensor for particulate media*. In: A.P.S. Selvadurai. *Proceedings of International Symposium on Mechanical Behaviour of Structured Media*, 1981: Elsevier, p. 469-486
- [120] K. Bagi, *Stress and strain in granular assemblies*. Mechanics of Materials, 1996. 22: p. 165-177.
- [121] J.E.S. Socolar, *Average stress and force fluctuations in noncohesive granular materials*. Physical Review E, 1998. 57(3): p. 3204-3215.
- [122] A.R. Leach, *Molecular modeling: Principles and applications*. 2001: Pearson Education Limited.
- [123] D. Frenkel and B. Smit, *Understanding molecular simulation: From algorithms to applications*. 2002: Academic Press.

- [124] L. Verlet, *Computer "experiment" on classical fluids. I. Thermodynamical properties of Lennard-Jones molecules*. Physical Review, 1967. 159(1): p. 98-103.
- [125] R.W. Hockney, *The potential calculation and some applications*. Methods in Computational Physics, 1970. 9: p. 136-211.
- [126] W.C. Swope, et al., *A computer simulation method for the calculation of equilibrium constants for the formation of physical clusters of molecules: Application to small water clusters*. Journal of Chemical Physics, 1982. 76: p. 637-649.
- [127] D. Beeman, *Some multistep methods for use in molecular dynamics calculations*. Journal of Computational Physics, 1976. 20: p. 130-139.
- [128] C.W. Gear, *Numerical initial value problems in ordinary differential equations*. 1971: Prentice Hall.
- [129] T. Pöschel and T. Schwager, *Computational granular dynamics: Models and algorithms*. 2005: Springer-Verlag.
- [130] F. Radjaï and F. Dubois, *Discrete-element modeling of granular materials*. 2011, New Jersey: John Wiley & Sons.
- [131] J. Schäfer, S. Dippel, and D.E. Wolf, *Force schemes in simulations of granular materials*. Journal de Physique I (France), 1996. 6: p. 5-20.
- [132] H.G. Matuttis, S. Luding, and H.J. Herrmann, *Discrete element simulations of dense packings and heaps made of spherical and non-spherical particles*. Powder Technology, 2000. 109(1-3): p. 278-292.
- [133] S.T. Nase, et al., *Discrete characterization tools for cohesive granular material*. Powder Technology, 2001. 116: p. 214-223.
- [134] W.L. Vargas and J.J. McCarthy, *Heat conduction in granular materials*. Aiche Journal, 2001. 47(5): p. 1052-1059.
- [135] X. Balandraud and J.B. Le Cam, *Some specific features and consequences of the thermal response of rubber under cyclic mechanical loading*. Archive of Applied Mechanics, 2014. 84(6): p. 773-788.
- [136] A. Chrysochoos and H. Louche, *An infrared image processing to analyse the calorific effects accompanying strain localisation*. International Journal of Engineering Science, 2000. 38: p. 1759-1788.
- [137] J.R. Samaca Martinez, et al., *Mechanisms of deformation in crystallizable natural rubber. Part 2: Quantitative calorimetric analysis*. Polymer, 2013. 54(11): p. 2727-2736.
- [138] G.A. Hopzapfel, *Nonlinear Solid Mechanics: A Continuum Approach for Engineering*. 2000, New York: John Wiley & Sons.
- [139] J.B. Le Cam, et al., *Thermomechanical Analysis of the Singular Behavior of Rubber: Entropic Elasticity, Reinforcement by Fillers, Strain-Induced*

- Crystallization and the Mullins Effect*. *Experimental Mechanics*, 2015. 55(4): p. 771-782.
- [140] J. Gough, *A description of a property of Caoutchouc, or Indian rubber*. *Memories of the Literacy and Philosophical Society of Manchester*, 1805. 1: p. 288-295.
- [141] J. J.P., *On some thermodynamic properties of solids*. *Philosophical Magazine* 4th, 1857. 227.
- [142] A. Chrysochoos, *Thermomechanical Analysis of the Cyclic Behavior of Materials*. IUTAM Symposium on Full-field Measurements and Identification in Solid Mechanics 2011, 2012. 4: p. 15-26.
- [143] A. Kylili, et al., *Infrared thermography (IRT) applications for building diagnostics: A review*. *Applied Energy*, 2014. 134: p. 531-549.
- [144] C.A. Balaras and A.A. Argiriou, *Infrared thermography for building diagnostics*. *Energy and Buildings*, 2002. 34: p. 171-183.
- [145] S. Bagavathiappan, et al., *Infrared thermography for condition monitoring - A review*. *Infrared Physics and Technology*, 2013. 60: p. 35-55.
- [146] Y.F. Venger, et al., *Infrared Thermography as an Effective Tool for Research and Industrial Application*. *Science and Innovation*, 2021. 17(5): p. 20-33.
- [147] P. Venegas, et al., *Towards the Automation of Infrared Thermography Inspections for Industrial Maintenance Applications*. *Sensors*, 2022. 22(2). Article no. 613.
- [148] D.L. Blunck, *Review: Applications of infrared thermography for studying flows with participating media*. *Experimental Thermal and Fluid Science*, 2022. 130. Article no. 110502.
- [149] T. Astarita and G.M. Carlomagno, *Infrared thermography for thermo-fluid-dynamics*. 2013: Springer-Verlag.
- [150] W. Herschel, *Experiments on the refrangibility of the invisible rays of the sun*. *Philosophical Transactions of the Royal Society of London*, 1800. 90: p. 284-292.
- [151] A. Rogalski and K. Chrzanowski, *Infrared devices and techniques*. *Opto-Electronics Review*, 2002. 10(2): p. 111-136.
- [152] X.P.V. Maldague, *Theory and practice of infrared technology for nondestructive testing*. 2001: John Wiley & Son.
- [153] V. Honorat, et al., *Calorimetric analysis of polymer behaviour using a pixel calibration of an IRFPA camera*. *Quantitative Infrared Thermography Journal*, 2005. 2(2): p. 153-171.
- [154] F. Sur and M. Grédiac, *Influence of the analysis window on the metrological performance of the grid method*. *Journal of Mathematical Imaging and Vision*, 2016. 56(3): p. 472-498.
- [155] E.M.C. Jones, et al., *Parameter covariance and non-uniqueness in material model calibration using the Virtual Fields Method*. *Computational Materials Science*, 2018. 152: p. 268-290.

- [156] J. Dym and H. Shames, *Solid Mechanics: A Variational Approach*. 1973, New York: McGraw-Hill Book Company.
- [157] L. MatWeb. *Overview of materials for High Density Polyethylene (HDPE), Injection Molded*. 23th June 2022]; Available from: <https://www.matweb.com/search/DataSheet.aspx?MatGUID=fce23f90005d4fbe8e12a1bce53ebdc8>.
- [158] E. ToolBox. *Friction - Friction Coefficients and Calculator*. 2004 23th June 2022]; Available from: [https://www.engineeringtoolbox.com/friction-coefficients-d\\_778.html](https://www.engineeringtoolbox.com/friction-coefficients-d_778.html).
- [159] Q. Bouyra, et al., *Using laser marking to engrave optimal patterns for in-plane displacement and strain measurement*. *Strain*, 2022. 58(2).
- [160] E. Toussaint, M. Grédiac, and F. Pierron, *The virtual fields method with piecewise virtual fields*. *International Journal of Mechanical Sciences*, 2006. 48(3): p. 256-264.
- [161] E.W. Grafarend, *Linear and Nonlinear Models: Fixed Effects, Random Effects, and Mixed Models*. 2006, Berlin: Walter de Gruyter.
- [162] K. Jongchansitto, et al., *Measuring forces in a 2D multi-contact system using the Virtual Fields Method: principle, simulations and experimental application to a three-particle system*. *European Journal of Mechanics - A/Solids*, 2023. [Under reviewing].
- [163] S.Y. Qin, et al., *Influence of the sampling density on the noise level in displacement and strain maps obtained by processing periodic patterns*. *Measurement*, 2021. 173. Article no. 108570.
- [164] F. Sur, B. Blaysat, and M. Grédiac, *Determining displacement and strain maps immune from aliasing effect with the grid method*. *Optics and Lasers in Engineering*, 2016. 86: p. 317-328.
- [165] F. Sur and M. Grédiac, *On noise reduction in strain maps obtained with the grid method by averaging images affected by vibrations*. *Optics and Lasers in Engineering*, 2015. 66: p. 210-222.
- [166] K. Shibata, T. Yamaguchi, and M. Kishi, *Friction and wear behavior of polyamide 66 composites filled with rice bran ceramics under a wide range of Pv values*. *Tribology Online*, 2015. 10(2): p. 213-219.
- [167] J. Batsale, et al., *Thermographic analysis of material behavior*, in *Full-field measurements and identification in solid mechanics*, M. Grédiac and F. Hild, Editors. 2012, Wiley: Hoboken. p. 439-468.
- [168] J.M. Dulieu-Barton, *Thermoelastic Stress Analysis*, in *Optical methods for solid mechanics: a full-field Approach*, P.K. Rastogi and E. Hack, Editors. 2012, Wiley-VCH: Weinheim.
- [169] P. Germain, Q.S. Nguyen, and P. Suquet, *Continuum thermodynamics*. *Journal of Applied Mechanics*, 1983. 105(50): p. 1010-1020.

- [170] B. Halphen and Q.S. Nguyen, *Sur les matériaux standards généralisés*. Journal de Mécanique, 1975. 14: p. 39-63.
- [171] F. Radjaï, J.N. Roux, and A. Daouadji, *Modeling granular materials: Century-long research across scales*. Journal of Engineering Mechanics, 2017. 143(4). Article no. 4017002.
- [172] J. Barés, et al., *Softer than soft: Diving into squishy granular matter*. Papers in Physics, 2022. 14. Article no. 140009.
- [173] M. Cárdenas-Barrantes, et al., *Experimental validation of a micromechanically based compaction law for mixtures of soft and hard grains*. Physical Review E. 106(2). Article no. L022901.
- [174] P. Pichon. *Fatigue thermomécanique des élastomères polyurethane : caractérisation expérimentale de l'évolution des microstructures et modélisation des échanges thermiques*. PhD thesis report, Institut National des Sciences Appliquées de Lyon, 2010: p. 136
- [175] A. Chrysochoos and R. Peyroux, *Experimental analysis and numerical simulation of thermomechanical couplings in solid materials*. Revue Générale de Thermique, 1998. 37(7): p. 582-606.
- [176] C. Douellou, X. Balandraud, and E. Duc, *Fatigue characterization by heat source reconstruction under continuously varying stress amplitude*. International Journal of Fatigue, 2022. 159. Article no. 106782.
- [177] D. Cantor, et al., *Rheology and structure of polydisperse three-dimensional packings of spheres*. Physical Review E, 2018. 98(5). Article no. 052910.
- [178] V.L. Popov, *Rigorous Treatment of Contact Problems – Hertzian Contact*, in *Contact Mechanics and Friction*. 2010, Springer Berlin: Heidelberg. p. 55-70.
- [179] K. Jongchansitto, et al., *Calorific Analysis of the Mechanical Response of Granular Materials Composed of Ellipsoidal Rubbery Particles*. Experimental Mechanics, 2023. 63(7): p. 1135-1155.

## APPENDIX A

### Preliminary simulation of heat transfer in a granular system

This section provide a preliminary numerical simulation relying on MD with heat diffusion modeling (see Section 1.2.7 in the bibliography and state-of-the-art chapter). The objective is to investigate the temperature fields in granular systems due to external mechanical loading. The present study is a first attempt from the present author to numerically investigate thermomechanical effects (temperature changes due to mechanical loading) in granular systems. This endeavor may pave the way for further research into the specifics of the thermomechanical effects discussed in Section 4.

#### A.1. Numerical preparation

Three granular composite configurations were prepared as the two-dimensional numerical composite samples in the present study. The granular systems were made of two different constitutive materials: one is polyoxymethylene (POM), used to prepare “stiff” particles; the other one is high-density polyethylene (HDPE), used to create “soft” particles. It must be noted that the stiff particles are approximately four times stiffer than the soft ones [69]. The locations of the particles in this numerical study corresponded to the locations from an earlier experimental study. This experimental study was performed in 2014 within the collaboration between my two establishments, namely Chiang Mai University and Clermont Auvergne University. In the experiments, the locations of particles for each configuration were extracted from an optical image of a real composite granular system. The extracted locations were then employed to prepare initial states for numerical simulations. Table A.1 presents configurations of all tested samples. Sample #1 is a monodisperse system, whereas Samples #2 and #3 are bidisperse systems due to their diameter ratio being different from 1.

Table A.1 List and details of the tests presented in the this numerical study.

Sample	Diameter ratio	Number of particles	Total number of particles
	$D_{stiff}/D_{soft}$	$N_{stiff} : N_{soft}$	
#1	1.0	638 : 597	1235
#2	1.6	334 : 371	705
#3	3.0	86 : 466	552

Each particle was deposited inside a box consisting of four rigid walls. In the simulation, a vertical compression force of 60 kN was incrementally applied to granular samples by the bottom wall under the quasi-static condition. The force was applied completely from 0 to 60 kN in 4 seconds. The time step is equal to 2E-6. The gravitational force was also taken into account, although it can be negligible compared to the magnitude of the external loading. The normal and tangential forces between the particles were calculated using Equation 1.22 and Equation 1.23, respectively. The contact forces between particles and wall were also computed. The effective contact stiffness  $k_{eff}$  depends on the type of contacting particles: it is defined by  $(k_{stiff} \times k_{soft}) / (k_{stiff} + k_{soft})$  for the inter-particle contacts, while the case of particle-wall contacts is defined by the stiffness of the particles in contact with the wall (assumed to be undeformable). The thermal conductivity and HDPE is equal to 0.31 and 0.49 W/m·C, respectively. The heat convection coefficient of still air is equal to 0.025 W/m·C.

After calculation, the contact forces and relative velocities were employed to compute the heat generation in each particle from Equation 1.24, which is associated to energy dissipation. a particle which has a temperature different from its neighbors exchanges heat with them (when they are in contact). This phenomenon can be expressed in terms of heat conduction depending on the contact area and the effective thermal conductivity, described in Equation 1.25 and Equation 1.26. Furthermore, the initial temperature of all particles in all configurations is defined to be 25 °C, corresponding to the ambient temperature in the experiments. It was assumed that the ambient air in the void of the granular systems was not flowing, which means the heat convection can be deduced from Equation 1.27. However, the heat convection of still air is rather low due

to its heat convection coefficient. The heat convection can be neglected. After the calculation of the local heat effect, it is possible to update the temperature of each particle at the next time step. Iterative calculation was performed until reaching the maximum external force.

## A.2. Results and discussion

Let us recall that the simulation provides one temperature per particle. The *normalized* temperature change (at the maximum external force applied) is then considered for the statistical analysis of the results. It is defined as the temperature change of the particle divided by the average temperature change of all the particles inside the granular sample. This normalized temperature change mimics the normalized contact force or stress, which are typically used in granular studies, in order to enable similarly the results.

### A.2.1. Field of normalized temperature changes

The normalized temperature change  $\Delta T_{norm}$  of all the particles was plotted with their positions to create a field of normalized temperature change, both for the simulation results: see Figure 4.1.

Figure A.1 show the fields of normalized temperature change of each sample from numerical simulation. It is clearly seen that the particles with high temperature change in numerical simulation occur at the top the granular system of sample #1 in Figure A.1-a. Considering samples #2 and #3 in Figures A.1-b and A.1-c, most of particles which their temperature change is lower than the average temperature change is stiff particles. It must be noted that this temperature change cannot imply to the amount of heat storage of each particle. In fact, not only the mass but also the specific heat capacity of stiff particles is larger than those of soft particles. This is a reason why the lower temperature occurs at the stiff particles instead of the soft particles. It means that the soft particles, which are HDPE, can give a higher temperature response and they require less external mechanical loading for investigating temperature change. This is a preliminary simulation to investigate the thermomechanics in granular materials. The self-heating observed in the



simulation can be deduced to mechanical dissipation effect, which is one of the thermomechanical phenomena.

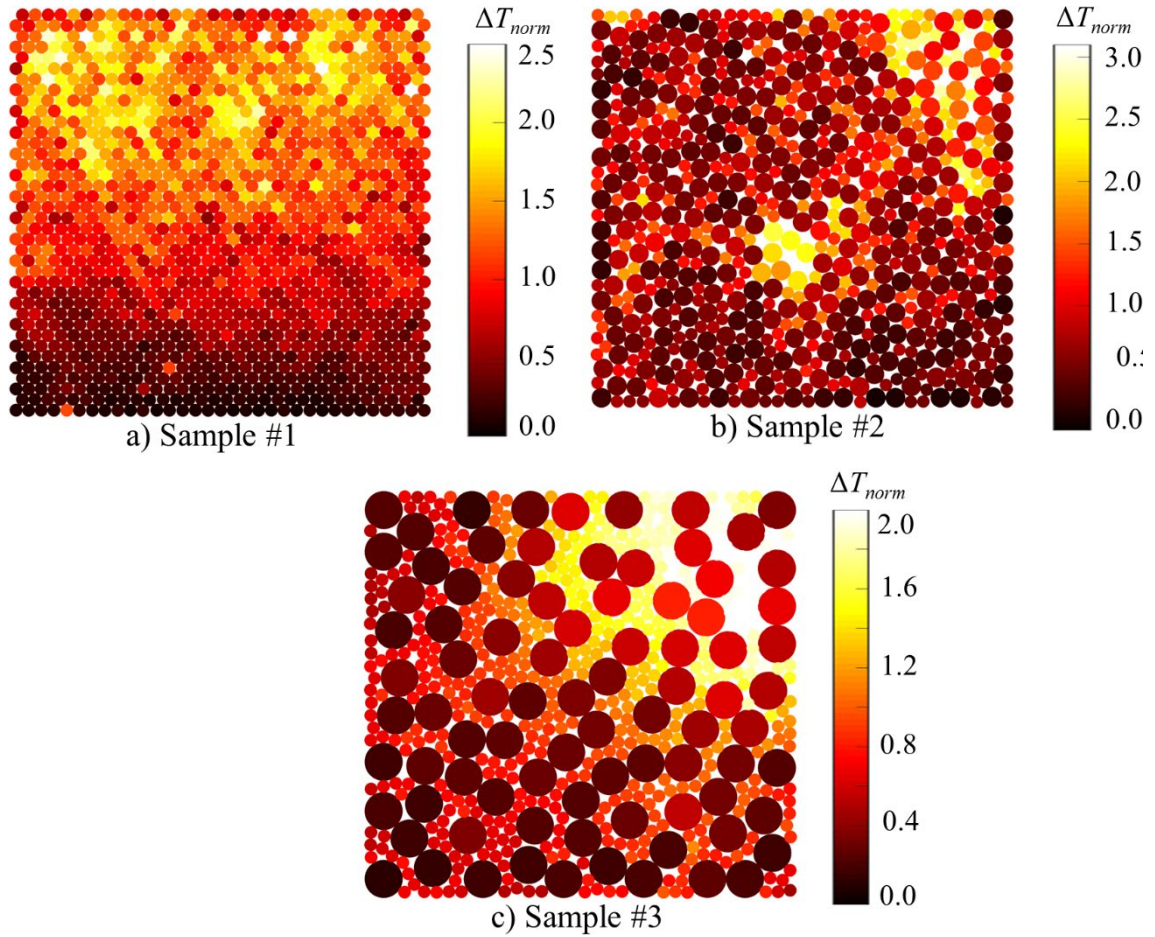


Figure A.1 Fields of normalized temperature changes generated by simulations: a) Sample #1; b) Sample #2; c) Sample #3.

#### A.2.2. Probability density function of normalized temperature change ( $P(\Delta T_{norm})$ )

In this section, a probability density function (PDF) of the normalized temperature change ( $P(\Delta T_{norm})$ ) was determined for each configuration. It must be noted that five additional simulations with randomly changed the particle locations were systematically performed for each sample: Simulations A, B, C, D, and E, respectively. Figure A.2 shows the PDF of the normalized temperature change of each configuration obtained from the simulations in semi-natural logarithmic scale. There are two types of PDFs which are the temperature change lower than the mean of the temperature change ( $P(\Delta T_{norm} < \Delta \bar{T}_{norm})$ )

and PDFs which are the temperature change higher than the mean of the temperature change ( $P(\Delta T_{norm} > \Delta \bar{T}_{norm})$ ) as illustrated in left and right columns in Figure A.2, respectively.

The distribution curves of  $P(\Delta T_{norm} < \Delta \bar{T}_{norm})$  of simulation are governed by power's law as discussed in section 1.2.4, except the simulation in sample #3. Furthermore, the percentage of particles having the temperature change lower than the mean of the temperature change are approximately 40%. On the contrary, the distribution curves of  $P(\Delta T_{norm} > \Delta \bar{T}_{norm})$  obtained by both simulations are in the same trend for all the samples, which exhibit as an exponential decay as discussed in section 1.2.4. This distribution law corresponds to the well-known force and stress distributions [69, 78]. Moreover, the function of exponential decreasing is also observed when considering only stiff particles and only soft particles separately. It is worth mentioning that simulation percentages of particles having the temperature change higher than the mean of the temperature change are approximately 40%. This is evidence that the PDF of thermal response can be analyzed in the same method as the PDFs of forces and stresses in granular material.

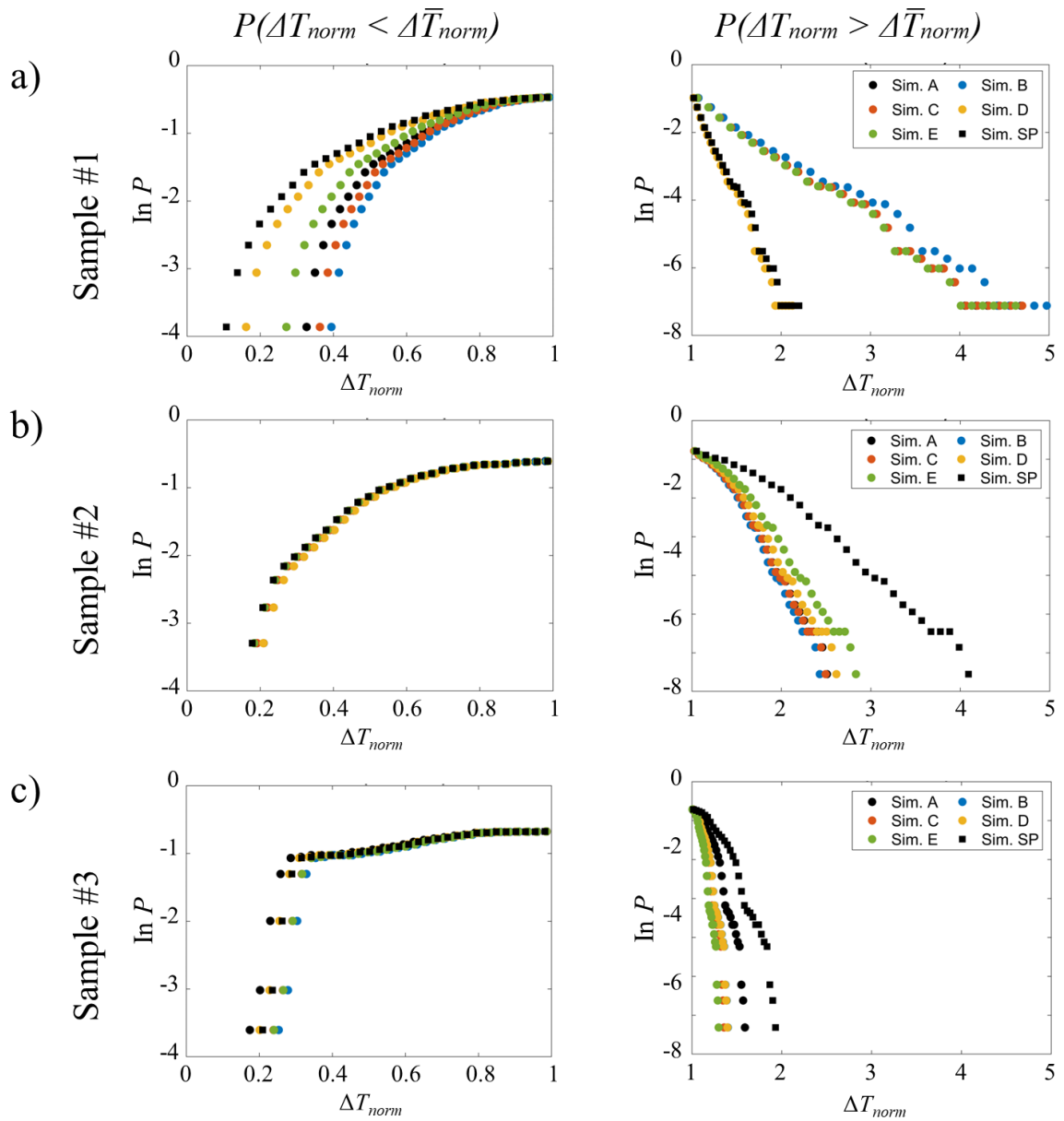


Figure A.2 Probability density function of normalized temperature change obtained from both simulations in semi-natural logarithmic scale for: a) Sample #1; b) Sample #2; c) Sample #3. Note that simulations “A”, “B”, “C”, “D”, and “E” were performed under the same experimental configuration, excluding the particle locations, while the simulation “SP” was conducted under all the same as in the experiments (the simulation in the previous section).

### **A.3. Conclusion**

In this study, the numerical simulation approach, MD was employed to validate the heat diffusion in 2D granular composites under a confined mechanical loading. Three configurations of experiments were chosen to prepare numerical samples for this purpose. Each sample was then subjected to a compressive loading. Only heat generation, heat conduction, and heat convection were taken into account in this study. Note that normalized temperature change, which can be determined from the temperature change in the particle divided by the means of the temperature change of all the particles inside the granular sample, is considered for the analysis. The normalized temperature change fields and the probability density function of normalized temperature change were then employed to statistically analyze for both results obtained from the simulations. Considering the temperature change fields, an inhomogeneous temperature distribution was clearly observed in all the samples for both simulations. The power's law and exponential decay distribution were clearly observed in the statistical analysis of all numerical simulations. This distribution corresponds to the well-known force and stress distribution law. The number of particles having the temperature change higher than the mean of the temperature change is approximately 40% for all tests. On the contrary, the particles having the temperature change lower than the mean of the temperature change is approximately 60%. These results are corresponding to the force distribution in the past study [11]. Additionally, it was found that HDPE, soft particle, can exhibit a high thermal response due to a high temperature change.



## APPENDIX B

### Estimating interpenetration and sliding between cylinders with ellipsoidal cross section

We consider two cylinders  $S_1$  and  $S_2$  in contact at point I, see the schematic view in Figure B.1. The objective here is to properly define how to estimate the relative movement between  $S_1$  and  $S_2$ . Assuming that the movement in terms of rotation and translation is small, the rigid-body movement of each cylinder  $S_i$ ,  $i = 1, 2$  can be modeled by two vectors  $\underline{\theta}_i$  and  $\underline{U}_{O_i}$  where  $O_i$  is the center of each cylinder  $S_i$ . Vectors  $\underline{\theta}_i$  and  $\underline{U}_{O_i}$  are respectively the rotation vector of  $S_i$  and the displacement vector of its center  $O_i$ . The coordinates of all the points represented in the figure are assumed to be identified manually in the images of the deformed and current configurations taken by the IR camera during the test. The components of vectors  $\underline{U}_{O_1}$ ,  $\underline{U}_{O_2}$ ,  $\underline{\theta}_1$  and  $\underline{\theta}_2$  are determined by hand, by considering the coordinates of the points in the deformed and in the reference configurations. Each vector  $\underline{\theta}_i$  is defined by a single angle  $\theta_i$  which is the rotation about a unit vector  $\underline{e}_z$  directly perpendicular to  $\underline{e}_x$  and  $\underline{e}_y$ . Thus,  $\underline{\theta}_i = \theta_i \underline{e}_z$ .  $\theta_i$  can be regarded as the small change, when the system is loaded, of the initial orientation  $\gamma_i$  of the major axis of cylinder  $S_i$ ; see Figure B.1 where this initial orientation  $\gamma_i$  is represented for each cylinder. Finally, it is worth noting that  $\theta_i$  can be negative or positive, depending on the orientation of the rotation when the cylinders slightly move between the initial and deformed systems.

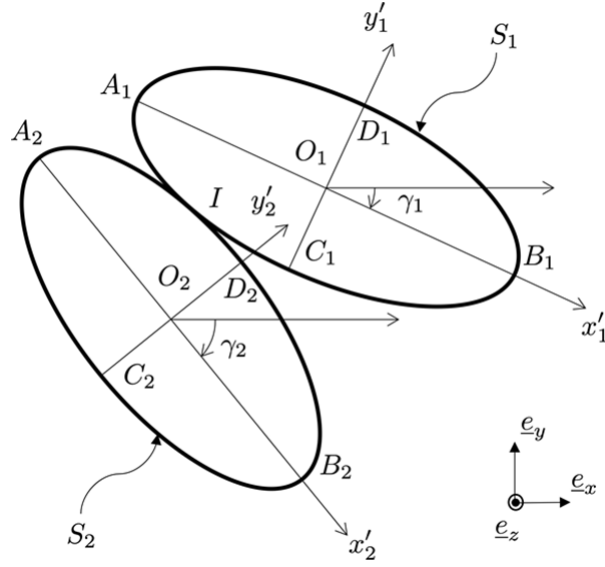


Figure B.1 Schematic view of the cross-sections of two cylinders in contact at point I.

The relative displacement between  $S_2$  and  $S_1$  is denoted  $\underline{U}_{S_2/S_1}$ . Vector  $\underline{U}_{S_2/S_1}$  is merely equal to the difference between  $\underline{U}_{I_{S_2}}$  and  $\underline{U}_{I_{S_1}}$ , where  $I_{S_1}$  and  $I_{S_2}$  denote point I belonging to cylinders  $S_1$  and  $S_2$  respectively. Their displacement is different if interpenetration or/and sliding occurs between  $S_2$  and  $S_1$ . Hence,  $\underline{U}_{S_2/S_1} = \underline{U}_{I_{S_2}} - \underline{U}_{I_{S_1}}$ . Vectors  $\underline{U}_{I_{S_2}}$  and  $\underline{U}_{I_{S_1}}$  can be deduced from both the displacement of the center of each cylinder and the rotation of these cylinders. Indeed, we have

$$\begin{cases} \underline{U}_{I_{S_1}} = \underline{U}_{O_1} + \underline{I}_{S_1} \underline{O_1} \times \underline{\Theta}_1 \\ \underline{U}_{I_{S_2}} = \underline{U}_{O_2} + \underline{I}_{S_2} \underline{O_2} \times \underline{\Theta}_2 \end{cases} \quad (\text{B.1})$$

where symbol “ $\times$ ” represents the cross product of two vectors. Thus

$$\underline{U}_{S_2/S_1} = \underline{U}_{O_2} - \underline{U}_{O_1} + \underline{I}_{S_2} \underline{O_2} \times \underline{\Theta}_2 - \underline{I}_{S_1} \underline{O_1} \times \underline{\Theta}_1 \quad (\text{B.2})$$

The idea is now to distinguish between the normal and the tangential projection of this relative displacement to determine the interpenetration between  $S_1$  and  $S_2$  as well as the sliding of  $S_2$  on  $S_1$ . For this, it is necessary to know the components of a unit vector  $\underline{t}$ , which is tangent to both ellipses at point I. Vector  $\underline{U}_{S_2/S_1}$  will then be projected on  $\underline{t}$  to determine sliding, and on  $\underline{n}$  to determine interpenetration.

*Calculation of the tangent and normal vectors at the contact point.*

To find  $\underline{t}$  and  $\underline{n}$ , we need to write the parametric equations of the ellipse modeling the border of  $S_i$ ,  $i = 1, 2$ . The local coordinate system of each ellipse being defined by the axes going through its major and minor axes (see Figure B.1), the Cartesian equation of the ellipse can be written as follows in this local coordinate system:

$$\left(\frac{x'_i{}^2}{a_i'^2}\right) + \left(\frac{y'_i{}^2}{b_i'^2}\right) = 1 \quad (\text{B.3})$$

where  $2a_i = \|\underline{A_i B_i}\|$ ,  $2b_i = \|\underline{C_i D_i}\|$  and  $x'_i$  and  $y'_i$  are the local coordinates of a point located on the ellipse defining the cross-section of  $S_i$ . The relationship between local and global coordinates writes as follows for each ellipse  $i$ :

$$\begin{pmatrix} x'_i \\ y'_i \end{pmatrix} = \begin{bmatrix} \cos \gamma_i & \sin \gamma_i \\ -\sin \gamma_i & \cos \gamma_i \end{bmatrix} \begin{bmatrix} x - x_{O_i} \\ y - y_{O_i} \end{bmatrix} \quad (\text{B.4})$$

In the global coordinate system, Equation B.6 becomes

$$\begin{aligned} & \left( \frac{\left( (x - x_{O_i}) \cos \gamma_i - (y - y_{O_i}) \sin \gamma_i \right)^2}{a_i^2} \right) \\ & + \left( \frac{\left( -(x - x_{O_i}) \sin \gamma_i + (y - y_{O_i}) \cos \gamma_i \right)^2}{b_i^2} \right) = 1 \end{aligned} \quad (\text{B.5})$$

where  $x_{O_i}$  and  $y_{O_i}$  are the coordinates of the center  $O_i$  of each ellipse  $i$ . Finally, the parametric equations of each ellipse  $i$  are deduced with the following change of variables:

$$\begin{cases} \frac{x'_i}{a_i} = \frac{(x - x_{O_i}) \cos \gamma_i - (y - y_{O_i}) \sin \gamma_i}{a_i} = \cos \alpha \\ \frac{y'_i}{b_i} = \frac{-(x - x_{O_i}) \sin \gamma_i + (y - y_{O_i}) \cos \gamma_i}{b_i} = \sin \alpha \end{cases} \quad (\text{B.6})$$

with  $\alpha \in [0, 2\pi]$ . The coordinates of point I, namely  $x_I$  and  $y_I$ , are picked by hand in the global coordinate system. The value of  $\alpha$  at point I, denoted by  $\alpha_I$ , is therefore directly



deduced from the following two equations, since all the quantities on the right side of both the equalities are known:

$$\begin{cases} \cos \alpha_1 = \frac{(x_1 - x_{O_i}) \cos \gamma_i - (y_1 - y_{O_i}) \sin \gamma_i}{a_i} \\ \sin \alpha_1 = \frac{-(x_1 - x_{O_i}) \sin \gamma_i + (y_1 - y_{O_i}) \cos \gamma_i}{b_i} \end{cases} \quad (\text{B.7})$$

The objective is now to find the components of the tangent vector  $\underline{t}$  in the local coordinate system  $i$ . These components are denoted  $t_{x'_i}$  and  $t_{y'_i}$ . First the parametric equations of ellipse  $i$  can be written as follows in this local coordinate system:

$$\begin{cases} x'_i = a_i \cos \alpha \\ y'_i = b_i \sin \alpha \end{cases} \quad (\text{B.8})$$

The components of the tangent vector  $\underline{t}$  in the local basis are obtained by derivativizing Equation B.11. This gives

$$\begin{cases} t_{x'_i} = -a_i \sin \alpha \\ t_{y'_i} = b_i \cos \alpha \end{cases} \quad (\text{B.9})$$

These components must finally be expressed in the global coordinate system, which gives

$$\begin{pmatrix} t_{x_i} \\ t_{y_i} \end{pmatrix} = \begin{bmatrix} \cos \gamma_i & -\sin \gamma_i \\ \sin \gamma_i & \cos \gamma_i \end{bmatrix} \begin{bmatrix} t_{x'_i} \\ t_{y'_i} \end{bmatrix} \quad (\text{B.10})$$

The components of vector  $\underline{n}$ , which is directly perpendicular to  $\underline{t}$ , are defined by

$$\begin{cases} n_{x_i} = t_{y_i} \\ n_{y_i} = -t_{x_i} \end{cases} \quad (\text{B.11})$$

The components of  $\underline{t}$  and  $\underline{n}$  at point I are simply obtained by feeding Equation B.12 above with  $\alpha_1$  found with Equation B.10 and then applying Equation B.13 and B.14 in this particular case. It should be checked that vector  $\underline{n}$  is correctly oriented, i.e., outwards.

**Remark** — Each cylinder  $i$  should provide its own vector  $\underline{t}$ . For a given contact, two cylinders being involved, it should be verified that these two versions of the same tangent vector are close to each other. The mean vector should be retained for the following and final calculations proposed in Equation B.15. The same remark holds for  $\underline{n}$ .

*Final estimation of interpenetration and sliding between ellipses.*

The  $\underline{n}$  and  $\underline{t}$  being defined at point I, the amplitude of the sliding  $sld$  of  $S_2$  on  $S_1$  can be obtained by projecting  $\underline{U}_{S_2/S_1}$  defined in Equation B.5 on vector  $\underline{t}$  calculated at point I, and the interpenetration  $int$  of  $S_2$  in  $S_1$  by projecting  $\underline{U}_{S_2/S_1}$  on vector  $\underline{n}$  calculated at point I. These two quantities are equal to:

$$\begin{cases} sld = \underline{U}_{S_2/S_1} \cdot \underline{t} \\ int = -\min(\underline{U}_{S_2/S_1} \cdot \underline{n}, 0) \end{cases} \quad (\text{B.12})$$

where “ $\cdot$ ” represents the dot product of two vectors. In Equation B.15 above,  $\underline{n}$  should have the same orientation of vector  $\underline{O_1O_2}$  to consider that interpenetration occurs only if the projection of  $\underline{U}_{S_2/S_1}$  onto  $\underline{n}$  is negative. If this projection is positive, it means that  $S_2$  and  $S_1$  are no longer in contact after loading the system, so no interpenetration occurs and  $int = 0$ . Concerning  $sld$ , it is worth mentioning that its absolute value should be considered for comparison purposes with mechanical dissipation, which is a positive calorific quantity.

The procedure above should be applied to each cylinder of the system and to each contact point between this cylinder and its neighbors.